Technical Physics, Vol. 45, No. 7, 2000, pp. 813–820. Translated from Zhurnal Tekhnicheskoĭ Fiziki, Vol. 70, No. 7, 2000, pp. 1–8.

Theory of Cyclotron Superradiance from a Moving Electron Bunch under Group Synchronism Conditions

N. S. Ginzburg, I. V. Zotova, and A. S. Sergeev

Institute of Applied Physics, Russian Academy of Sciences, ul. Ul'yanova 46, Nizhni Novgorod, 603600 Russia

Received August 5, 1999

Abstract—A theory is presented of cyclotron superradiance from an electron bunch rotating in a uniform magnetic field and drifting at a velocity close to the group velocity of a wave propagating in a waveguide. It is shown that, in a comoving frame of reference, the bunch emits radiation at a frequency close to the cutoff frequency of the waveguide. Superradiance implies the azimuthal self-bunching of electrons, which is accompanied by coherent emission of the stored rotational energy in a short electromagnetic pulse. Linear and nonlinear stages of the process are analyzed. The growth rate of the superradiance instability is determined. It is shown that the maximum growth rate is attained under group synchronism conditions. The peak power and the characteristic duration of the cyclotron superradiance pulse are determined by numerical simulation. The characteristic features of the superradiance pulses are described in the comoving and laboratory frames. The results of theoretical analysis are compared with experimental data. *© 2000 MAIK "Nauka/Interperiodica".*

INTRODUCTION

Induced emission from a spatially localized electron ensemble (bunch) whose size significantly exceeds the emission wavelength but is much smaller than the interaction scale length is one of the promising methods for generating ultrashort electromagnetic pulses. Emission from such a bunch can be considered a classical analog of a quantum effect known as Dicke superradiance [1–3], which is the emission of an electromagnetic pulse with a duration shorter than the relaxation time of the emitting atomic ensemble with population inversion. In classical electrodynamics, superradiance (SR) can be attributed to various mechanisms for induced emission [4–21]; in particular, SR can be produced by an electron bunch rotating in a uniform magnetic field (cyclotron SR) [10–22].

Cyclotron SR implies the azimuthal self-bunching of electrons, which is accompanied by coherent emission of the stored rotational energy. The phase self-locking is related to the relativistic dependence of the gyrofrequency on the particle energy [23] and is similar to that occurring in cyclotron resonance masers (CRM). However, in CRMs, quasi-continuous electron beams are used; i.e., the electrons that leave the interaction region are replaced by the electrons continuously injected from the cathode, thus providing the conditions for steady-state generation. In contrast, SR is pulsed in character and can be realized when each particle stays in a moving or resting electron bunch for a long time (ideally, for an infinitely long time). This fact also accounts for the absence of an SR threshold [18].

Earlier, we showed [19] that the regime of group synchronism is the most favorable for the observation of cyclotron SR. In this regime, the drift velocity of the electron bunch is close to the group velocity of the electromagnetic wave:

$$V_{\parallel} \approx V_{\mathrm{gr}}. \tag{1}$$

The low rate at which the energy outflows from the electron resonator formed by the electron bunch allows the maximum growth rate of the SR instability [16, 19].

Condition (1) can be met, e.g., when the radiation propagates in a waveguide; in this case, the dispersion curves of the wave and of the electron flux are tangent (Fig. 1a).[1] Note that, in the comoving frame, in which the bunch as a whole is at rest, the regime of group synchronism corresponds to the emission of radiation at a frequency close to the cutoff frequency and, therefore, exhibits several advantages typical of electron–wave interaction in gyrotrons, in which the operating mode is also excited at the quasi-cutoff frequency [22]. In particular, SR at the quasi-cutoff frequency is less sensitive to the scatter in the electron bunch parameters, including the longitudinal bunch spreading caused by both Coulomb repulsion and the spread in the initial electron velocities.

Earlier, we reported on the first experimental observations of cyclotron SR in the millimeter wavelength range [20, 21]. In those experiments, we used electron bunches with a length of 5–7 cm, particle energy of up to 200–250 keV, and current of about 200–500 A. The electron bunches propagated in a 30-cm smooth cylindrical waveguide placed in a uniform magnetic field. We observed the generation of ultrashort (up to 400 ps) electromagnetic pulses with the peak power higher than

[1] Group synchronism condition (1) can also be met in the case when an electron bunch propagates in a dispersive medium, e.g., in a homogeneous plasma.

1063-7842/00/4507-0813$20.00

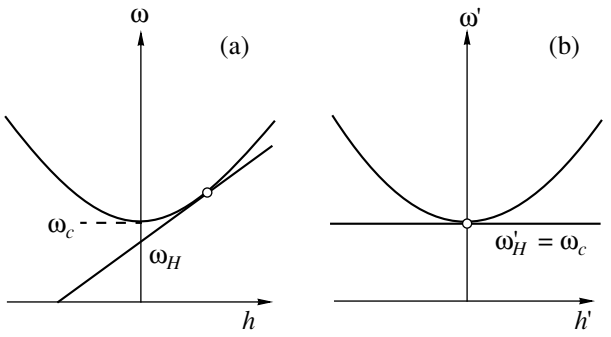

Fig. 1. Dispersion curves corresponding to the regime of group synchronism in (a) laboratory frame and (b) comoving frame.

200 kW. SR pulses were recorded only under conditions close to the condition of group synchronism with various waveguide modes. Far from group synchronism, the generation of SR pulses was absent. Thus, the experimental results proved that the regime of group synchronism is optimum for SR.

This paper is devoted to a theoretical study of cyclotron SR in the regime of group synchronism.

1. CYCLOTRON SUPERRADIANCE IN THE COMOVING FRAME

1.1. Basic Equations

Let a planar bunch of cyclotron oscillators of length b move in a cylindrical waveguide at a longitudinal velocity close to the group velocity of an electromagnetic wave, so that condition (1) is satisfied. In the laboratory frame, the dispersion curve of the electromagnetic wave ($h = c^{-1}(\omega^2 - \omega_c^2)^{1/2}$) and of the electron flux ($\omega - hV_\parallel = \omega_H$) are tangent (Fig. 1a). Here, ω_c is the waveguide cutoff frequency and $\omega_H = eH_0/mc\gamma$ is the relativistic gyrofrequency.

We consider the emission from the electron bunch in the comoving frame K', in which the bunch as a whole is at rest. The Lorentz transformation for the longitudinal wave number h' is

$$h' = \gamma_\parallel\left(h - \frac{\omega V_\parallel}{c^2}\right) = \gamma_\parallel h\left(1 - \frac{V_\parallel}{V_{\rm ph}c^2}\right),$$

where $V_{\rm ph} = \omega/h$ is the phase velocity of the electromagnetic wave and $\gamma_\parallel = (1 - V_\parallel^2/c^2)^{-1/2}$.

It is well known that, when an electromagnetic wave propagates in a waveguide, the relationship $V_{\rm gr}V_{\rm ph} = c^2$ holds [23]. It is seen from the group synchronism condition (1) that the longitudinal wavenumber vanishes in the comoving frame. Similarly, the allowance for the relationship $\mathbf{E}_\perp = [\mathbf{H}_\perp, \mathbf{z}_0]V_{\rm ph}/c$ (where $\mathbf{z}_0$ is a unit vector), which is valid for transverse electric (TE) waveguide modes, yields the following expression for the transverse component of the magnetic field:[2]

$$\mathbf{H}'_\perp = \gamma_\parallel\left(\mathbf{H}_\perp - \frac{V_\parallel}{c}[\mathbf{z}_0, \mathbf{E}_\perp]\right) = \gamma_\parallel\mathbf{H}_\perp\left(1 - \frac{V_\parallel V_{\rm ph}}{c^2}\right) \longrightarrow 0.$$

Therefore, the regime of group synchronism in the laboratory frame (the dispersion curves are tangent) corresponds to the emission of radiation at a quasi-cutoff frequency in the comoving frame (Fig. 1b).

Thus, in the K' frame, the bunch electrons rotate in the magnetic field but the bunch as a whole is at rest. The linear size of the bunch in the z' direction is $b' = b\gamma_{\parallel 0}$. The bunch radiates isotropically in the $\pm z'$ directions. Assuming that the transverse field structure of the emitted radiation coincides with that of one of the waveguide modes $\mathbf{E}_\perp(\mathbf{r}_\perp)$, we represent the radiation field in the form

$$\mathbf{E}' = {\rm Re}[\mathbf{E}_\perp(\mathbf{r}_\perp)A'(z', t')\exp(i\omega_c t')], \qquad (2)$$

where ω_c is the carrier frequency coinciding with the cutoff frequency of the operating mode. According to the dispersion relations, the evolution of the axial field $A'(x', t')$ distribution is described by the inhomogeneous parabolic equation

$$i\frac{\partial^2 a}{\partial Z'^2} + \frac{\partial a}{\partial \tau'} = 2if(Z')GJ. \qquad (3)$$

The transverse electric current $J = 1/\pi\int_0^{2\pi}\hat{\beta}_+ d\Theta_0$ exciting the electromagnetic field can be found from the equations of electron motion. Assuming that the transverse electron velocity is nonrelativistic ($V'_\perp \ll c$), these equations can be represented in the form of equations for nonisochronous oscillators, which are well-known in the CRM theory:

$$\frac{\partial\hat{\beta}_+}{\partial\tau'} + i\hat{\beta}_+(|\hat{\beta}_+|^2 - \Delta - 1) = ia. \qquad (4)$$

Equation (4) describes azimuthal self-bunching of electrons caused by the dependence of the gyrofrequency on the electron energy. In Eqs. (3) and (4), we use the following dimensionless variables: the normalized transverse electron velocity $\hat{\beta}_+ = \exp(i\omega_c t)(\beta'_x + i\beta'_y)'/\beta'_{\perp_0}$;

$$a = (2eA'/mc\omega_c\beta'^3_{\perp_0})J_{m-1}(R_0\omega_c/c),$$

$$Z' = z'\beta'_{\perp_0}\omega_c/c, \quad \tau' = t'\beta'^2_{\perp_0}\omega_c/2;$$

[2] Similar considerations for transverse magnetic (TM) modes show that the transverse component of the electric field vanishes in the comoving frame when condition (1) is satisfied. For this reason, the interaction with TM modes is ineffective in the regime of group synchronism.

the detuning of the unperturbed cyclotron frequency from the cutoff frequency (in the comoving frame) $\Delta = 2(\omega'_H - \omega_c)/\omega_c\beta'^2_{\perp_0}$; and the form factor

$$G = \frac{1}{4\pi}\frac{eI_0}{mc^3}\frac{1}{\beta^4_{\perp_0}\beta_{\parallel_0}\gamma^5_{\parallel_0}}\frac{\lambda^2}{\pi R^2}\frac{J^2_{m-1}(R_0\omega_c/c)}{J^2_m(\nu_n)(1-m^2/\nu^2_n)}$$

written under the assumption that an annular electron bunch with the injection radius R_0 radiates in a circular waveguide of radius R, where I_0 is the total current in the laboratory frame, $\lambda = 2\pi c/\omega_c = 2\pi R/\nu_n$, m is the azimuthal index of the waveguide mode, and ν_n is the nth root of the equation $J'_m(\nu) = 0$. The function $f(Z')$ describes the axial distribution of the electron density.

A uniform (correct to small fluctuations specified by the parameter $r \ll 1$) initial distribution of the electrons over cyclotron rotation phases yields the following initial conditions for the set of equations (3) and (4):

$$\hat{\beta}_+\big|_{\tau'=0} = \exp[i(\Theta_0 + r\cos\Theta_0)], \quad \Theta_0 \in [0, 2\pi], \quad a|_{\tau'=0} = 0. \tag{5}$$

1.2. The Linear Stage of Cyclotron SR

In the linear approximation, the bunch of cyclotron oscillators can be regarded as a finite-length active medium that forms an active resonator exhibiting a discrete eigenmode spectrum. To determine the eigenmodes, we assume that the electrons are distributed uniformly in the bulk of a planar electron bunch of length $B = \beta'_{\perp_0} b'\omega_c/c$, so that $f(Z') = 1$ at $Z' \in [-B/2, B/2]$. The emission field can be presented as $a(Z', t') = a(Z')\exp(i\Delta\tau' + i\Omega\tau')$, where

$$a(Z') = C_1\exp(i\chi Z') + C_2\exp(-i\chi Z')$$

in the bulk of the layer and

$$a(Z') = C_{3,4}\exp(\mp i\hat{h}Z')$$

on the left (the upper sign) and on the right (the lower sign) of the electron bunch. We linearize Eqs. (3) and (4) with allowance for the boundary conditions

$$\{a\}, \left\{\frac{\partial a}{\partial Z'}\right\}_{Z' = \pm\frac{B}{2}} = 0, \tag{6}$$

corresponding to the continuity of the transverse electric and magnetic fields at the boundaries of the electron bunch. As a result, we obtain a characteristic equation determining the complex eigenfrequencies Ω:

$$\exp(-2i\chi B) = \left(\frac{\hat{h}+\chi}{\hat{h}-\chi}\right)^2, \tag{7}$$

where $\hat{h} = (\Omega + \Delta)^{1/2}$ and $\chi = (\Omega + \Delta - 4G(\Omega - 1)/\Omega^2)^{1/2}$ are the wavenumbers outside and inside the bunch, respectively.

First, we consider a relatively short electron bunch

$$h'b' \ll 1; \tag{8}$$

i.e., we assume that the bunch length is much smaller than the wavelength of the waveguide mode $\lambda' = 2\pi/h'$. In this case, $\chi B \ll 1$ and $\chi/\hat{h} \ll 1$, which makes it possible to reduce the characteristic equation (7) [19] to

$$i\Omega^2\sqrt{\Omega + \Delta} + 2GB\Omega = 2GB. \tag{9}$$

In the regime of exact group synchronism $\Delta = 0$ ($\omega'_H = \omega_c$), assuming that the bunch is rarefied ($G \ll 1$), we can neglect cyclotron absorption [the second term on the left-hand side of Eq. (9)] and find an analytical solution to Eq. (9). Among the solutions to Eq. (9), there is a unique solution,

$$\Omega = (2GB)^{2/5}\exp\left(i\frac{\pi}{5}\right), \tag{10}$$

corresponding to the excitation of a mode that grows in time ($\mathrm{Im}\,\Omega < 0$) and whose electromagnetic energy flux is directed to the bunch periphery ($\mathrm{Re}\,\hat{h} > 0$). According to (10), the growth rate of the SR instability is

$$|\mathrm{Im}\,\Omega| = (2GB)^{2/5}\sin(\pi/5) \tag{11}$$

or, in the dimension variables,

$$|\mathrm{Im}\,\omega'| = \frac{1}{2}\omega_c\left(\sin\frac{\pi}{5}\right)\left(\frac{eI_0}{mc^3}\frac{\beta^2_{\perp_0}}{\beta_{\parallel_0}\gamma^3_{\parallel_0}}\frac{\lambda b}{\pi R^3} \times \frac{J^2_{m-1}(R_0\omega_c/c)}{J^2_m(\nu_n)(1-m^2/\nu^2_n)}\right)^{2/5}. \tag{12}$$

Note that, according to Eqs. (11) and (12), in spite of the fact that the bunch is limited in the longitudinal direction and there are energy losses due to emission of radiation, the instability has no threshold, which is explained by an infinite lifetime of electron oscillators in the region of interaction with the electromagnetic field.

Due to a positive electron frequency shift

$$\mathrm{Re}\,\Omega = (2GB)^{2/5}\cos(\pi/5) > 0, \tag{13}$$

the emission frequency exceeds the cutoff frequency even at $\Delta = 0$. As a result, the real part of the longitudinal wavenumber $\mathrm{Re}\,\hat{h}$ becomes positive. This means that the group velocity also becomes nonzero, which causes the energy outflow from the electron bunch.

Figure 2 shows the dimensionless growth rate $\mathrm{Im}\,\Omega$, electron frequency shift $\mathrm{Re}\,\Omega$, and real ($\mathrm{Re}\,\hat{h}$) and imaginary ($\mathrm{Im}\,\hat{h}$) parts of the wavenumber versus the

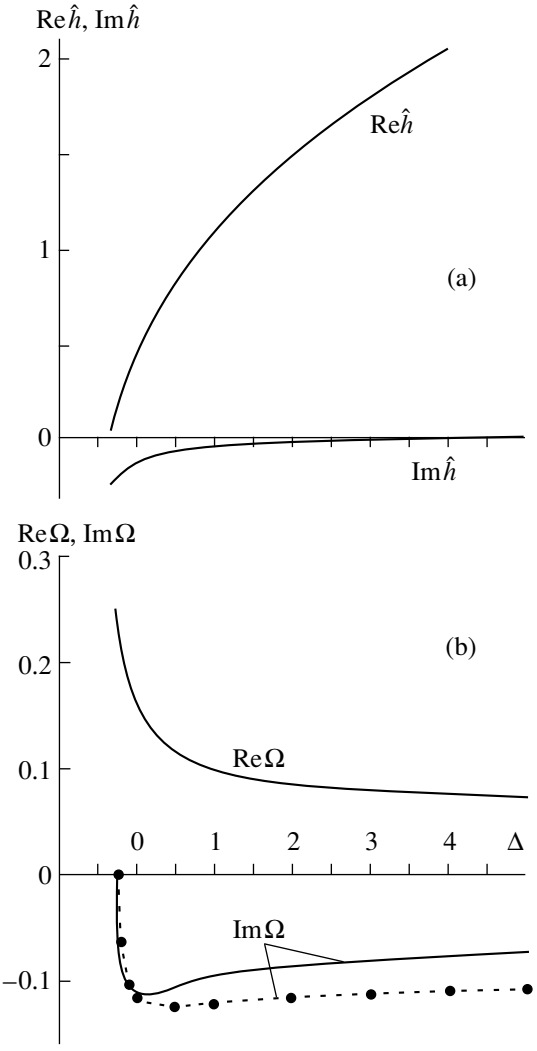

Fig. 2. (a) The real (Re$\hat{h}$) and imaginary (Im$\hat{h}$) parts of the longitudinal wavenumber and (b) the electron frequency shift ReΩ and the growth rate of the SR instability ImΩ versus the detuning parameter Δ for a short electron bunch at $GB = 0.01$. The dashed curve shows to the space charge parameter $q = 0.015$.

detuning parameter Δ. It is seen that detuning from the cutoff frequency (i.e., the violation of the tangent regime) leads to a decreasing growth rate. If the detuning is positive ($\omega'_H > \omega_c$), the instability develops at any arbitrarily large value of the parameter Δ. At $\Delta \gg 1$, the asymptotics

$$\begin{aligned} \Omega &= (GB)^{1/2}\Delta^{-1/4}(1-i), \\ \hat{h} &= \Delta^{1/2} + (GB)^{1/2}\Delta^{-3/4}(1-i)/2, \end{aligned} \tag{14}$$

corresponding to crossing of the dispersion curves [15], are valid. In the range of negative detunings ($\omega'_H < \omega_c$), the instability ceases at $\Delta < \dot{\Delta} \approx -0.3$.

Since, in the vicinity of the cutoff frequency, the longitudinal wavenumber is $h' \sim c^{-1}\sqrt{2\omega_c(\omega' - \omega_c)}$ and it follows from (10) and (11) that the frequency shift is of the same order as the growth rate ($|\omega' - \omega_c| \sim \mathrm{Im}\,\omega'$), we can rewrite inequality (8) in the form

$$\frac{b'^2}{\lambda c T'} \ll 1, \tag{15}$$

where $T' = (\mathrm{Im}\,\omega')^{-1}$ is the characteristic growth time of the SR instability (inverse growth rate).

Note that, under condition (15), the characteristic equation (9) can be obtained by linearizing Eqs. (3) and (4), in which we should set $f(Z') = B\delta(Z')$, where $\delta(Z')$ is the delta function.

An electron bunch of an arbitrary length exhibits an infinite number of unstable modes that differ from each other by the number of field oscillations along the longitudinal coordinate. Figure 3 shows the growth rate of the first symmetric and first antisymmetric modes versus the parameter B at a constant number of particles in the bunch (constant bunch charge). It is seen that the first symmetric mode [its growth rate is given by (11) at $B \ll 1$ has the maximum growth rate at any electron bunch length. As the bunch length increases, the growth rates of the other modes get closer to the growth rate of the first symmetric mode.

In the limiting case of an extended layer ($B \gg 1$), the characteristic equation (7) can be represented in the form

$$\Omega^3 - \frac{l^2\pi}{B^2}\Omega^2 - 4G\Omega + 4G = 0, \tag{16}$$

where $l = 0, 2, 4, \ldots$ for symmetric modes and $l = 1, 3, 5, \ldots$ for antisymmetric modes.

If the particle density is sufficiently low ($G \ll 1$), the first order of the perturbation theory over the small parameter B^{-1} yields the following solution to this equation:

$$\Omega = (4G)^{1/3}\exp\left(i\frac{\pi}{3} + i\frac{2\pi}{3}(j-1)\right), \quad \text{where } j = 1\text{–}3. \tag{17}$$

Expression (17) apparently coincides with a well-known relationship for the instability growth rate in an infinitely long bunch of nonisochronous oscillators [24]. The limiting value of the growth rate in Fig. 3 at $B \longrightarrow \infty$ is determined by the root $j = 3$ in (17), corresponding to the solution that grows in time.

Figure 4 shows the growth rate versus the detuning parameter Δ at a fixed total charge and two different lengths of the bunch. It is seen that the larger the bunch

length, the more pronounced the decrease in the growth rate with detuning from the regime of group synchronism.

1.3. The Nonlinear Stage of Cyclotron SR

We studied the nonlinear stage of the cyclotron SR instability under the group synchronism conditions by numerically solving Eqs. (3) and (4) for the parameters close to the experimental ones (see above): the operating mode was TE_{21}; the waveguide radius was about 0.5 cm; the electron injection radius was 0.25 cm; and $\beta_\perp/\beta_\parallel \sim 1$. The corresponding values of the dimensionless parameters were $G = 0.12$ and $B = 10$. Figure 5a shows the waveforms of the amplitude of the emission field at three values of the detunings Δ. It is seen that the radiation is emitted in the form of a short pulse. The main part of the transverse oscillatory energy of electrons is transformed into the radiation energy in a time of a few inverse growth rates. The characteristic duration of the electromagnetic pulse is determined by the electron azimuthal phasing and dephasing times. Indeed, a comparison of Figs. 5a and 5b shows that the duration of the electromagnetic pulse is almost equal to the duration of the azimuthal current pulse. For $\beta'_\perp \sim 0.5$, the duration the main SR pulse is about ten cyclotron periods. The additional maxima of the radiation field in Fig. 5a are apparently related to the additional maxima of the current, which are typical of the inertial azimuthal bunching of the particles.

According to the linear theory, the growth rate of the SR instability is maximum at $\Delta = 0$. However, SR pulses can be generated at both positive and negative values of the detuning parameter Δ. Detuning from the group synchronism condition decreases the growth rate and slightly lowers the SR peak power.

1.4. Allowance for the Space Charge Field

The transverse Coulomb field arising in the course of the azimuthal bunching of the particles may significantly influence the SR process. This field may give rise to a "negative" mass effect [25, 26] and sometimes increase the growth rate of the SR instability.

We consider the effect of the space charge within a model widely used in the gyrotron theory [22]. If the radius and length of an annular electron bunch are substantially larger than its thickness, we can assume that the space charge field has only a radial component and that the field structure coincides with that of a planar charged bunch. The bunch is formed of electrons whose Larmor-orbit centers lie on one line and that have different azimuthal positions with respect to the guiding centers. The bunch can be presented as an ensemble of charged planes consisting of electrons that fall into a narrow interval of the initial azimuthal angle $d\psi$ and differ from each other by the position of the Larmor-orbit center. Then the effective force acting on a given

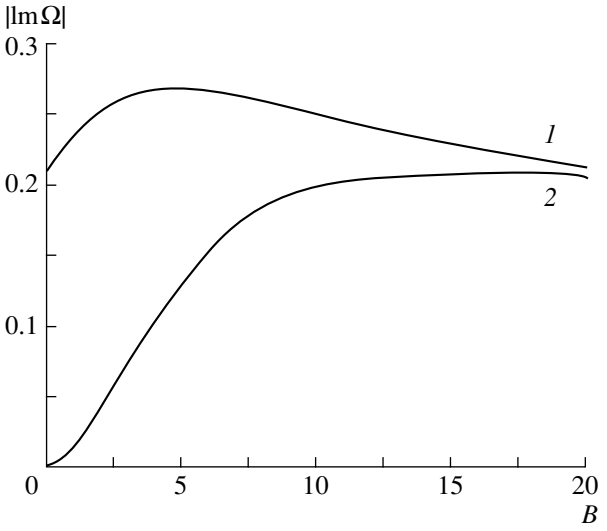

Fig. 3. The absolute values of the growth rates of (*1*) the first symmetric and (*2*) the first antisymmetric modes as functions of the bunch length B for $GB = 0.1$.

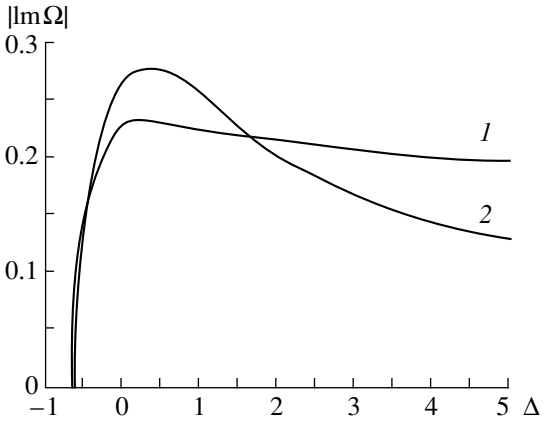

Fig. 4. The absolute value of the growth rate of the first symmetric mode as a function of the detuning parameter Δ for the fixed bunch charge $GB = 0.1$ and bunch lengths of $B =$ (*1*) 0.5 and (*2*) 10.

electron can be found by averaging over the positions of all the other planes. As a result, the equation of motion (4) takes the form (see [26] for details)

$$\frac{\partial\hat{\beta}_+}{\partial\tau'} + i\hat{\beta}_+\left(\left|\hat{\beta}_+\right|^2 - \Delta - 1\right) = ia - iq\frac{1}{2\pi}\int_0^{2\pi} d\psi \frac{\hat{\beta}_+(\tau', \Theta_0) - \hat{\beta}_+(\tau', \psi)}{\left|\hat{\beta}_+(\tau', \Theta_0) - \hat{\beta}_+(\tau', \psi)\right|}, \quad (18)$$

where $q = 2(\omega_b/\beta'_{\perp_0}\omega_H)^2$ is the space charge parameter, $\omega_b = \sqrt{4\pi e n_e/m}$ is the plasma frequency, and n_e is the electron density.

Equation (18) and the excitation equation in its former representation (3) describe SR with allowance

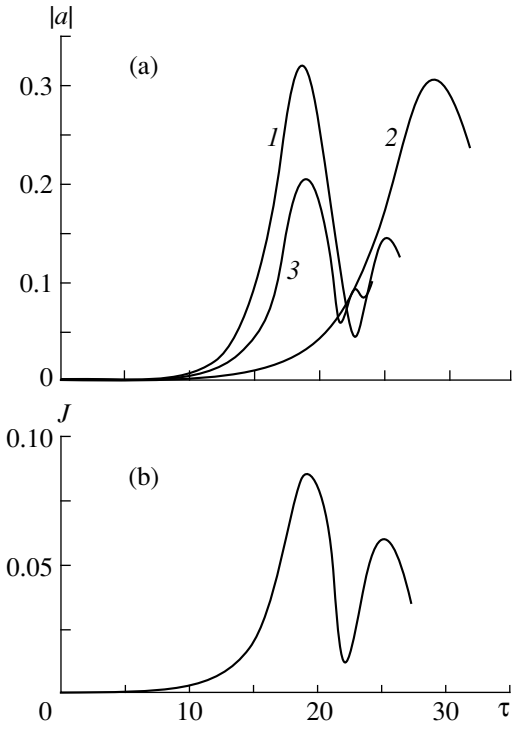

Fig. 5. (a) The field amplitude at the edge of the electron bunch versus time in the comoving frame at $B = 10$; $G = 0.1$; and $\Delta = (1)\ 0$, $(2)\ 1$, and $(3)\ -0.7$. (b) The transverse electron current in the same cross section as a function of time at $\Delta = 0$.

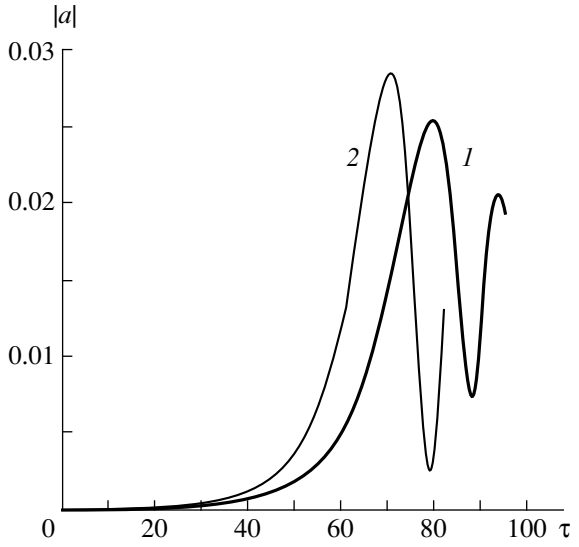

Fig. 6. The electric field amplitude in the comoving frame versus time (*1*) with and (*2*) without allowance for the space charge field in a short-bunch model at $GB = 0.01$ and $q = 0.015$.

for the space charge field. The form of characteristic equation (7) derived within the linear approximation is also conserved, but, in the case under consideration, the wavenumbers outside and inside the electron bunch are given by

$$h = (\Omega + \tilde{\Delta})^{1/2},$$
$$\chi = \left(\Omega + \tilde{\Delta} - 4G\frac{\Omega + 2\tilde{q} - 1}{(\Omega - \tilde{q})^2 - 4\tilde{q}(\tilde{q} - 1)}\right)^{1/2}, \quad (19)$$

where $\tilde{q} = 2q/3\pi$, $\tilde{\Delta} = \Delta - 3\tilde{q}$, and only the first harmonic of the space charge field is taken into account.

We will analyze the effect of the space charge in the case of a relatively short electron bunch satisfying inequality (8), which means that the bunch length b is less than the wavelength of the waveguide mode. At the same time, we assume that the bunch length is larger than the radius of electron cyclotron rotation and use the right-hand side of (18) to write the expression for the space charge field. With the use of (19), the characteristic equation (7) transforms into

$$i\sqrt{\Omega - \tilde{\Delta}}\{(\Omega - \tilde{q})^2 - 4\tilde{q}(\tilde{q} - 1)\} + 2GB\Omega = 2GB. \quad (20)$$

The dashed line in Fig. 2 shows the growth rate of the SR instability as a function of Δ with allowance for the space charge field. It is seen that the space charge slightly increases the growth rate of the SR instability. This can be attributed to the "negative mass" effect, which causes the azimuthal bunching of electrons even in the absence of the radiation field [25]. Numerical solution of Eqs. (3) and (18) in the case of a short electron bunch also proves that allowance for the space charge field leads to an increase in the growth rate and a slight increase in the peak amplitude of the radiation field (Fig. 6).

2. CYCLOTRON SR IN THE LABORATORY FRAME

It follows from the above analysis that, in the comoving frame K', the electron bunch radiates isotropically in both $+z'$ and $-z'$ directions along the waveguide axis. Since, in this frame, the radiation frequency is close to the cutoff frequency, the group velocities V'_{gr} of the electromagnetic pulses emitted in both directions are rather low (their difference from zero is related to the electron frequency detuning, see Section 1.2). In the laboratory frame, the bunch moves with the longitudinal velocity $V_\parallel > V'_{gr}$ (under the experimental conditions, $V_\parallel \sim 0.7c$). If the bunch moves towards a detector, the radiation emitted in the $+z'$ (forward) direction in K' frame affects the detector earlier than that emitted in the $-z'$ (backward) direction. Indeed, it follows from the velocity addition law that, if the source (electron bunch) velocity is higher than the electromagnetic wave group velocity in the source frame, then, in the laboratory frame, both the radiation components propagate in the direction of the source motion. The group velocity of the "forward" pulse in the laboratory frame is slightly higher and that of the "back-

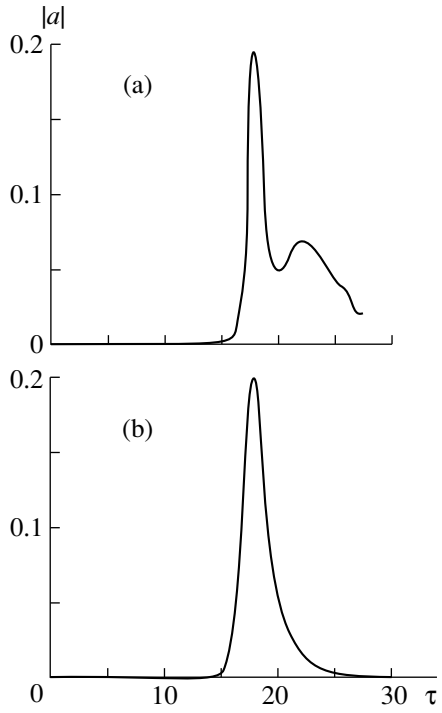

Fig. 7. The field amplitude recorded by a detector in the laboratory frame as a function of time at Δ = (a) 0 and (b) –0.4.

ward" pulse is slightly lower than the longitudinal velocity of the electron bunch. Thus, the distance between the two pulses increases with increasing observation length.

The shape of the SR pulse at the detector can be obtained as follows. First, we calculate the field distribution in the (z', t') plane and then determine the field on the $z' = -V_{\|}t'$ + const line, along which the detector moves. Figure 7a shows the electric field amplitude at the detector versus time calculated for the case of the exact group synchronism (Δ = 0). It is seen that the detector signal has a two-hump shape; i.e., the emitted radiation consists of two pulses. The first and second pulses are formed by photons emitted by the bunch in the K' frame in the positive and negative directions along the z'-axis, respectively. Due to the Doppler effect, the carrier frequency of the first pulse is higher than that of the second pulse. Hence, the first pulse turns out to be substantially shorter than the second pulse. The amplitude of the first pulse is larger, because it arrives at the detector earlier than the second pulse and, thus, is less subjected to dispersion spreading.

Note that, for negative values of the detuning parameter Δ, the difference between the group velocities becomes negligible. Hence, the signal detected in the laboratory frame at a given observation length looks like a single pulse (Fig. 7b).

Therefore, the SR pulse shape can be varied by changing the observation length at a constant Δ or/and changing the detuning parameter at a given observation length, which was experimentally demonstrated in [20, 21].

The radiation power at the detector that is at rest in the laboratory frame is determined by the vector product of the electric and magnetic fields on the trajectory of the detector motion in the (t', z') plane. These fields can be obtained by the Lorentz transformation of the fields in the comoving frame. Integration over the waveguide cross section yields the following expression for the power in the laboratory frame:

$$P = \frac{\pi}{2}\frac{m^2c^5}{e^2}\frac{\pi R^2}{\lambda^2}\frac{J^2(\nu_n)(1-m^2/\nu_n^2)}{J_{m-1}^2(R_0\omega_c/c)}\gamma_{\|_0}^8\beta_{\perp_0}^6 \times\left(\beta_{\|_0}|a|^2+\beta_{\perp_0}\gamma_{\|_0}(1+\beta_{\|_0}^2)\mathrm{Im}\left(a\frac{\partial a^*}{\partial Z'}\right)\right). \quad (21)$$

Note that (21) is written with allowance for the fact that the transverse component of the magnetic field is small in the K' frame.

CONCLUSIONS

Therefore, we have shown that cyclotron SR can be used to generate short (about ten cyclotron oscillations) electromagnetic pulses. The group synchronism regime appears to be the most favorable for cyclotron SR observation. A detuning from this regime leads to a decrease in both the growth rate of the SR instability and the SR peak power. Note than this decrease is even more pronounced for positive detunings Δ if we take into account the longitudinal dynamics of a real electron bunch caused by the spread in the initial longitudinal velocities and longitudinal Coulomb repulsion. These two factors cause relative displacement of electrons in the comoving frame, which may result in substantial suppression of the SR instability if the displacement is comparable with the wavelength of the waveguide mode $\lambda' = 2\pi/h'$. Under the exact group synchronism regime (Δ = 0), h' tends to zero, the wavelength λ' of the waveguide mode becomes infinitely large, and the radiation is almost independent of the longitudinal displacement of electrons. However, as Δ increases (i.e., the regime of group synchronism is violated), the longitudinal wavenumber increases and, accordingly, the wavelength of the waveguide mode decreases and tends to the vacuum wavelength $\lambda_\nu' = 2\pi c/\omega'$. In this case, the same longitudinal displacement can result in substantial suppression of SR. Experimental results [20, 21] demonstrate almost complete suppression of the microwave signal as the detuning from the exact group synchronism increases.

Finally, we estimate the parameters of cyclotron SR pulses in the regime of exact group synchronism under the conditions close to experimental (see the Introduction). The pulse duration, which can be found from Fig. 5, is approximately 300 ps and agrees well with the experimental data. The corresponding growth rate of

the SR instability in the comoving frame is equal to 0.9×10^{10} s^{-1}. For the bunch drift velocity $V_{\|} = 0.5$ s, the distance corresponding to the *e*-fold increase in the power in the laboratory frame is about 1.6 cm. In experiments, such an increase was observed at a distance of approximately 4 cm. Numerical results predict a peak power of 8 MW, whereas the experimentally detected power amounted to 200–300 kW. Such a discrepancy between the calculated and experimental values of the growth rate and the peak power can be attributed to the presence of a spread in the initial electron energies and pitch angles, which are typical of real electron bunches. Note also that the emission power reported in [20, 21] should only be considered a lower estimate, because, at present, the methods for recording individual subnanosecond electromagnetic pulses require additional improvement.

ACKNOWLEDGMENTS

We are grateful to A. D. R. Phelps and M. I. Yalandin for fruitful discussions. This work was supported by the Russian Foundation for Basic Research, project no. 95-02-04791.

REFERENCES

1. R. H. Dicke, Phys. Rev. **99**, 131 (1954).
2. A. V. Andreev, V. I. Emel'yanov, and Yu. A. Il'inskiĭ, *Cooperative Phenomena in Optics* (Nauka, Moscow, 1988), p. 277.
3. V. V. Zheleznyakov, V. V. Kocharovskiĭ, and Vs. V. Kocharovskiĭ, Usp. Fiz. Nauk **159** (2), 193 (1989) [Sov. Phys. Usp. **32**, 835 (1989)].
4. R. Bonifachio, C. Maroli, and N. Piovella, Opt. Commun. **68**, 369 (1988).
5. R. Bonifachio, N. Piovella, and B. W. J. McNeil, Phys. Rev. A **44**, 3441 (1991).
6. R. Bonifachio, L. D. Salvo, L. Narducci, and E. D. Angelo, Phys. Rev. A **150**, 50 (1994).
7. N. S. Ginzburg, Pis'ma Zh. Tekh. Fiz. **14**, 440 (1988) [Sov. Tech. Phys. Lett. **14**, 197 (1988)].
8. N. S. Ginzburg and A. S. Sergeev, Pis'ma Zh. Éksp. Teor. Fiz. **54**, 445 (1991) [JETP Lett. **54**, 446 (1991)].
9. D. A. Jarosynski, P. Chaix, N. Piovella, *et al.*, Phys. Rev. Lett. **78**, 1699 (1997).
10. V. I. Kanavets and A. Yu. Stabinis, Vestn. Mosk. Gos. Univ., Ser. Fiz. **14**, 186 (1973).
11. V. V. Zheleznyakov, V. V. Kocharovskiĭ, and Vs. V. Kocharovskiĭ, Izv. Vyssh. Uchebn. Zaved. Radiofiz. **29**, 1095 (1986).
12. Yu. A. Il'inskiĭ and N. S. Maslova, Zh. Éksp. Teor. Fiz. **94**, 171 (1988) [Sov. Phys. JETP **67**, 96 (1988)].
13. L. A. Vaĭnshteĭn and A. I. Kleev, Dokl. Akad. Nauk SSSR **311**, 862 (1990) [Sov. Phys. Dokl. **35**, 359 (1990)].
14. E. S. Mchedlova and D. I. Trubetskov, Pis'ma Zh. Tekh. Fiz. **19** (24), 26 (1993) [Tech. Phys. Lett. **19**, 784 (1993)].
15. N. S. Ginzburg, I. V. Zotova, and A. S. Sergeev, Pis'ma Zh. Tekh. Fiz. **15** (14), 83 (1989) [Sov. Tech. Phys. Lett. **15**, 573 (1989)].
16. N. S. Ginzburg and A.S. Sergeev, Zh. Tekh. Fiz. **60** (8), 40 (1990) [Sov. Phys. Tech. Phys. **35**, 896 (1990)].
17. N. S. Ginzburg and A. S. Sergeev, Zh. Éksp. Teor. Fiz. **99**, 438 (1991) [Sov. Phys. JETP **72**, 243 (1991)].
18. N. S. Ginzburg and A. S. Sergeev, Fiz. Plazmy **17**, 1318 (1991) [Sov. J. Plasma Phys. **17**, 762 (1991)].
19. N. S. Ginzburg, I. V. Zotova, and A. S. Sergeev, Pis'ma Zh. Éksp. Teor. Fiz. **60**, 501 (1994) [JETP Lett. **60**, 513 (1994)].
20. N. S. Ginzburg, I. V. Zotova, A. S. Sergeev, *et al.*, Pis'ma Zh. Éksp. Teor. Fiz. **63**, 322 (1996) [JETP Lett. **63**, 331 (1996)].
21. N. S. Ginzburg, I. V. Zotova, A. S. Sergeev, *et al.*, Phys. Rev. Lett. **78**, 2365 (1997).
22. A. V. Gaponov, M. I. Petelin, and V. K. Yulpatov, Izv. Vyssh. Uchebn. Zaved. Radiofiz. **28**, 1538 (1975).
23. J. D. Jackson, *Classical Electrodynamics* (Wiley, New York, 1975; Inostrannaya Literatura, Moscow, 1965).
24. V. V. Zheleznyakov, Izv. Vyssh. Uchebn. Zaved. Radiofiz. **3**, 57 (1960).
25. V. L. Bratman and M. I. Petelin, Izv. Vyssh. Uchebn. Zaved. Radiofiz. **28**, 1538 (1975).
26. V. L. Bratman, Zh. Tekh. Fiz. **46**, 2030 (1976) [Sov. Phys. Tech. Phys. **21**, 1188 (1976)].

Translated by A. Chikishev

Technical Physics, Vol. 45, No. 7, 2000, pp. 821–825. Translated from Zhurnal Tekhnicheskoĭ Fiziki, Vol. 70, No. 7, 2000, pp. 9–13.

The Classification of Anisotropic Stressed States in Spherical Bodies

A. S. Baranov

Pulkovo Observatory, Russian Academy of Sciences,
Pulkovskoe sh. 65, St. Petersburg, 196140 Russia

Received April 19, 1999

Abstract—Tensor fields (for example, of pressure) with desired properties of symmetry under rotation were constructed in an explicit form. Tensor components represented as polynomials in Cartesian coordinates satisfy a biharmonic equation. Possible applications of the obtained results in various domains of technical physics are discussed. © *2000 MAIK "Nauka/Interperiodica".*

STATEMENT OF THE PROBLEM

Harmonic and biharmonic functions are of frequent use in technical physics. They are applied in the theories of elasticity, plasticity, equilibrium figures in a rotating liquid, etc. An apparatus for expanding the functions over an appropriate basis depends on the body shape. Most often, spherical functions are used [1]. Spheroidal functions are less known [2]. Spheroidal bodies are usually characterized by harmonic functions. In [3], we elaborated the biharmonic function apparatus for spheroidal bodies to tackle a variety of problems when the bounding surface is close to spheroidal. Spherical bodies, however, can also be treated in wider mathematical terms than is generally appreciated.

Indeed, in technical physics, we handle not only scalar characteristics. The tensor character of pressure and pressure-related parameters is perhaps the most prominent example. Such an anisotropic analog of pressure is used in magnetometric prospecting for gas fields, as well as in exploration of bulk materials, interior of the Earth and other planets, etc. In star dynamics and the theory of plasma, the analog of pressure also exhibits more or less anisotropic properties [4]. The same is true for applications such as the study of equilibrium in round elastic bodies. The only difference here is that gravitational forces are replaced by external forces applied to the surface [5]. Therefore, it is of interest to classify spatial distributions of anisotropic pressure inside a body in terms of symmetry under rotation.

Pressure tensor components will be assumed to be harmonic or biharmonic functions. Such a restriction often follows from additional physical conditions [1, 3]. Then, a random pressure distribution that satisfies the harmonicity or biharmonicity condition, as well as the condition of equilibrium inside the volume, can be represented as a superposition of simpler distributions that satisfy certain symmetry requirements.

For the specific case of spherical bodies, the classification of tensor fields is naturally related to the symmetry under rotation of the entire body, in contrast to the more general case [3], where it may seem somewhat formal. That is why we consider the spherical case separately. It requires a solution to the biharmonic equation $\Delta\Delta U = 0$ to meet representations of rotation group [6]. Such representations may be one- or two-valued, but we are certainly interested in the former. Each representation is characterized by an index n, which runs over 0, 1, 2, … values and combines $2n + 1$ states of an object into a unified set. Under any rotations, the states are linearly transformed into each other. One cannot get by with a lesser number of states; otherwise, new states will arise at some rotations. A trivial example is the transformation of a single vector under rotations: in this transformation, all three vector components are involved. An example of another sort is the transformation of scalar fields on a sphere. In this case, the standard basis of representation at fixed n's is a set of $2n + 1$ spherical harmonics with the same index [7].

In general, spinor, vector, and tensor fields on a sphere have been studied by Gel'fand and coworkers, but the derived formulas are of a rather abstract character. They are hard to apply to specific technical problems, especially if the harmonicity or biharmonicity condition is additionally set. Therefore, we will address the problem in a somewhat different way.

CONDITIONS OF EQUILIBRIUM

Of basis states (or vectors) corresponding to a given n, we shall consider the one which is the easiest to express in Cartesian coordinates. With scalar fields, experience suggests that this is the extreme "vector," which, being rotated about the polar axis through an angle Θ, acquires the factor $\exp(in\Theta)$. In the case of scalar fields, this vector is called sectorial harmonic.

1063-7842/00/4507-0821$20.00

Let m be the degree of polynomials describing pressure tensor components. A pressure tensor is known to have the form of a symmetrical matrix

$$\begin{pmatrix} P_{xx} & P_{xy} & P_{xz} \\ P_{yx} & P_{yy} & P_{yz} \\ P_{zx} & P_{zy} & P_{zz} \end{pmatrix} \quad (P_{xy} = P_{yx}, P_{xz} = P_{zx}, P_{yz} = P_{zy}),$$

where x, y, and z are Cartesian coordinates and z is the polar axis.

Since the component P_{zz} by itself does not change when rotated about the polar axis, the azimuth dependence must show up through the factor $\exp(in\Theta)$ or, in Cartesian coordinates, the factor φ_n [$\varphi_n = (x + iy)^n$], where the other factor is some polynomial in z and $R^2 = x^2 + y^2$. Hence, if we start with the component P_{zz}, it should be sought in the form $P_{zz} = c_0\varphi_n$ ($m = u$), $P_{zz} = c_1 z\varphi_n$ ($m = n + 1$), or $P_{zz} = (c_1R^2 + c_2z^2)\varphi_n$ ($m = n + 2$); for $m < n$, it is necessary to construct a similar polynomial and put $P_{zz} = 0$. It will be shown below that the case $|m - n| > 2$ is impossible.

When rotated about the polar axis, the quantity $\Phi = P_{xx} + P_{yy}$, also a scalar, is transformed in a quite similar way but with other coefficients. We will pursue our consideration as follows. When rotated about the polar axis, the components P_{xz} and P_{yz} by themselves transform following the same law as the components of a two-dimensional vector; that is, $P_{xz} \longrightarrow P_{xz}\cos\Theta - P_{yz}\sin\Theta$ and $P_{yz} \longrightarrow P_{xz}\sin\Theta + P_{yz}\cos\Theta$. For their complex combination, we have $P_{xz} + iP_{yx} \longrightarrow F\exp(i\Theta)$ and $P_{yz} - iP_{xz} \longrightarrow F_1\exp(i\Theta)$, where $F = P_{yz} + iP_{xz}$ and $F_1 = P_{yz} - iP_{xz}$.

In this way, the components P_{xz} and P_{yz} by themselves transform. Here, account is taken of the fact that, under rotation, as was noted, a point in space to which they are related changes when the field as a whole rotates. Hence, to find these components in a fixed coordinate system, the factor $\exp(in\Theta)$ must be included in the above formulas. Thus, unlike P_{zz}, the general expression $P_{xz} \pm iP_{yz}$ must involve the factor φ_n. The second factor should again be either a polynomial of the $[m - (n \pm 1)]$ degree in z and R^2 or zero if the expression in the brackets is a negative. Finally, the components P_{xx}, P_{xy}, and P_{yy} transform under rotation about the polar axis in the same way as the components of a two-dimensional tensor, that is, in the same way as pair products of two different vectors. The combinations $H = P_{xx} - P_{yy} - 2iP_{yx}$ and $H_1 = P_{xx} - P_{yy} + 2iP_{yx}$ show simple properties under rotation. Similar considerations indicate that H and H_1 must involve the factors $\varphi_{n\pm2}$ and φ_{n-2}, respectively [if $m - (n \pm 2) \geq 0$].

The previous argument referred to rotations about the polar axis. However, they are insufficient to prove the desired total symmetry of the field. A typical feature of the extreme state under consideration is that it must vanish when the operator $\mathbf{I}_x + i\mathbf{I}_y$ is applied, where $\mathbf{I}_x$ and $\mathbf{I}_y$ are the infinitesimal operators of rotations about the axes x and y, respectively (it is assumed that rotation, viewed from the positive ends of both horizontal axes, proceeds in the same direction).

For the $\mathbf{I}_x + i\mathbf{I}_y$ operator, the table of action on the tensor components alone is easily constructed in the same way as for rotations about the x-axis (with the changed roles of coordinates). Eventually, six equations that relate the pressure tensor components are obtained [6]. On rearrangement (details are omitted), we come to the following set:

$$\begin{gathered}
-z\left(\frac{\partial}{\partial x} + i\frac{\partial}{\partial y}\right)P_{zz} + (x + iy)\frac{\partial P_{zz}}{\partial z} - 2(P_{xz} + iP_{yz}) = 0, \\
(x + iy)\left(\frac{\partial P_{xz}}{\partial z} + i\frac{\partial P_{yz}}{\partial z}\right) \\
-z\left(\frac{\partial}{\partial x} + i\frac{\partial}{\partial y}\right)(P_{xz} + iP_{yz}) - H_1 = 0, \\
(x + iy)\frac{\partial \Phi}{\partial z} - z\left(\frac{\partial \Phi}{\partial x} + i\frac{\partial \Phi}{\partial y}\right) + 2(P_{xz} + iP_{yz}) = 0, \\
(x + iy)\frac{\partial H_1}{\partial z} - z\left(\frac{\partial}{\partial x} + i\frac{\partial}{\partial y}\right)H_1 = 0, \\
-(x + iy)\frac{\partial H}{\partial z} + z\left(\frac{\partial}{\partial x} + i\frac{\partial}{\partial y}\right)H - 4(P_{xz} - iP_{yz}) = 0, \\
(x + iy)\left(\frac{\partial P_{xz}}{\partial z} - i\frac{\partial P_{yz}}{\partial z}\right) \\
-z\left(\frac{\partial}{\partial x} + i\frac{\partial}{\partial y}\right)(P_{xz} - iP_{yz}) + 2P_{zz} - \Phi = 0.
\end{gathered} \tag{1}$$

Equations (1) are basic in our problem. Recall that we are interested in only those tensor fields satisfying the mechanical equilibrium condition

$$\frac{\partial P_{xx}}{\partial x} + \frac{\partial P_{xy}}{\partial y} + \frac{\partial P_{xz}}{\partial z} = \frac{\partial P_{yx}}{\partial x} + \frac{\partial P_{yy}}{\partial y} + \frac{\partial P_{yz}}{\partial z} = \frac{\partial P_{zx}}{\partial x} + \frac{\partial P_{zy}}{\partial y} + \frac{\partial P_{zz}}{\partial z} = 0,$$

where $P_{xx} = p_{xx} + \rho V$ in the presence of self-gravitation; $P_{xy} = p_{xy}$, …; ρ is the material density, which is assumed to be constant; p_{xx}, p_{xy}, … are the components of pressure as such; and $V(x, y, z)$ is the gravitational potential. Naturally, P and p coincide in the absence of external forces.

After transformation, the equilibrium condition can be written in the form [3]

$$2\frac{\partial}{\partial z}(P_{xz}+iP_{yz})+\left(\frac{\partial\Phi}{\partial x}+i\frac{\partial\Phi}{\partial y}\right)-\left(\frac{\partial}{\partial x}-i\frac{\partial}{\partial y}\right)H_1 = 0,$$

$$2\frac{\partial}{\partial z}(P_{xz}-iP_{yz})+\left(\frac{\partial\Phi}{\partial x}-i\frac{\partial\Phi}{\partial y}\right)+\left(\frac{\partial}{\partial x}+i\frac{\partial}{\partial y}\right)H = 0,$$

$$\left(\frac{\partial}{\partial x}+i\frac{\partial}{\partial y}\right)(P_{xz}-iP_{yz}) \tag{2}$$

$$+\left(\frac{\partial}{\partial x}-i\frac{\partial}{\partial y}\right)(P_{xz}+iP_{yz})+2\frac{\partial P_{zz}}{\partial z} = 0.$$

In what follows, we will consider various indexes n at a given degree m of the polynomials.

DETERMINATION OF THE BASIC FUNCTIONS

The extreme case $n = m + 2$ is the easiest. In this case, as was noted, the tensor components are free from the factors $\exp(in\Theta)$, $\exp[i(n \pm 1)\Theta]$, and $\exp[i(n + 2)\Theta]$. Then, $H = c\varphi_n$ remains as the only other-than-zero combination, so that, with the constant coefficient c properly selected ($c = 4$), we have

$$P_{xx} = \varphi_n, \quad P_{yy} = -\varphi_n, \quad P_{xy} = i\varphi_n,$$
$$P_{xz} = P_{yz} = P_{zz} = 0.$$

Notice that this solution automatically satisfies both the equilibrium and harmonicity conditions. Next, we take $n = m + 1$. The factors $\exp(in\Theta)$, $\exp[i(n + 1]\Theta$, and $\exp[i(n + 2)\Theta]$ are impossible here, hence $P_{zz} = \Phi = P_{xz} + iP_{yz} = H_1 = 0$. However, $H = cz\varphi_{n-1}$ and we obtain $P_{xz} - iP_{yz} = -(c/4)\varphi_n$ from the last but one equation in (1). For example, at $c = 8$,

$$P_{xz} = -\varphi_n, \quad P_{yz} = -i\varphi_n, \quad P_{xx} = 2z\varphi_{n-1},$$
$$P_{yy} = -2z\varphi_{n-1}, \quad P_{xy} = 2iz\varphi_{n-1}.$$

Again, the equilibrium and harmonicity conditions are satisfied automatically. Now let us pass to the case $m = n$. The possibility of the factors $\exp[i(n + 1)\Theta]$ and $\exp[i(n + 2)\Theta]$ is eliminated; that is, $P_{xz} + iP_{yz} = H_1 = 0$. We can start with the component $H = (c_1R^2 + c_2z^2)\varphi_{n-2}$. Then, the last but one equation in (1) yields $P_{xz} - iP_{yz} = (c_1 - c_2)z\varphi_{n-1}/2$, and the last equation gives $\Phi - 2P_{zz} = (c_1 - c_2)\varphi_n/2$. The second equation in (2) yields $\Phi = (c_2 - 3c_1)\varphi_n/(2n)$, so that $P_{zz} = (1/4)[(c_2 - 3c_1)/n - (c_1 - c_2)]\varphi_n$.

In the previous calculation, we invoked equilibrium condition (2). The components remain harmonic or biharmonic functions. The difference from the preceding cases is that we are dealing with two linearly independent solutions. One of them is obtained if the harmonicity condition is imposed on the components. Then, $2(n - 1)c_1 + c_2 = 0$. For example, at $c_1 = 4$ and $c_2 = -8(n - 1)$, we have

$$P_{xz} - iP_{yz} = 2(2n-1)\varphi_{n-1}, \quad P_{xz} = (2n-1)z\varphi_{n-1},$$
$$P_{yz} = i(2n-1)z\varphi_{n-1},$$
$$\Phi = P_{xx} + P_{yy} = -2(2 + 1/n)\varphi_n,$$
$$P_{zz} = -(2n + 1 + 1/n)\varphi_n,$$
$$H = [4R^2 - 8(n-1)z^2]\varphi_{n-2},$$
$$P_{xx} - P_{yy} = 2[R^2 - 2(n-1)z^2]\varphi_{n-2},$$
$$P_{xy} = i[R^2 - 2(n-1)z^2]\varphi_{n-2}.$$

The other solution will be essentially biharmonic rather than harmonic. For $c_1 = 4(n + 1)$ and $c_2 = 4(n + 2)$, we have

$$P_{xz} - iP_{yz} = -4z\varphi_{n-1}, \quad P_{xz} = -2z\varphi_{n-1},$$
$$P_{yz} = -2iz\varphi_{n-1},$$
$$P_{xx} - P_{yy} = [2(n+1)R^2 + 2(n+3)z^2]\varphi_{n-2},$$
$$P_{xy} = i[(n+1)R^2 + (n+3)z^2]\varphi_{n-2},$$
$$\Phi = P_{xx} + P_{yy} = -4\varphi_n, \quad P_{zz} = 0.$$

Consider now the case $n = m - 1$. Only H_1 vanishes immediately. Let $P_{zz} = cz\varphi_{n-1}$ (according to the general rule). Then, the first equation in (1) yields $P_{xz} + iP_{yz} = (c/2)\varphi_n$. We can, however, take $H = (c_1z^3 + c_2zR^2)\varphi_{n-3}$. Substituting this equality into the last but one equation in (1) yields $P_{xz} - iP_{yz} = (1/4)[-c_2R^2 + (2c_2 - 3c_1)z^2]\varphi_{n-2}$.

From the last equation in (1), we find $\Phi = [2c + 3(c_2 - c_1)/2]z\varphi_{n-1}$. Finally, the third equation in (1) relates the coefficients through the expression $(c_2 - c_1)/2 + c = 0$. Eventually, we arrive at $\Phi = (c_2 - c_1)z\varphi_{n-1}/2$. Taking into account the second equilibrium condition in (2), one finds the unique relationship between the coefficients c_1 and c_2: $(n + 2)c_1 - (n + 3)c_2 = 0$. We can take $c_1 = 4(n + 3)$, $c_2 = 4(n + 2)$, and $c = 2$. Then,

$$P_{xz} + iP_{yz} = \varphi_n,$$
$$P_{xz} - iP_{yz} = -[(n+2)R^2 + (n+5)z^2]\varphi_{n-2},$$
$$P_{xx} + P_{yy} = -2z\varphi_{n-1},$$
$$P_{xx} - P_{yy} = 2z[(n+3)z^2 + (n+2)R^2]\varphi_{n-3},$$
$$P_{xy} = iz[(n+3)z^2 + (n+2)R^2]\varphi_{n-3}, \quad P_{zz} = 2z\varphi_{n-1}.$$

Finally, consider the last case $n = m - 2$. Symmetry considerations cannot immediately eliminate any of the combinations. Let us start with the component $P_{zz} = (cR^2 + \bar{c}z^2)\varphi_{n-2}$. Then, the first equation in (1) yields

$P_{xz} + iP_{yz} = (\bar{c} - c)z\varphi_{n-1}$. In addition, $H = (c_1z^4 + c_2R^2z^2 + c_3R^4)\varphi_{n-4}$. After substitution into the last but one equation of (1), we obtain

$$P_{xz} - iP_{yz} = z[(c_3 - c_2/2)R^2 + (c_2/2 - c_1)z^2]\varphi_{n-3}.$$

From the last equation of (1), it follows that

$$\Phi = \left[\left(c_3 - \frac{c_2}{2} + 2c\right)R^2 + \left(\frac{5}{2}c_2 - 3c_1 - 2c_3 + 2\bar{c}\right)z^2\right]\varphi_{n-2}.$$

Return to the second equation in (1). It yields the relationship $H_1 = (\bar{c} - c)\varphi_n$. Finally, the third equation in (1) relates the coefficients by the expression

$$\bar{c} - c = c_3 + c_1 - c_2. \quad (3)$$

Turn to the equilibrium condition again. The substitution of the functions found above into Eqs. (2) yields relationships that are partly dependent on the previous one and on each other. Two independent equations remain:

$$\begin{aligned} 2(n+1)(\bar{c} - c) + 2c_3 - c_2 + 4c &= 0, \\ 2(n+2)c_3 - nc_2 + 4(n-1)c &= 0. \end{aligned} \quad (4)$$

As a result, we have found three relationships for five parameters; hence, two independent parameters are actually available. These may be, for example, c_1 and c_2. Then, in particular,

$$\bar{c} = [(n+4)(n-1)c + c_2]/[(n+1)(n+2)].$$

Consider the biharmonicity condition. It is nontrivial only for the function H (the other functions under consideration become biharmonic automatically) and yields $3c_1 + 2(n-3)c_2 + 4(n-2)(n-3)c_3 = 0$.

Combining the obtained relationships with (3) and (4), we find, with an accuracy to an arbitrary common coefficient,

$$c_1 = 2(n-3)(n+2), \quad c_2 = 2n^2 - 5n - 6$$

and then

$$c_3 = -\frac{2n^2 - 2n - 3}{2(n-2)}, \quad c = \frac{2n^3 - 5n^2 + n + 6}{4(n-2)},$$

$$\bar{c} = \frac{2n^3 - 5n^2 - 3n + 12}{4(n-2)}.$$

It is easy to check that, for $n = m + 2$, any nonnegative values of m are admissible. In the other cases, m should be bounded below; otherwise, fractional functions, rather than polynomials, would have been the result. Specifically, at $n = m + 1$ or $n = m$, m should be ≥ 1 (for $n = m$, the only variant among those considered in this work, i.e., the linear combination, remains). Similarly, for $n = m - 1$ and $n = m - 2$, the restriction $m \geq 3$ is imposed.

It is easy to verify that, in all of the cases, the values of the quadratic form $Q = x^2P_{xx} + y^2P_{yy} + z^2P_{zz} + 2xyP_{xy} + 2xzP_{xz} + 2yzP_{yz}$ give a space field with a desired type of symmetry; in other words, at a given r $(= (x^2 + y^2 + z^2)^{1/2})$, they are proportional to the spherical harmonic of order n.

OPERATOR APPROACH

It would be worthwhile to consider another approach to constructing found solutions that is based on the direct construction of the pressure matrix components. It uses some initial scalar function φ_n and symmetry-preserving operations.

For $n = m$, we, as expected, have two variants of the pressure tensor. The first is $P_{xx} = (2J_x^2 - n - 1)\varphi_n$ and $P_{xy} = (J_xJ_y + J_yJ_x)\varphi_n$, where

$$J_x = y\frac{\partial}{\partial z} - z\frac{\partial}{\partial y}, \quad J_y = z\frac{\partial}{\partial x} - x\frac{\partial}{\partial z}, \quad J_z = x\frac{\partial}{\partial y} - y\frac{\partial}{\partial x}$$

are rotation operators [3].

The other components are easily constructed by analogy.

The second variant for our case is

$$P_{xx} = 2x\frac{\partial\varphi_n}{\partial x} - (n+3)\varphi_n, \quad P_{xy} = x\frac{\partial\varphi_n}{\partial y} + y\frac{\partial\varphi_n}{\partial x}.$$

Consider the case $n = m - 1$. We have

$$P_{xx} = 2(n+4)J_x\frac{\partial U}{\partial x} - 2xJ_x\Delta U,$$

$$P_{xy} = (n+4)J_y\frac{\partial U}{\partial x} + J_x\frac{\partial U}{\partial y} - (yJ_x + xJ_y)\Delta U,$$

where $U = r^2\varphi_n$.

Finally, consider $n = m - 2$. Then,

$$P_{xx} = r^2\frac{\partial^2 U}{\partial x^2} - \alpha x^2\Delta U + \beta x\frac{\partial U}{\partial x} + \gamma U + \delta r^2\Delta U,$$

$$P_{xy} = r^2\frac{\partial^2 U}{\partial x\partial y} - \alpha xy\Delta U + \frac{\beta}{2}\left(y\frac{\partial U}{\partial x} + x\frac{\partial U}{\partial y}\right),$$

where

$$\alpha = -\frac{2n+5}{2(n+3)}, \quad \beta = -\frac{2n^2 + 9n + 8}{n+3},$$

$$\gamma = -\frac{2n^3 + 15n^2 + 37n + 28}{2(n+3)}, \quad \delta = -1.$$

In these formulas, the coefficients are such that the pressure tensor components satisfy biharmonicity and equilibrium conditions (2). Using the formulas, we performed the necessary calculations to make sure that the results obtained are in agreement with those reported in the basic part of the paper (with an accuracy to multi-

plying the pressure tensor matrix by an arbitrary factor).

The agreement occurs for any n but, obviously, is most readily established for not too large n's.

Notice the following easy-to-check feature of the solutions found; namely, the biharmonic solutions for $n = m$, $m - 1$, and $m - 2$ subjected to the Laplace operator are transformed, with an accuracy to a constant factor, into the harmonic solutions for, respectively, $n = m + 2$, $m + 1$, and m (this m differing from the previous m). This feature can also serve as a means to check the solutions.

CONCLUSION

Thus, for each m, we can construct only six linearly independent tensor fields satisfying the equilibrium and biharmonicity conditions for each of the components. The six fields refer to five types of symmetry, the duality of the solutions being observed only at $n = m$.

Recall that each of the symmetry types is $(2n + 1)$-fold degenerate; that is, $2n + 1$ linearly independent tensor fields result when the configurations considered rotate about different axes. Similar degeneracy of scalar, vector, and other fields is frequently encountered in applications (see, for example, [8]). The symmetry of internal states is usually due to external conditions. Naturally, the geometrical symmetry group is narrower for spheroidal bodies [3]. It is, however, reasonable to expect that some deeper symmetry formally similar to the considered symmetry of the fields in spherical bodies will also be found for spheroidal bodies.

The constructed stress fields can be useful for representing equilibrium and vibratory states in elastic and plastic bodies largely of spherical or close-to-spherical shape. Certainly, in many applications, it will be necessary to use a superposition of a finite or infinite number of found solutions.

REFERENCES

1. V. A. Antonov, E. I. Timoshkova, and K. V. Kholshevnikov, *Introduction to the Newtonian Potential Theory* (Nauka, Moscow, 1988).
2. E. W. Hobson, *The Theory of Spherical and Ellipsoidal Harmonics* (Cambridge Univ. Press, Cambridge, 1931; Inostrannaya Literatura, Moscow, 1952).
3. A. S. Baranov, Zh. Vychisl. Mat. Mat. Fiz. **37**, 395 (1997).
4. K. F. Ogorodnikov, *Dynamics of Stellar Systems* (Fizmatgiz, Moscow, 1958; Pergamon, Oxford, 1965).
5. A. E. H. Love, *A Treatise on the Mathematical Theory of Elasticity* (Cambridge University Press, Cambridge, 1927; ONTI, Moscow, 1935).
6. G. Ya. Lyubarskiĭ, *The Theory of Groups and Its Application* (Fizmatgiz, Moscow, 1958).
7. N. Ya. Vilenkin, *Special Functions and the Theory of Group Representations* (Nauka, Moscow, 1965; American Mathematical Society, Providence, 1968).
8. A. S. Baranov, Astron. Zh. **70**, 223 (1993) [Astron. Rep. **37**, 117 (1993)].

Translated by V. Isaakyan

Technical Physics, Vol. 45, No. 7, 2000, pp. 826–830. Translated from Zhurnal Tekhnicheskoĭ Fiziki, Vol. 70, No. 7, 2000, pp. 14–17.

Relativistic Particle in a Traveling Magnetic Field

A. I. Toropova

Advanced Education and Science Center, Moscow State University, Moscow, 121357 Russia
E-mail: toporova@simlab.ilc.msu.su

Received April 27, 1999

Abstract—A Hamiltonian formalism is applied to derive an exact solution to the equation of motion of a charged particle in the electromagnetic field of a traveling current wave. The particle motion is studied in a monochromatic magnetic field and in the traveling jump-like front of the magnetic field, and the wave mechanism for betatron acceleration is analyzed. It is shown that, in each of these situations, a charged particle can be accelerated simultaneously in both the longitudinal and transverse directions. © *2000 MAIK "Nauka/Interperiodica".*

INTRODUCTION

In present-day relativistic mechanics, only a few problems relevant to the motion of charged particles in the field of an electromagnetic wave excited in a real electrodynamic system are known to possess exact analytic solutions. Pavlenko *et al.* [1] solved the equations of motion of a charged particle in the field of a TEM wave propagating in a quadrupole waveguide. This electrodynamic waveguide system, which was first proposed by V. Paul, made it possible to develop a high-resolution mass spectrometer of nonrelativistic particles [2, 3]. An analysis of the domains of stable particle motion showed that quadrupole waveguides can also be used to focus relativistic particles, to separate them out by mass and specific charge, and to reduce the spread in transverse velocities of the beam particles.

In this paper, we derive exact analytic solutions to the Hamiltonian equations of motion of a relativistic particle in the electromagnetic field of a traveling current wave in an axisymmetric electrodynamic system. The solutions obtained make it possible to investigate the stability domains and to determine the kinetic energy and longitudinal momentum of the particle. We consider particle acceleration in a monochromatic magnetic field and in the traveling jumplike front of the magnetic field. We show that, in the regime of betatron wave acceleration, a condition analogous to the well-known 2 : 1 rule should hold. The solution method proposed here is based on the theory of canonical transformations and applies to any mechanism for field excitation.

ELECTROMAGNETIC FIELD OF AN ELECTRODYNAMIC SYSTEM

The 4-potential of the electromagnetic field can be represented as

$$A^\mu(x) = [(e_2x)e_1^\mu - (e_1x)e_2^\mu]B(kx)/2, \qquad (1)$$

where $x^\mu = (ct, x, y, z)$; $e_{(1)}^\mu = (0, 1, 0, 0)$; $e_{(2)}^\mu = (0, 0, 1, 0)$; $n^\mu = (1, 0, 0, 1)$; $k^\mu = (\omega/c)n^\mu$; $B(kx)$ is an arbitrary function of the argument $kx = \omega t - \omega z/c$ [4]; the metric tensor is $g^{\mu\nu} = \mathrm{diag}(1, -1, -1, -1)$; the scalar product of two 4-vectors is defined as $ab = a^\mu b_\mu = a_0b_0 - \mathbf{ab}$, so that $a^2 \equiv a^\mu a_\mu$; and the 4-potential satisfies the wave equation $\partial^\nu\partial_\nu A^\mu = 0$ and the Lorentz gauge $\partial_\mu A^\mu = 0$.

The electromagnetic field tensor has the form

$$F^{\mu\nu} = t^{\mu\nu}B(kx) + [(e_1x)1^{\mu\nu} - (e_2x)f^{\mu\nu}]B'/2,$$

where $t^{\mu\nu} = e_{(2)}^\mu e_{(1)}^\nu e_{(1)}^\mu e_{(2)}^\nu$, $f^{\mu\nu} = e_{(1)}^\mu k^\nu - k^\mu e_{(1)}^\nu$, $1^{\mu\nu} = e_{(2)}^\mu k^\nu - k^\mu e_{(2)}^\nu$, and $B' = dB/d(kx)$.

The electric and magnetic fields are equal to

$$\mathbf{E} = (yk_0B'/2, -xk_0B'/2, 0),$$

$$\mathbf{B} = (xk_0B'/2, yk_0B'/2, B), \quad k_0 = \omega/c.$$

Obviously, we have $\mathbf{EB} = 0$. Note that, in the case $B = \mathrm{const}$, potential (1) defines a constant uniform magnetic field. The traveling magnetic field $B_z = B(\omega t - \omega z/c)$ initiates vortex electric and magnetic fields in the plane orthogonal to the symmetry axis of the system. The function $B(kx)$ satisfies the natural boundary conditions: $B(kx) \longrightarrow B_1$ for $kx \longrightarrow -\infty$ and $B(kx) \longrightarrow B_2$ for $kx \longrightarrow +\infty$, where B_1 and $B_2 > B_1$ are positive constants.

SOLUTION OF THE EQUATIONS OF MOTION

We describe the particle trajectory in parametric form: $x^\mu = x^\mu(\tau)$, where τ is the intrinsic time. The 4-velocity of the particle is $\dot{x}^\mu = (c\dot{t}, \dot{x})$; the superior dot indicates the derivative with respect to τ, so that we have $\dot{x}^\mu = \gamma(c, \mathbf{v})$, where $\gamma = [1 - v^2/c^2]^{-1/2}$. We solve the

1063-7842/00/4507-0826$20.00

equations of motion of a charged particle in terms of the Hamiltonian formalism. The particle motion in the electromagnetic field defined by the 4-potential (1) is described by the Hamiltonian [5]

$$H(x, p) = -(1/2m)[p - (e/c)A(x)]^2 + mc^2/2. \quad (2)$$

Taking into account the relationship $[x^\mu, p^\nu] = -g^{\mu\nu}$ for the fundamental Poisson bracket, we arrive at the equations

$$\dot{x}^\mu = [x^\mu, H], \quad m\dot{x}^\mu = p^\mu - (e/c)A^\mu, \quad (3)$$

$$\dot{p}_\mu = [p_\mu, H], \quad \dot{p}_\mu = (e/c)\dot{x}_\alpha \partial A^\alpha/\partial x^\mu, \quad (4)$$

with the boundary conditions $x^\mu(0) = (0, x_0, y_0, z_0)$ and $\dot{x}^\mu(0) = u^\mu$, where $u^\mu = \gamma_0(c, \mathbf{v}_0)$ and $\gamma_0 = [1 - (\mathbf{v}_0/c)^2]^{-1/2}$. Equations (3) and (4) have three integrals of motion. One of the integrals can be obtained by taking the scalar product (convolution) of Eq. (4) with the 4-vector k^μ: $kp = mku$. Then, taking the convolution of Eq. (3) with k_μ yields the second integral of motion: $k\dot{x} = ku$, which can also be written in terms of coordinates as

$$c\dot{t} - \dot{z} = nu. \quad (5)$$

We thus obtain the wave phase along the particle trajectory: $kx = ku\tau + kx_0$. The third integral of motion for Eqs. (3) and (4) has the form $\dot{x}^2 = c^2$ or

$$(c\dot{t})^2 - \dot{x}^2 - \dot{y}^2 - \dot{z}^2 = c^2. \quad (6)$$

Resolving Eqs. (5) and (6) in $\dot{t}$ and $\dot{z}$, we obtain

$$\begin{aligned} c\dot{t} &= nu/2 + (1/2nu)(c^2 + \dot{x}^2 + \dot{y}^2), \\ \dot{z} &= -nu/2 + (1/2nu)(c^2 + \dot{x}^2 + \dot{y}^2). \end{aligned} \quad (7)$$

The integral of motion (5) is actually a consequence of Eqs. (3) and (4) taken with $\mu = 0.3$:

$$\begin{aligned} mc\dot{t} &= p_0, \quad m\dot{z} = p_z, \\ \dot{p}_0 &= (e/c)k_0(y\dot{x} - x\dot{y})B'/2, \\ \dot{p}_z &= (e/c)k_0(y\dot{x} - x\dot{y})B'/2. \end{aligned} \quad (8)$$

Since the increment $E = mc^2\dot{t}$ in the particle kinetic energy is governed by the vortex electric field, we can write

$$dE/d\tau = c\dot{x}E, \quad dE/d\tau = -(e\omega/c)(x\dot{y} - y\dot{x})B'/2. \quad (9)$$

Equations (3) and (4) taken with the integral of motion (5) and $\mu = 1.2$ can be reduced to the Hamiltonian system

$$\begin{aligned} m\dot{x} &= p_x + (c/c)yB(\sigma)/2, \\ m\dot{y} &= p_y - (c/c)xB(\sigma)/2, \end{aligned} \quad (10)$$

$$\dot{p}_x = (e/c)\dot{y}B(\sigma)/2, \quad \dot{p}_y = -(e/c)\dot{x}B(\sigma)/2, \quad (11)$$

where $\sigma(\tau) = ku\tau + kx_0$. Equations (10) and (11) are generated by the part of Hamiltonian (2) that is independent of the momentum components p_0 and p_z:

$$\begin{aligned} H_{12} = (1/2m)[p_x^2 + p_y^2] + (e/2mc)[yp_x - xp_y]B(\sigma) \\ + (e^2/8mc^2)(x^2 + y^2)B^2(\sigma). \end{aligned} \quad (12)$$

The first integral of Eqs. (10) and (11) is the projection of the generalized particle momentum onto the z-axis:

$$M_z = m(x\dot{y} - y\dot{x}) + (e/2c)(x^2 + y^2)B(\sigma),$$

in which case law (9) describing how the particle kinetic energy increases becomes

$$dE/d\tau = (e^2\omega/8mc^2)(x^2 + y^2)(B^2)' - e\omega M_z/mc.$$

From Eq. (8), we find $cdp_z/d\tau = dE/d\tau$, which allows us to draw the important conclusion that the longitudinal momentum of the particle increases simultaneously with its energy.

Equations (10) and (11) can also be solved by carrying out a sequence of canonical transformations (CTs). First, we make the CT $x, y, p_x, p_y \longrightarrow x', y', p_x', p_y'$ such that

$$\begin{aligned} x &= (1/2m)^{1/2}(x' + y'), \quad y = -i(1/2m)^{1/2}(x' - y'), \\ p_x &= (m/2)^{1/2}(p_x' + p_y'), \quad p_y = i(m/2)^{1/2}(p_x' - p_y'). \end{aligned} \quad (13)$$

In the new variables, Hamiltonian (12) becomes

$$\begin{aligned} H_{12}' = p_x'p_y' + (ie/2mc)(y'p_y' - x'p_x')B \\ + (eB/2mc)^2x'y'. \end{aligned} \quad (14)$$

Now, we eliminate the second term in (14) by performing the CT

$$\begin{aligned} x' &= \exp(-i\beta/2)x_1', \quad y' = \exp(i\beta/2)x_2', \\ p_x' &= \exp(i\beta/2)p_1', \quad p_y' = \exp(-i\beta/2)p_2', \\ \beta(\tau) &= (e/mc)\int_0^\tau d\Theta B|\sigma(\Theta)|, \end{aligned} \quad (15)$$

which puts the Hamiltonian in the form

$$H_{12}'' = p_1'p_2' + (eB/2mc)^2x_1'x_2'. \quad (16)$$

The solution to the canonical equations

$$dx_1'/d\tau = p_2', \quad dx_2'/d\tau = p_1',$$

$$dp_1'/d\tau = -(eB/2mc)^2x_2', \quad dp_2'/d\tau = -(eB/2mc)^2x_1'$$

can be represented as

$$\begin{aligned} x_1' &= (1/2)^{1/2}(wa_1 + w^*a_2^*), \\ x_2' &= (1/2)^{1/2}(wa_2 + w^*a_1^*), \\ p_1' &= (1/2)^{1/2}(\dot{w}a_2 + \dot{w}^*a_1^*), \\ p_2' &= (1/2)^{1/2}(\dot{w}a_1 + \dot{w}^*a_2^*), \end{aligned} \tag{17}$$

where a_1 and a_2 are constants. The function $w\tau$ is a complex solution to the oscillator equation

$$d^2w/d\tau^2 + [eB(\sigma)/2mc]^2 w = 0 \tag{18}$$

with the initial condition $w = (2/\omega_1)^{1/2}\exp(-i\omega_1\tau/2)$ (where $\omega_1 = eB_1/mc$) for $\tau \longrightarrow -\infty$. The Wronskian of the two functions w and w^* is independent of τ: $w\dot{w}^* - \dot{w}w^* = 2i$. We substitute (15) and (17) into (13) to arrive at the solution to the equations of motion (10) and (11):

$$\begin{aligned} x &= (1/\sqrt{m})\mathrm{Re}[(wa_1 + w^*a_2^*)\exp(-i\beta/2)], \\ y &= (1/\sqrt{m})\mathrm{Im}[(wa_1 + w^*a_2^*)\exp(-i\beta/2)]. \end{aligned} \tag{19}$$

In order to determine the functions $t(\tau)$ and $z(\tau)$, we insert (19) into (7). Below, we will be interested only in the solutions to Eq. (18) in the limit $\tau \longrightarrow \infty$, in which the function $B(kx)$ approaches a constant value B_2. In this case, we can use the asymptotic expressions

$$\begin{aligned} w = (2/\omega_1)^{1/2}[C_1\exp(-i\omega_2\tau/2) + C_2\exp(i\omega_2)\tau/2], \\ \omega_2 = eB_2/mc. \end{aligned} \tag{20}$$

Let us make two remarks.

(i) The coefficients C_1 and C_2 can be found from the solutions known in quantum mechanics, because asymptotics (20) are consistent with the problem of particle scattering by a one-dimensional potential. According to [6], the quantities $1/C_1$ and C_2/C_1 play the role of the amplitudes of the forward and backward waves into which the wave that is incident on the potential from the right is scattered. Let $1/p$ be the characteristic scale on which the function $B(\sigma)$ varies. Then, if this function changes adiabatically, $|dB(\sigma)/d\tau| \ll pkuB(\sigma)$, we can see that the ratio $C_2/C_1 \sim \exp(-\pi\omega_1/pku)$ is exponentially small [6].

(ii) Since the Wronskian of the linearly independent solutions w and w^* is equal to $2i$, solution (17) is a CT $x_n', p_n' \longrightarrow x_n = a_n, p_n = ia_n^*$ $(n = 1, 2)$ whose generating function depends on both the old and new variables [5]:

$$p_n' = \partial F_1/\partial x_n', \quad p_n = \partial F_1/\partial x_n,$$

$$F_1 = (1/w^*)[\dot{w}^*x_1'x_2' - i\sqrt{2}(x_1'x_2 + x_2'x_1) + wx_1x_2].$$

With this Wronskian, the Hamiltonian transformed to the new coordinates using the above procedure, $h = H_{12}'' + \partial F_1/\partial\tau$, is identically zero.

PARTICLE MOTION IN THE TRAVELING JUMPLIKE FRONT OF THE MAGNETIC FIELD

Of particular importance is the magnetic field (1), for which the function

$$B^2(\sigma) = (1/2)(B_1^2 + B_2^2) + (1/2)(B_2^2 - B_1^2) \times \tanh[p(\sigma - \sigma_0)] + [B_0/2\mathrm{ch}p(\sigma - \sigma_0)]^2$$

takes on the limiting values B_1^2 and B_2^2 and has a maximum in the range $B_0^2 > B_2^2 - B_1^2$. In quantum mechanics, this function is known as the Eckart potential [6]. The most interesting case here is $pku \gg \omega_1$, which corresponds to a sharp jump in the function $B(\sigma)$. Setting $B_0 = 0$, we arrive at a function such that $B(\sigma) \approx B_1$ for $\sigma < \sigma_0$ and $B(\sigma) \approx B_2$ for $\sigma > \sigma_0$. Since the relationship $\sigma - \sigma_0 = ku(\tau - \tau_c)$ with $\tau_c = (\sigma_0 - kx_0)/ku > 0$ holds along the trajectories of a particle, we can integrate the second-order differential equations following from (10) and (11) over a small vicinity of the point $\tau = \tau_c$ in order to obtain the boundary conditions in the form of the incremental velocity components $\Delta\dot{x}(\omega_2 - \omega_1)y(\tau_c)/2$ and $\Delta\dot{y} = -(\omega_2 - \omega_1)x(\tau_c)/2$. In accordance with (20), the solution to Eq. (18) can be written as

$$\begin{aligned} w_{(1)} &= (2/\omega_1)^{1/2}\exp(-i\omega_1\tau/2), \quad \tau \le \tau_c; \\ w_{(2)} &= (2/\omega_1)^{1/2}[D\exp(-i\omega_2\tau/2) + S\exp(i\omega_2\tau/2)], \\ &\tau \ge \tau_c, \end{aligned} \tag{21a}$$

$$\begin{aligned} D, S &= (D_0, S_0)\exp(-i\omega_1\tau_c/2 \pm i\omega_2\tau_c/2), \\ D_0, S_0 &= (1/2)(1 \pm \omega_1/\omega_2). \end{aligned} \tag{21b}$$

Let us set $x_0 = 0$, $y_0 > 0$, $z_0 = 0$, and $\mathbf{v}_0 = (v_1, 0, 0)$. Then $\dot{x}^\mu(0) = (c\gamma_0, u_1, 0, 0)$, $u_1 = \gamma_0 v_1$, and $\beta = \omega_1\tau$ follow. Substituting (21a) into (19) and setting $\tau = 0$ gives $(m\omega_1)^{-1/2}a_1 = iR$ and $(m\omega_1)^{-1/2}a_2^* = i(y_0 - R)$ with $R = u_1/\omega_1$. In the interval $0 \le \tau \le \tau_c$, the particle trajectory is described by the equations $x(\tau) = R\sin\omega_1\tau$, $y(\tau) = R\cos\omega_1\tau + (y_0 - R)$, and $z(\tau) = 0$; i.e., the trajectory is a circle of radius R centered at $(0, y_0 - R, 0)$. Inserting (21b) into (19), we obtain the solution to Eqs. (10) and (11) in the interval $\tau > \tau_c$: $x(\tau) = \mathrm{Re}x_+$ and $y(\tau) = \mathrm{Im}x_+$, where $x_+(\tau) = x + iy$, which can also be written as

$$x_+(\tau) = i[D_0R\exp(-i\omega_1\tau_c) + S_0(y_0 - R)] \times \exp[-i\omega_2(\tau - \tau_c)] + i[S_0R\exp(-i\omega_1\tau_c) + D_0(y_0 - R)].$$

Setting $[D_0R\exp(-i\omega_1\tau_c) + S_0(y_0 - R)] = R_2\exp(-i\eta)$ yields the components of the 4-velocity:

$$\begin{aligned} \dot{x}(\tau) &= \omega_2 R_2 \cos[\omega_2(\tau - \tau_c) + \eta], \\ \dot{y}(\tau) &= -\omega_2 R_2 \sin[\omega_2(\tau - \tau_c) + \eta]. \end{aligned} \tag{22}$$

The kinetic energy $T = E - mc^2$ (where $E = mc^2\dot{t}$), and the longitudinal momentum $p_z = m\dot{z}$ can be found from (7):

$$\begin{aligned} c\dot{t} &= c\gamma_0 + [(\omega_2 R_2)^2 - (\omega_1 R)^2]/(2c\gamma_0), \\ \dot{z} &= [(\omega_2 R_2)^2 - (\omega_1 R)^2]/(2c\gamma_0). \end{aligned} \tag{23}$$

This indicates that the particle moves along a spiral trajectory of radius R_2, with the axis lying at a distance $r_2 = |S_0R\exp(-i\omega_1\tau_c) + D_0(y_0 - R)|$ from the z-axis. Note that, for $v_1 = 0$, we have $\dot{x}(\tau) = \omega_2 R_2 \cos\omega_2(\tau - \tau_c)$, $\dot{y}(\tau) = -\omega_2 R_2 \sin\omega_2(\tau - \tau_c)$, $R_2 = S_0 y_0$, and $r_2 = D_0 y_0$. In the other particular case, $y_0 = R$, we obtain $\dot{x}(\tau) = \omega_2 R_2 \cos[\omega_2(\tau - \tau_c) + \omega_1\tau_c]$,

$$\dot{y}(\tau) = -\omega_2 R_2 \sin[\omega_2(\tau - \tau_c) + \omega_1\tau_c],$$

$$R_2 = D_0 R, \quad r_2 = S_0 R.$$

From (23), we can see that, after the particle passes through the magnetic field front, its energy becomes higher.

PARTICLE MOTION IN A MONOCHROMATIC FIELD

We consider the function $B(kx) = B_0 + b\cos kx$. Then, from (18) we obtain the Hill equation

$$d^2w/d\tau^2 + (1/4)[\Omega_0 + \omega_0 \cos\sigma(\tau)]^2 w = 0,$$

$$\Omega_0 = eB_0/mc, \quad \omega_0 = eb/mc.$$

Setting

$$2s = ku\tau + kx_0, \quad \mu = (\Omega_0^2 + \omega_0^2/2)/(4ku)^2,$$

$$q = \omega_0\Omega_0/(4ku)^2, \quad q_2 = (\omega_0/8ku)^2,$$

we arrive at the Hill equation in the standard form:

$$d^2w/ds^2 + (\mu + 2q\cos 2s + 2q_2\cos 4s)w = 0. \tag{24}$$

The exponential index in (15) is equal to

$$\beta(\tau) = \Omega_0\tau + (\omega_0/ku)[\sin(ku\tau + kx_0) - \sin(kx_0)].$$

In the case $q_2 \ll q$ (or $b \ll 2B_0$), we arrive at the Mathieu equation [7, 8]. The theory of Mathieu functions implies that, in the plane of the parameters (μ, q), there are regions that correspond to either bounded or unbounded solutions [7]. In the region of small μ and q in the (μ, q) plane, the solution to Eq. (24) is finite in the first stability domain, which is located to the right of the curve $\mu_{c0}(q) = -q^2/2 + 7q^4/128 + \ldots$ and is bounded by the curve $\mu_{c1}(q) = 1 - q - q^2/8 + \ldots$ in the upper half-plane ($q > 0$) and by the curve $\mu_{c1}(q) = \mu_{c1}(-q)$ in the lower half-plane ($q < 0$).

Of particular interest is the case of parametric resonance, in which it may be expected that the energy and longitudinal momentum will increase significantly at $\mu = 1, 4, 9, \ldots$. An analysis of the stability domains allows us to conclude that charged particles can be accelerated in the regime of parametric resonance and can be separated out by specific charge.

BETATRON ACCELERATION REGIME

It is well known that particle losses can be prevented by a focusing magnetic field which decreases away from the axis of the system. We consider particle motion in a traveling nonuniform magnetic field defined by the following components of the 4-potential in cylindrical coordinates:

$$A_0 = A_\rho = A_z = 0, \quad A_\varphi = (1/\rho)\int_0^\rho d\rho\rho B(\rho, kx),$$

where $kx = \omega t - \omega z/c$.

The Lagrangian describing the motion of a relativistic particle can be written in terms of the intrinsic time (in SI units) as [9]

$$L = (m/2)[\dot{\rho}^2 + \rho^2\dot{\phi}^2 + \dot{z}^2 - c^2\dot{t}^2] + e\dot{\phi}\int_0^\rho d\rho\rho B(\rho, \omega t - \omega z/c).$$

The Euler–Lagrange equations have the first integrals (5) and (6): $kx = \sigma(\tau)$ and $\sigma(\tau) = ku\tau + kx_0$. We solve the equations of motion by analyzing the acceleration cycle on a cylindrical surface of constant radius. Setting $\dot{\phi} = \Omega$ and $\rho = R$, we obtain the equations

$$\begin{aligned} dE/d\tau &= -(e\Omega\omega/2\pi)d\Phi/d\sigma, \\ \Phi(\sigma) &= 2\pi\int_0^R d\rho\rho B(\rho, \sigma), \end{aligned} \tag{25}$$

$$0 = m\Omega + eB(R, \sigma), \tag{26}$$

$$mR^2 d\Omega/d\tau + (e/2\pi)d\Phi/d\tau = 0, \tag{27}$$

$$md^2z/d\tau^2 = -(e\Omega\omega/2\pi c)d\Phi/d\sigma, \tag{28}$$

where Φ is the total magnetic flux through a membrane bounded by the particle orbit.

From (26) and (27), we obtain the equation $d\Phi/d\tau = 2\pi R^2 dB/d\tau$. We supplement this equation with the initial conditions $B(R, \sigma) = 0$ and $\Phi(\sigma) = 0$ at $\tau = 0$ and integrate it over the acceleration cycle. As a result, we arrive at an analogue of the "betatron rule": $\Phi(\sigma_m) =$

$2\pi R^2 B(R, \sigma_m)$, where $\sigma_m = ku\tau_m + kx_0$. Substituting Φ and Ω into (25) and (28), we find the kinetic energy $T = E - mc^2$ and the z-component of the 4-velocity:

$$E(\tau_m) = mc^2\gamma_0 + e^2R^2B^2(R, \sigma_m)/(2mnu),$$

$$m\dot{z} = m\dot{z}(0) + e^2R^2B^2(R, \sigma_m)/(2mcnu).$$

We denote the maximum magnetic field strength by $B(R, \sigma_m) = B_m$ and assume that $\dot{z}(0) = 0$. Then, we have $\gamma_0 = 1$, so that the particle kinetic energy at the end of the acceleration cycle is $T(\tau_m) = e^2R^2B_m^2/(2m)$. Since $ecRB_m = 300[R(m)B_m(T)]$ MeV, the kinetic energy $T(\tau_m)$ can be represented as $T(\tau_m) = 45[R^2(m)B_m^2(T)/mc^2\ (\text{MeV})]$ GeV. For proton acceleration, we have $T_p(\tau_m) = 45[R^2(m)B_m^2(T)]$ MeV; and, for electron acceleration, we have $T_e(\tau_m) = 90[R^2(m)B_m^2(T)]$ GeV. Note that, in the regime of conventional betatron acceleration, the kinetic energy of a particle is equal to $T(\tau_m) = [(mc^2)^2 + (ecRB_m)^2]^{1/2} - mc^2 \approx ecRB_m$.

ACKNOWLEDGMENTS

I am grateful to Yu.G. Pavlenko for useful discussions. This work was supported by the Russian Foundation for Basic Research, project no. 97-01-00957.

REFERENCES

1. Yu. G. Pavlenko, N. D. Naumov, and A. I. Toropova, Zh. Tekh. Fiz. **67** (7), 98 (1997) [Tech. Phys. **42**, 809 (1997)].
2. W. Paul, Usp. Fiz. Nauk **160** (12), 109 (1990).
3. Pradip K. Ghosh, *Ion Traps*, The International Series of Monographs on Physics (Clarendon, Oxford, 1995).
4. I. A. Malkin and V. I. Man'ko, *Dynamic Symmetries and Coherent States in Quantum Systems* (Nauka, Moscow, 1979).
5. Yu. G. Pavlenko, *Hamiltonian Methods in Electrodynamics and Quantum Mechanics* (Mosk. Gos. Univ., Moscow, 1988).
6. A. I. Baz', Ya. B. Zel'dovich, and A. M. Perelomov, *Scattering, Reactions and Decays in Nonrelativistic Quantum Mechanics* (Nauka, Moscow, 1971; Israel Program for Scientific Translations, Jerusalem, 1966).
7. P. M. Morse and H. Feshbach, *Methods of Theoretical Physics* (McGraw-Hill, New York, 1953; Inostrannaya Literatura, Moscow, 1958), Vol. 1.
8. N. W. McLachlan, *Theory and Application of Mathieu Functions* (Clarendon, Oxford, 1947; Inostrannaya Literatura, Moscow, 1953).
9. Yu. G. Pavlenko, *Lectures on Theoretical Mechanics* (Mosk. Gos. Univ., Moscow, 1991).

Translated by O.E. Khadin

Technical Physics, Vol. 45, No. 7, 2000, pp. 831–835. Translated from Zhurnal Tekhnicheskoĭ Fiziki, Vol. 70, No. 7, 2000, pp. 18–21.

Electromagnetic Transitions between Rydberg States of a Hydrogen Atom: Violation of the Dipole Selection Rules in a Strong Field

O. B. Prepelitsa

Institute of Applied Physics, Academy of Sciences of Moldova, Chisinau, 277028 Moldova

Received November 30, 1998; in final form, August 3, 1999

Abstract—One-quantum bound–bound transitions between high-excited states of a hydrogen atom are considered. Electron wave functions involving an electromagnetic field even in a zero-order approximation are constructed semiclassically. With these functions, it is shown that transitions accompanied by violation of the dipole selection rules are possible in strong fields. The probability of such transitions is a nonlinear function of electromagnetic field intensity. *© 2000 MAIK "Nauka/Interperiodica".*

The probability of transitions between states of hydrogen-like atoms under the action of an electromagnetic field has been studied in detail (e.g., [1–4]). Basically, the available tables of oscillator forces [1] and the values of reduced matrix elements for the dipole moment [2–4] make it possible to calculate the probabilities of one-photon transitions between arbitrary states of a hydrogen-like atom in the dipole approximation. However, such calculations are valid for moderately strong electromagnetic fields weakly perturbing the corresponding atomic states. Therefore, stationary wave functions for the Coulomb problem are used as wave functions in the zero-order approximation [1, 5]. As follows from classical treatment, such an approach is valid for electromagnetic field strengths bounded by the inequality

$$E_0 \ll \frac{E_{\text{at}}}{(2n_{i,f})^2}, \tag{1}$$

where $E_{\text{at}} = M^2e^5/\hbar^4$ is the atomic field strength; e and M are the electron charge and mass, respectively; and $n_{i,f}$ are the principal quantum numbers of the initial and final states.

In this paper, we consider the probability of one-photon transitions between high-excited states of a hydrogen atom with large orbital angular momenta. In contrast to the standard approach [1–4], quasistationary wave functions describing an electron in the field of both the Coulomb potential and a high-frequency electromagnetic wave are used as wave functions in zero-order approximation (we will further refine the condition on the field frequency). Taking into account the electromagnetic field in the zero-order wave function makes it possible to relax constraints on the strength of the external electromagnetic field and fall outside the framework of perturbation theory. As we will show, the dipole selection rules for the orbital quantum number are violated in strong fields (the selection rules for the magnetic quantum number holds true), and the probabilities of one-photon transitions become nonlinear functions of the electromagnetic field intensity.

Since high-excited states are semiclassical, an electron in such a state is located basically in the vicinity of its classical trajectory. Therefore, it is worthwhile to consider the motion of a classical electron in a wave field in more detail. It is well known that, if in the absence of an electromagnetic field, an electron moves in a path $\mathbf{r}(t)$, then in a field with strength $\mathbf{E}(t)$ and frequency ω and under the conditions

$$\min \mathbf{r}(t) \gg \max \boldsymbol{\alpha}(t), \tag{2}$$

$$\omega \gg \frac{1}{T}, \tag{3}$$

where

$$\boldsymbol{\alpha}(t) = \frac{e\mathbf{E}(t)}{m\omega^2},$$

and T is the period of the unperturbed electron motion, it will move in the quasistationary path (see the figure)

$$\mathbf{r}'(t) = \mathbf{r}(t) - \boldsymbol{\alpha}(t). \tag{4}$$

Thus, the influence of a high-frequency wave is basically reduced to the appearance of oscillations about unperturbed electron trajectory $\mathbf{r}(t)$ (for more details, see [6, Section 30]). This trajectory formally coincides with the electron trajectory in the absence of the external field in a noninertial reference frame with coordinates related to the initial ones by (4). Therefore,

1063-7842/00/4507-0831$20.00

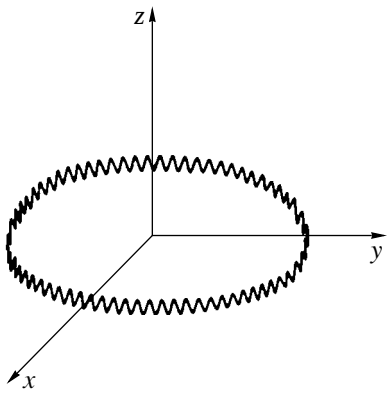

Figure.

we may semiclassically conclude that the electron wave function in the wave field is approximately represented by the Coulomb wave function in the noninertial reference frame:

$$\Psi(\mathbf{r}, t) = \Psi^c(\mathbf{r} - \boldsymbol{\alpha}(t), t)\exp\left(-\frac{i}{\hbar}\int_{-\infty}^{t} d\tau \frac{e^2\mathbf{A}^2(\tau)}{2Mc^2}\right), \quad (5)$$

where $\mathbf{A}(t)$ is the vector potential of the external electromagnetic field in the dipole approximation, c is the speed of light, and $\Psi^c(\mathbf{r}, t)$ is the Coulomb wave function.

Note that (5) is a state with indefinite energy and orbital angular momentum. However, it is convenient to characterize it by the number triple (nlm), which refers to the corresponding Coulomb wave function.

Relation (5) can be obtained more accurately. The Hamiltonian of an electron in both the Coulomb and electromagnetic fields has the form

$$H = \frac{\left(\hat{\mathbf{P}} - \frac{e}{c}\mathbf{A}(t)\right)^2}{2M} - \frac{e^2}{|\mathbf{r}|}.$$

The Hamiltonian of the system can be represented as follows:

$$H = H_0 + V_{\text{int}},$$

$$H_0 = \frac{\left(\hat{\mathbf{P}} - \frac{e}{c}\mathbf{A}(t)\right)^2}{2M} - \frac{e^2}{\mathbf{r} - \boldsymbol{\alpha}(t)}, \quad (6)$$

$$V_{\text{int}} = \frac{e^2}{\mathbf{r} - \boldsymbol{\alpha}(t)} - \frac{e^2}{\mathbf{r}}. \quad (7)$$

One can readily see that (4) is the solution of the classical equations of motion resulting from Hamiltonian (6). Thus, precisely (6) basically determines the electron trajectory in the wave field. Therefore, expression (6) is the Hamiltonian in the zero-order approximation, whereas (7) should be considered as a small perturbation. The validity of dividing the Hamiltonian into the principal term H_0 and perturbation V_{int} also follows from comparison of the magnitudes of (6) and (7) (they are treated classically here) in the trajectory $\mathbf{r}(t)$. Indeed, one can consider V_{int} as a small perturbation if it is much less than H_0. Using the virial theorem, it is sufficient to ascertain that (7) is much less than the second term in (6). Since the latter is proportional to $1/|\mathbf{r}|$ at large distances, whereas (7) is proportional to $1/\mathbf{r}^2$, one can easily see that (7) is small when (2) is satisfied. Since the Feynman paths located in the vicinity of a classical electron trajectory make a major contribution to the evolution of a high-excited electron (due to the semiclassical nature of the state), the division of the Hamiltonian into the principal term H_0 and perturbation V_{int} holds true from the quantum-mechanical point of view as well. Therefore, the solutions of the Shrödinger equation with the Hamiltonian H_0

$$i\hbar\frac{\partial\Psi(\mathbf{r}, t)}{\partial t} = H_0\Psi(\mathbf{r}, t). \quad (8)$$

should be used as wave functions in the zero-order approximation.

Immediate substitution implies that function (5) satisfies Eq. (8), while $\Psi^c(\mathbf{r}, t)$ is the subject to the Shrödinger equation in the Coulomb problem:

$$i\hbar\frac{\partial\Psi^c(\mathbf{r}, t)}{\partial t} = \left(\frac{\hat{\mathbf{P}}^2}{2M} - \frac{e^2}{|\mathbf{r}|}\right)\Psi^c(\mathbf{r}, t).$$

Using well-known formulas of the Coulomb problem, we represent criteria of the applicability of (2) and (3) to the model in the form

$$\frac{E_0}{E_{\text{at}}}\left(\frac{\omega_{\text{at}}}{\omega}\right)^2 \frac{1}{n^2\left(1 - \sqrt{1 - \left(\frac{l}{n}\right)^2}\right)} \ll 1, \quad (9)$$

$$\frac{\omega_{\text{at}}}{\omega}\frac{1}{n^3} \ll 1, \quad (10)$$

where $\omega_{\text{at}} = Me^4/\hbar^3$ is the atomic frequency and n and l are the principal and orbital quantum numbers.

Since the interaction of an atom with the field is considered in the dipole approximation (vector potential $\mathbf{A}(t)$ is independent of coordinates), conditions (9) and (10) should be complemented with a condition setting an upper bound on the field frequency:

$$\frac{\omega}{c}\max|\mathbf{r}(t)| \ll 1,$$

or, alternatively,

$$n^2\left(1+\sqrt{1-\left(\frac{l}{n}\right)^2}\right)\frac{\omega}{\omega_{at}}\frac{e^2}{\hbar c}\ll 1. \tag{11}$$

The more the orbital quantum number l, the better inequalities (9) and (11) are satisfied, since this is the very case when the electron is located far from the nucleus with overwhelming probability. Furthermore, due to the semiclassical nature of the state that implies $l \gg 1$ along with $n \gg 1$, we will assume $n, l \gg 1$ hereafter. For a state with $l/n \sim 1$, conditions (9) and (11) can be represented in the form

$$\frac{E_0}{E_{at}}\left(\frac{\omega_{at}}{\omega}\right)^2\frac{1}{n^2}\ll 1, \tag{12}$$

$$n^2\frac{\omega}{\omega_{at}}\frac{e^2}{\hbar c}\ll 1. \tag{13}$$

Conditions (9)–(13) are consistent in a wide range of parameters. Note that inequalities (9) and (12) bounding the electromagnetic field strength essentially differ from similar inequality (1), which determines the applicability region of the standard perturbation theory. Expressions (9) and (12) reflect the fact that the influence of the field on electrons increases with decreasing field frequency, so that, in the limiting case of $\omega = 0$ (stationary field), perturbation theory is no longer valid.

We consider the transition from the initial atomic state $\Psi_i(\mathbf{r}, t)$ characterized by quantum numbers $(n_i l_i m_i)$ to the final state $\Psi_f(\mathbf{r}, t)$ with quantum numbers $(n_f l_f m_f)$. According to the above discussion, wave functions of the considered states in the wave field have the form (5). Operator V_{int} defined by (7) is the operator that mixes states $\Psi_i(\mathbf{r}, t)$ and $\Psi_f(\mathbf{r}, t)$. Thus, the transition amplitude takes the form

$$A_{if}(t) = -\frac{i}{\hbar}\int_0^t dt'\int d\mathbf{r}\Psi_f^*(\mathbf{r}, t')V_{int}\Psi_i(\mathbf{r}, t').$$

We consider a circularly polarized electromagnetic field. We also assume that the atom is oriented in such a manner that the quantization axis is perpendicular to the polarization plane of the external electromagnetic field. Choosing the coordinate frame where the quantization axis is directed along the 0z-axis, we represent the electromagnetic field strength in the form

$$\mathbf{E}(t) = E_0(\mathbf{e}_x\cos\omega t + \mathbf{e}_y\sin\omega t),$$

where $\mathbf{e}_x$ and $\mathbf{e}_y$ are the unit vectors directed along $0x$ and $0y$, respectively.

Taking into account the explicit form of the Coulomb wave functions $\Psi^c(\mathbf{r}, t)$, after a simple change of the integration variable and some transformations we obtain

$$A_{if}(t) = \sum_{l=1}^{\infty}\sum_{m=-l}^{l} C_{fi}^{lm}M_{fi}^{l}(\alpha_0) \times \frac{\exp\left(\frac{i}{\hbar}(\varepsilon_f-\varepsilon_i-m\hbar\omega)t\right)-1}{\varepsilon_f-\varepsilon_i-m\hbar\omega}, \tag{14}$$

$$C_{fi}^{lm} = \frac{2l+1}{4\pi}\sqrt{(2l_i+1)(2l_f+1)\frac{(l-|m|)!}{(l+|m|)!}} \times P_l^m(0)\begin{pmatrix} l_f & l & l_i \\ -m_f & m & m_i\end{pmatrix}\begin{pmatrix} l_f & l & l_i \\ 0 & 0 & 0\end{pmatrix}, \tag{15}$$

$$M_{fj}^{l}(\alpha_0) = \int_0^{\infty} dr R_{n_f l_f}(r)\frac{e^2\alpha_0^l}{r^{l-1}}R_{n_i l_i}(r), \qquad \alpha_0 = \frac{eE_0}{M\omega^2}, \tag{16}$$

where $P_l^m(x)$ is the associated Legendre polynomial, $\begin{pmatrix} l_f & l & l_i \\ m_f & m & m_i\end{pmatrix}$ is the Wigner $3j$-symbol, index i (f) means that the corresponding magnitude refers to the initial (final) state, and $R_{nl}(r)$ is the radial part of the Coulomb wave function.

It is worth noting here that integral (16) can be calculated analytically, but we do not present the result here because it is rather cumbersome (detailed calculation of integrals of the form (16) is presented in the mathematical appendix in [5]).

The properties of the Wigner $3j$-symbols (e.g., [5]) and zeros of Legendre polynomials

$$P_l^m(0) \sim \cos\left((l+|m|)\frac{\pi}{2}\right)$$

imply that transition amplitude (14) is nonzero if the following conditions are satisfied:

$$m_f - m_i = m, \tag{17}$$

$$l_i - l \le l_f \le l_i + l; \tag{18}$$

$$l_f + l_i + l = 2p, \quad p = 1, 2, 3, \ldots; \tag{19}$$

$$l + |m| = 2p', \quad p' = 1, 2, 3, \ldots. \tag{20}$$

Expression (17) implies that the number of photons m coincides with the difference between the magnetic quantum numbers of the final and initial states. This corresponds to the well-known selection rule for magnetic quantum numbers in dipole transitions under the

action of circularly polarized radiation. Furthermore, we will restrict our consideration to one-photon transitions and, hence, take $m = 1$ in (14) and (15). In this case, it follows from (20) that l should be an odd number. Taking (19) into account, one can conclude that the difference between the orbital quantum numbers of the final and initial states should be an odd number as well:

$$|l_f - l_i| = 2p + 1, \quad p = 0, 1, 2, \ldots. \tag{21}$$

Otherwise, the probability of transition turns out to be zero. The term with the smallest l satisfying the presented conditions makes the major contribution to the sum in (14). According to the summation rule for angular momentum (18), the smallest l is

$$l = |l_f - l_i|. \tag{22}$$

On this basis, the transition amplitude takes the final form

$$A_{if}(t) = C_{fi}^{l1} M_{fi}^{l}(\alpha_0) \frac{\exp\left(\frac{i}{\hbar}(\varepsilon_f - \varepsilon_i - \hbar\omega)t\right) - 1}{\varepsilon_f - \varepsilon_i - \hbar\omega}. \tag{23}$$

Here, l is defined by (22) and the denominator in (23) is assumed to be nonzero.

In the case $l_f = l_i \pm 1$ ($l = 1$), the obtained expressions coincide with those describing one-photon transitions in ordinary perturbation theory when the transition operator is expressed in the "acceleration representation" (e.g., [7]). Such transitions are dipole-allowed in perturbation theory, and they are the most likely. However, as expression (21) shows, transitions between the states with $l = |l_f - l_i| = 2p + 1$, where $p = 1, 2, 3, \ldots$, are also possible. It is clear that such transitions are dipole-forbidden in the standard approach.

Since the transition probability is proportional to the intensity of the exciting field to the l power, as is seen from (16) and (23), the transition probability becomes a nonlinear function of the field intensity for $l \geq 3$. This fact essentially differs from the result of the standard perturbation theory where the probability of a one-photon transition is proportional to the intensity to the first power. Therefore, the observation of nonlinear dependence of the probability of the process on the intensity of the applied electromagnetic field can be an experimental verification of the results obtained in this paper. Note that $|n_f - n_i| \gg 1$, as follows from both condition (10) and a natural assumption that quantum $\hbar\omega$ is of the order of the energy level spacing between the initial and final atomic states.

We present some numerical estimations. For example, for the ratio of matrix elements $\eta = M_{fi}^{1}(\alpha_0)/M_{fi}^{3}(\alpha_0)$ (see (16)), we obtain $\eta \sim 10$, where $M_{fi}^{1}(\alpha_0)$ defines the amplitude of the ordinary dipole transition from the state $n_i = 10$, $l_i = 5$, and $m_i = 0$ to the state $n_f = 30$, $l_f = 6$, and $m_f = 1$; and $M_{fi}^{3}(\alpha_0)$ determines the amplitude of the forbidden dipole transition from the same initial state to the final state $n_f = 30$, $l_f = 8$, and $m_f = 1$ for $E_0 = 9 \times 10^5$ V/cm, $\omega = 10^{14}$ s^{-1}. Thus, the probability of the forbidden dipole transition turns out to be only 10^2 times less than the probability of the ordinary dipole transition in the perturbation theory.

The above consideration of bound–bound transitions in a high-frequency electromagnetic field is an advance outside the framework of perturbation theory (compare criteria (12) and (1)). It became possible due to a more accurate account of the interaction of the atom with the wave field compared to a standard approach, even at the beginning of solving the problem, i.e., in the zero-order wave functions (5). Note that similar wave functions for the states of continuous spectrum were considered in multiphoton ionization of atoms [8–11]. This made it possible to fall outside the framework of perturbation theory and obtain the limiting case of atom ionization by a stationary field (it is well known that perturbation theory is inapplicable to the case of a stationary field, since the radius of convergence for the corresponding series is equal to zero). Note also that the obtained results are applicable not only to a hydrogen atom but to multielectron atoms as well. Since for $n \gg 1$, an electron is located on average far from the atomic residual, the influence of the latter can be taken into account by replacing n by $n - \delta_l$, where δ_l is the quantum defect.

The resonance case ($\varepsilon_f - \varepsilon_i = \hbar\omega$) has remained beyond consideration since it requires other mathematical methods. The problem is complicated by the fact that, in the resonance case, the standard two-level approximation is no longer valid for two reasons: the electron quickly leaves the selected two-level system, and the wave packet spreads due to strong mixing of the states coupled by transitions accompanied by violation of the dipole selection rules. From the classical point of view, this means that electron motion in the wave field becomes stochastic (for more details, see [12]).

REFERENCES

1. H. A. Bethe and E. E. Salpeter, *Quantum Mechanics of One- and Two-Electron Atoms* (Academic, New York, 1957; Fizmatgiz, Moscow, 1960).
2. V. B. Berestetskii, E. M. Lifshitz, and L. P. Pitaevskii, *Quantum Electrodynamics* (Nauka, Moscow, 1980; Pergamon, Oxford, 1982).

3. L. A. Bureeva, Astron. Zh. **45**, 1215 (1968) [Sov. Astron. **12**, 962 (1968)].
4. S. P. Goreslavskiĭ, N. B. Delone, and V. P. Kraĭnov, Zh. Éksp. Teor. Fiz. **82**, 1789 (1982) [Sov. Phys. JETP **55**, 1032 (1982)].
5. L. D. Landau and E. M. Lifshitz, *Quantum Mechanics: Non-Relativistic Theory* (Nauka, Moscow, 1989, 4th ed.; Pergamon, Oxford, 1977, 3rd ed.).
6. L. D. Landau and E. M. Lifshitz, *Mechanics* (Nauka, Moscow, 1973; Pergamon, Oxford, 1976).
7. M. Ya. Amus'ya, *The Photoelectric Effect in Atoms* (Nauka, Moscow, 1987).
8. L. V. Keldysh, Zh. Éksp. Teor. Fiz. **47**, 1945 (1964) [Sov. Phys. JETP **20**, 1307 (1964)].
9. A. I. Nikishov and V. I. Ritus, Zh. Éksp. Teor. Fiz. **50**, 255 (1966) [Sov. Phys. JETP **23**, 168 (1966)].
10. A. M. Perelomov, V. S. Popov, and M. V. Terent'ev, Zh. Éksp. Teor. Fiz. **50**, 1391 (1966) [Sov. Phys. JETP **23**, 922 (1966)].
11. A. M. Perelomov, V. S. Popov, and M. V. Terent'ev, Zh. Éksp. Teor. Fiz. **51**, 309 (1966) [Sov. Phys. JETP **24**, 207 (1966)].
12. N. B. Delone, V. P. Kraĭnov, and D. L. Shepelyanskiĭ, Usp. Fiz. Nauk **140**, 355 (1983) [Sov. Phys. Usp. **26**, 551 (1983)].

Translated by M.S. Fofanov

Technical Physics, Vol. 45, No. 7, 2000, pp. 836–839. Translated from Zhurnal Tekhnicheskoĭ Fiziki, Vol. 70, No. 7, 2000, pp. 22–25.

ATOMS, SPECTRA, AND RADIATION

Positron Scattering by Phonons in Metals

D. A. Gryaznykh

All-Russia Research Institute of Technical Physics, Russian Federal Nuclear Center, Snezhinsk, Chelyabinsk oblast, 456770 Russia

E-mail: d.a.gryaznykh@vniitf.ru

Received March 23, 1999; in final form, October 26, 1999

Abstract—Processes involved in positron–matter interaction are studied. The stopping power and mean free path are calculated for positrons with an energy of about 1 eV, which are scattered mostly by phonons. The mean free path and range of positrons in tungsten, as well as the stopping power of tungsten, are calculated for positron energies between 0.025 and 10 eV. © *2000 MAIK "Nauka/Interperiodica".*

INTRODUCTION

Low-energy positron sources are finding wide application in atomic physics, solid-state physics, physics and chemistry of surfaces and thin films, materials technology, study of lattice defects, etc. One of the methods for producing high-flux low-energy positron beams is the use of a charged particle accelerator. This method has been implemented, for example, in the *SPring-8* complex [1]. Superconductive wiggler magnets installed in the electron–positron storage ring generate high-power synchrotron radiation with a photon energy significantly higher than the pair-production threshold. The positrons thus produced are thermalized by passing through a decelerator. The process of positron deceleration should be taken into account to properly assess the thermalization efficiency and yield of slow positrons.

The ionization processes have been well studied both theoretically and experimentally [2], whereas the intricate lattice processes (collective excitations, interaction with holes and phonons) have not yet been subjected to adequate experimental study. The goal of this work was to calculate the parameters of positron scattering by phonons in tungsten. Calculations were made using the existing theoretical models of positron–phonon interaction and experimental data on the positron energies in metals.

KINETIC EQUATION FOR POSITRONS

Positron interaction with matter involves different processes depending on the positron energy. High-energy positrons induce ionization [2]; positrons with an energy higher than the plasmon-production threshold may cause collective excitations [3]; positrons with lower energies may cause, production of electron–hole pairs; and those with an energy of about 1 eV experience mostly phonon scattering.

The kinetic equation for positron distribution function $f(\mathbf{r}, \mathbf{p}, t)$, where $\mathbf{p}$ is the positron wave vector, is

$$\left(\frac{\partial}{\partial t} + \mathbf{v}(\mathbf{p})\nabla_{\mathbf{r}} + \mathbf{F}\nabla_{\mathbf{p}}\right) f(\mathbf{r}, \mathbf{p}, t) = \left[\frac{\partial}{\partial t}\right]_s - (\lambda_b + \kappa) f + f_i(\mathbf{r}, \mathbf{p}, t). \quad (1)$$

Here, λ_b is the rate of annihilation of delocalized protons; κ is the rate of positron trapping by lattice defects; f_i is the source function; and $[]_s$ is the rate of scattering

$$\left[\frac{\partial}{\partial t}\right]_s = \int d\mathbf{q}[R(\mathbf{q}, \mathbf{p}) f(\mathbf{r}, \mathbf{q}, t) - R(\mathbf{p}, \mathbf{q}) f(\mathbf{r}, \mathbf{p}, t)], \quad (2)$$

where R is the scattering amplitude.

The intensity of low-energy positron scattering by conduction electrons can be calculated in terms of the random-pulse approximation for electron–positron interaction [4]:

$$R_{el}(\mathbf{p}, \mathbf{q}) = \frac{1}{\pi\hbar}\left(\frac{e^2 a_0}{4\pi k_F}\right)^2 \int d\mathbf{k}\,\delta\left[\frac{\hbar^2(\mathbf{k} + \mathbf{p} - \mathbf{q})^2}{2m_e} + \frac{\hbar^2\mathbf{q}^2}{2m^*} - \frac{\hbar^2\mathbf{k}^2}{2m_e}\frac{\hbar^2\mathbf{p}^2}{2m^*}\right] \times \left[1 - f_F^0\left(\frac{\hbar^2(\mathbf{k} + \mathbf{p} - \mathbf{q})^2}{2m_e}, T\right)\right] f_F^0\left(\frac{\hbar^2\mathbf{k}^2}{2m_e}, T\right), \quad (3)$$

where a_0 is the Bohr radius, k_F is the Fermi wave vector, m^* is the positron effective mass, and $f_F^0(E, T) = \{\exp[(E - E_F)/k_B T] + 1\}^{-1}$. The random-pulse approximation can be applied if the positron energy is lower than the ionization threshold (about 10 eV).

A comprehensive review of the theory of positron–matter interaction and its applications to materials technology is given in [5].

1063-7842/00/4507-0836$20.00

POSITRON–PHONON INTERACTION

Thermalized positrons are scattered mainly by longitudinal acoustic phonons. In the Debye approximation with $E(k) = \hbar sk$, the expression for scattering amplitude takes the form [2]

$$R_{ph}(\mathbf{p}, \mathbf{q}) = \frac{\gamma^2}{4\pi^2}|\mathbf{q}-\mathbf{p}|\left\{[f_B^0(\hbar s|\mathbf{q}-\mathbf{p}|, T)+1]\delta \times\left(\frac{\hbar^2\mathbf{p}^2}{2m^*}-\frac{\hbar^2\mathbf{q}^2}{2m^*}-\hbar s|\mathbf{q}-\mathbf{p}|\right)+ f_B^0(\hbar s|\mathbf{q}-\mathbf{p}|, T)\delta \times\left(\frac{\hbar^2\mathbf{q}^2}{2m^*}-\frac{\hbar^2\mathbf{p}^2}{2m^*}-\hbar s|\mathbf{q}-\mathbf{p}|\right)\right\}\theta(\omega_D - s|\mathbf{q}-\mathbf{p}|), \quad (4)$$

where s is the sound velocity, $\omega_D = s(6\pi n)^{1/3}$ is the Debye frequency, and $f_B^0(E, T) = [\exp(E/k_BT) - 1]^{-1}$ is the Bose–Einstein distribution function. The first summand in equation (4) represents phonon emission; and the second summand, phonon absorption. Feynman diagrams of the processes of phonon emission and absorption are given in Fig. 1.

The positron–phonon coupling constant in the deformation potential approximation is given by

$$\gamma = \frac{E_d}{(2\rho s)^{1/2}}, \quad (5)$$

where ρ is the density, E_d is the deformation potential given by

$$E_d = V\frac{\partial E_+}{\partial V}, \quad (6)$$

and E_+ is the total energy of a crystal with a positron at the lowest energy level ($\mathbf{k} = 0$). Experimental [6] and theoretical data [7] for the deformation potentials of several materials are given in the table.

For tungsten, $E_+ = -1.31$ eV. It belongs to the same group as molybdenum. Therefore, $E_d \approx -11$ eV.

POSITRON RANGE

In Eq. (4), R depends only on the absolute values $p = |\mathbf{p}|$, $q = |\mathbf{q}|$, and $\Delta = |\mathbf{p} - \mathbf{q}|$. Therefore, Eq. (2) can be written as

$$\left[\frac{\partial f(p)}{\partial t}\right]_s = \frac{2\pi}{p}\int q\,dq\,\Delta\,d\Delta[R(q, p, \Delta)f(q) - R(p, q, \Delta)f(p)]. \quad (7)$$

Integrating with respect to Δ yields

$$\left[\frac{\partial f(p)}{\partial t}\right]_s = \int dq[R_1(q, p)f(q) - R_1(p, q)f(p)], \quad (8)$$

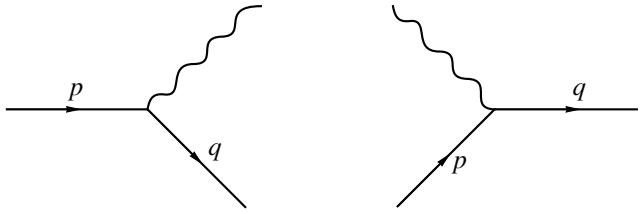

Fig. 1. Feynman diagrams for phonon emission and absorption.

where $R_1(p, q)dqdt$ is the probability that a positron will pass from the state with the wavenumber p to the state with the wavenumber between q and $q \pm dq$ in a time dt.

Using Eq. (4) and removing delta functions, we obtain

$$R_1 = \frac{\gamma^2}{2\pi}\frac{q}{p}\frac{\Delta_0^2}{\hbar s}\begin{cases} f_B^0(\hbar s\Delta_0)+1, & q_{\min} < q < p, \\ f_B^0(\hbar s\Delta_0), & p < q < q_{\max}, \end{cases} \quad (9)$$

where

$$\Delta_0 = \frac{\hbar}{2ms}|p^2 - q^2|. \quad (10)$$

Substituting (10) into (9), we come to

$$R_1 = \frac{\gamma^2}{2\pi}\frac{q}{p}\frac{\hbar}{4m^2s^3}(q^2-p^2)^2 \times\begin{cases} f_B^0\left(\frac{\hbar^2}{2m}(p^2-q^2)\right)+1 & q_{\min} < q < p, \\ f_B^0\left(\frac{\hbar^2}{2m}(q^2-p^2)\right), & p < q < q_{\max}. \end{cases} \quad (11)$$

Now consider the energy distributions using the energy variable $y_p = \hbar^2p^2/2mk_BT$:

$$R_y(y_p, y_q) = \frac{\gamma^2}{2\pi}\frac{m(k_BT)^3}{\hbar^5s^3p}(y_p - y_q)^2 \times\begin{cases} f_B^0(y_p - y_q)+1, & y_{\min} < y_q < y_p, \\ f_B^0(y_q - y_p), & y_p < y_q < y_{\max}. \end{cases} \quad (12)$$

The values of $y_{\min}$ and $y_{\max}$ are determined from the conditions

$$|p - q| \le \Delta \le p + q, \quad s\Delta < \omega_D \quad (13)$$

and are equal to

$$y_{\min} = \max\left(y_p + \frac{2ms^2}{k_BT} - s\sqrt{\frac{2my_p}{k_BT}}, y_p - y_D\right),$$
$$y_{\max} = \min\left(y_p + \frac{2ms^2}{k_BT} + s\sqrt{\frac{2my_p}{k_BT}}, y_p + y_D\right), \quad (14)$$

where $y_D = (\hbar\omega_D)/(k_BT)$.

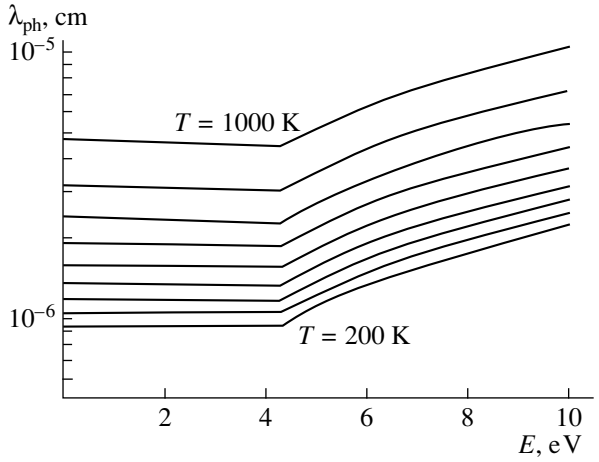

Fig. 2. Mean free path of positrons in tungsten with regard for positron scattering by phonons at T = 200–1000 K.

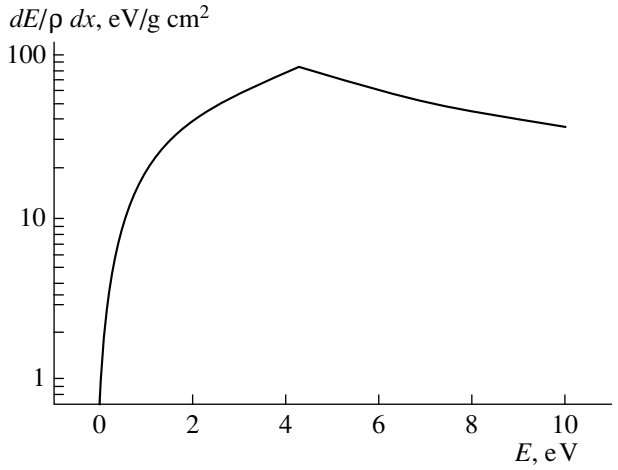

Fig. 3. Stopping power of tungsten with regard for positron scattering by phonons at T = 300 K.

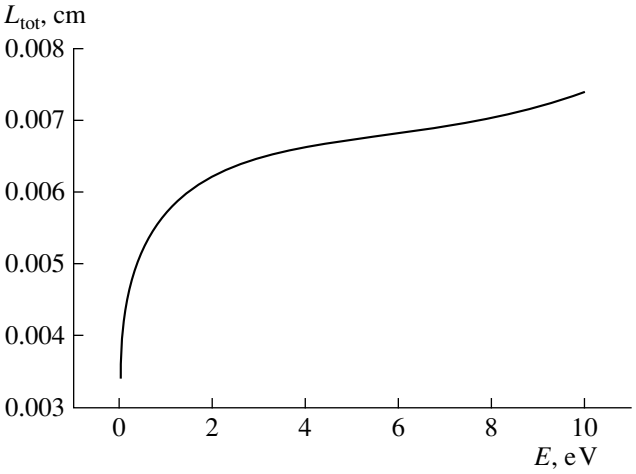

Fig. 4. Positron range in tungsten calculated with regard for positron scattering by phonons at T = 300 K.

Consider the energy range where positron backscattering does not occur; i.e., $x_{\min(\max)} = y_p \pm y_D$. This is the case when

$$y_p > \frac{k_B T}{2m}\left(\frac{y_D}{s} + \frac{2ms}{k_B T}\right)^2.$$

The mean time between interactions is

$$\frac{1}{\tau_{ph}} = \int R_y(y_p, y_q)\,dy_q = \frac{\gamma^2}{2\pi}\frac{m(k_B T)^3}{\hbar^5 s^3}\frac{1}{p}\mathcal{A}, \qquad (15)$$

where

$$\mathcal{A} = 2\int_0^{y_D} x^2 f_B^0(x)\,dx + \frac{y_D^3}{3}. \qquad (16)$$

Therefore, the mean free path is

$$\lambda_{ph} = \tau_{ph}\frac{\hbar p}{m} = \frac{4\pi}{\gamma^2}\frac{\hbar^4 s^3}{m(k_B T)^3}\frac{E}{\mathcal{A}}, \qquad (17)$$

where E is the positron kinetic energy.

The energy loss is given by

$$\frac{dy_p}{dt} = \int (y_q - y_p) R_y(y_p, y_q)\,dy_q = -\frac{\gamma^2}{8\pi}\frac{m(k_B T)^3 y_D^4}{\hbar^5 s^3}\frac{1}{p} \qquad (18)$$

and the stopping power by

$$-\frac{dE}{dx} = -(k_B T)\frac{m}{\hbar p}\frac{dy_p}{dt} = \frac{\gamma^2}{16\pi}\frac{m(\hbar\omega_D)^4}{\hbar^4 s^3}E^{-1}. \qquad (19)$$

Let us calculate the same parameters for phonons in tungsten. For tungsten (in the system of units c = 1), $|E_d|$ = 11 eV, $\omega_D = 3.534 \times 10^{13}$ s^{-1}, $\rho = 19.3$ g cm^{-3} = 2.917×10^{65} eV s^{-3}, $s = 1.112 \times 10^{-5} = 3.33$ km s^{-1}, and $\gamma^2 = 1.865 \times 10^{-59}$ eV s^3.

Putting T = 293 K, we obtain $k_B T$ = 0.0252 eV, y_D = 0.9230, and $\mathcal{A}$ = 0.8819.

The range under consideration is E > 4.58 eV. Within this range, calculations yield ($[E_p]$ = eV)

$$\tau_{ph} = 1.219 \times 10^{-14}\sqrt{E_p}\ \text{s},$$
$$\lambda_{ph} = 7.228 \times 10^{-7} E_p\ \text{cm}, \qquad (20)$$
$$-\frac{dE}{\rho dx} = 372 E^{-1}\ \text{eV cm}^2\ \text{g}^{-1}.$$

To calculate the mean time between interactions and the energy loss in the entire range, the following

Deformation potential E_d determined by Eq. (6) and positron lifetime for several materials

Material	$E_d^{\exp}$, eV	E_d^{th}, eV	$E_\perp$, eV	τ, ps
Al	–6.7	–7.70	–4.41	166
Cu	–9.4	–9.45	–4.81	106
Ag	–11	–9.48	–5.36	120
Mo	–16	–14.3	–1.92	111
W			–1.31	100
Au			–4.59	10

equations should be used:

$$\frac{1}{\tau_{ph}} = \frac{\gamma^2}{2\pi}\frac{m(k_BT)^3}{\hbar^5 s^3}\frac{1}{p}\left\{\mathcal{F}_2(y_p - y_{\min}) + \mathcal{F}_2(y_{\max} - y_p) + \frac{1}{3}(y_p - y_{\min})^3\right\},$$
$$\frac{dy_p}{dt} = \frac{\gamma^2}{2\pi}\frac{m(k_BT)^3}{\hbar^5 s^3}\frac{1}{p}\left\{-\mathcal{F}_3(y_p - y_{\min}) + \mathcal{F}_3(y_{\max} - y_p) - \frac{1}{4}(y_p - y_{\min})^4\right\}, \quad (21)$$

where

$$\mathcal{F}_n(x) = \int_0^x \frac{y^n dy}{\exp(y) - 1}.$$

Assuming $E \gg ms^2$, we obtain

$$\lambda_{ph} = \frac{4\pi\hbar^4 s^4}{\gamma^2}\frac{E}{2T^3\mathcal{F}_2\left(\dfrac{E - E_{\min}}{T} + \dfrac{1}{3}(E - E_{\min})\right)}, \quad (22)$$

$$-\frac{dE}{dx} = \frac{\gamma^2}{16\pi}\frac{m}{\hbar^4 s^3}\frac{(E - E_{\min})^4}{E}, \quad (23)$$

$$L_{\text{tot}} = \int_0^E \frac{dx}{dE}dE = \frac{\pi\hbar^4}{\gamma^2 m^3 s} \times \begin{cases} \ln\dfrac{E}{2ms^2}, & E < \tilde{E}, \\ \ln\dfrac{\tilde{E}}{2ms^2} + \dfrac{m^2 s^4}{\hbar^4\omega_D^4(E^2 - \tilde{E}^4)}, & E > \tilde{E}, \end{cases} \quad (24)$$

where

$$E_{\min} = \max(E - s\sqrt{2mE}, E - \hbar\omega_D), \quad \tilde{E} = \frac{\hbar^2\omega_D^2}{2ms^2}. \quad (25)$$

The temperature dependences of dE/dx and positron range L_{tot} are involved only in the expressions for sound velocity and Debye frequency. In the approximation used and within the temperature range under consideration, these values can be regarded as temperature-independent.

The mean free path of a positron in tungsten and the stopping power of tungsten were calculated for positron energies between 0.025 and 10 eV and temperatures ranging from 200 to 1000 K. A plot of the mean free path vs. positron energy is presented in Fig. 2; the stopping power vs. energy, in Fig. 3; and the positron range vs. energy, in Fig. 4.

CONCLUSION

Thermalized positrons are scattered mainly by acoustic phonons. The Debye approximation allows the phonon contribution to positron scattering to be estimated. In this work, the mean free path of a positron in tungsten and the stopping power of tungsten were calculated for the positron energies 0.025–10 eV and temperatures 200–1000 K.

ACKNOWLEDGMENTS

This work was supported by the International Science and Technology Center, project no. 767.

REFERENCES

1. F. Ando, J. Synchrotron Radiat. **S3**, 201 (1996).
2. A. Perkins and J. R. Carbotte, Phys. Rev. B: Condens. Matter **1**, 101 (1970); W. R. Frensley, Rev. Mod. Phys. **62**, 745 (1990).
3. J. Oliva, Phys. Rev. B: Condens. Matter **21**, 4909 (1980).
4. E. R. Woll and J. P. Carbotte, Phys. Rev. **164**, 985 (1967).
5. M. J. Puska and R. M. Niemenen, Rev. Mod. Phys. **66**, 841 (1994).
6. E. Soinen, H. Huono, P. A. Huttunen, *et al.*, Phys. Rev. B: Condens. Matter **41**, 6227 (1990).
7. O. V. Boev, M. J. Puska, and R. M. Niemenen, Phys. Rev. B: Condens. Matter **36**, 7786 (1987).

Translated by K. Chamorovskiĭ

Technical Physics, Vol. 45, No. 7, 2000, pp. 840–848. Translated from Zhurnal Tekhnicheskoĭ Fiziki, Vol. 70, No. 7, 2000, pp. 26–34.

Instability of a Charged Spherical Viscous Drop Moving Relative to a Medium

A. I. Grigor'ev, V. A. Koromyslov, and S. O. Shiryaeva

Yaroslavl State University, Sovetskaya ul. 14, Yaroslavl, 150000 Russia

E-mail: rectorat@uniyar.ac.ru

Received July 12, 1999

Abstract—It is shown that, as the velocity of the flow around a charged drop of viscous liquid increases the drop charge value critical for the occurrence of drop instability rapidly decreases. It is found that, for some domains of values of the charge, the ratio of densities of the media, and the ambient velocity, the even and odd modes of the drop capillary oscillations pairwise couple with each other, which represents drop vibrational instability against the tangential discontinuity of the velocity field at the drop surface. At medium velocities larger than those associated with such domains, the instability growth rates for odd modes exceed the increments of even modes with smaller orders, which corresponds to the parachute-like deformation of the drop in the flow. *© 2000 MAIK "Nauka/Interperiodica".*

INTRODUCTION

The instability of a charged viscous drop moving relative to a medium is manifested in a number of academic, engineering, and technological problems. The problem of stability against the tangential discontinuity of velocity field at the drop free surface arises in operation of various drip–jet devices, in paint sputtering, and in the atomization of liquid fuels [1–3]. This problem is of considerable interest for studying thunderstorm electricity in the context of investigation of the physical mechanism of lightning initiation: lightning may start with corona discharge in the neighborhood of a free-falling, large, water-bearing hailstone [4–6]. The instability of a drop either falling in the atmosphere or moving with a constant speed in a medium with higher density was studied in a large number of papers [7]. Nevertheless, the conditions of occurrence of the instability against the tangential discontinuity of the velocity field at the surface of a drop moving relative to a medium are still poorly understood. The same problem in the case of a charged drop is almost unstudied. Instabilities of two types must evidently occur in this case: the instability of the drop against its charge [3, 8] and the instability of the drop–medium interface against the tangential discontinuity of the velocity field, i.e., the instability of the Kelvin–Helmholtz type [9, 10].

Therefore, it is of interest to study the conditions for occurrence of instability of a charged viscous-liquid drop moving with a constant speed in a medium. We solve the problem treating the surrounding medium as a perfect liquid.

1. Let a perfect incompressible dielectric liquid of density ρ_1 and dielectric constant ε move with the constant velocity $\mathbf{U}$ relative to a spherical drop that consists of a perfectly conducting liquid with density ρ_2 and kinematic viscosity ν_2 and has radius R and charge Q. Let us find the critical conditions for instability of the drop capillary oscillations under these assumptions. We will use spherical coordinates with the origin at the center of the drop and employ the linear approximation in the perturbation value $\xi(\Theta, t)$ of the equilibrium spherical surface of the drop that is caused by the capillary wave motion of the liquid. The equation for the perturbed surface of the drop is taken in the form $r(\Theta, t) = R + \xi(\Theta, t)$.

The set of hydrodynamic equations modeling the capillary motion of the liquid in the system includes the Euler equation for the potential ($\mathrm{curl}\mathbf{V}_1 = 0$) motion of the medium and the Navier–Stokes equation for the drop

$$\frac{\partial \mathbf{V}_1}{\partial t} + \frac{1}{2}\nabla(V_1^2) = -\frac{1}{\rho_1}\nabla P_1, \tag{1}$$

$$\frac{\partial \mathbf{V}_2}{\partial t} = -\frac{1}{\rho_2}\nabla P_2 + \nu_2 \Delta \mathbf{V}_2; \tag{2}$$

continuity equations

$$\mathrm{div}\,\mathbf{V}_j = 0, \quad j = 1; 2 \tag{3}$$

with the boundary conditions

$$r = 0: \quad V_2 = 0, \tag{4}$$

$$r = R: \quad \frac{\partial \xi}{\partial t} = V_{1r} - \frac{1}{r}V_{1\Theta}\frac{\partial \xi}{\partial \Theta}, \quad \frac{\partial \xi}{\partial t} = V_{2r}, \tag{5}$$

$$\mathbf{n}(\mathbf{r}\cdot\nabla)\mathbf{V}_2 + \boldsymbol{\tau}(\mathbf{n}\cdot\nabla)\mathbf{V}_2 = 0, \tag{6}$$

$$-P_1 - P_\sigma + P_E = -P_2 + 2\rho_2\nu_2\mathbf{n}_1(\mathbf{n}\cdot\nabla)\mathbf{V}_2, \tag{7}$$

1063-7842/00/4507-0840$20.00

$$r \longrightarrow \infty: \quad \mathbf{V}_1 = \mathbf{U}; \tag{8}$$

the condition reflecting the invariance of the volumes of both media

$$\int_\Omega \xi(\Theta, \varphi, t)\, d\Omega = 0; \tag{9}$$

and the following condition meaning that the center of mass of the system is fixed:

$$\int_\Omega (\Theta, \varphi, t)\mathbf{e}_r\, d\Omega = 0. \tag{10}$$

Hereafter, subscript 1 relates to parameters of the external medium; subscript 2 relates to the parameters of the drop; $\mathbf{n}$ and $\boldsymbol{\tau}$ are the unit vectors, respectively, normal and tangent to the drop–medium interface; $\mathbf{V}_j(\mathbf{r}, t)$ and $P_j(\mathbf{r}, t)$ are the velocity and pressure fields, respectively; P_σ is the following perturbation of the pressure of the surface tension forces [9]:

$$P_\sigma(\xi) = -\frac{\sigma}{R^2}(2 + \Delta_\Omega)\xi, \tag{11}$$

where σ is the surface tension at the interface; Δ_Ω is the angular part of the Laplacian in the spherical coordinate system; P_E is the following perturbation of the electric field pressure related to the perturbation of the drop surface [11]:

$$P_E = \frac{Q^2}{4\pi\varepsilon}\sum_{n=0}^{\infty}\sum_{m=-n}^{n}(n+1)A_{nm}Y_n^m(\Theta, \varphi) - \frac{Q^2}{2\pi\varepsilon}\xi,$$
$$A_{nm} = Q\int_0^{\pi}\int_0^{2\pi}\xi(\Theta, \varphi, t)Y_n^m(\Theta, \varphi)\sin\Theta\, d\Theta\, d\varphi, \tag{12}$$

where $Y_n^m(\Theta, \varphi)$ are the normalized spherical functions; and $d\Omega$ is the solid angle element.

The term proportional to $\sim V_1^2$ was retained in (1), because it includes the first- and second-order terms. Conditions (9) and (10) set a lower bound on the spectrum of the system capillary oscillations [11].

2. To simplify the solution procedure, it is appropriate to go over from the dimensional *MTL* basis, where *M*, *L*, and *T* are the units of mass, length, and time, respectively, to another, more convenient, basis reducing the number of the model parameters. In this basis, the units of the volume density ρ_2 of the constituent substance of the drop, drop radius *R*, and surface tension σ are taken as the basic units and are equated to unity: $\rho_2 = R = \sigma = 1$. The characteristic scales corresponding to the new basis have the form

$$r_* = R, \quad t_* = R^{3/2}\rho_2^{1/2}\sigma^{-1/2}, \quad U_* = R^{-1/2}\rho_2^{-1/2}\sigma^{1/2},$$
$$P_* = R^{-1}\sigma, \quad Q_* = R^{3/2}\sigma^{1/2}, \quad \nu_* = R^{1/2}\rho_2^{-1/2}\sigma^{1/2}.$$

We denote the dimensionless quantities as $\nu_2 \equiv \nu_1$ and $\rho_1 \equiv \rho$.

Taking into account the axial symmetry of the problem, we will ignore the dependence of the quantities on the angle φ. This means that the velocity field has no azimuthal rotational component, which is of no interest, because it does not couple with the potential and rotational poloidal velocity components [11] and does not affect the drop stability. The velocity field V_2 in the drop is represented as the sum of two orthogonal fields [11]:

$$\mathbf{V}_2(\mathbf{r}, t) = \nabla\Psi_1(\mathbf{r}, t) + \nabla\times(\nabla\times\mathbf{r})\Psi_2(\mathbf{r}, t), \tag{13}$$

where the first term defines the potential part of the velocity field and the second one is the rotational poloidal part.

In accordance with [9, 10], the velocity field in the medium in a neighborhood of the unperturbed surface of the spherical drop is written in the form

$$\mathbf{V}_1 = \nabla\varphi + \nabla\varphi^{(0)},$$
$$\mathbf{V}_1^{(0)} = \nabla\varphi^{(0)} = -\frac{R^3}{2r^3}[3\mathbf{n}(\mathbf{U}\cdot\mathbf{n}) - \mathbf{U}] + \mathbf{U}, \tag{14}$$

where Ψ_1, Ψ_2, and φ are the first-order quantities.

3. Scalar functions $\Psi_1(\mathbf{r}, t)$, $\Psi_2(\mathbf{r}, t)$, and $\varphi(\mathbf{r}, t)$ appearing in the expression for the velocity fields of liquid motion in the medium and in the drop, as well as the perturbation $\xi(\mathbf{r}, t)$, are sought in the form

$$\Psi_j(\mathbf{r}, t) = \sum_n \Psi_{jn}(r)Y_n(\Theta)\exp(St) \quad (j = 1, 2),$$
$$\varphi(\mathbf{r}, t) = \sum_n \varphi_n(r)Y_n(\Theta)\exp(St); \tag{15}$$
$$\xi(\mathbf{r}, t) = \sum_n Z_n Y_n(\Theta)\exp(St).$$

We solve the problem (1)–(15) by using the scalarization method described in detail elsewhere [11] and applied to particular problems in [12–15]. Omitting intermediate calculations, we write the following final system of algebraic equations for unknown amplitudes Z_n of the liquid capillary motion forming the contour of the perturbed interface:

$$\rho U^2 K_n Z_{n-2} - \rho USL_n Z_{n-1} + \{\kappa_n S^2 + 2\nu F_n(x)S$$

$$-\rho U^2 M_n + \gamma_n\} Z_n + \rho U S I_n Z_{n+1} + \rho U^2 J_n Z_{n+2} = 0,$$

$$W \equiv \frac{Q^2}{4\pi\varepsilon}, \quad M_n \equiv \frac{9\alpha_n\beta_{n-1}}{2n} + \frac{9\beta_n\alpha_{n+1}}{2(n+2)},$$

$$K_n \equiv \frac{9\alpha_n\alpha_{n-1}}{2n}, \quad L_n \equiv \frac{(9n+6)\alpha_n}{2n(n+1)},$$

$$I_n \equiv \frac{(9n+12)\beta_n}{2(n+1)(n+2)}, \quad J_n \equiv \frac{9\beta_n\beta_{n+1}}{2(n+2)}, \qquad (16)$$

$$\alpha_n \equiv \frac{n(n-1)}{\sqrt{(2n-1)(2n+1)}}, \quad \beta_n \equiv \frac{(n+1)(n+2)}{\sqrt{(2n+1)(2n+3)}},$$

$$x = \sqrt{\frac{S}{\nu}}, \quad \kappa_n \equiv \frac{\rho}{(n+1)} + \frac{1}{n}, \quad \gamma_n \equiv (n-1)[n+2-W],$$

$$F_n(x) = \frac{1}{n}(n-1)(2n+1)$$

$$+ \frac{1}{n}(n-1)^2(n+1)\left[1 - \frac{x}{2}\frac{i_n(x)}{i_{n+1}(x)}\right]^{-1},$$

where $i_n(x)$ represents the spherical Bessel functions.

In the limit of a nonviscous drop, the problem under consideration transforms to the problem of motion of a perfect-liquid drop with constant velocity U in a perfect medium, which was solved in [10]. Since $F_n(x)$ also tends to zero at $\nu \longrightarrow 0$ [11], Eq. (16) reduces to the corresponding equation obtained in [10]. In the case when $\rho = 0$, the problem transforms to the problem of capillary oscillations of a charged viscous drop in vacuum, which was solved in [11, 12], and Eq. (16) reduces to the equation derived in these papers. At $U = 0$, we have the problem of capillary oscillations of a charged drop in a dielectric medium. This problem is the limiting case of the problem studied in [15] at $\nu_1 = 0$. Thus, the problem correctly reduces to simpler limiting cases.

4. In the limiting case of a drop of low-viscosity liquid, one can analytically study the effect of viscosity on the natural frequencies of capillary oscillations, their damping rates, and the growth rate of instability. In this case, $x \gg 1$ and we use the following asymptotic expansion of the spherical Bessel functions at large values of argument [11]:

$$i_n(x)|_{x \gg 1} \approx \frac{1}{2x} e^x \left[1 + 0\left(\frac{1}{x}\right)\right],$$

Then, the ratio of the Bessel functions has the asymptotic behavior

$$\left.\frac{i_n(x)}{i_{n+1}(x)}\right|_{x \gg 1} \approx 1 + 0\left(\frac{1}{x}\right),$$

and the second term in the braces in (16) depends on the viscosity ν and the frequency S as

$$2\nu F_n(x) S \sim 2\nu F_{n0} S - 2\nu\sqrt{\nu s},$$

$$F_{n0} = \frac{1}{n}(n-1)(2n+1).$$

Retaining in (16) the terms of no higher than the first degree in ν and neglecting the coupling of modes, we obtain the dispersion equation

$$\kappa_n S^2 + 2\nu F_{n0} S - \rho U^2 M_n + \gamma_n = 0. \qquad (17)$$

Solutions to (17) are as follows:

$$S = -\nu(n-1)(2n+1)\left(\frac{n\rho}{(n+1)} + 1\right)^{-1}$$

$$\pm\sqrt{[n(n-1)[W-(n+2)] + n\rho U^2 M_n]\left(\frac{n\rho}{(n+1)} + 1\right)^{-1}}.$$

Three different cases can be realized:

(a) If

$$W < (n+2) - \frac{1}{(n-1)}\rho U^2 M_n, \qquad (18)$$

the quantity S determines the natural frequencies ω_n of the surface oscillations for the charged drop of low-viscosity liquid. These frequencies coincide with the natural frequencies of oscillations of the drop of perfect liquid; and the allowance for viscosity results in the appearance of the damping decrement β_n of the drop surface natural oscillations, which is proportional to the viscosity:

$$S = -\beta_n \pm i\omega_n \equiv -\nu(n-1)(2n+1)\left(\frac{n\rho}{(n+1)} + 1\right)^{-1}$$

$$\pm i\sqrt{[n(n-1)[(n+2)-W] - n\rho U^2 M_n]\left(\frac{n\rho}{(n+1)} + 1\right)^{-1}}.$$

(b) If the condition opposite to (18) is valid, S describes the rising rate δ_n for instability of the charged drop of low-viscosity liquid,

$$S = \delta_n = \delta_{n0} - \beta_n \equiv |\omega_n| - \beta_n,$$

where $\delta_{n0} = |\omega_n|$ is the rising rate of instability of the charged drop of perfect liquid.

(c) As in the case of perfect liquid [10], equality in (18) determines both the boundary separating stable and unstable solutions and the critical relation between the charge of the drop and its velocity with respect to the medium.

5. To analyze the case of a high-viscosity liquid, i.e., $x \longrightarrow 0$, we use the following asymptotic expansion of

the spherical Bessel functions for small argument [11]:

$$\left[\frac{x}{2}\frac{i_n(x)}{i_{n+1}(x)} - 1\right]^{-1} \approx \frac{2}{(2n+1)}\left[1 - \frac{x^2}{(2n+1)(2n+5)} + \frac{x^4}{(2n+1)(2n+5)^2(2n+7)}\cdots\right]. \quad (19)$$

Substituting (19) into (16), neglecting the coupling of modes, and collecting the terms with the same powers in S, we obtain the following dispersion equation in the approximation of high viscosity:

$$\left[A_n + \frac{n\rho}{(n+1)}\right]S^2 + B_n S\nu - n\rho U^2 M_n + n\gamma_n = 0,$$

$$A_n = \frac{3(4n^3 + 8n^2 + 6n + 3)}{(2n+1)^2(2n+5)}, \quad (20)$$

$$B_n = \frac{2(n-1)(2n^2 + 4n + 3)}{(2n+1)}.$$

Solutions to (20) have the form

$$S = \left[-B_n\nu \pm \sqrt{B_n\nu^2 + 4\left[A_n + \frac{n\rho}{n+1}\right][n(n-1)[W-(n-2)] + n\rho U^2 M_n]}\right]\left[A_n + \frac{n\rho}{n+1}\right]^{-1}. \quad (21)$$

Let us analyze the dependence of these solutions on the parameter W.

(a) If condition (18) is fulfilled and the radicand is negative, the expression for S becomes complex. The imaginary part of S determines the frequencies ω_n of the surface natural oscillations, and the absolute value of the real part represents damping decrements β_n:

$$S = -\beta_n \pm i\omega_n.$$

Therefore, the drop surface undergoes damped oscillations.

(b) If condition (18) is valid and viscosity ν is large enough so that the radicand is positive, both roots of equation (21) are negative. Their absolute values determine damping decrements $\beta_n^{(1)}$ and $\beta_n^{(2)}$ of the perturbation of the drop surface. The time dependence of the amplitude of the perturbation described by the nth-order spherical function $Y_n(\Theta)$ in (15) has the form of the sum of two exponents

$$Z_n = C_1\exp(-\beta_n^{(1)}t) + C_2\exp(-\beta_n^{(2)}t).$$

At small values of time t ($t \longrightarrow 0$), the perturbation damping is characterized by the smaller decrement $\beta_n^{(1)}$, because the exponent with the larger value $\beta_n^{(2)}$ vanishes faster.

The condition that the radicand in (21) is equal to zero separates the periodic and aperiodic, decaying in time solutions

$$[n(n-1)[n+2-W] - n\rho U^2 M_n]\nu_{kp}^{-2} = \frac{B_n}{4}\left[A_n + \frac{n\rho}{n+1}\right]^{-1}. \quad (22)$$

Equation (22) determines the bifurcation points, i.e., the values ν_{kp} of viscosity for given drop charge Q and oscillation mode order n such that the oscillation frequency ω_n vanishes and, instead of one damping decrement β_n, two decrements, $\beta_n^{(1)}$ and $\beta_n^{(2)}$, appear. The numerical calculations with $W = 0$, $\rho = 0$, and $U = 0$ yield the following critical values of dimensionless viscosity at which the capillary oscillations vanish: $\nu \approx 2.1$, 2.66, 3.15, 3.57, 3.96, and 4.31 for $n = 2$, 3, 4, 5, 6, and 7, respectively. It is seen from (22) that, as the Rayleigh parameter W and velocity U of the medium increase, the critical value of the dimensionless viscosity ν decreases. The increase of the relative density of the medium results in the increase of the critical value of the dimensionless viscosity ν for low velocity values, i.e., when $U \le 1$, and leads to the decrease of the critical value for high velocity values.

(c) If the condition opposite to (18) is valid and the roots of (21) are real and have opposite signs, the drop surface is unstable, because solutions exponentially rising in time appear. The positive root determines the rate δ_n of instability rising, which depends strongly on viscosity as follows:

$$\delta_n = \left[\sqrt{B_n\nu^2 + 4\left[A_n + \frac{n\rho}{n+1}\right][n(n-1)[W-(n+2)] + n\rho U^2 M_n]} - B_b\nu\right]\left[A_n + \frac{n\rho}{n+1}\right]^{-1}.$$

Therefore, as in the limiting cases of perfect and low-viscosity liquids, the equality in (18) in the case of high-viscosity liquids describes both the boundary between stable and unstable solutions and the critical relation between the charge of the drop and its velocity with respect to the medium.

6. Let us return to the general case of arbitrary viscosity. The condition necessary and sufficient for the

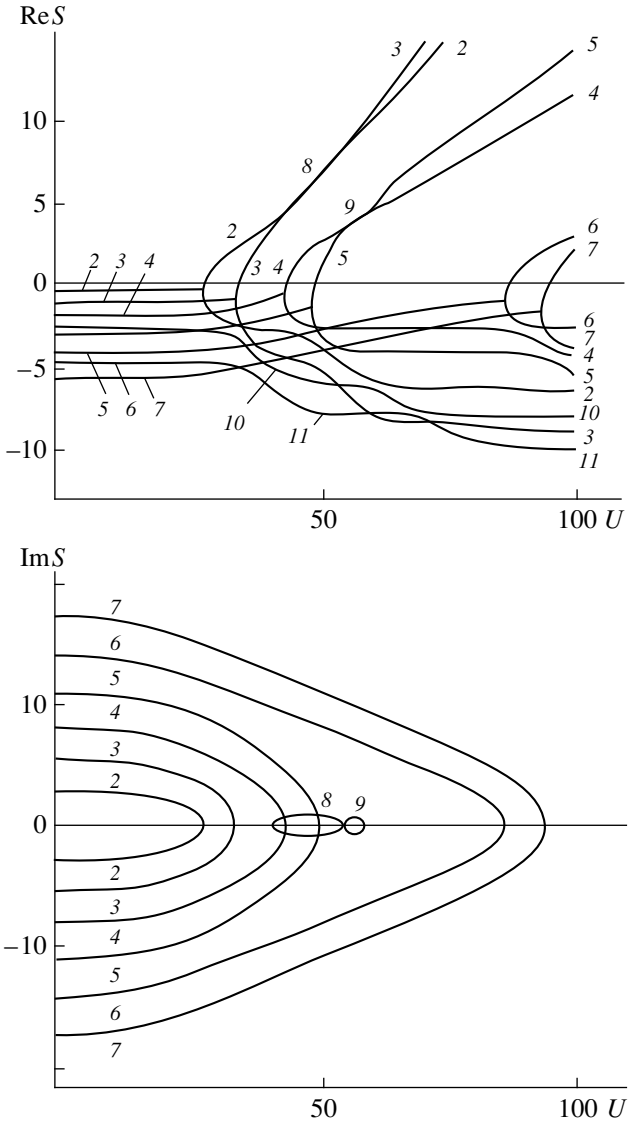

Fig. 1. Real Re*S*(*U*) and imaginary Im*S*(*U*) parts of the dimensionless frequency *S* of the drop capillary oscillations against dimensionless ambient velocity *U* for $\rho = 10^{-3}$, $\nu = 0.1$, and $W = 0$.

existence of nontrivial solutions to homogeneous system (16) is that the determinant composed of the coefficients of desired amplitudes Z_n be equal to zero:

$$\begin{vmatrix} \chi_2 & \rho USI_2 & \rho U^2 J_2 & 0 & \dots \\ -\rho USL_3 & \chi_3 & \rho USI_3 & \rho U^2 J_3 & \dots \\ \rho U^2 K_4 & -\rho USL_4 & \chi_4 & \rho USI_4 & \dots \\ 0 & \rho U^2 K_5 & -\rho USL_5 & \chi_5 & \dots \\ \dots & \dots & \dots & \dots & \dots \end{vmatrix} = 0, \quad (23)$$

$$\chi_j = \kappa_j S^2 + 2\nu F_j - \rho U^2 M_j + \gamma_j;$$
$$j = 2, 3, 4, 5, \dots.$$

This equality represents the dispersion equation describing the spectrum of the drop capillary oscillations depending on the dimensionless physical parameters *W*, *U*, ρ, and ν. Variation in these parameters changes the spectrum of capillary oscillations: at definite values of *W*, *U*, and ρ, certain solutions S_n^2 vanish and become positive with further variation of the parameters. Amplitudes of the corresponding capillary oscillations increase exponentially in time; i.e., the drop becomes unstable and decomposes [3]. The zero solutions to the dispersion equation appear under the condition that the free term in equation (23) vanishes. This condition determines the relation between the charge and velocity of the drop that is critical for the drop instability occurrence, and it can be easily obtained by putting $S = 0$ in (23). The numerical calculation for the resulting equation demonstrates that the desired critical relation between *W* and *U* differs little from the analytical form obtained by neglecting the coupling modes:

$$W_n = (n+2) - (n-1)^{-1} \rho U M_n^2. \quad (24)$$

As ρU^2 increases, the *W* parameter value critical for occurrence of the drop instability against drop charge rapidly decreases, which gives reason to revive the physical model of lightning initiation developed in [4–6]. This model is based on the idea that the corona discharge lights in the neighborhood of a large melting hailstone freely falling in a thundercloud. The results obtained above enable us to derive correct numerical estimates and to fit the model of discharge initiation to real thundercloud parameters using measured values of charge, velocity of falling drops, and strength of electric field inside the cloud.

Successive-approximation numerical calculations for dispersion equation (23) reveals that the frequency $S = S(U)$ of the drop capillary oscillations as a function of the velocity of the incident flow has the same qualitative character for various modes at $W = 0$ and $\nu = 0.1$; it is shown in Fig. 1 for the first six modes at $\rho = 10^{-3}$. Curves *2* to *7* display the respective modes. Curve *1* is absent, because the corresponding mode is responsible for the translational displacement of the drop [9]. Note that the second mode couples with the third; and the fourth mode couples with the fifth, which results in the appearance of oscillatory solutions *8* and *9*, respectively. The parts $\mathrm{Re}S > 0$ of the curves $\mathrm{Re}S = \mathrm{Re}S(U)$ correspond to the rate of instability rising of relevant modes of the drop capillary oscillations. Thus, for the velocity region associated with curves *8* and *9*, the vibrational instability of the drop takes place that is typical of the Kelvin–Helmholtz type instabilities [9, 10, 16]. Curves *10* and *11* correspond to the aperiodic rotational polar motion of liquid. This motion does not affect the instability of the drop and was analyzed in more detail in [13, 15].

It is of interest that, to the right of the velocity region where the second and third modes couple with one

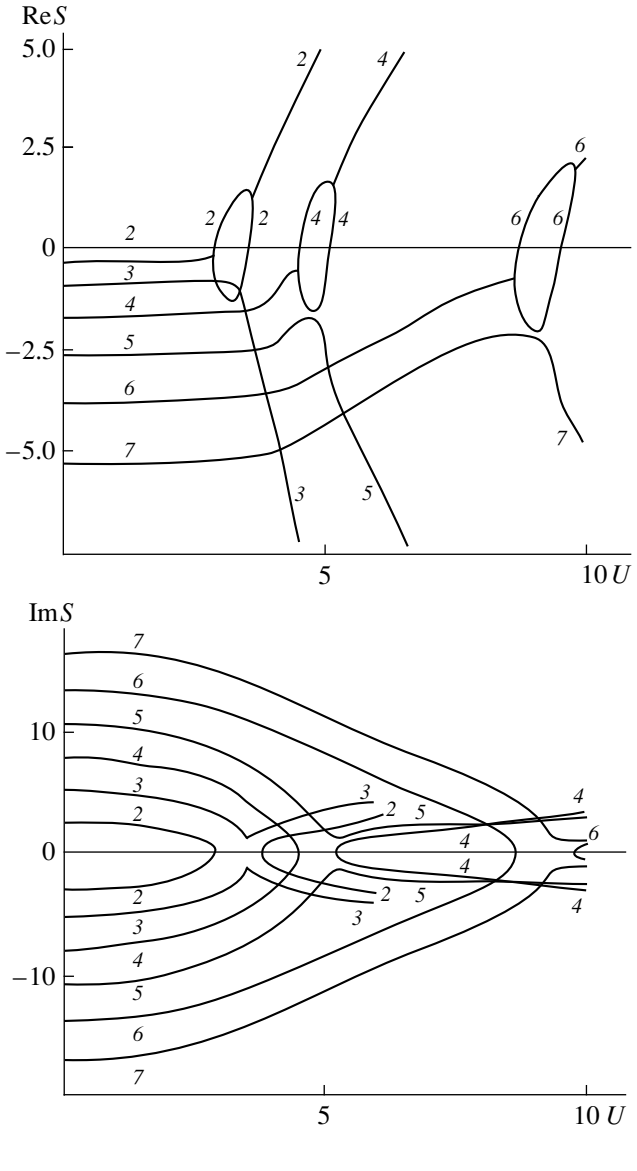

Fig. 2. The same as in Fig. 1, but for ρ = 0.1. The curves for polar motions are not shown.

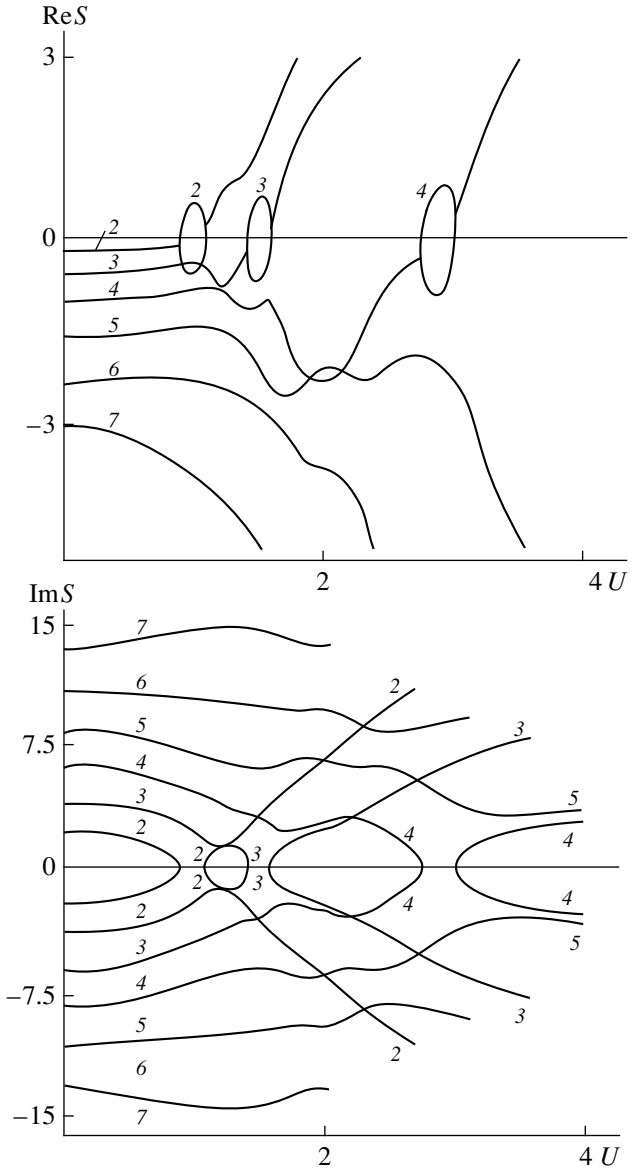

Fig. 3. The same as in Fig. 1, but for ρ = 1.

another, the rising rate for aperiodic instability of the third mode is larger than that of the second mode. The same is true for the fourth and fifth modes. This fact can be explained on the basis of Eqs. (16) with neglect of the coupling of modes. Indeed, the derivative of S_n^2 with respect to ρU^2 determines the rate of S_n increase with varying U and is proportional to $nM_n \sim n^3$. It means that, even in the absence of the coupling of modes, the rising rate for the instability of high modes against increasing ambient velocity increases with the order of modes. An analysis of the classical Kelvin–Helmholtz instability at the plane free surface of a liquid also revealed the increase in the wave number of the most unstable mode with the velocity of the displacement flow [9, 16].

The above-mentioned difference between rising rates for the second and third modes must be phenomenologically manifested in the pattern of the decomposition of the unstable drop. If the second fundamental mode has the maximum instability rising rate at given drop and medium densities and ambient velocity (velocity of the drop falling in the rest medium), the unstable drop takes a shape close to the spheroid defined by the second Legendre polynomial $P_2(\cos\Theta)$ and then decomposes as described in [8, 17]. If the third mode has the maximum instability rising rate, the unstable drop takes the parachute-like shape defined by the third Legendre polynomial $P_3(\cos\Theta)$ and decomposes into a wealth of small, and several large, fragments [7]. The vibrational instability of a free falling drop was also observed in experiments [7].

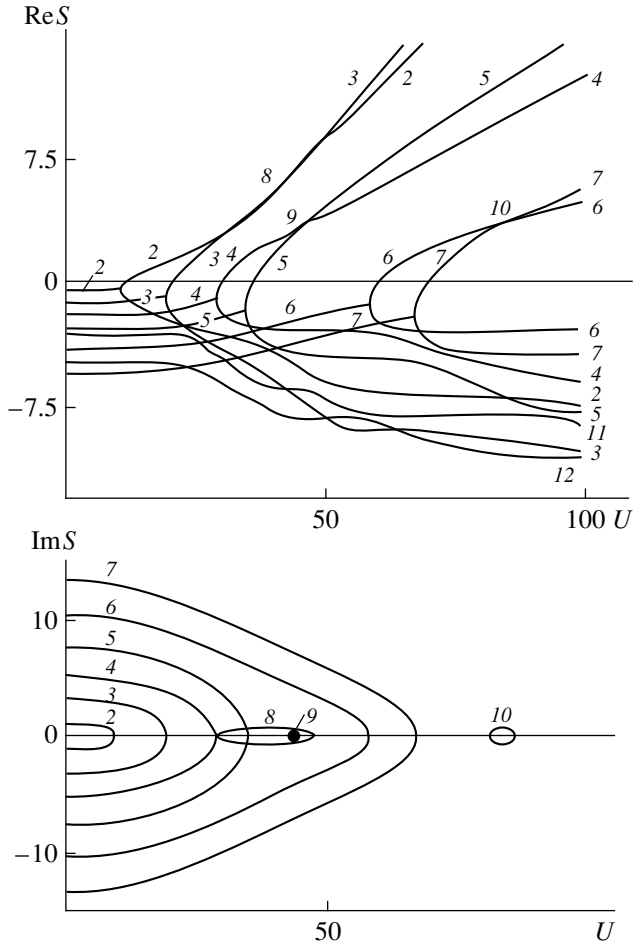

Fig. 4. The same as in Fig. 1, but for the drop charge $W = 3.5$ subcritical in the Rayleigh sense. Curves *2–7* display respective modes. Curve *10* results from the coupling between modes 6 and 7. Curves *11* and *12* correspond to the rotational polar motions of the liquid.

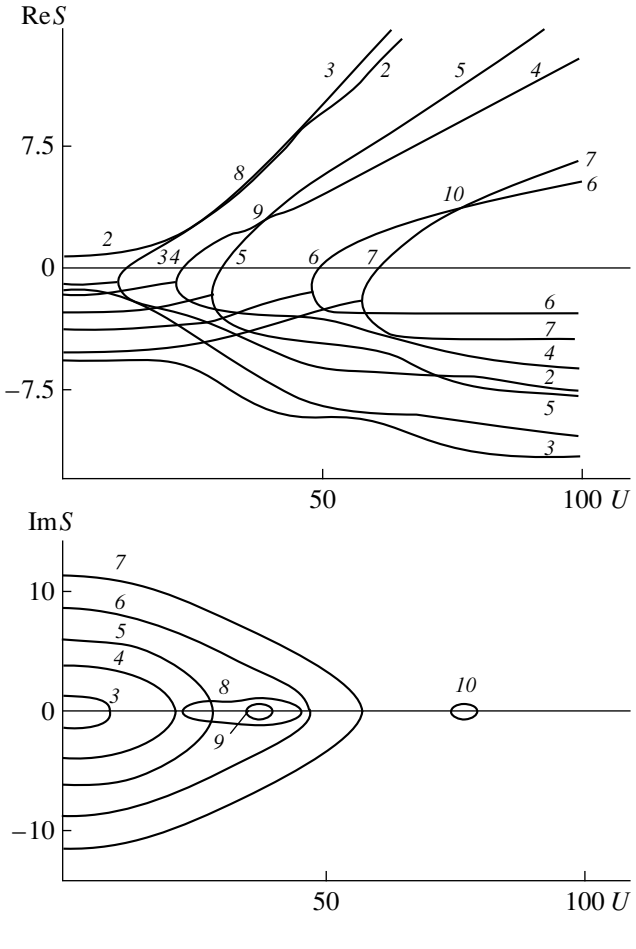

Fig. 5. The same as in Fig. 4, but for the drop charge $W = 4.5$ supercritical in the Rayleigh sense. The curves for polar motions are not shown.

Numerical calculations reveal that, as the medium density increases, the critical value of dimensionless velocity U ensuring the instability of the nth mode decreases and the variety of liquid motions slightly changes. The vibrational instability resulting from the coupling of the second and third modes takes place over the entire region $U > 12$. The domain of the Kelvin–Helmholtz type instability is extended, and the frequencies corresponding to given solutions increase. In all other respects, the curves $S = S(U)$ are qualitatively similar to the curves in Fig. 1.

Figures 2 and 3 show the functions $S = S(U)$ calculated for $\rho = 0.1$ and 1, respectively, and demonstrate that only the even modes are unstable. The damping decrements of the odd modes of capillary motions in the domain where these modes should be unstable rapidly increase with the ambient velocity.

The critical velocities at which various modes of the drop capillary oscillations become unstable against the tangential discontinuity of the velocity field at drop surface, as well as the spectrum of unstable oscillations, depend on the ratio of densities of the media. It is seen from Figs. 2 and 3 that only the even modes are unstable at $\rho = 10^{-1}$, whereas both the even and the odd modes are unstable at $\rho = 1$ and at smaller values of the velocities. As the velocity of the medium increases, the amplitudes of all unstable modes first increase aperiodically and then, at larger velocities, the instability becomes vibrational. The many-valued functions in Figs. 2 and 3 correspond to the aperiodically unstable branches.

If the drop carries a charge subcritical in terms of the Rayleigh stability (see Fig. 4), the basic features of the function $S = S(U)$ coincide with those described above. The charge presence only decreases the critical velocity values at which the drop becomes unstable, which is in agreement with the analytical result (24).

Figure 5 presents the pattern for the case when the drop charge is slightly supercritical ($W = 4.5$) in terms of the Rayleigh instability (the drop becomes unstable

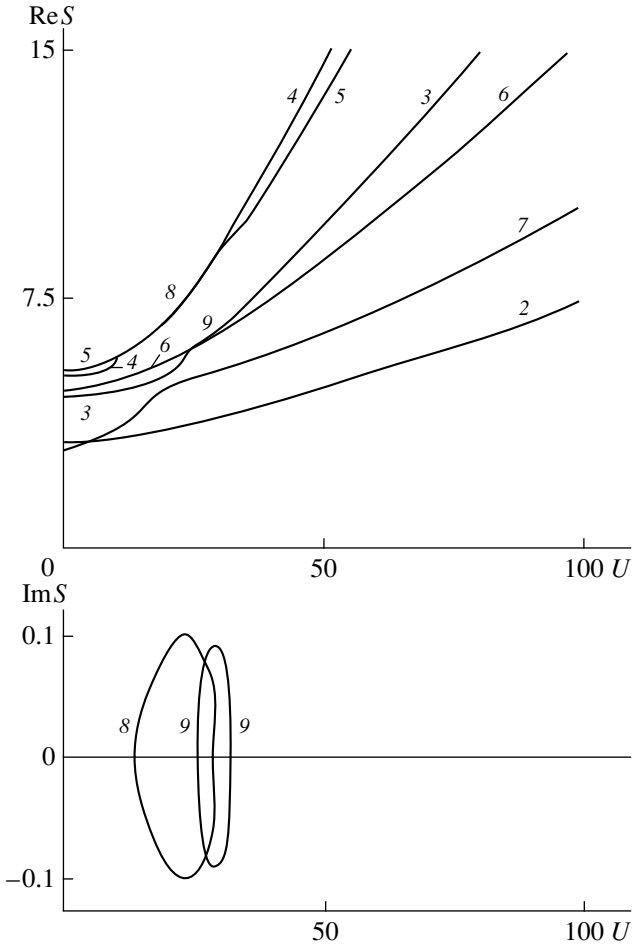

Fig. 6. The same as in Fig. 4, but for the drop charge $W = 10$ highly supercritical in the Rayleigh sense. The curves for polar motions are not shown.

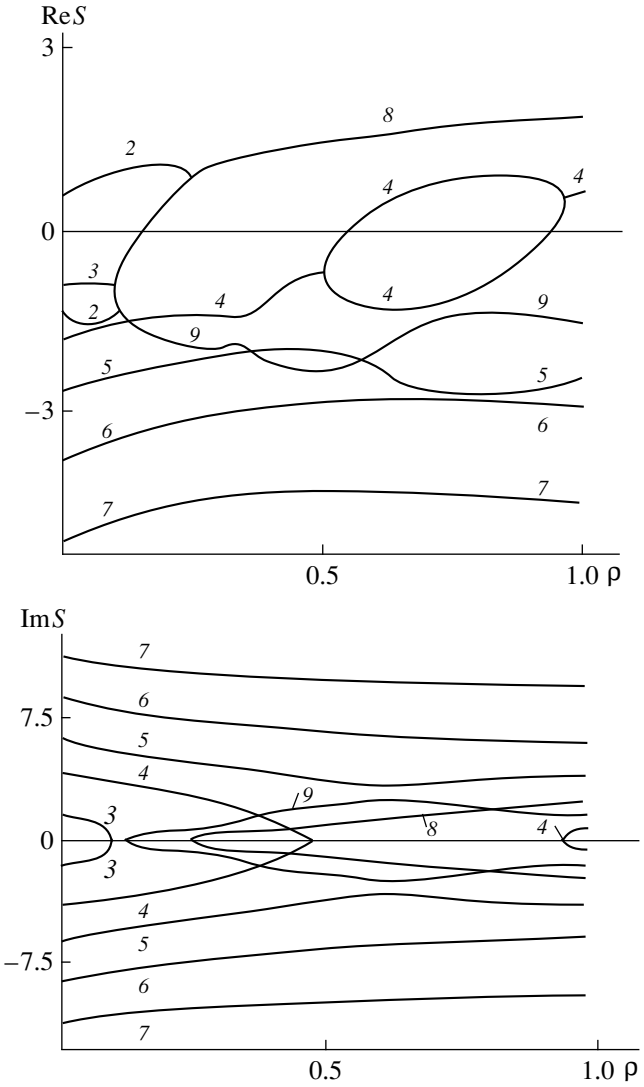

Fig. 7. Real Re$S(\rho)$ and imaginary Im$S(\rho)$ parts of the frequency S of the drop capillary oscillations as functions of the ratio of densities of the medium and the drop for $\nu = 0.1$, $U = 1$, and $W = 4.5$. Curves *2–7* display respective modes. Branches *8* and *9* are formed due to the coupling of modes.

at $W = 4$ [3]). The function $S = S(U)$ in this figure is similar to that given in Fig. 4, but, as compared to Fig. 4, the critical velocity value at which the drop is unstable in the Kelvin–Helmholtz sense is lower and the second mode is initially unstable.

The function $S = S(U)$ for highly supercritical charge $W = 10$ is plotted in Fig. 6. In contrast to the cases considered above, the rising rate for the fundamental mode takes the minimum value as compared to the values of instability rising rates for higher modes whose instability is vibrational or aperiodic (depending on velocity U) and determines the drop decomposition. It is of interest that nonsequential, i.e., third and sixth, modes couple with one another, which results in the formation of the branch of the vibrational instability.

Numerical calculations reveal that both decrements and frequencies of liquid capillary motions decrease only slightly with increasing ρ. Figure 7 shows the real and imaginary parts of the frequency as functions of the ratio of the densities of the medium and the drop for the supercritical drop charge value $W = 4.5$. Curves *8* and *9* represent the motions resulting from the coupling of modes. Curves *8* and *9* correspond to the vibrationally unstable and oscillatory damped motions, respectively.

CONCLUSIONS

A charged drop in a flow around it can decompose into highly charged drops when the drop charge is less than that in the rest of the surrounding medium. This behavior is due to the composition of two instability types: the instability of the drop free surface against the tangential discontinuity of the velocity field and the instability against the drop charge. Depending on the ratio of the densities of the drop and the medium, the drop charge, and ambient velocity, the drop can decompose due to both aperiodic and vibrational instabilities.

Owing to the aperiodic instability at low ambient velocities, the drop is deformed to a stretched spheroid and, because of the electrostatic repulsion, decomposes either via the Rayleigh mechanism [8] or into several fragments of comparable dimensions [17]. The aperiodic instability at high ambient velocities leads to the instability of odd modes; as a result, the drop is deformed to a parachute-like shape and, due to the aerodynamic forces, decomposes into a wealth of small, and several large, drops. The results of the study are in qualitative agreement with experimental data [7].

REFERENCES

1. *Monodisperse Substances: Principles and Application*, Ed. by V. A. Grigor'ev (Énergoatomizdat, Moscow, 1991).
2. S. I. Shevchenko, A. I. Grigor'ev, and S. O. Shiryaeva, Nauchn. Priborostr. **1** (4), 3 (1991).
3. A. I. Grigor'ev and S. O. Shiryaeva, Izv. Akad. Nauk, Mekh. Zhidk. Gaza, No. 3, 3 (1994).
4. V. M. Muchnik and Yu. S. Rud'ko, Tr. Ukr. Nauchno-Issled. Gidrometeorol. Inst., No. 103, 96 (1971).
5. V. A. Dyachuk and V. M. Muchnik, Dokl. Akad. Nauk SSSR **248**, 60 (1979).
6. A. I. Grigor'ev and S. O. Shiryaeva, Phys. Scr. **54**, 660 (1996).
7. A. L. Gonor and V. Ya. Rivkind, Itogi Nauki Tekh., Ser.: Mekh. Zhidk. Gaza **17**, 98 (1982).
8. A. I. Grigor'ev and S. O. Shiryaeva, Zh. Tekh. Fiz. **61** (3), 19 (1991) [Sov. Phys. Tech. Phys. **36**, 258 (1991)].
9. L. D. Landau and E. M. Lifshitz, *Fluid Mechanics* (Nauka, Moscow, 1986; Pergamon, Oxford, 1987).
10. A. I. Grigor'ev, V. A. Koromyslov, and S. O. Shiryaeva, Zh. Tekh. Fiz. **69** (5), 7 (1999) [Tech. Phys. **44**, 486 (1999)].
11. S. O. Shiryaeva, A. É. Lazaryants, *et al.*, Preprint No. 27, IMRAN (Institute of Microelectronics, Russian Academy of Sciences, Yaroslavl, 1994).
12. A. I. Grigor'ev and A. É. Lazaryants, Zh. Vychisl. Mat. Mat. Fiz. **32**, 929 (1992).
13. S. O. Shiryaeva, M. I. Munichev, and A. I. Grigor'ev, Zh. Tekh. Fiz. **66** (7), 1 (1996) [Tech. Phys. **41**, 635 (1996)].
14. A. I. Grigor'ev and S. O. Shiryaeva, Izv. Akad. Nauk, Mekh. Zhidk. Gaza, No. 5, 107 (1997).
15. A. I. Grigor'ev, S. O. Shiryaeva, and V. A. Koromyslov, Zh. Tekh. Fiz. **68** (9), 1 (1998) [Tech. Phys. **43**, 1011 (1998)].
16. V. A. Grigor'ev and S. O. Shiryaeva, Zh. Tekh. Fiz. **66** (2), 23 (1996) [Tech. Phys. **41**, 124 (1996)].
17. V. A. Koromyslov, A. I. Grigor'ev, and S. O. Shiryaeva, Zh. Tekh. Fiz. **68** (8), 31 (1998) [Tech. Phys. **43**, 904 (1998)].

Translated by V. Gursky

Technical Physics, Vol. 45, No. 7, 2000, pp. 849–853. Translated from Zhurnal Tekhnicheskoĭ Fiziki, Vol. 70, No. 7, 2000, pp. 35–39.

SOLIDS

Phase-Transition Radiation and the Growth of a New Phase

S. A. Sall' and A. P. Smirnov

Vavilov State Optical Institute, All-Russia Research Center, ul. Babushkina 36/1, St. Petersburg, 199034 Russia

Received July 16, 1999

Abstract—It was shown that, under certain conditions, the growth of a new phase becomes much like a cooperative optical phenomenon during which the heat of phase transition evolves as a sequence of superradiance pulses (phase-transition radiation). The optical control of new-phase growth and the effect of optical properties of substances on the kinetics of phase transitions are considered. © *2000 MAIK "Nauka/Interperiodica".*

INTRODUCTION

The phenomenon of strong near-infrared above-thermal radiation of boiling-up water has been described in [1]. The radiation intensity from the water–glass interface at a wavelength $\lambda = 1.7$–1.8 μm is approximately two orders of magnitude greater than that of absolutely black body at 100°C. This effect was related to the evolution of condensation heat as a nonequilibrium radiation, which was called phase-transition radiation. A similar phenomenon also takes place upon the boiling up of metals [2]. In metallurgy, the condensation and solidification of metal vapors are known to be attended with a burst of radiation at frequencies that are considerably higher than that of the heat radiation peak at the phase transition temperature. The bursts were also observed at the crystallization of alkali halides and sapphire from the melt [3, 4]. The spectra of the above-thermal radiation were relatively wide (of the order of 10^{13} s^{-1}) and free of emission lines and bands. The photon energy in the peak of the spectra corresponded to the melting heat of the substance per molecule. It was found that the intensity of the above-thermal radiation depends on melt cooling conditions, and the leading and trailing edges of the burst do not necessarily coincide with the beginning and completion of crystallization. The radiant energy of the burst includes a significant part of the total radiant energy of a crystallizing melt. Note that the spectrum of the phase-transition radiation of boiling-up water [1] contains the fundamental absorption bands and the radiation peak is shifted to the short-wave spectral range.

Although experimental evidence on phase-transition radiation is still poor, the mere fact of its occurrence is surprising. This phenomenon does not follow from the available phase-transition conceptions and is not considered in analysis of the transition kinetics.

THE FORMATION OF PHASE-TRANSITION RADIATION PULSES

Three stages of new-phase growth (fluctuation nucleation, extension of nuclei, and coalescence) are usually recognized. Here, the second stage is the concern. Let us assume that, in a single-component supercooled melt, nuclei grow to the point where the transition heat and temperature take macroscopic values. For metals, this is attained at $r_0 > 20$ nm [5], where r_0 is the nucleus radius. As chemical bonds form, each molecule or atom relaxes from the melt-related state to the crystal-related one. The former condition can be treated as excited in relation to the latter.

We estimate the probability of excitation energy being converted to light emission at phase transition. For a free molecule in the excited state, its optical lifetime (the longitudinal relaxation time) is equal to $T_1 = 10^{-7}$–10^{-8} s. For transitions in the near-infrared range at $T \sim 10^3$ K, the nonradiative multiphonon relaxation time in solids is $T_1^* \lesssim 10^{-9}$ s [6]. Then, the probability of light emission $p \sim T_1^*/T_1 \ll 1$. Therefore, most of the transition energy is converted to heat. It is assumed here that bonding does not change the position of a particle passing from the melt into the crystal. Hence, in accordance with the Franck–Condon principle, the optical transition to the crystal ground state is allowed and the probabilities of optical transitions to the excited states of the crystal are small. Actually, the particle position may vary and the transition to the crystal ground state

1063-7842/00/4507-0849$20.00

may go through a number of intermediate states, for which multiphonon relaxation is more essential [6]. Then, the probability of light emission will be still lower. Phase transitions with $p \ll 1$ will be called nonradiative.

For a radiative phase transition with $p \sim 1$, the time T_1 of the optical transition between the melt and crystal ground states has to be less than or comparable to the nonradiative relaxation time T_1^*. This is obtainable in a great ensemble of particles. The feasibility of radiative phase transition in an ensemble of particles was originally treated in terms of quantum electrodynamics even before the phenomenon of collective spontaneous radiation (or superradiation) had been experimentally discovered [7, 8]. As is known, the phenomenon of superradiation is that a system of excited particles undergoes the optical transition to the lower state due to their interaction with each other through the common radiation field, the transition time being much shorter than the radiative decay time of an individual particle [9]. Next, the feasibility of radiative phase transition will be considered in terms of the theory of superradiation, where the semiclassical approach is often employed [10].

Let us have an ensemble of K ($K \gg 1$) particles that surround nuclei in a melt area of size $l \ll \lambda$, where λ is the wavelength of radiation corresponding to the specific (per particle) transition heat. Also, let parameters T_2 and T_2^* stand for the dephasing times of the wave functions of excited particles due to uniform and nonuniform line broadening (the parameter T_2 is also referred to as the transverse relaxation time). For cubic crystals with homogeneous line broadening, $T_2 = 10^{-10}$–10^{-9} s; for noncubic and impure crystals with inhomogeneous broadening, $T_2^* = 10^{-11}$–10^{-10} s [6]. Thus, the condition $T_2^* \ll T_2 < T_1^* < T_1$ is met. We assume that the optical transitions of particles from the ground state of the melt to that of the crystal are allowed. For superradiation to take place, its pulse duration τ should be much less than the dephasing times T_2 or T_2^* and the photon transit time through the melt area of size l should be much less than τ; that is, $l/c \ll \tau$, where c is the velocity of light (we assume that the refractive index of the medium $n \sim 1$). The initial level Q_0 of noncoherent spontaneous radiation at a transition frequency ω_0 depends on the new-phase growth rate K/T_1^*:

$$Q_0 \sim p\hbar\omega_0 K/T_1^* = \hbar\omega_0 K/T_1, \qquad (1)$$

where $\hbar$ is Planck's constant (thermal radiation from the melt is neglected). The time T_1 is conventionally related to the dipole matrix element d of the transition as $T_1 = 3\hbar c^3/4|d|^2\omega_0^3$.

With no regard for transverse relaxation and in the adiabatic approximation, the dynamics of radiation Q and the inversion ΔK of the system ($\Delta K = K - K_c$, where K_c is the number of particles passed to the ground state of the crystal) are written as in [10]:

$$\frac{dQ}{dt} = -\frac{4\pi^2 Q\omega_c^2 V}{3\omega_0\lambda^3}, \quad \frac{d\Delta K}{dt} = -\frac{2Q}{\hbar\omega_0}, \qquad (2)$$

where V is the domain volume, t is time, and $\omega_c^2 = -8\pi|d|^2\Delta K\omega_0/\hbar V$ is the square of the so-called cooperative frequency of the medium.

The solution of system (2) has the form

$$\Delta K = -K\tanh[(t - t_d)/2\tau],$$
$$Q = \hbar\omega_0 K/4\tau\cosh^2[(t - t_d)(2\tau)^{-1}]. \qquad (3)$$

The superradiation pulse duration $\tau = T_1/K$ is K times shorter than that of the spontaneous radiation from an individual particle. The maximum power $Q_{\max} = \hbar\omega_0 K/4\tau$, varying in proportion to K^2, is approximately K times higher than the initial spontaneous radiation level Q_0 and is achieved within the delay time $t_d = \tau\ln[Q_{\max}/Q_0]$ or, in view of Eq. (1),

$$t_d = \frac{T_1}{K}\ln\frac{K}{4}. \qquad (4)$$

In our case, the superradiation mode is realized only if $t_d < T_2, T_2^*$. Assuming that $T_1 = 10^{-7}$ s, $T_1^* = 10^{-9}$ s, and $T_2 = 10^{-10}$ s and taking into account (4), we arrive at the requirement for the threshold number of particles $K_t \gtrsim 10^5$ for uniform-broadening media (cubic crystals). This requirement is readily met even for one nucleus. The lumped model of superradiation ($l \ll \lambda$) in media with nonuniform broadening seems to be unlikely [9]. In this case, phase-transition superradiation may occur in a melt transparent at the frequency ω_0, when the radiation propagates from one nucleus to another practically without loss and superradiation pulses are simultaneously generated from the whole melt area of size $l \gtrsim \lambda$. The radiation dynamics in this system is similar, most of the energy being radiated along the greatest extension of the area. In the melts of cubic metals having a high conductivity, the penetration depth of radiation with the frequency ω_0 is about 10^2 nm [11]. Hence, if the internuclear distance is much greater than this value, each nucleus is able to indepen-

dently generate superradiation pulses with a duration of $\tau \lesssim 10^{-12}$ s.

NEW-PHASE COLLECTIVE GROWTH IN THE SUPERRADIATION MODE

The nonradiative growth rate ν of a nucleus, which is defined as the number of new-phase particles formed in a unit time, equals K/T_1^*. Therefore, there is a threshold value for this rate, $\nu_t = K_t/T_1^*$, that marks the beginning of the superradiative process. If $\nu < \nu_t$, the new phase grows nonradiatively; if ν exceeds ν_t, after a delay time t_d, a superradiation pulse is generated and a nucleus grows up jumpwise. In this case, most of the transition heat is removed from the nucleus into the ambient melt by radiation and the heating of the interface limits the growth rate to a lesser degree. Then, other superradiation pulses may form. In the case of high-melting crystals, the thermal radiation from the melt is essential for the initiation of a superradiation pulse. The orientation ordering of the dipole moments of molecules due to the reradiation field at the second-harmonic frequency may also contribute to the new-phase growth rate [9].

The classical theory of new-phase growth suggests that the maximum growth rate is observed when, at some temperature, an optimum relation between the supercooling of the melt and its viscosity is set. Actually, for the majority of substances, the crystal growth rate turns out to be well above the theoretical value and, in addition, does not vary over a wide temperature range [12]. This inconsistency is still left unexplained. Within the framework of our model, it finds a natural explanation. Indeed, if the phase transition is radiative, the growth rate considerably increases and the temperature, supercooling, and viscosity at the interface are governed not by external conditions but by transport of radiation inside the crystal.

Consider bulk crystallization in a supercooled metal melt. Let the bulk of the melt have nuclei of radius $r_0 >$ 20 nm. If the nonradiative growth rate of a nucleus or a number of nuclei in an area of size $l \ll \lambda$ reaches ν_t, then a delay time t_d later, a superradiation pulse forms. We assume roughly that, if this pulse, acting on other nuclei, reaches the level of Q_0, they also start to superradiate. At $T_1 = 10^{-7}$ s, $T_1^* = 10^{-9}$ s, and $K = 10^5$, the value of $Q_{\max}$ will exceed Q_0 approximately by a factor of 10^5. During a superradiation pulse, a nucleus with $r_0 = 20$ nm increases its radius by less than 1 nm. If nonlinear adsorption is neglected, the radiation flux density falls with distance r as $(r_0/r)^2\exp(-kr)$, where k is the absorption factor of the melt at the frequency ω_0. Putting $r_0 = 20$ nm and $k = 0.01$ nm^{-1}, we will find that the initial (driving) pulse has an effect up to the distance $a \approx 500$ nm. Then, the maximum interface velocity in such a melt will be $a/t_d \approx 5 \times 10^6$ cm/s. The evolution of crystallization heat results in the partial melting of nuclei, and levels for new superradiation pulses arise. Heat transfer in the melt becomes due to radiant heat conduction. This equalizes the temperature in the melt, and the heat is quickly removed toward the crystallizer walls. At the stage of coalescence, when growing grains come closer together, polaritonic solitons and the effect of self-induced transparency [10] may add to the rate of heat removal from the melt.

Because of the temperature spread ΔT of an actual phase transition [13], the integrated-over-time spectrum of phase-transition radiation broadens by a value of $\Delta\omega_i \sim \Delta H_f \Delta T/\hbar T N_A$ (ΔH_f is the transition heat per mole of a substance, T is the average temperature of transition, and N_A is Avogadro's number), which may be far in excess of the linewidth $\Delta\omega \approx \tau^{-1}$ of an individual superradiation pulse (in [4], $\Delta\omega_i \approx 10^{13}$ s^{-1}). Moreover, when passing through the medium, phase-transition radiation may broaden further due to nonlinear optical effects [14].

As shown in [15], optical radiation is stimulatory to the formation of large-scale density fluctuations (dilatons and compressons) and new-phase nuclei. Because of this, phase-transition radiation, acting on an area free of nuclei, makes for nucleation and fast growth of the new phase over the medium. This point calls for special investigation and is beyond the scope of this article.

In melts transparent at the frequency ω_0, the superradiation pulses will appear from large regions if the temperature distribution over them is rather uniform ($\Delta T \lesssim N_A \hbar T/\tau \Delta H_f$). When the parameter l/c becomes comparable to τ, superradiation may appear as a train of pulses with decreasing height (the oscillatory mode). At $l/c > T_2$, superradiation may change to superluminescence (when $Q_{\max} \sim K$) and the radiation becomes induced [10]. The duration of such pulses is of the order of l/c, and light emission, in this case, carries away no more than half the energy stored by excited levels (induced amplification occurs at $\Delta K > 0$).

The oscillation threshold is defined by the condition $\beta/\alpha = 3\lambda^2 K T_2 l/4\pi V T_1 > 1$, and the transition to the superluminescence mode is observed when $3\lambda^2 K \tau l/8\pi V T_1 > 10$ [16]. Cooling a melt transparent to the radiation at the frequency ω_0 generates a train of superradiation pulses, which cause nuclei to grow jumpwise with each pulse.

OPTICAL CONTROL OF NEW-PHASE GROWTH

If the melt is inside an optical resonator, the emerging radiation increases and crystallization proceeds faster. For instance, if a superradiating medium with $\alpha = 10^{-3}$ and $\beta = 10^{-1}$ is placed into a resonator with plane-parallel semitransparent mirrors with a reflectivity $\rho = 0.8$, the radiation peak increases and the delay time is reduced by almost one order of magnitude [16].

In this case, the pulse width decreases by a factor of $1/\ln\rho^{-1} \approx 4.5$. For media with nonuniform broadening, the influence of the resonator on the radiation parameters is qualitatively similar; that is, the resonator can be used to provide the superradiation condition $t_d < T_2, T_1^*$. On the contrary, the use of the resonator at superluminescence will result in a decrease in the radiation peak intensity [16] and rate of crystallization. Notice that generators of phase-transition radiation are radically distinguished from those of coherent radiation, which are known in quantum electronics; namely, in the former case, pumping can be performed by low-grade heat (ordinary heating) rather than by electric current, high-power gaseous-discharge lamp, etc. This may also be essential in designing low-grade heat utilizers.

The use of laser pulses or continuous infrared radiation from a high-power source (laser, arc lamp, globar, etc.) to promote superradiation is another way of controlling the crystallization rate. Optical control of the crystallization rate seems to be rather intriguing in producing materials not only with desired properties but also with desired grain size distribution (for instance, in devices of gradient optics). In this case, it should be taken into consideration that coarse grains will enhance radiation scattering in the melt and the oscillatory mode may eventually break down.

Optical control would be also appropriate for use in the case of vapor–liquid transitions taking place in gas liquefiers and solid–solid transitions in the technology of producing different crystal modifications.

A considerable rise in the phase-transition rate due to the radiative processes should cut the lifetime of metastable states such as supercooled vapor and liquid. It is evident that a high crystallization rate associated with the radiative phase transition inhibits the occurrence of the vitreous state under rapid cooling of the melt. One can substantially reduce the radiative growth rate or even break down the superradiation mode by adding impurities that absorb the radiation at the frequency ω_0 or cause significant nonuniform broadening of a radiation line into the melt. This effect should be allowed for in technologies of glasses and Pyroceram-like materials.

The complex crystal structure, polymorphism, a great discrepancy between maxima in the temperature dependences of the nucleation rate and crystal growth rate, high viscosity of the melt, rapid cooling, and the absence of foreign inclusions are all thought to cause the formation of amorphous solids. It follows from our consideration that the parameters k and T_2 or T_2^*, as well as the system geometry, which specifies the parameters K, α, and β, play a key role in the formation of amorphous substances. In many cases, they become deciding. The amorphous phase is most difficult to form in substances with low k and high T_2, that is, in salts with the cubic crystal lattice (NaCl, KCl, KJ, etc.), which are transparent to the radiation at the frequency of transition. In substances with large values of k and T_2 (that is, in metals with the cubic crystal lattice) or with low values of k and T_2^* (that is, in noncubic crystals, such as Si, Ge, Al_2O_3, etc., which are transparent at the frequency of transition), the amorphous phase is more plausible. Finally, the amorphous phase readily forms in substances with large k and low T_2^*, that is, in dielectrics with the noncubic crystal lattice (SiO_2, B_2O_3, GeO_2, etc.), which are opaque at the transition frequency. While amorphous substances of the first group are unknown, the substances of the second and third groups have been obtained amorphous only under superfast cooling of the melt or in the form of films, small particles, and gels; the substances of the fourth group form glasses when the melt solidifies. The substances of the fourth group crystallize from the melt, solution, or vapor exclusively nonradiatively, that is, particle by particle and comparatively slowly. Small particles and thin films (water drops, metal and semimetal films, carbon black particles, Al_2O_3, etc.) are fairly prone to vitrification or supercooling, because the requirement for K_t is not met here.

Phase transitions occurring with energy absorption (evaporation, melting, and polymorphous transformations) may likewise bear some resemblance to a cooperative optical phenomenon, However, in this case, it is associated with energy collective absorption, or superabsorption. It is this phenomenon that can apparently explain experiments where substances melted when exposed to $\lesssim$1-ps (subpicosecond) laser pulses.

Our method of analyzing new phase growth can be extended to the more general case of multicomponent systems, as well as to a number of related (in our opinion) phenomena: chemical reactions (including self-propagating high-temperature synthesis), explosive crystallization, polymorphous transformations, sonoluminescence, explosive emission, etc.

REFERENCES

1. W. R. Potter and J. G. Hoffman, Infrared Phys. **18**, 265 (1968).
2. V. A. Burtsev, N. V. Kalinin, and A. V. Luchinskiĭ, *Electrical Explosion of Conductors and Its Application in Electrophysical Equipment* (Énergoatomizdat, Moscow, 1990).
3. V. A. Tatarchenko, Kristallografiya **24**, 408 (1979) [Sov. Phys.–Crystallogr. **24**, 238 (1979)].
4. V. A. Tatarchenko and L. M. Umarov, Kristallografiya **25**, 1311 (1980) [Sov. Phys.–Crystallogr. **25**, 748 (1980)].
5. Yu. I. Petrov, *The Physics of Ultimate Particles* (Nauka, Moscow, 1982).
6. N. V. Karlov, *Lectures on Quantum Electronics* (Nauka, Moscow, 1988).
7. M. E. Perel'man, Dokl. Akad. Nauk SSSR **203**, 1030 (1972).

8. N. Scribanowitz, I. P. Hermann, I. C. MacGillivray, and M. S. Feld, Phys. Rev. Lett. **30**, 309 (1973).
9. A. V. Andreev, V. I. Emel'yanov, and Yu. A. Il'inskiĭ, *Cooperative Phenomena in Optics* (Nauka, Moscow, 1988).
10. V. V. Zheleznyakov, V. V. Kocharovskiĭ, and Vl. V. Kocharovskiĭ, Usp. Fiz. Nauk **159** (2), 194 (1989) [Sov. Phys.–Usp. **32**, 835 (1989)].
11. N. I. Koroteev and I. L. Shumaĭ, *The Physics of High-Power Lasing* (Nauka, Moscow, 1991).
12. M. Vollmer, *Kinetik der Phasenbildung* (Steinkopff, Dresden, 1939; Nauka, Moscow, 1986).
13. A. P. Smirnov, in *A Set of Singular Temperature Points in Solids* (Nauka, Moscow, 1986), pp. 210–239.
14. S. A. Akhmanov, V. A. Vysloukh, and A. S. Chirkin, *The Optics of Femtosecond Laser Pulses* (Nauka, Moscow, 1988).
15. G. I. Grozovskiĭ, N. V. Krasnogorskaya, and A. P. Smirnov, in *Current Problems in Biosphere Research and Protection* (Gidrometeoizdat, St. Petersburg, 1992), Vol. 2, pp. 427–430.
16. A. V. Andreev, Usp. Fiz. Nauk **160** (12), 1 (1991) [Sov. Phys.–Usp. **33**, 997 (1990)].

Translated by B.A. Malyukov

Technical Physics, Vol. 45, No. 7, 2000, pp. 854–857. Translated from Zhurnal Tekhnicheskoĭ Fiziki, Vol. 70, No. 7, 2000, pp. 40–43.

SOLIDS

On the Turbulization of the Viscocrystalline Phase

S. O. Gladkov

Semenov Institute of Chemical Physics, Russian Academy of Sciences, ul. Kosygina 4, Moscow, 117977 Russia

Received October 13, 1997; in final form, December 24, 1999

Abstract—The dependence of the mean size of dispersed phase particles on the physical parameters of a system (temperature, density, and sound velocity in a substance) was found. The generalized Fokker–Planck equation was used to calculate the particle size distribution. The obtained binary distribution function was proved to adequately describe a large array of experimental data in actual physical conditions. It was shown rigorously that the fine-grain phase (powder) results when the viscocrystalline phase is subjected to shear loads. The shape of the distribution turned out to be independent of external actions, i.e., remained the same both on sedimentation and at pressure drop. © *2000 MAIK "Nauka/Interperiodica".*

Interest in the properties of fine-grain powders stems largely from the fact that many industrial techniques are intimately related to powder metallurgy. It is particularly remarkable that theoretical findings are quickly employed in practice in this field. The problem discussed below also has a direct bearing on powder technology, since its solution physically justifies a number of processes and makes it possible to produce high-quality fine powder.

Let us have a viscocrystalline phase where the viscous liquid and crystalline phase occupy 85–95 and 5–15 vol.%, respectively. A very thin ($\delta = 10^{-4}$–10^{-6} cm) near-surface layer of this substance is subjected to a shear load F (Fig. 1). Upon being stripped off, this layer is released to a thermostat and is converted into a powder. The first question immediately arises as to what forces are behind the formation of the fine-grain phase. To tackle the question, imagine the following situation (Fig. 2a). Let a Δx-long thin layer of a viscocrystalline structure be dropped into a thermostat. Because of temperature fluctuations δT in the thermostat, each piece of the structure is under its own temperature $T + \delta T(x)$ that differs from others. The characteristic range of x has a very small dimension R on the order of δ. As follows from Fig. 2b, "icicles" that form under the action of the gravity force began to nonuniformly "freeze" from the lower end. The freezing process is in no way related to heat conduction (we are dealing with very short times!) but is due to the phonon transfer of the given local temperature by a distance on the order of R. The transfer time $\tau = R/c_s$, where c_s is the sound velocity in the solid phase (for example, polipropylene or metal). The upper portion (lower end) of an icicle thus cooled for a time τ begins to "pool" the as yet liquid lower portion (upper end). This results in necking, and the neck eventually breaks. As a result, many fine pellets with a characteristic linear size R are produced.

To describe this picture mathematically, we should first elucidate how the shape of the pellet size distribution depends on R. For simplicity and without loss of generality (as will be seen later), we will assume the pellets to be spherical.

Initially, the pellets were absent. This means that the distribution function at $t = 0$ (t is time) equals zero and, hence, no equilibrium (or quasi-equilibrium) distribution function existed. It appeared at times on the order of τ, when thermostatic control due to phonons set in. The situation when phonons do not interact and are free to move from boundary to boundary is known as Knudsen situation [1]. This would have been the case if the pellets had roughly equal sizes. Actually, however, the dispersed phase derived is highly nonuniform and contains pellets of different sizes. Then, along with the Knudsen mechanism, one must also take into consideration phonon interaction. Formally, this means replacing the time τ by τ^*, where $1/\tau^* = \tau_0^{-1} + \tau_1^{-1}$. (Here, τ_0 is used instead of τ.). The time τ_1 can be given by the

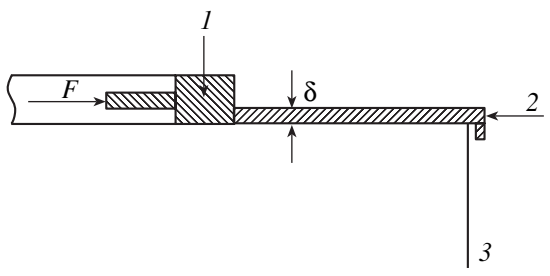

Fig. 1. Fine powdering process: V_{sh}, shear rate; δ, removed layer thickness; (*1*) shear stress; (*2*) viscocrystalline substance; and (*3*) thermostat.

formula

$$1/\tau_1 = \lambda R^3, \quad (1)$$

where λ depends on the ambient temperature T.[1]

This function is readily determined if a specific mechanism of phonon interaction is known (see, for example, [2]). Here, consideration must be given to one important point. In a "normal" crystalline substance, the time τ_1 is proportional to N/V, where N is the number of atoms in the lattice and V is the crystal volume. Therefore, as applied to our case (highly nonequilibrium state), the assumption (as yet purely hypothetical) should be made that the core of a forming pellet has a fixed number of atoms (of the already crystalline structure!). Then, we can introduce into consideration a phonon gas and treat volume as a parameter that fluctuates. This is included in formula (1). It will be shown below that this assumption makes possible the exact determination of the distribution function with allowance for a spread in particle sizes. Running ahead, we notice that the distribution function obtained by solving the generalized Fokker–Planck equation has two peaks.

Thus, for the time τ^*, pellets can grow up only to a certain (limiting) size. This circumstance is reflected in the macroscopic equation

$$dR/dt = \gamma R(\langle R^2\rangle - R^2), \quad (2)$$

where λ is a parameter (that will be discussed later) and $\langle R\rangle$ is the limiting radius of the pellets.

CALCULATION OF THE DISTRIBUTION FUNCTION

For our specific problem, the general form of a kinetic equation that takes into account gravity forces or pressure drops must have the form

$$\partial f/\partial t + (dR/dt)\partial f/\partial R + \mathbf{F}\partial f/\partial \mathbf{p} = L_{\mathbf{p}}\{f\} + f/\tau^*, \quad (3)$$

where $f = f(R, \mathbf{p}, t)$ is a desired distribution function and $\mathbf{F}$ is an external force acting on pellets.

In the case of sedimentation (motion in a gravitational field),

$$\mathbf{F} = m\mathbf{g} - 6\pi\eta R\mathbf{u}, \quad (4)$$

and in the case of a pressure drop,

$$\mathbf{F} = (P_1 - P_2)\pi R^2\mathbf{n}. \quad (5)$$

[1] Notice that ballistic (collisionless) phonon movement from boundary to boundary is actually an n-fold process. Phonons striking one boundary pass to it a part of their energy, reflect, reach another boundary, pass to it a part of the energy again, etc. The process is repeated n times until the phonons are thermalized and acquire the mean kinetic energy. Such phonons in combination are nothing else than a thermostat. As the pellet size R grows, phonon interaction comes into play. Generally, at a certain (critical) size R_{cr}, phonon collisions become competitive with the τ_0 mechanism (the condition $\tau_1 \gg \tau_0$ is violated). In this case, the formula $1/\tau^* = 1/\tau_0 + 1/\tau_1$ is valid.

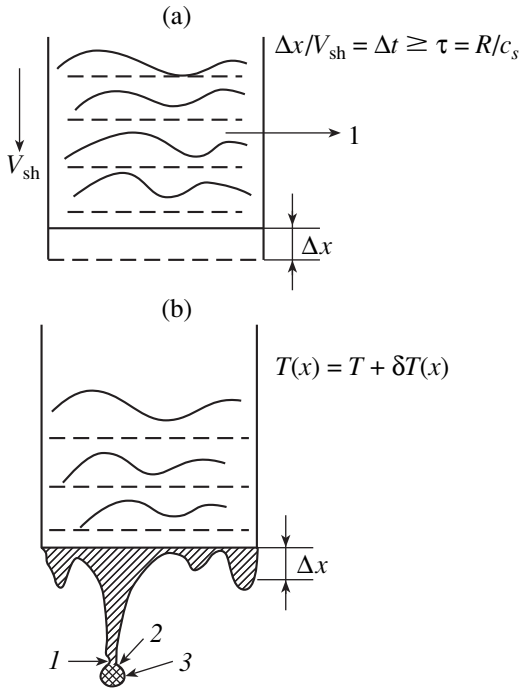

Fig. 2. (a) Origination of fine powder: Δx, small displacement of viscocrystalline phase 1 for a time τ_0 ($\tau_0 = \Delta x/c_s$) and R, radius of formed crystalline structure. (b) Early stage of icicle formation: (*1*) neck; (*2*) grain; and (*3*) finely dispersed phase.

In formulas (3)–(5), $\mathbf{n}$ is the normal to the spherical pellet surface, $\mathbf{p} = m\mathbf{u}$ is the pellet momentum, m is the pellet mass ($m = \rho\nu$, where ρ is the pellet density and $\nu = 4\pi R^3/3$ is the pellet volume), and $\mathbf{u}$ is the pellet velocity.

The operator $L_{\mathbf{p}}\{f\}$ describes the particle velocity distribution (see, e.g., [3, 4]). Its form is typical of the Fokker–Planck equation:

$$L_{\mathbf{p}}\{f\} = \partial(D\partial f/\partial \mathbf{p} + k\mathbf{p}f)/\partial \mathbf{p}, \quad (6)$$

where k and D are coefficients.

The solution of (3) should be sought only for the case $\partial f/\partial t = 0$. In fact, for times less than τ, the classical consideration fails and the problem must be treated as purely quantum. For times comparable to τ, the pellet distribution function has already been established and only the steady-state solution should be found. In connection with this, we put $f = f_1\{\mathbf{u}\}f_2\{R\}$ and, after separation of variables, obtain

$$[(\partial f_2/\partial R)\gamma R(\langle R^2\rangle - R^2) f_2^{-1} - 1/\tau^*] = f_1^{-1}[L_{\mathbf{p}}\{f_1\} - \mathbf{F}\partial f_1/\partial \mathbf{p}]. \quad (7)$$

Equation (7) is solvable if the right- and left-hand sides equal some constant B. The simple mathematics in view of the relationship $1/\tau^* = \tau_0^{-1} + \tau_1^{-1}$ yields the

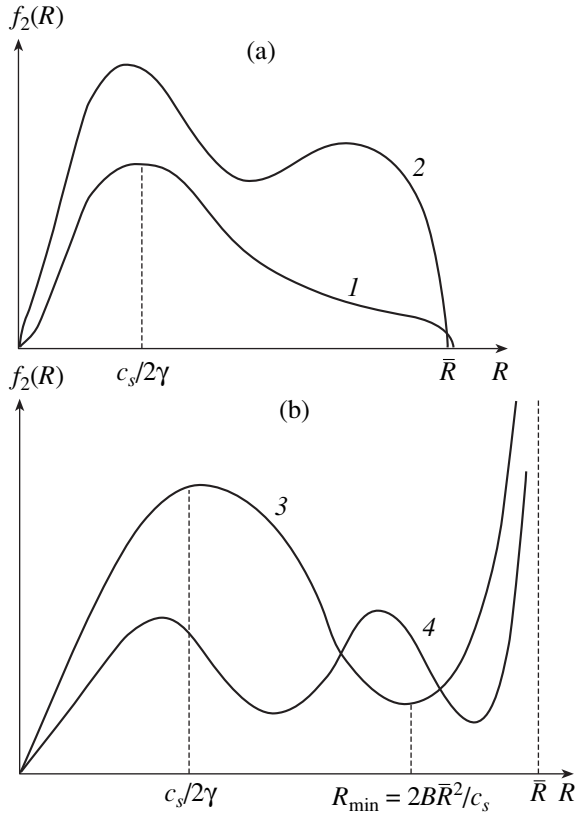

Fig. 3. (a) Particle size distribution function for $B < [c_s + \lambda\langle R\rangle^4]/\langle R\rangle$. (*1*) Peak at $R_{1\,\max} = \langle R\rangle(1 - \varepsilon)$ for $\varepsilon = 0.25 + b/4(1 - a)$, $B < 0$, $a < 0$; (*2*) $B < 0$, $b \ll 1$, $a < 0$, $R_{1\,\max} = 4\langle R\rangle b^{1/2}/3$, $R_{2\,\min} = \langle R\rangle(1 - \varepsilon)$, and $R_{3\,\min} = 3\langle R\rangle/4$. (b) Distribution function for $B > [c_s + \lambda\langle R\rangle^4]/\langle R\rangle$: (*3*) $B > 0$, $a > 0$, $B \ll 1$, $R_{1\,\max} + 4\langle R\rangle b^{1/2}/3$, and $R_{2\,\min} = \langle R\rangle(1 - \varepsilon)$; (*4*) $B > 0$, equation (9) has four real roots. In this case, an analytic solution is impossible to find, and the distribution function vs. radius curve is shown schematically.

desired pellet size distribution function:

$$f_2\{R\} = AR^{-B/\gamma}(\langle R\rangle + R)^{\mu}(\langle R\rangle - R)^{\nu} \times \exp\{-(c_s/\gamma R) - (\lambda R/\beta)\}, \quad (8)$$

where A is a normalizing constant, which is found from the conservation-of-mass condition $\int f_2\{R\}dR = M$ (M is the total mass of one removed layer); $\mu = (c_s + \lambda\langle R\rangle^4)/2\gamma\langle R\rangle + B/2\gamma$; and $\nu = -\mu$.

$f_2\{R\}$ curves for cases of practical value are demonstrated in Fig. 3. Their extrema are found by solving the algebraic equation of the fourth order

$$x^4 + ax^3 + ax^2 - ax + b = 0, \quad (9)$$

where

$$x = R/\langle R\rangle, \quad a = B/\lambda\langle R\rangle^3, \quad b = c_s/\lambda\langle R\rangle^4.$$

Two cases are possible: $B < 0$ ($a < 0$) and $B > 0$ ($a > 0$). In the former case, the distribution function has either one maximum or two maxima and one minimum (Fig. 3a); in the latter, either one maximum and one minimum or two maxima and two minima (Fig. 3b). In both cases, the distribution function reflects the actual physical situation dealt with in the process of powder production.

Now we turn to the constant γ, involved in (1). The formation of a crystalline structure is known [5] to be a highly nonequilibrium process. Under such conditions, crystallization formally depends on two temperatures: thermostat temperature T and crystallization temperature T_{cr}. As the temperatures are close to each other in our given case, the coefficient γ, which characterizes the rate of nucleus growth, depends on their difference. The growth rate can be related only to the viscosity of the system. The latter is known [6, 7] to be described by the expression

$$\eta = \eta_0 \exp(+\Delta/k_B(T - T_{cr})), \quad (10)$$

where Δ is the energy gap and η_0 is the viscosity at $T = \infty$.

The nucleation rate (the rate at which a hydrodynamic viscous flux adheres to the basic crystalline structure) must be inversely proportional to η. The only possible relation in this case has the form

$$\gamma = u_0^2/\nu, \quad (11)$$

where the kinematic viscosity ν and dynamic viscosity η are conventionally related as $\eta = \nu\rho$ (ρ is the density).

The velocity u_0 is defined by the exchange interaction integral J_{ex} and mean interatomic spacing $\langle a\rangle$; i.e.,

$$u_0 = J_{ex}\langle a\rangle/\hbar, \quad (12)$$

where $\hbar$ is Planck's constant.

Eventually, the desired growth rate of a microscopic nucleus is given by

$$\gamma = (J_{ex}\langle a\rangle/\hbar)^2/\nu. \quad (13)$$

This expression adequately covers real situations, since it includes all the basic physical parameters needed for growth description at both the micro- and macroscopic levels.

THE EFFECT OF A HIGH-FREQUENCY ELECTRIC FIELD ON THE FORMATION OF THE DISPERSED STRUCTURE

When the molten material is exposed to an ac electric field whose frequency satisfies the inequality

$$\omega \gg K \quad (14)$$

(K is the rate of a chemical reaction that specifies the exchange interaction), the exchange integral diminishes, affecting the crystallization process [see, e.g., [8, 9]). This is associated with the fact that exchange

coupling sets in because the wave functions of electrons of neighboring atoms overlap. Since the electrons strongly interact with the ac field, the exchange energy becomes frequency-dependent. It is significant that the frequency range where this takes place is rather narrow and only specific frequencies of the field can influence the exchange energy. From the physical standpoint, condition (14) merely indicates that the chemical reaction has no time to be completed during the cycle of the electric field; hence, exchange coupling weakens.

If the field begins to act from the instant that the entire substance represents a viscocrystalline structure, it must act to the end of crystallization. Only then can one expect the realization of the above effect: dispersed pellets become still finer (exchange interaction weakens); and their agglomerate, more homogeneous.

As follows from the above formulas, the structure will be homogeneous if (1) the substances to be dispersed are selected such that the sound velocity is as low as possible, (2) the relaxation time τ_1 is as long as possible, (3) the melting (crystallization) point is as high as possible, and (4) the applied field frequency is such that the exchange interaction does not show up [8, 9]. The field frequency ω must be such that electron bonds have no time to form; that is, it must exceed K, where K is the chemical reaction rate.

ACKNOWLEDGMENTS

This work was partially supported by the Russian Foundation for Basic Research (grant no. 96-03-03237).

REFERENCES

1. J. M. Ziman, *Principles of the Theory of Solids* (Cambridge Univ. Press, London, 1972; Mir, Moscow, 1982).
2. V. L. Gurevich, *Kinetics of Phonon Systems* (Nauka, Moscow, 1980).
3. W. Coffey, M. Evans, and P. Grigolini, *Molecular Diffusion and Spectra* (Wiley, New York, 1984; Mir, Moscow, 1987).
4. S. O. Gladkov, Phys. Rep. **182** (4-5), 211 (1989).
5. J. Frenkel, Z. Phys. **26**, 117 (1924).
6. H. Fogel, Z. Phys. **22**, 645 (1921).
7. G. S. Fulcher, J. Am. Ceram. Soc. **8**, 339 (1925).
8. S. O. Gladkov, Chem. Phys. Lett. **174**, 636 (1990).
9. S. O. Gladkov, Phys. Lett. A **163** (5), 460 (1992).

Translated by V. Isaakyan

Technical Physics, Vol. 45, No. 7, 2000, pp. 858–864. Translated from Zhurnal Tekhnicheskoĭ Fiziki, Vol. 70, No. 7, 2000, pp. 44–51.

OPTICS, QUANTUM ELECTRONICS

Short-Laser-Pulse-Induced Photoelectric Phenomena and Reorientation in Nematics Activated with Ionic Dyes

S. V. Serak, A. A. Kovalev, and A. V. Agashkov

Institute of Electronics, Belarussian Academy of Sciences, Minsk, 220090 Belarus
E-mail: inel@inel.bas-net.by

Received March 16, 1999; in final form, December 21, 1999

Abstract—The photoelectric phenomena and orientational nonlinearity induced by nanosecond laser pulses in planar layers of liquid crystals oriented by silicon oxide (SiO) and activated with polymethine dyes were investigated. These phenomena are due to the photogeneration of surface and bulk charges in the liquid crystal cell, their spatial distribution between the grating vector and the beam propagation directions, and the electrohydrodynamic instability. *© 2000 MAIK "Nauka/Interperiodica".*

Previously [1, 2], we have observed the phenomenon of static grating recording in the planar layers of nematics oriented with silicon oxide and activated with dyes such as phthalocyanines, bisanthenes, and polymethines used for the passive Q-switching of ruby lasers [3, 4] and laser wave front inversion [5, 6]. The gratings were recorded at a radiation power of 5×10^6 W/cm^2 and had a spatial frequency of not less than 500 line/mm. They existed for a long time (several weeks) and could be erased either by heating liquid crystals above the temperature of transition to the isotropic state or by applying an electric voltage of about 30 V. The lattices represented the regions of "domains," where the director orientation deviated from the initial, surrounded by disclinations [7, 8]. Study of the reorientation in these regions by means of polarization microscopy and dynamic holography revealed a number of spectral features connected with the photorefractive properties of dye-activated liquid crystals.

The experimentally observed photorefraction in liquid crystals (LCs) [9,10] is of considerable interest due to the unusually large nonlinear response of the medium. By now, various mechanisms for the photorefraction phenomena observed in nematics activated with dyes [9,10], fullerene C_{60} [11], and discotic nematics [12] have been proposed. A space charge field induced by the interference field of continuous wave gas lasers at a small static voltage (1–2 V) can be explained by diffusion, drift, or transport of the photogenerated charges or by anisotropy of the dielectric permittivity and conductivity (Karr–Helfrich effect). Another possible reason for the photorefraction can be the photovoltaic effect in LC cells reported in [13, 14].

We have used nanosecond ruby laser emission pulses to record orientational dynamic holograms of high diffraction efficiency in nematics activated with ionic polymethine (cyanine) dyes [15]. The accompanying photoelectric phenomena were studied in this work.

LIQUID CRYSTAL SAMPLES

The experiments were performed with planar oriented liquid crystals of two types. Samples of the first type had both conducting and orienting coatings, while those of the second type had only the orienting coating. The orientation was performed by the oblique vacuum deposition of SiO layers with a thickness of about 300 Å. Director slope angle to the substrate surface varied within 1°–3°. Stoichiometry of the near-surface silicon oxide layer to a depth of 14 Å was studied by means of X-ray photoelectron spectroscopy using an ESCA spectrometer ($E_{\mathrm{MgK}\alpha 1,2}$ = 1253.6 eV). A maximum attributed to Si^{4+}, characteristic of silicon dioxide, was observed in the Si_{2p} electron band. After the ion sputter cleaning, an additional maximum shifted by 0.5 eV, which is characteristic of SiO, was observed as well. The ratio of oxygen to silicon was equal to approximately 1.2. Such an inhomogeneous structure contains oxygen vacancies, which favor the formation of local energy levels in the bandgap of the dielectric SiO film. We must also note that the evaporated films exhibit some absorption at the ruby laser wavelength (λ = 694.3 nm), with the absorption coefficient equal to $\alpha \approx 1.5$ cm^{-1}. To study the conductivity, we used LC cells with transparent evaporated electrodes of indium oxide In_2O_3 covered with a SiO film.

We used nematics with a small positive dielectric anisotropy such as 5TsB ($\Delta\varepsilon$ = 5) and a mixture of ZhK-440 ($\Delta\varepsilon$ < 0) with up to 15 wt. % ZhK-497 ($\Delta\varepsilon$ > 0) (NIOPIK, Moscow). Figure 1a shows the structures of polymethine dyes PK-686 and PK-742 (Institute of Organic Chemistry, Kiev) used as the activating agents. The absorbtion dichroism of PK-686 and PK-742 additives in 5TsB was equal to 0.02 and 0.33;

1063-7842/00/4507-0858$20.00

and that in the ZhK-440+ZhK-497 mixture was 0.46 and 0.69, respectively. The LC cell thickness was equal to 50 μm.

INTRINSIC CONDUCTION OF LC ACTIVATED WITH IONIC POLYMETHINE DYES

LCs activated with ionic dyes represent weak electrolyte solutions. In polar LC solvents, polymethine dyes dissociate into organic cations and iodine anions (J^-). In the stationary case, when the electric current density satisfies the condition $dj(t)/dt = 0$, the conductivity is determined by the well-known equation [16]

$$\sigma = e(\mu^+ + \mu^-)n^{\pm} = e(\mu^+ + \mu^-)[\gamma_D(E)n_0/\gamma_R]^{1/2}, \quad (1)$$

where e is the carrier charge; $\mu^{\pm}$ are the positive and negative ions mobilities; $n = n^+ = n^-$ is the concentration of charge carriers; n_0 is the impurity concentration; and $\gamma_D(E)$ and γ_R are the constants of dissociation and recombination, respectively (γ_D depends on the field strength in strong electric fields).

The conductivity measurements were performed using the scheme presented in Fig. 1b. The value of σ was determined as $\sigma = dU'/[SR_H(U - U')]$, where d is the layer thickness, S is the sample cross section through which the current flows, R_H is the load resistance, U is the source voltage, and U' is the voltmeter reading. The perpendicular conductivity component $\sigma_\perp$ ($\mathbf{j} \perp \mathbf{L}$, L being the layer director) was measured during the study of planar layer. The parallel component $\delta_\parallel$ was 1.5 times larger. Figure 2 shows a typical current–voltage characteristic of an LC activated with polymethine dyes and the plots of conductivity versus voltage across the sample for various dye concentrations. As is seen, the current increases slowly and the conductivity remains virtually constant and equal to $\sigma \approx 10^{-9}\,\Omega^{-1}\,\mathrm{cm}^{-1}$ in the range of voltages from 0 to 1 V. Note for comparison that the intrinsic conductivity of 5TsB is $\sigma_0 \approx 2 \times 10^{-11}\ \Omega^{-1}\ \mathrm{cm}^{-1}$ and that of the ZhK-440 + ZhK-497 mixture is approximately $5 \times 10^{-11}\ \Omega^{-1}\ \mathrm{cm}^{-1}$.

Already at a small voltage (~0.1 V), the LC cell exhibits the properties of a galvanic cell. This might be evidence of the electric double layer existence in the vicinity of the electrode. According to the formula for the Debye screening radius, the layer thickness is $r_D = (D\varepsilon/4\pi\sigma)^{1/2}$, where D is the diffusion coefficient. For the molar concentrations of impurities typically used in experiments (10^{-4}…10^{-3} mol/l), the screening radius is usually smaller than 1 μm [17]. Taking this into account, we obtain the value of diffusion coefficient $D = 10^{-6}\ \mathrm{cm}^2\ \mathrm{s}^{-1}$ for the conductivity value $\sigma = 10^{-9}\ \Omega^{-1}\ \mathrm{cm}^{-1}$. Using the Einstein relationship $D = k_BT\sigma/ne^2$ for the diffusion coefficient, we may estimate the concentration of carriers $n = 1.4 \times 10^{13}\ \mathrm{cm}^{-3}$. It is also possible to

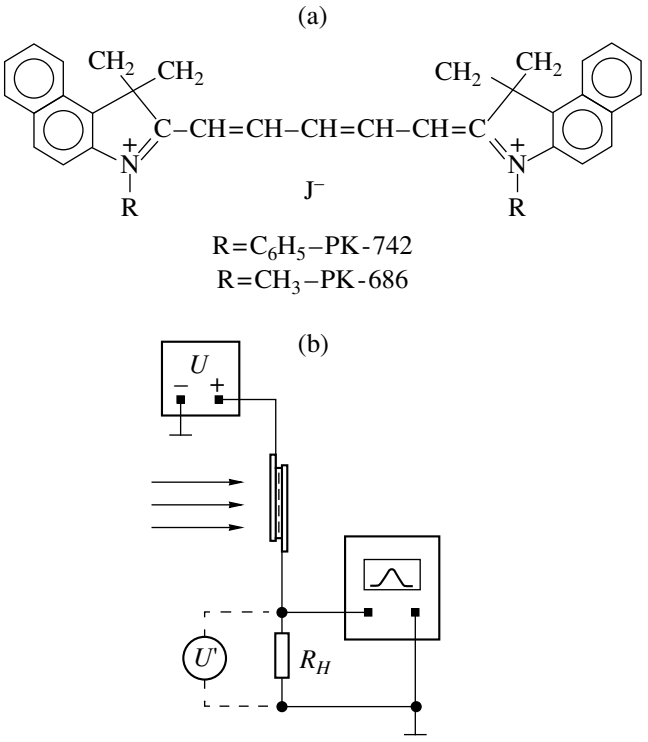

Fig. 1. The structure of polymethine dye (a) and the scheme of conductivity measurements in LCs activated with polymethine dyes (b).

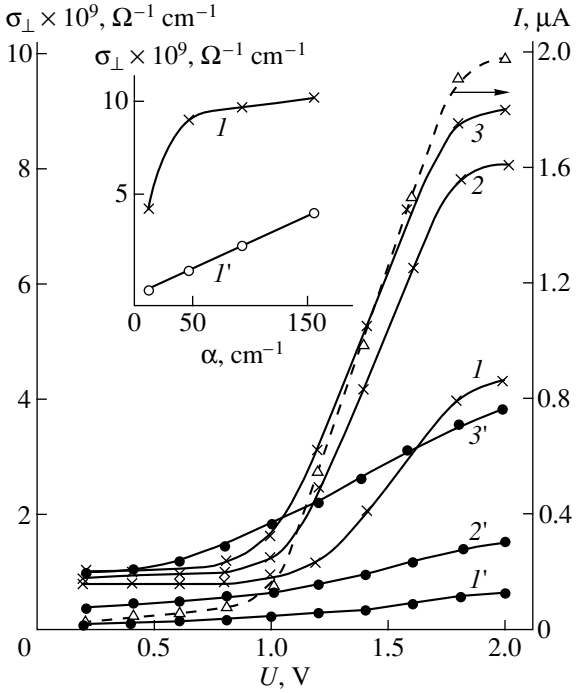

Fig. 2. A current–voltage characteristic of the LC cell (dashed line) and the plots of (*1*–*3*) conductivity and (*1*'–*3*') photoconductivity versus absorbance α and voltage U for (*1*, *1*') $n_0 = 3 \times 10^{16}\ \mathrm{cm}^{-3}$ ($\alpha = 14\ \mathrm{cm}^{-1}$); (*2*, *2*') $9.6 \times 10^{16}\ \mathrm{cm}^{-3}$ ($\alpha = 48\ \mathrm{cm}^{-1}$); (*3*, *3*') $3 \times 10^{17}\ \mathrm{cm}^{-3}$ ($\alpha = 154\ \mathrm{cm}^{-1}$).

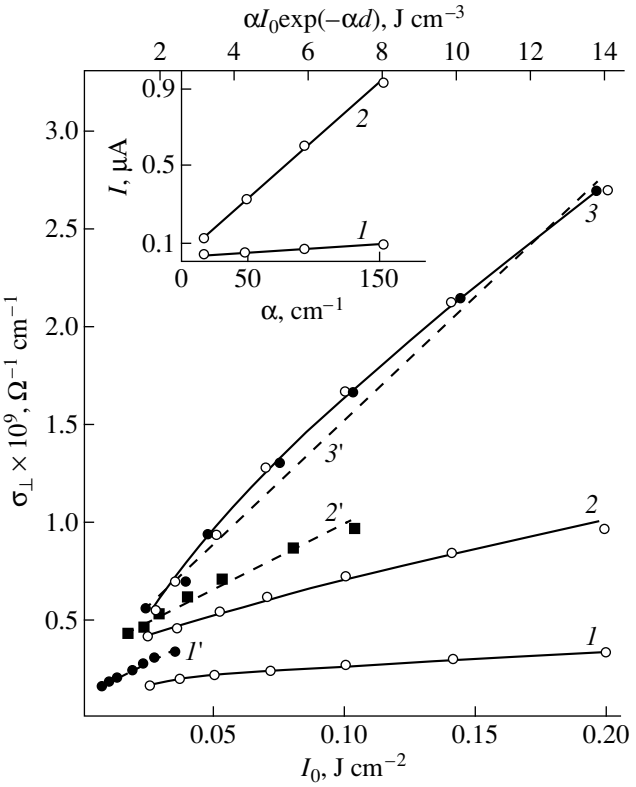

Fig. 3. The plots of photoconductivity versus energy density at various α, cm^{-1}: (*1*) 14; (*2*) 48; (*3*) 154. The inset shows the plots of photocurrent versus absorbance in (*1*) the absence and (*2*) the presence of voltage across the cell electrodes. $U = 1.6$ V.

calculate the mobility of the carriers $\mu = \sigma/2en = 2 \times 10^{-5}\,cm^2\,V^{-1}\,s^{-1}$. The mobilities and diffusion coefficients of ions are not the same because of a considerable difference in size (iodine ion radius is $r_{j_-} \approx 2.19$ Å, while that of the organic cation is $r_{OC+} \approx 20$ Å). A relationship between the mobility of ions and the viscosity of a liquid insulator established by Walden [18] gives $\mu\chi = e/6\pi r$, where χ is the viscosity. This allows one to estimate $\mu^{\pm}$ and $D^{\pm}$ using the ratio r_{j_-}/r_{OC+}. The final values are $\mu^- = 1.8 \times 10^{-5}$ cm^2 V^{-1} s^{-1}, $\mu^+ = 2 \times 10^{-6}$ cm^2 V^{-1} s^{-1}; $D^- = 9 \times 10^{-7}$ cm^2 s^{-1}, and $D^+ = 10^{-7}$ cm^2 s^{-1}. Then the parameter $\nu = (D^+ - D^-)/(D^+ + D^-)$ characterizing the relative mobility of ions is 0.8, which is considerably higher than the values in other photorefractive LCs [9, 10]. In practice, this value is slightly smaller than the estimate due to the different degrees of cation and anion coupling with the molecules of solvent.

In contrast to the region of voltages below 1 V, where the current grows slowly, both conductivity and current increase rapidly in the interval from 1 to 2 V. This is due to the growing role of dye ionization with increasing electric field strength in accordance with the Onsager theory $\sigma \sim \exp(E)^{1/2}$ [18]. The conductivity of a solution with the concentration $n_0 = 3 \times 10^{17}$ cm^{-3} rises from 10^{-9} to 9×10^{-9} Ω^{-1} cm^{-1}, and the concentration of carriers also grows by almost one order of magnitude to reach $n = 1.3 \times 10^{14}$ cm^{-3}. At a large current, the concentrational emf causes saturation of the current–voltage characteristic.

PHOTOINDUCED CONDUCTION IN LIQUID CRYSTALS ACTIVATED WITH POLYMETHINE DYES

The conductivity of LC cells increased as a result of pulsed excitation by radiation of the ruby laser (pulse duration, 60 ns). The radiation beam was expanded with a lens to fit the size of the sample, after which the energy density was equal to ~0.1 J/cm^2. The photocurrent was measured by means of an oscillograph (Fig. 1b) using the maximum value in a pulse response. In the presence of a static electric field, the current relaxed to its stationary value within a time period of about 10 ms. Here we can see a steady growth of the photoconductivity with an increase in the solution concentration and the voltage across the electrodes (Fig. 2, curves *1*'–*3*'), which makes these curves different from the initial ones (Fig. 2, curves *1*–*3*). One of the possible reasons for the photoconductivity growth is the additional dissociation of excited molecules into ions, which are distributed in the cell volume in accordance with formula $\rho(z) = \rho_0 \exp(-\alpha z)$, where α is the absorption coefficient. Here, the z axis is parallel to the beam propagation and perpendicular to the layer director **L** and the substrate. This is confirmed by the growth of conductivity with an increase in the absorption coefficient and radiation intensity (Fig. 3). For the cell with $\alpha = 154$ cm^{-1}, the number of carriers increases from 1.3×10^{14} up to 2×10^{14} cm^{-3}. We may describe the dependence of the photoconductivity on the radiation intensity I and the absorption coefficient α under some simplifying assumptions. The balance equation of the photoinduced ion production is as follows [9]:

$$\frac{\partial n}{\partial t} + \gamma_R n^+ n^- = aI(z), \qquad (2)$$

where $\gamma_R = D^{\pm}e^2/k_BT$, $I = I_0\exp(-\alpha z)$, and $a = a_0\alpha$ is a constant characterizing the photodissociation efficiency.

The dissociation of the excited dye molecules can occur in the presence of states with large lifetimes, where the probability of collisions with molecules of the crystal matrix is sufficiently large. On the other hand, the intercombination conversion from a triplet level increases the temperature in a local interaction region and also results in a growth of the degree of dissociation. Study of the kinetics of interaction of pulsed ruby laser radiation with polymethine dyes in LCs showed that dye molecules radiate via a three-level scheme involving a metastable state with a lifetime of

~1.5 μs [19]. Thus, the main processes of ion recombination and dissociation occur after termination of the laser pulse. Then the balance equation (2) splits into two parts:

$$\frac{\partial n}{\partial t} = aI_0\exp(-\alpha z) \quad \text{for} \quad t < \tau, \tag{3}$$

$$\frac{\partial n}{\partial t} = +\gamma_R n^+ n^- = 0 \quad \text{for} \quad t > \tau, \tag{4}$$

where τ is the pulse duration.

The first equation gives the number of radiation-induced charge carriers $n_0' = aI_0\exp(-\alpha z)\tau$. The second equation allows us to determine variation of the induced charge density with time after the laser pulse:

$$n'(t) = \frac{n_0'}{n_0'\gamma_R t + 1}. \tag{5}$$

For the parameters $\gamma_R \approx 5.7 \times 10^{-13}$ cm^3 s^{-1}, $t = 100$ μs (the moment the maximum current amplitude is reached), and $n_0' \approx 0.7 \times 10^{14}$ cm^{-3} (the maximum number of induced charge carriers under our experimental conditions) we obtain the value $n_0'\gamma_R t \approx 0.004$, which is much less than unity. Taking into account Eqs. (1) and (5), the photoinduced conductivity can be expressed as

$$\sigma'(t) \approx e(\mu^+ + \mu^-)a_0\alpha I_0\exp(-\alpha z)z. \tag{6}$$

Here, the function $\sigma'\{\alpha I_0\exp(-\alpha d)\}$ is in fact close to linear, which is illustrated in Fig. 3 (curves *1*'–*3*').

We observed the phenomenon of photocurrent excitation in the absence of any external static electric field. This effect qualitatively differs from that discussed above. In the presence of an external field, the photocurrent polarity follows the polarity of the applied voltage, while without the field, the polarity of the signal on the load resistor R_H is determined by the direction of the incident light beam. The photocurrent flows from the illuminated electrode to the dark one (i.e., cations move from the bulk of the crystal toward the input electrode).

High-power laser radiation (~10^6 W/cm^2) may give rise to the injection of electrons from the electrode (this effect was observed experimentally) and to the generation of charges on the surface of silicon oxide films. Combined thermal and field effects of the laser radiation will result in the accumulation of negative charge at the film surface [20]. This process is favored by the existence of local energy levels in the bandgap of insulating SiO film, by the light absorption in the film, and by the injection of charge carriers from the electrode. Recombination of the free charge carriers and cations of the solution at the relief film surface [15] will cause the formation of radical ions of dye molecules. These ions can settle as defects on the surface, which is one of the possible reasons for the formation of disclinations, bounding the regions with different orientations induced in the bulk of the LC by the interference radiation field as a static lattice of domains.

The relaxation time of the induced charge was of the order of milliseconds. The Debye relaxation time of the volume charge is $\tau_D = \varepsilon_\perp/4\pi\sigma_\perp$. For $\varepsilon_\perp = 10$ and $\sigma_\perp = 3 \times 10^{-9}$ Ω^{-1} cm^{-1}, this formula gives $\tau_D = 0.3$ ms, which is smaller by one order of magnitude than the value observed in experiment. Thus, inhomogeneous distribution of the volume charge along the beam direction up to a depth exceeding the electric double layer thickness arises as a result of the photoinduced unipolar injection of charge carriers at the surface and the dissociation of dye molecules. This leads to the appearance of a photoinduced electric field E_z. Photogeneration of the volume charge also results in the electric double layer destruction and more intensive growth of the current beginning with very small voltages, as can be seen in Fig. 2 (curves *1*'–*3*').

DIFFRACTION GRATINGS IN LIQUID CRYSTALS ACTIVATED WITH POLYMETHINE DYES

The orientational photorefractive nonlinearity in LCs induced by the pulsed radiation of the ruby laser operating in the TEM_{00} mode (pulse energy $E = 60$ mJ, pulse duration $\tau \approx 60$ ns) was studied by means of dynamic holography using the radiation of a He–Ne laser as a probe. The geometry of experiment in which the direction of the lattice vector **q** coincides with that of the director **L** (see Fig. 4a) was selected from a number of various possible geometries. If the polarization vectors of the pumping waves E_1 and E_2 and the probing wave E_3 are parallel to the director L, the diffraction efficiency of the gratings is 2–3 times greater than in the case of $E_{1,2} \parallel L$, $E_3 \perp L$ and an order of magnitude larger than that for $E_{1,2} \perp L$. The director is mainly reoriented in the *xz* plane.

The radiation field generates charges inhomogeneously distributed in space along the *x*-axis (with a grating constant Λ) and along the *z*-axis (Fig. 4b). In the absence of an external static electric field, a photoinduced field E_z arises in the region of diffraction maxima along the *z*-axis and the diffusion of induced charges is observed along the *x*-axis with a lattice relaxation time $\tau_D = \Lambda^2/4\pi^2 D$. Weak electric current accompanied by the gradient of positive ion concentration along the *z* direction might cause isotropic electrohydrodynamic instability. The mechanism of this instability formation under conditions of unipolar injection was considered by Felici [21]. Figure 4b shows a model describing the mechanism of instability in our case. Due to inhomogeneous charge density distribution, both in the laser beam direction and along the substrate, an electrostatic force $F = \delta\rho E_z$ arising in the bulk of the layer will cause the formation of two vortices over a length equal to the grating constant Λ. Rotation of the director as a result of the hydrodynamic flow will have a period close to

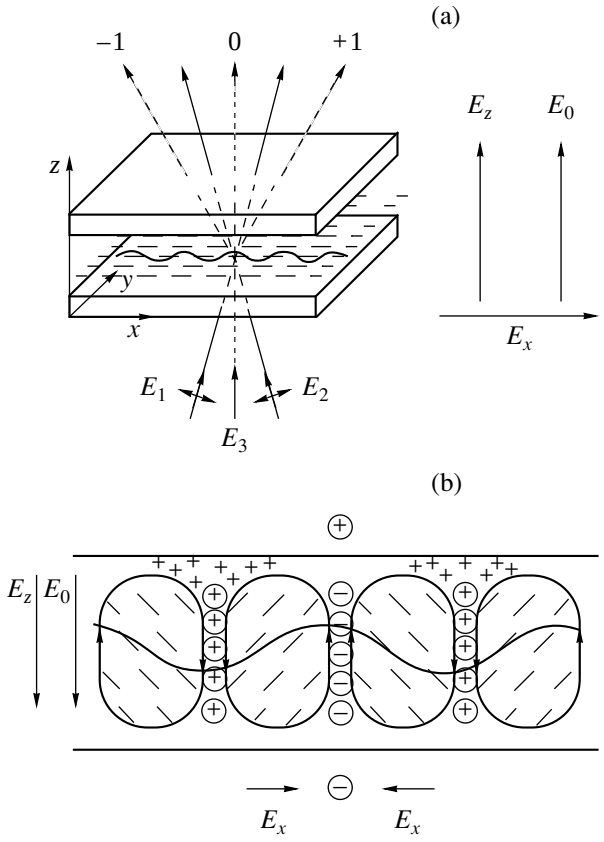

Fig. 4. Schematic diagrams showing (a) the interaction geometry and (b) a model of the electrohydrodynamic instability formation in LCs activated with polymethine dyes.

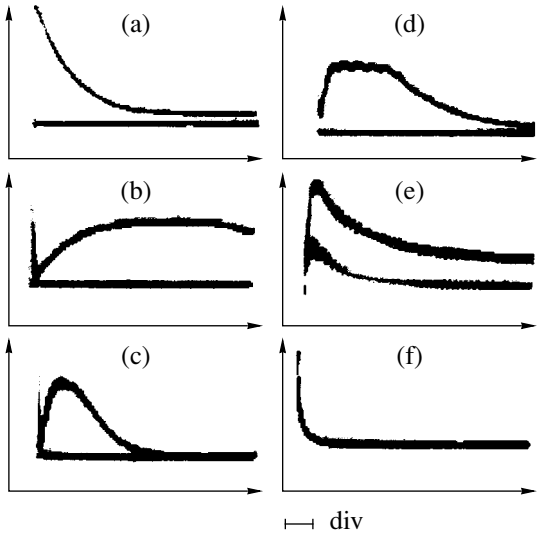

Fig. 5. Osscillograms of the first-order diffraction intensity for the probing beam of a He–Ne laser in LC cells oriented with (a–e) silicon oxide and (f) polyimide. Time scale (ms/div): (a) 0.1, (b) 5, (c–f) 100; $\alpha = 14\text{cm}^{-1}$; (e) lattice relaxation in the presence of electric field $U = 1.2$ V (higher amplitude) and in the absence of the field.

the cell thickness [22]. The threshold voltage of instability of an LC with $\Delta\varepsilon > 0$ may be lower than that of a electrohydrodynamic instability of the anisotropic type according to the Karr–Helfrich model [16].

In the presence of a static electric field E_0, the interference field of the laser radiation gives rise to the photoinduced field E_x (Fig. 4b) due to anisotropic conductivity (the conductivity is equal to $\sigma_\parallel$ along the x-axis and to $\sigma_\perp$ along the z-axis. In accordance with the Karr–Helfrich model, the field E_x is determined by the formula [23]

$$E_{x,\sigma} = -\frac{(\sigma_\parallel - \sigma_\perp)\cos\Theta\sin\Theta}{\sigma_\parallel\cos^2\Theta + \sigma_\perp\sin^2\Theta}E_0, \qquad (7)$$

where Θ is the angle of director deviation in the xz plane.

Electrohydrodynamic instability of the anisotropic type arises if there is an initial disturbance of the director orientation in the layer, which can be induced by an isotropic instability. The rotation of the layer director is enhanced when the direction of the static field E_0 coincides with the direction of the induced field E_z. The period of sinusoidal deformation of the director remains the same and is close to the layer thickness.

Typical oscillograms of the first-order diffraction in the LC cells oriented with SiO without electrodes are presented in Fig. 5. Two types of the characteristic relaxation time are observed, the first being the thermal diffusion time $\tau_T = \rho_0 C_p^2 \Lambda^2/4\pi^2\lambda_T$ (equal to 0.5 ms, see Fig. 5a) and the second, the orientational time, which is determined essentially by the charge diffusion $\tau_D = \Lambda^2/4\pi^2 D$ (Figs. 5b–5f). Typical values of the LC parameters are as follows: $\rho_0 = 10^3$ kg/m^3, $\chi = 7 \times 10^{-2}$ kg/(m s), $C_p = 1500$ J/(kg K), $\lambda_1 = 0.16$ J (K s m), $D = 10^{-6}$ cm^2/s. For a grating constant of $\Lambda = 40$ μm the time constants τ_T and τ_D are equal to 0.5 ms and 400 ms, respectively, in good agreement with experiment. The orientational component is observed after vanishing of the thermal component and has a buildup period of 20 ms (a), while the relaxation time varies from 0.4 to 1 s. The time parameters of the holograms depend not only on the lattice constant and properties of LC media, but on the conditions of orientant deposition and the laser radiation intensity as well, which results in the formation of both dynamic and static gratings. A typical oscillogram of variation of the probing beam of a rectangular shape in the case of equilibrium of the hydrodynamic and orientational moments is shown in Fig. 5d. A grating constant Λ close to 40 μm is the optimum value for effective gratings (Fig. 6). The diffraction efficiency η grows with increasing radiation intensity and absorption coefficient, reaching a maximum at $\alpha I_0 = 16$ J/cm^3 (Fig. 7a). With the further growth of αI_0, the value of η drops as a result of convective motions in the bulk of the cell. Heating of the liquid crystal does not affect the diffraction efficiency but results in a decrease of the relaxation

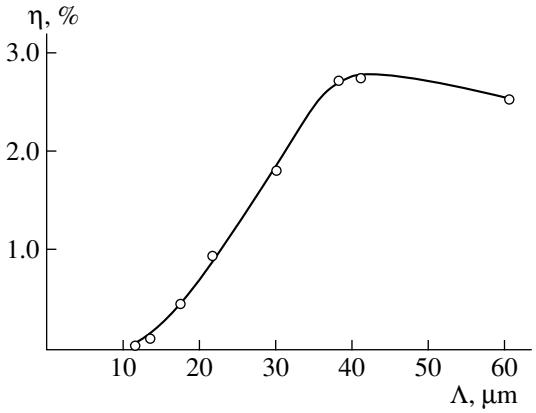

Fig. 6. The plot of diffraction efficiency η versus grating constant Λ.

time $\tau_\Theta = \chi\Lambda^2/4\pi^2$ K from 600 (T = 20°C) to 150 ms ($T - T_{is}$ = 1°C), which corresponds to the reduction in viscosity χ (in the isotropic phase, this time is 50 ms). The maximum diffraction efficiency of the gratings was equal to 3–4%.

The efficiency of the gratings can be increased using an additional static field. Typical oscillograms of the diffraction beam intensity with and without voltage across the cell electrodes are presented in Fig. 5e. Here, no relaxation of the cell to the initial state is observed because of a static grating formation. The character of the diffraction efficiency variation as function of the absorbed radiation αI_0 is not altered in the presence of the field (Fig. 7b). The results of our study reveal several subsequent stages in the variation of η with increasing voltage. The efficiency does not change considerably in the region below 0.6…0.8 V, where the conductivity and also exhibits no significant variation (Fig. 2). The range 0.6…1.3 V reveals the growth of both η and conductivity. Here the value of η is approximately three times greater than the value without bias voltage. At U = 1.4 V, which is close to the Fredericksz transition (for our LCs, the threshold voltage is $U_{Fr} \approx$ 2 V), η decreases, because the geometry of experiment does not provide for the formation of electrohydrodynamic instability. The diffraction efficiency in the presence of electric field was equal to 10%.

As a result of comparative experiments involving nonionic dyes and other orienting substances, we may conclude that the reorientation described above has remarkable features in the ionic compositions LC + dye with orienting SiO layers. Figure 5 compares orientational components for the LC cells with SiO and polyimide orientants. The conductivity and the grating appear in the LC cells without a static electric field and are only enhanced by the external field. Apparently, we initially observe an isotropic electrohydrodynamic instability with a lower threshold and then the instability of anisotropic character, which is similar to the optical Karr–Helfrich effect in liquid crystals. Our experimental conditions provide for the observation of these effects [22]. Indeed, the efficiency of gratings in planar layers is maximum when the grating constant Λ is close to the cell thickness. In addition, the cells exhibit a positive anisotropy of conductivity ($\sigma_\parallel \approx 1.5\sigma_\perp$). Finally, the effect in LCs with positive dielectric anisotropy ($\Delta\varepsilon > 0$) is observed at voltages $U < U_{Fr}$. Dynamics of the orientational grating shows that reorientation occurs within a period of ~20 ms simultaneously with the photocurrent relaxation (10 ms) and the onset of macroscopic mobility in the liquid crystal volume.

Thus, the photogeneration of surface and bulk charges in the LC cell, the distribution of these charges in space in the beam direction and along the grating vector, and the interaction of photoinduced fields with the applied static field result in the phenomena of elec-

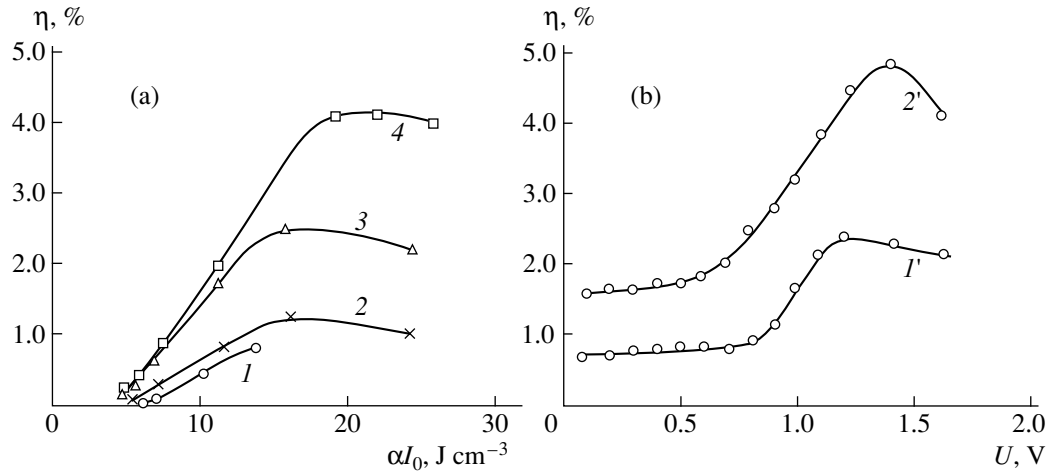

Fig. 7. The plots of diffraction efficiency versus (a) parameter αI_0 and (b) voltage for α = 14 (*1*), 48 (*2*, *1*'), 154 cm^{-1} (*3*, *4*, *2*') and U = 0 (*1*–*3*), 1.2 V (*4*).

trohydrodynamic instability and effective reorientation of the LC layer director.

ACKNOWLEDGMENTS

Authors gratefully acknowledge discussions with S.P. Zhvavyĭ and N.A. Usov and the valuable assistance of E.A. Tyavlovskaya in the study of X-ray photoelectron spectra of SiO films.

The work was supported by the International INTAS-Belarus foundation (grant no. 0635).

REFERENCES

1. V. A. Pilipovich, A. A. Kovalev, G. L. Nekrasov, and S. V. Serak, Dokl. Akad. Nauk BSSR **22**, 36 (1978).
2. G. L. Nekrasov, Yu. V. Razvin, and S. V. Serak, *Optical Data-Processing Techniques*, Ed. by V. A. Pilipovich (Nauka i Tekhnika, Minsk, 1978).
3. A. A. Kovalev, G. L. Nekrasov, and S. V. Serak, Mol. Cryst. Liq. Cryst. **193**, 51 (1990).
4. A. A. Kovalev and S. V. Serak, Zh. Prikl. Spektrosk. **52**, 197 (1990).
5. A. A. Kovalev, S. V. Serak, G. L. Nekrasov, *et al.*, Kvantovaya Élektron. (Moscow) **22**, 838 (1995).
6. A. A. Kovalev, S. V. Serak, and G. L. Nekrasov, Mol. Cryst. Liq. Cryst. **320**, 425 (1997).
7. G. L. Nekrasov and A. A. Kovalev, Izv. Akad. Nauk BSSR, Ser. Fiz.-Mat. Nauk, No. 3, 105 (1980).
8. S. V. Serak and A. A. Kovalev, Mol. Cryst. Liq. Cryst. **320**, 417 (1998).
9. E. V. Rudenko and A. V. Sukhov, Zh. Éksp. Teor. Fiz. **105**, 1621 (1994) [JETP **78**, 875 (1994)].
10. I. C. Khoo, H. Li, and Y. Liang, Opt. Lett. **19**, 1723 (1994).
11. I. C. Khoo, Mol. Cryst. Liq. Cryst. **282**, 53 (1996).
12. R. Macdonald, P. Meindl, G. Chilaya, and D. Sikharulidze, Mol. Cryst. Liq. Cryst. **320**, 115 (1998).
13. S. Sato, Jpn. J. Appl. Phys. **20**, 1989 (1981).
14. I. C. Khoo, B. D. Guenther, and S. Slussarenko, Mol. Cryst. Liq. Cryst. **321**, 419 (1998).
15. A. A. Kovalev and S. V. Serak, Proc. SPIE **3318**, 327 (1998).
16. L. M. Blinov, *Electro- and Magnetooptics of Liquid Crystals* (Nauka, Moscow, 1978).
17. P. de Genues, *The Physics of Liquid Crystals* (Clarendon, Oxford, 1974; Mir, Moscow, 1977).
18. S. N. Koĭkov, *Physics of Dielectrics* (Leningrad Politekh. Inst., Leningrad, 1967).
19. A. A. Kovalev, G. L. Nekrasov, and S. V. Serak, Zh. Prikl. Spektrosk. **45**, 400 (1986).
20. *Handbook of Thin Film Technology*, Ed. by L. I. Maissel and R. Glang (McGraw-Hill, New York, 1970), Vol. 2.
21. N. J. Felici, Rev. Gen. Electr. **78**, 717 (1969).
22. S. A. Pikin, *Structural Transformations in Liquid Crystals* (Nauka, Moscow, 1981).
23. W. Helfrich, J. Chem. Phys. **51**, 4092 (1969).

Translated by S. Egorov

Technical Physics, Vol. 45, No. 7, 2000, pp. 865–869. Translated from Zhurnal Tekhnicheskoĭ Fiziki, Vol. 70, No. 7, 2000, pp. 52–56.

Analogs of the Brewster Effect and Total Internal Reflection for Cylindrical Waves

M. A. Kaliteevskiĭ and V. V. Nikolaev

Ioffe Physicotechnical Institute, Russian Academy of Sciences, Politekhnicheskaya ul. 26, St. Petersburg, 194021 Russia

Received July 6, 1999

Abstract—Analogs of the Brewster effect and total internal reflection were investigated for cylindrical waves passing through a cylindrical interface. It was found that, in the case of cylindrical geometry, the Brewster effect is also observed but weakens with decreasing moment of momentum of a cylindrical wave. Wave reflection from a small-radius cylindrical interface is analyzed. Asymptotic expressions for the reflection factor of a cylindrical wave are obtained when the radius of the interface tends to zero. It was found that, as the radius the interface decreases, the reflection factor of a cylindrical wave with a nonzero moment of momentum approaches unity from the left but does not reach this value. *© 2000 MAIK "Nauka/Interperiodica".*

.INTRODUCTION

The incidence of a plane light wave on the planar interface between two media with refraction indices n_1 and n_2 seems to be the physical phenomenon that has been investigated in most detail [1, 2]. The Brewster effect (the reflection factor is exactly equal to zero when a *p*-polarized wave is incident at an angle θ_{BR} that satisfies the relationship $\tan\theta_{BR} = n_2/n_1$) and total internal reflection (the reflection factor is exactly equal to unity when $n_1 > n_2$ and the angle of incidence exceeds the critical value $\sin\theta_{tot} = n_2/n_1$) are finding wide application in technology. In the last few years, designers have been trying to use cylindrical structures in various optoelectronic devices [3, 4]. Several theoretical papers are devoted to the propagation of cylindrical waves in laminated cylindrical structures and through a cylindrical interface [5–7]. However, a number of intriguing features, such as an increase in the reflection factor when the radius of the interface is small and the dependence of optical properties on the light polarization, call for further investigation. In this paper, we try to contribute to the study of these effects.

RESULTS AND DISCUSSION

Consider a cylindrical light wave with a frequency ω that propagates perpendicularly to the axis of structure symmetry (*z*-axis) and is incident on the cylindrical interface between two media with refraction indices n_1 (internal medium) and n_2 (external medium). The media are assumed to be infinite along the *z*-axis (Fig. 1). Cylindrical waves of arbitrary polarization can be represented as a superposition of *E* (electric field **E** is parallel to the axis of symmetry) and *H* (magnetic field **H** is parallel to the axis of symmetry) waves [7]. The reflection amplitude factor r_d (introduced as the ratio between the tangential electric field components in the reflected and incident waves) for the *E*- and *H*-polarized cylindrical light waves scattered from a cylindrical interface of radius ρ is given by [7]

$$r_d = \frac{n_2 C_{m2}^{(1)} - n_1 C_{m1}^{(1)}}{n_1 C_{m1}^{(2)} - n_2 C_{m2}^{(2)}}, \quad (1)$$

and

$$r_d = \frac{n_2/C_{m2}^{(1)} - n_1/C_{m1}^{(1)}}{n_1/2C_{m1}^{(2)} - n_2/C_{m2}^{(1)}}, \quad (2)$$

respectively. Here, $C_{ml}^{(1,2)} = H_m^{(1,2)'}(n_l K\rho)/H_m^{(1,2)}(n_l K\rho)$, $H_m^{(1,2)}(n_l K\rho)$ is the Hankel function, $K = \omega/c$, c is the speed of light, and the derivative sign means differentiation with respect to the whole argument and not just to ρ.

Figures 2 and 3 show the variations of the phase and squared absolute value of the reflection amplitude factor for the *E*-polarized cylindrical wave scattered from the interface between media with refraction indices of 1.0 and 3.0. In the figures, the three curves correspond to moments of momentum $m = 0$, 2, and 5. Figure 2 illustrates the situation when the external medium is optically denser, while in Fig. 3, the situation is reversed. Figures 4 and 5 present the same for the *H*-polarized wave.

In a cylindrical wave, Poynting's vector is radially directed when $m = 0$. When the moment of momentum is nonzero, the angle Θ between Poynting's vector and the radius depends on ρ and satisfies the approximate relationship

$$\sin\Theta = m/nK\rho, \quad (3)$$

1063-7842/00/4507-0865$20.00 © 2000 MAIK "Nauka/Interperiodica"

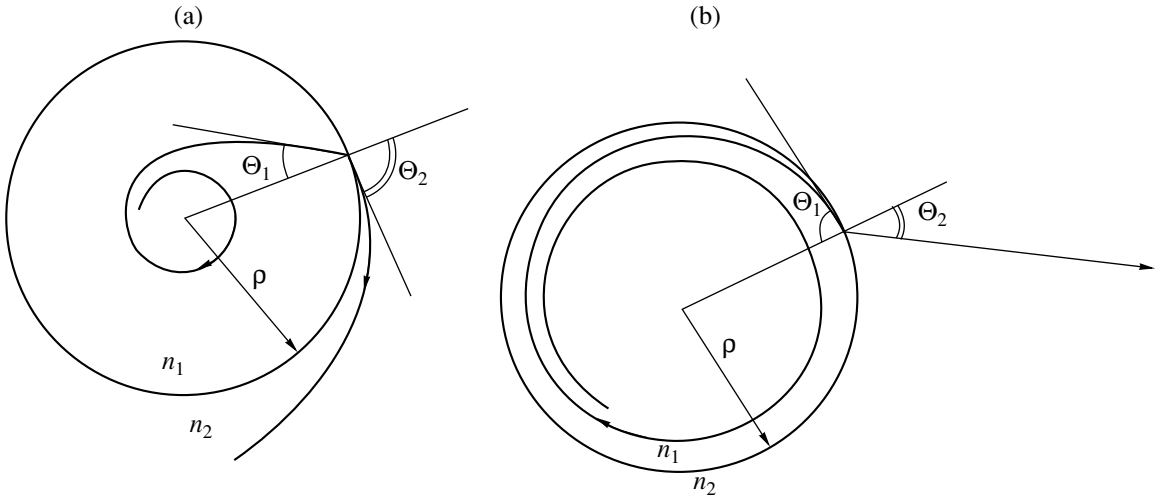

Fig. 1. Trajectory of energy transfer in a refracted cylindrical wave for $\rho = 0.55*(2\pi/K)$ and $m = 5$: (a) $n_1 = 3$ and $n_2 = 1$ and (b) $n_1 = 1$ and $n_2 = 3$.

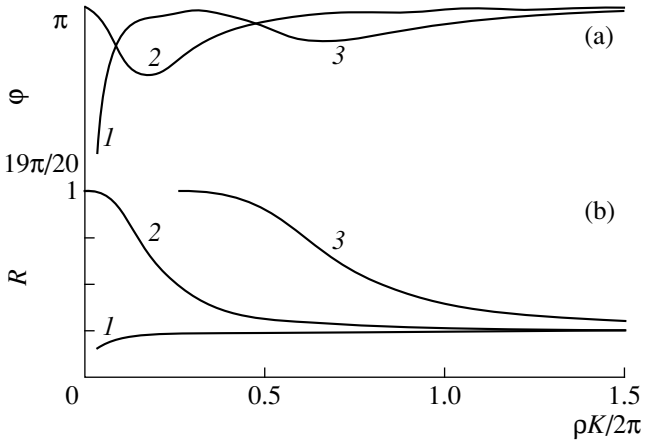

Fig. 2. (a) Phase and (b) square of the absolute value of the reflection amplitude factor for the *E*-polarized scattered cylindrical wave vs. interface radius. $n_1 = 1$, $n_2 = 3$, and $m =$ (*1*) 0, (*2*) 2, and (*3*) 5.

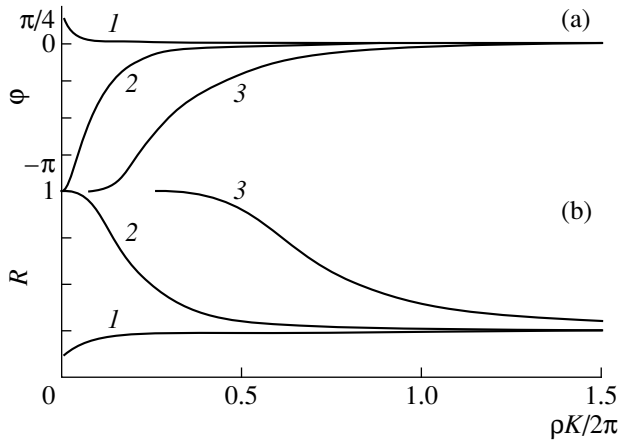

Fig. 3. The same as in Fig. 2 for $n_1 = 3$ and $n_2 = 1$.

The azimuth component of Poynting's vector being proportional to m/ρ. Within a small portion of the interface, one could consider an incident cylindrical wave as a plane wave incident on the plane interface at an angle Θ. This, however, may yield qualitatively false results, as demonstrated below.

As ρ increases, the azimuth component of Poynting's vector vanishes and angle Θ approaches zero; i.e., the incidence of a cylindrical wave on a cylindrical interface of large radius is equivalent to the normal incidence of a plane wave on a planar interface [7]. Indeed (Figs. 2–5), for large ρ's, the square of the reflection factor magnitude tends to 25% and its phase approaches zero or π, depending on medium alternation, for both polarizations.

As ρ decreases, the angle Θ determined by (3) increases. When $n_1 > n_2$ and a light wave comes from the internal medium, total internal reflection is observed if $\rho = \rho_{tot}$ and $\Theta = \Theta_{tot}$. The critical value of the radius ρ_{tot} is determined by the formula $K\rho_{tot} = m/n_2$. When $n_1 < n_2$, total internal reflection must be absent.

The above considerations are in conflict with the following properties of cylindrical waves. First, using (1), one can show (taking into account that $C_{ml}^{(1)}$ is the complex conjugate to $C_{ml}^{(2)}$) that the reflection intensity factor does not depend on the sequence of layers, as in the case of the normal incidence of a plane wave on a planar interface (Figs. 2–5) [7]. Second, after the wave crosses the interface, Θ determined by (3) does not

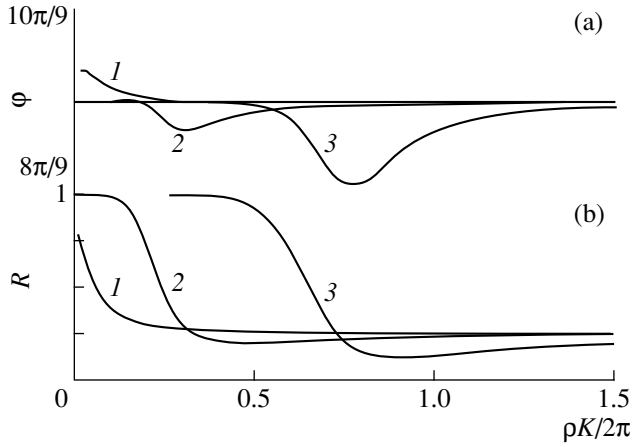

Fig. 4. The same as in Fig. 2 for the *H*-polarized cylindrical wave.

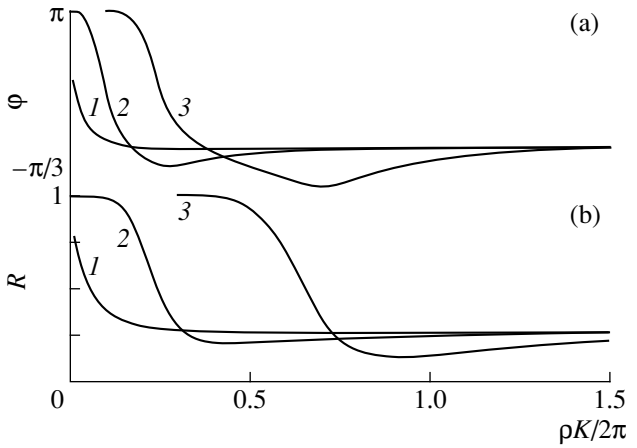

Fig. 5. The same as in Fig. 3 for the *H*-polarized cylindrical wave.

depend on the refraction index of the layer from which the wave comes. However, the angles Θ on both sides of the interface are formally related by Snell's law [1, 2] [see (3)].

In fact, when the radius ρ of the interface decreases and reaches a certain *m*-dependent characteristic value (*m* is assumed to be nonzero), the reflection intensity factor starts increasing, asymptotically approaching unity from the left (see Figs. 2–5 and Appendix). This phenomenon, briefly described in [5], was called total reflection at small radius. It was indicated that the reflection amplitude factor is equal to $(-1)^{m+1}i$ at a small (but nonzero!) radius. According to our calculations, the absolute value of the reflection factor, while approaching unity as ρ tends to zero, always remains less than unity at any nonzero ρ. The phase of the reflection factor behaves in a quite different way, approaching π. A small variation of the reflection factor magnitude from unity may affect the observed optical properties of an actual cylindrical structure only slightly. However, being involved in the phase of the reflection factor, such an error radically changes the calculated spectrum of the optical eigenmodes in the cylindrical system.

Thus, total internal reflection is not observed for cylindrical waves propagating perpendicularly to the axis of symmetry, which can be explained in simple physical terms.[1] In the plane case, when total internal reflection occurs, light passes through the interface into the lower index medium, turns, and comes back to the higher index medium. Such is not the case in cylindrical systems, because the curvature of the interface exceeds that of the light "trajectory."

For *H*-polarized waves, one can find, for every *m*, a radius ρ_{BR} such that Θ determined by (3) will be equal to the Brewster angle Θ_{BR}. It is easy to check that this "Brewster radius" satisfies the relationship

$$K\rho_{BR} = m\sqrt{n_1^{-2} + n_2^{-2}}. \quad (4)$$

Figures 4 and 5 demonstrate that, when $m \neq 0$, the dependences of the reflection factor for the *H*-polarized wave on interface radius have minima located close to those predicted by (4). This fact enables us to argue that these minima reflect the Brewster effect. In the minima, the reflection factor is other than zero but the minimum for $m = 5$ is deeper than for $m = 2$. This can be explained if we take into account that the Brewster effect is a result of the transversality of electromagnetic waves [1, 2]. Hence, this effect must be weaker in the case of cylindrical waves, whose Poynting's vector is locally transverse. As the moment of momentum *m* increases, the Brewster radius grows, the curvature of the surface decreases, the situation more and more resembles the plane case, and the minimum becomes deeper.

Our analysis demonstrates that, for cylindrical structures, a phenomenon similar to the Brewster effect is observed but, instead of total internal reflection, the reflection factor grows at a small radius.

APPENDIX

Asymptotics of the Reflection Factor for the Small-Radius Interface

The reflection factor of the *E*-polarized wave scattered from the interface between media 1 and 2 is represented by

$$r = \frac{n_2 C_{m2}^{(1)} - n_1 C_{m1}^{(1)}}{n_1 C_{m1}^{(2)} - n_2 C_{m2}^{(1)}}.$$

[1] Note that the situation under consideration has nothing to do with light propagation in fibers, where total internal reflection takes place for light waves propagating along the axis of symmetry.

Replacing the Hankel functions by combinations of the Bessel (J_m) and Weber (Y_m) functions in the formula for $C_m^{(1,2)}$, one can use the approximate expressions

$$C_m^{(1)} = \frac{J_m' + iY_m'}{J_m + iY_m} \cong \frac{Y_m'}{Y_m} + i\left(\frac{Y_m' J_m}{Y_m^2} - \frac{J_m'}{Y_m}\right) + \frac{J_m' J_m}{Y_m^2} - \frac{Y_m' J_m^2}{Y_m^3}, \quad (1A)$$

and

$$C_m^{(2)} = \frac{J_m' - iY_m'}{J_m - iY_m} \cong \frac{Y_m'}{Y_m} - i\left(\frac{Y_m' J_m}{Y_m^2} - \frac{J_m'}{Y_m}\right) + \frac{J_m' J_m}{Y_m^2} - \frac{Y_m' J_m^2}{Y_m^3}, \quad (2A)$$

as the argument of the functions approaches zero. This is valid, since, at small arguments, the Weber function tends to infinity, while the Bessel function approaches zero (or unity when $m = 0$). The formula for $C_{ml}^{(1,2)}$ can be written in the form $C_m^{(1,2)}(x) = F(x) + iG(x)$. When $m = 0$, $F(x)$ and $G(x)$ are defined by

$$F(x) = \mathrm{Re}\left[\frac{2i}{\pi + 2i(\ln(x/2) + \gamma)}\frac{1}{x}\right] + O(x), \quad (3A)$$

$$G(x) = \mathrm{Im}\left[\frac{2i}{\pi + 2i(\ln(x/2) + \gamma)}\frac{1}{x}\right] + O(x). \quad (4A)$$

For $m = 1$,

$$F(x) = -\frac{1}{x} - x\ln x + O(x), \quad (5A)$$

$$G(x) = \frac{\pi}{2}x + \frac{\pi}{4}(2\ln(x/2) - 1 + 2\gamma)x^3 + O(x^5), \quad (6A)$$

where γ is the Euler constant.

For $m \geq 2$,

$$F(x) = -m\left(\frac{1}{x}\right) + \frac{1}{2(m-1)}x + O(x^3). \quad (7A)$$

$$G(x) = \frac{\pi}{(m-1)!^2 2^{2m-1}}x^{2m-1} + O(x^{2m+1}). \quad (8A)$$

The reflection amplitude factor of the *E*-polarized wave can be written in the form

$$r = -1 - i\frac{2n_1 G(n_1 K\rho)}{(n_1 F(n_1 K\rho) - n_2 F(n_2 K\rho))} + 2\frac{((n_1 G(n_1 K\rho))^2 + n_1 G(n_1 K\rho) * n_2 G(n_2 K\rho))}{(n_2 F(n_2 K\rho) - n_1 F(n_1 K\rho))^2} + O\left(\left(\frac{G}{F}\right)^3\right). \quad (9A)$$

At $m = 0$, this yields for the reflection amplitude (r) and intensity (R) factors

$$\lim_{\rho \to 0}(r) = \frac{i\ln(n_1/n_2)}{\pi - i\ln(n_1/n_2)} \quad (10A)$$

and

$$\lim_{\rho \to 0}(R) = \frac{\ln^2(n_2/n_1)}{\pi^2 + \ln^2(n_2/n_1)}, \quad (11A)$$

respectively.[2]

For $m = 1$,

$$r = -1 + i\frac{\pi n_1^2}{(n_1^2 - n_2^2)\ln(K\rho)} + \frac{\pi^2(n_1^4 + n_1^2 n_2^2)}{2(n_2^2 - n_1^2)^2 \ln^2(K\rho)} + O(K\rho) \quad (12A)$$

and

$$R = 1 - \frac{\pi^2 n_1^2 n_2^2}{(n_2^2 - n_1^2)^2 \ln^2(K\rho)} + O((K\rho)^2). \quad (13A)$$

For $m \geq 2$,

$$r = -1 + i\frac{\pi(m-1)n_1^{2m}}{(m-1)!^2 2^{2m-3}(n_2^2 - n_1^2)}(K\rho)^{2m-2} + \frac{\pi^2(m-1)^2}{(m-1)!^4 2^{4m-5}}\frac{(n_1^{4m} + n_1^{2m}n_2^{2m})}{(n_2^2 - n_1^2)^2}(K\rho)^{4m-4} + O((K\rho)^{6m-6}) \quad (14A)$$

and

$$R = 1 - \frac{\pi^2(m-1)^2 n_1^{2m} n_2^{2m}}{(m-1)!^4 2^{4m-6}(n_2^2 - n_1^2)^2}(K\rho)^{4m-4} + O((K\rho)^{8m-8}). \quad (15A)$$

The reflection amplitude factor of the *H*-polarized

[2] For $m = 0$, one should prefer exact formula (1) rather than the asymptotic approximation, which is too awkward.

wave can be represented in the form

$$r = -1 - i\frac{2n_2^{-1}G(n_1k_0\rho)}{(n_1^{-1}F(n_1k_0\rho) - n_2^{-1}F(n_2k_0\rho))} + 2\frac{((n_2^{-1}G(n_1K\rho))^2 + n_1^{-1}G(n_1K\rho)*n_2^{-1}G(n_2K\rho))}{(n_2^{-1}F(n_2K\rho) - n_1^{-1}F(n_1K\rho))^2} + O\left(\left(\frac{G}{F}\right)^2\right), \quad (16A)$$

which, at $m = 0$, yields [9]

$$\lim_{\rho \to 0}(r) = 1 \quad (17A)$$

and

$$\lim_{\rho \to 0}(R) = 1. \quad (18A)$$

For $m = 1$,

$$r = -1 - i\frac{\pi n_1^3 n_2}{(n_2^2 - n_1^2)}(K\rho)^2 + \frac{\pi^2 n_1^4 n_2^2 (n_2^2 + n_1^2)}{2(n_2^2 - n_1^2)^2}(K\rho)^4 + O((K\rho)^6) \quad (19A)$$

and

$$R = 1 - \frac{\pi^2 n_1^4 n_2^4}{(n_2^2 - n_1^2)^2}(K\rho)^4 + O((K\rho)^8). \quad (20A)$$

For $m \geq 2$,

$$r = -1 - i\frac{\pi n_1^{2m+1} n_2}{(m-1)!^2 m 2^{2m-2}(n_2^2 - n_1^2)}(K\rho)^{2m} + \frac{\pi^2 (n_1^{4m} + n_1^{2m} n_2^{2m}) n_1^2 n_2^2}{(m-1)!^4 m^2 2^{4m-3}(n_2^2 - n_1^2)^2}(K\rho)^{4m} + O((K\rho)^6) \quad (21A)$$

and

$$R = 1 - \frac{\pi^2 n_1^{2m+2} n_2^{2m+2}}{(m-1)!^4 m^2 2^{4m-4}(n_2^2 - n_1^2)^2}(K\rho)^{4m} + O((K\rho)^{8m}). \quad (22A)$$

ACKNOWLEDGMENTS

This work was supported by the Russian Foundation for Basic Research and Scientific and Technical Program “Nanostructures.”

REFERENCES

1. M. Born and E. Wolf, *Principles of Optics* (Pergamon, Oxford, 1969; Nauka, Moscow 1973).
2. N. I. Kaliteevskiĭ, *Wave Optics* (Nauka, Moscow, 1971).
3. T. Egrogan and D. G. Hall, J. Appl. Phys. **68**, 1435 (1990).
4. D. Libilloy, H. Benisty, C. Weisbuch, *et al.*, Appl. Phys. Lett. **73**, 1314 (1998).
5. Y. Jiang and J. Hacker, Appl. Opt. **33**, 7431 (1994).
6. A. A. Tovar and G. H. Clark, J. Opt. Soc. Am. A **14**, 3333 (1997).
7. V. V. Nikolaev, M. A. Kaliteevskiĭ, and G. S. Sokolovskiĭ, Fiz. Tekh. Poluprovodn. (St. Petersburg) **33**, 174 (1999) [Semiconductors **33**, 147 (1999)].

Translated by I. Efimova

Technical Physics, Vol. 45, No. 7, 2000, pp. 870–877. Translated from Zhurnal Tekhnicheskoĭ Fiziki, Vol. 70, No. 7, 2000, pp. 57–64.

OPTICS, QUANTUM ELECTRONICS

Evolution of the Glow of an Aerogel Irradiated with a High-Power Pulse Electron Beam

B. A. Demidov, V. P. Efremov, M. V. Ivkin, I. A. Ivonin, V. A. Petrov, and V. E. Fortov

Russian Research Centre, Kurchatov Institute, pl. Kurchatova 1, Moscow, 123182 Russia

Received July 6, 1999

Abstract—The evolution of the glow of the energy-release zone in porous transparent aerogel, with a density of 0.03–0.25 g/cm^3, which is irradiated by a high-power pulse electron beam, is studied experimentally. In addition to a fast ($\tau \le \tau_{beam}$) and a luminescent ($\tau \approx 10^{-6}$ s) glow components, a slow glow component ($\tau \approx 2 \times 10^{-5}$ s) has been revealed. The appearance of this slow component is associated with an aerogel rarefaction wave and its destruction (cracking) arising after its isochoric bulk heating by electron radiation, which may occur due to an electrostatic field induced under irradiation. The discovered glow is utilized to visually determine the current position of the rarefaction wave front. The sound velocity measured as a function of the density of SiO_2 aerogels with porosities of 10–100 allowed us to experimentally determine the percolation parameter of the aerogel equation of state. © *2000 MAIK "Nauka/Interperiodica".*

INTRODUCTION

Porous condensed media are widely used to solve numerous important problems in science and technology. They are promising materials for damping short-term impact loads, are used as radiation converters on heavy-ion accelerators, and are included in targets for inertial thermonuclear fusion [1, 2].

Shock-induced compression of porous substances has long been used in shock-wave physics for constructing equations of state [3, 4]. The effects of intense energy fluxes on condensed substances are being investigated in many laboratories [5, 6], but the analysis of the action of pulse radiation fluxes on porous media is incomplete; the models for describing such media under isochoric heating and formation of shock waves under these conditions have not been considered.

The interaction of a high-power high-current pulse electron beam with a highly porous material (SiO_2 aerogels) was studied in [7–9]. In these experiments, the aerogel was a homogeneous medium, because the typical irradiation and rarefaction time was sufficient for the pressure in the aerogel structural elements to be equalized. In experiments performed in [10], the interaction of high-power pulse laser radiation with an "Agar-agar"-type ($C_{14}H_{18}O_7$) low-density porous substance (irregularly alternating cavities and particles of various shapes and normal solid-state density) was analyzed. Therefore, under pulse irradiation [10], "Agar-agar" is a heterogeneous medium. The absorption of intense radiation fluxes, energy transfer mechanisms, and hydrodynamic processes in homogeneous and heterogeneous porous media have specific features and are currently attractive to researchers [11, 12].

Upon impact compression of porous aerogels, the temperature behind the shock wave front with an amplitude of about 10 kbar is large enough to cause an intense glow. In this case, the glow front position virtually coincides with the position of the shock wave front, which is used for determining the shock adiabat of the weakly ionized plasma that appears [13]. However, the most interesting physical effects manifest themselves in studies of aerogels under pressures of 1 to 50 kbar, when aerogels preserve the features of their internal structure. In this loading range, an aerogel with a high optical transparency is able to emit light in the visible region under irradiation by an intense electron beam. This allows one to use convenient optical diagnostics for obtaining information on the equation of state of an aerogel with a porosity that changes several times under rarefaction [8]. A nonlinear self-consistent equation of state representing fractional properties of highly porous materials was modeled in precisely this way. In particular, this equation allowed one to calculate the velocities of the flying-apart irradiated and rear aerogel parts, which differ by two orders of magnitude, under irradiation with a high-power pulse electron beam [9].

The objective of this study is to analyze the glow evolution along the beam radius and into the depth of an aerogel irradiated by a high-power pulse electron beam, as well as to investigate the interaction of the electron beam with targets of complex configurations consisting of several aerogel layers of different densities.

This work also aims to study the sound velocity as a function of the density of porous SiO_2 aerogels with a porosity $\Pi = \rho_0/\rho - 1$ in a porosity range of 10–100 in order to directly verify the power dependence of the

1063-7842/00/4507-0870$20.00

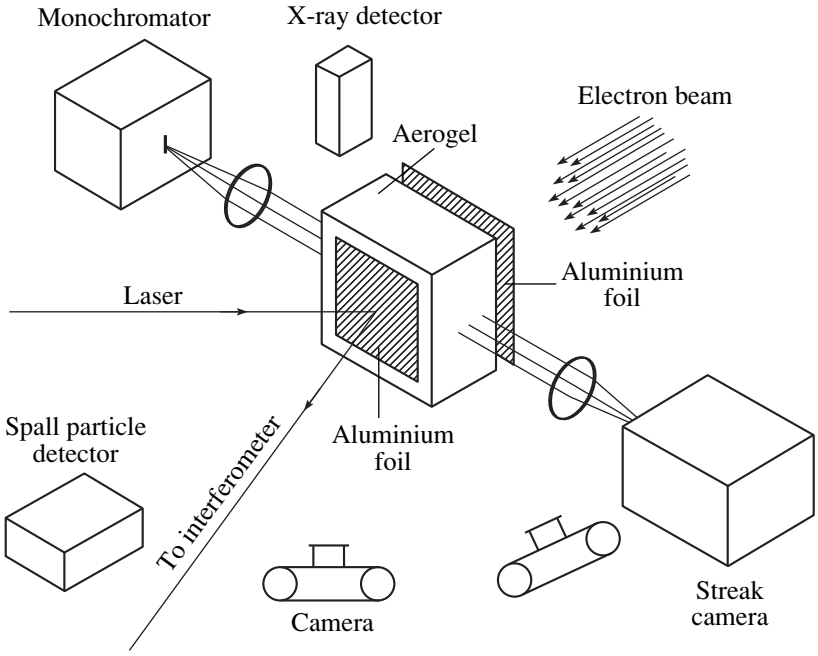

Fig. 1. Layout of the diagnostic equipment.

sound velocity in an aerogel on its porosity and to directly determine the percolation coefficient that can be used in the equation of the aerogel state [9].

EXPERIMENTAL CONDITIONS

The behavior of transparent porous SiO_2 aerogels with a density $\rho = 0.03$–0.25 g/cm^3 under fast isochoric heating was studied experimentally on the Kal'mar electron accelerator operating with the following parameters of the electron beam: the current is $I = 10$–15 kA, the electron energy is $U = 270$–300 keV, and the current pulse FWHM duration is $\tau = 150$ ns. Aerogel samples 5–34 mm thick with cross sections of 25–50 mm were exposed to the electron beam. The sample under study was placed in a vacuum chamber of the Kal'mar accelerator behind the anode foil. Figure 1 shows the arrangement of the diagnostic equipment.

An electron beam with an effective diameter of 11–12 mm passed through the 10-μm-thick aluminum foil (the accelerator anode) and hit the sample positioned immediately adjacent to the foil or at a 5-mm distance from it. A 10-μm-thick aluminum foil set up on the rear of the aerogel served to reflect a diagnostic laser beam. The following diagnostic devices were used: an FÉR-7 streak camera with slit scanning that allowed us to obtain a time-scanned aerogel glow intensity distribution in the radial and longitudinal directions; a differential laser interferometer (based on an LGN-215 laser) with an interference period of 26 m/s that records the time of arrival and mass velocity of a disturbance at the rear surface of the aerogel; an MDR-2 monochromator with a special cassette extending the range of the emission spectrum under study; a spall particle detector for measuring the velocity of split-off fragments by using the time-of-flight technique; an X-ray detector for registering the instant of the interaction between the electron beam and aerogel; and cameras for recording the trajectories of flying-away glowing fragments in the integral regime. The velocity of the elastic disturbance propagation in the aerogel was measured under modified experimental conditions. The anode aluminum foil was replaced by a 4.5-mm-thick stainless steel disk with a diameter of 90 mm, to which an aerogel sample was attached by a special holder. A pulse electron beam excited a short pressure pulse in the metallic anode, which was transmitted to the aerogel sample and propagated in it as an elastic disturbance. The instant at which this disturbance reached the free aerogel surface was recorded by a differential laser interferometer.

EXPERIMENTAL RESULTS

The time dependence of the aerogel glow along the radius is shown in Fig. 2 presenting photochronograms of the interaction process between the electron beam ($j = 15$ kA/cm^2, $U = 300$ keV) and aerogels of different densities. The entrance slit of the FÉR-7 streak camera was positioned perpendicular to the electron beam axis and, in both cases, was focused 2–3 cm from the irradiated sample surface.

The dynamics of electron beam interaction with layered aerogel targets is illustrated by the photochronograms in Fig. 3 (here, the FÉR-7 entrance slit is parallel to the electron beam axis). The photochronogram in Fig. 3a refers to the action of the electron beam ($j =$

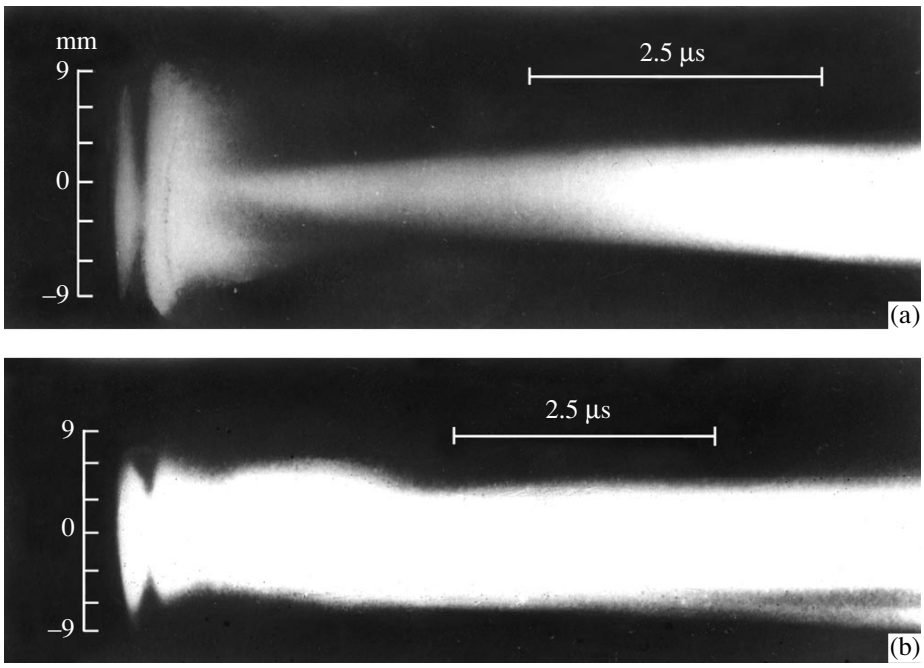

Fig. 2. Time-dependent aerogel glow along the radius of the zone of the electron-beam energy release; ρ = 0.25 (a), 0.034 (b) g/cm^3.

15 kA/cm^2, U = 300 keV) on a four-layer target with the following aerogel densities: ρ_1 = 0.08, ρ_2 = 0.15, ρ_3 = 0.05, and ρ_4 = 0.15 g/cm^3 with the corresponding thicknesses h_1 = 4, h_2 = 4, h_3 = 4, and h_4 = 3 mm. The layers are numbered from the front (irradiated) target surface.

Figure 3b shows a photochronogram for the interaction of the electron beam (with the same parameters) with a three-layer target at a faster scan. The target consists of the following aerogel layers: ρ_1 = 0.05 g/cm^3, h_1 = 10 mm; ρ_2 = 0.25 g/cm^3, h_2 = 2.5 mm; and ρ_3 = 0.05 g/cm^3, h_3 = 9 mm.

The photochronogram in Fig. 3c shows the interaction dynamics between the electron beam and a three-layer target, in which the first layer has the highest density (ρ_1 = 0.25 g/cm^3, h_1 = 5 mm; ρ_2 = 0.034 g/cm^3, h_2 = 10 mm; and ρ_3 = 0.25 g/cm^3, h_3 = 5 mm).

The studies performed with the MDR-2 monochromator have shown that the aerogel emission from the zone of the electron-beam energy release spans the entire visible spectrum region. For example, Fig. 4 shows a part of the emission spectrum for an aerogel with ρ = 0.034 g/cm^3 exposed to the electron beam (j = 10 kA/cm^2, U = 270 keV). The slit of the monochromator is adjusted to the region of the electron-beam energy release. The bright lines in the upper part of the spectrum are the reference lines of a mercury lamp.

The electron beam interacts with the aerogel and excites a shock wave with a velocity reaching 500–600 m/s in dense aerogels. Arriving at the free aerogel surface, the shock wave causes a spall destruction. Figure 5a shows aerogel samples with a density of 0.25 g/cm^3 with a cross section of 25 × 25 mm and an initial thickness of 22.5 mm after being exposed to the electron beam (j = 15 kA/cm^2, U = 300 keV). As a result of the separation of a split-off plate, the sample thickness decreased by 5 mm. For a low-intensity irradiation mode (j = 8 kA/cm^2, U = 250 keV), irreversible effects occur in the bulk of a similar aerogel sample, resulting in its turbidity. However, the spalling effect is absent (Fig. 5b) and the sample thickness remains unchanged.

The velocity of flying-apart fragments at constant parameters of the electron beam (j = 15 kA/cm^2, U = 290 keV) depends heavily on the aerogel thickness and density. For example, the velocity of spalled fragments of an aerogel sample with a density of 0.16 g/cm^3 changes from 500 m/s at a 5.5-mm sample thickness to 80 m/s at a 14.6-mm thickness.

Figure 6 shows a set of interferograms characterizing the propagation velocity of elastic disturbances in aerogels of various densities under the same parameters of the electron beam producing pressure pulses in the metallic anode of the accelerator. The densities of the aerogels under study were as follows: ρ_1 = 0.02, ρ_2 = 0.057, ρ_3 = 0.076, ρ_4 = 0.13, ρ_5 = 0.16, and ρ_6 = 0.25 g/cm^3. The sample thicknesses were h_1 = 22, h_2 = 34, h_3 = 30, h_4 = 18, h_5 = 25, and h_6 = 26 mm, respectively (*1–6* in Fig. 6).

The results of processing the interferograms are presented in Fig. 7 in the form of a plot of the propagation

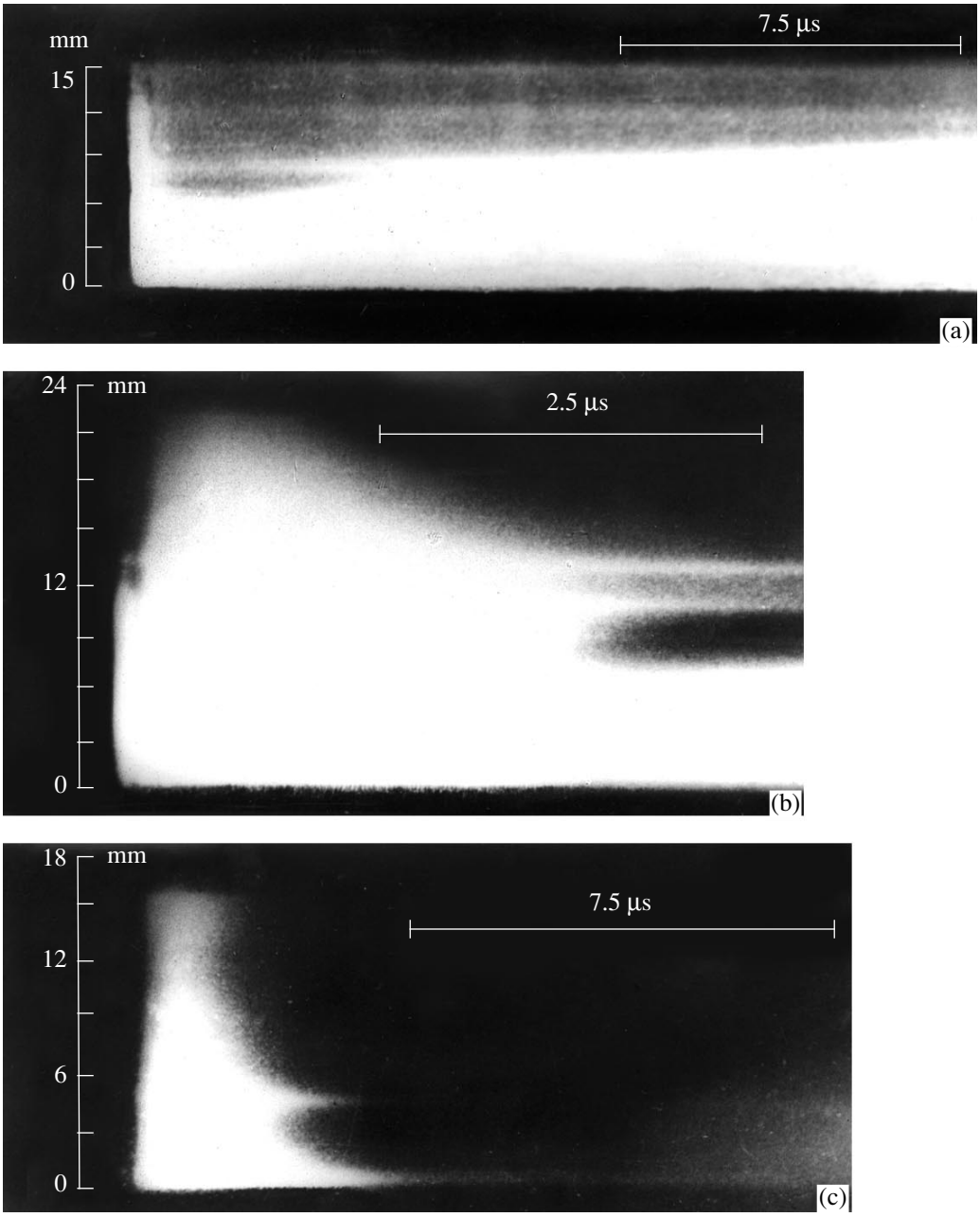

Fig. 3. Time-dependent aerogel glow along the depth of multilayer targets: (a) four-layer target and (b, c) three-layer target.

velocity of an elastic disturbance as a function of the aerogel density.

ANALYSIS OF EXPERIMENTAL RESULTS

The comparison of the photochronograms shown in Figs. 2a and 2b allows us to conclude that the aerogel density appreciably affects the character of the glow in the region of the electron-beam energy release. In contrast to Fig. 2b, three stages of the aerogel glow with significantly differing durations are clearly observed in Fig. 2a. The first glow stage lasts $\tau_1 \approx 10^{-7}$ s; and the durations of the second and third stages are 10^{-6} and 2×10^{-5} s, respectively. The duration of the first glow stage coincides with that of the electron-beam action, causing a glow through the excitation of aerogel atoms and molecules (mainly by secondary electrons) and subsequent reemission in the visible spectrum region [14, 15]. Changes in the intensity of this glow along the target radius show that the electron-beam current density decreases from the center to the periphery, making it possible to estimate the effective electron-beam diameter (11–12 mm).

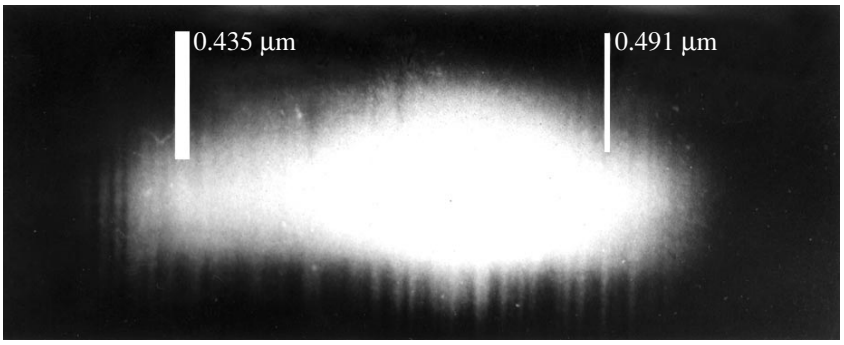

Fig. 4. Integrated spectrum of the glow in the blue-green wavelength region in the zone of the electron-beam energy release.

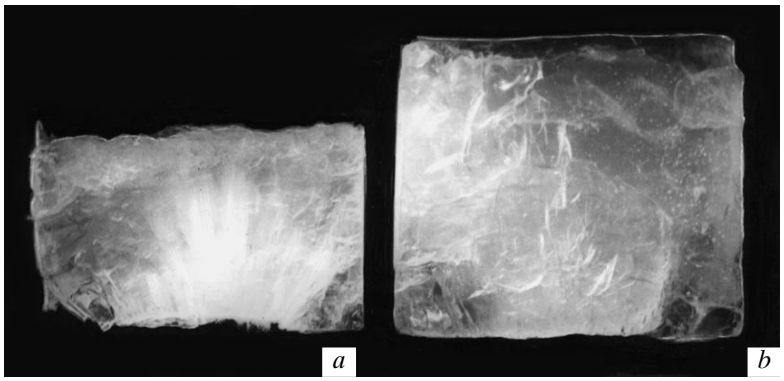

Fig. 5. Aerogel samples exposed to an electron beam: (a) high-intensity and (b) low-intensity irradiation modes.

The glow induced by the direct action of the electron beam on optically transparent dielectric media can be divided into two stages, taking into account the degree of its origin and decay delays. The first, most intense glow stage has virtually no time lag ($\tau \approx 10^{-12}$–10^{-10} s) and is directly associated with cascade cooling of high-energy secondary electrons with energies $\varepsilon \approx \varepsilon_g \approx 10$–$15$ keV. The second stage, with a time lag $\tau \leq 1$ μs, is determined by the slow relaxation of the excited atoms and molecules with excitation energies of about ε_g and is responsible for the luminescence effect.

The third stage of the aerogel glow revealed in our experiments has the longest time lag and is of the greatest interest. This glow propagates in the radial direction from the central region of the target to its periphery with a velocity of 500–550 m/s. The measured velocity is close to the maximum propagation velocity of the region with a glow duration $\tau \approx 20$ μs from the zone of the electron-beam energy release to deep into the target [9]. Hence, this glow coincides with the pattern of the aerogel dynamic rarefaction, with the mass compression wave propagating deep into the aerogel.

The high bulk electrization of the aerogel, which arises under its irradiation by a pulse electron beam, is evidently responsible for the appearance of the slow glow component. Experiments on recording the profile of the fast glow component in an aerogel with the initial density $\rho \leq 0.2$ g/cm^3 [8] have revealed a strong influence of the aerogel electrization on the formation of the zone of electron-beam energy release. In experiments with high-porosity aerogels, the internal electrostatic field reaches the maximum possible threshold field $E_{th} \approx$ 70–80 kV/cm for high-energy secondary electrons with energies of the order of the optical phonon energy $\varepsilon \approx (h\omega - \varepsilon_g)$. Therefore, a mass rarefaction wave propagating into the aerogel (≈1 cm) may lead to an increase in the electrostatic electron energy, with a subsequent excitation and reemission of atoms in the optical wavelength region.

When a highly porous aerogel was irradiated with an electron beam (Fig. 2b), the FÉR-7 entrance slit was adjusted to the beginning of the energy-release zone (in contrast to the experiment in Fig. 2a). Therefore, the aerogel rarefaction in the slit zone began immediately after termination of the irradiation, and no pronounced separation of the second and third glow stages was observed.

The photochronograms shown in Fig. 3 also confirm a great influence of the induced electrostatic field on the glow evolution during the interaction between the electron beam and the aerogel. Experiments with a depth-inhomogeneous aerogel directly point to the existence of internal rarefaction waves due to inhomogeneities causing a prolonged glow of the aerogels' interfaces,

which are clearly seen in Fig. 3. The glow duration of the aerogels' interfaces in Figs. 3a and 3b is longer than that of the interfaces in Fig. 3c. This is explained by the first layer in the layered targets in Figs. 3a and 3b being a highly porous aerogel, which ensures a higher electrization at the interface of aerogels and, correspondingly, a longer glow. Note that the difference in the interface glow durations for various layered targets shows only an insignificant contribution of the plasma in the accelerator diode chamber to the glow.

The integrated aerogel-emission spectrum presented in Fig. 4 is actually continuous. In the short-wavelength region, a system of bands typical of molecular spectra is observed. Fairly intense isolated Si lines, which could help diagnose macroscopic parameters of the aerogel, are absent. In order to extract quantitative information from spectroscopic data, further experimental and theoretical investigations are necessary.

Figure 5 shows spalling phenomena in porous media, which are nontrivial for such media. It is clear that such phenomena have a threshold effect that depends on the medium porosity.

Figure 7 shows a linear dependence of the propagation velocity of an elastic disturbance in the aerogel on its density. This velocity can be considered as the sound velocity C_s, at least for comparatively dense aerogels.

According to the cluster model of the equation of state for a porous medium [16], thermodynamic parameters depend on the density according to a power law. In particular, the sound velocity in the aerogel can be represented by the dependence $C_{si} = C_{sk}(\rho_i/\rho_k)^{(\gamma-1)/2}$, where ρ_i and ρ_k are the densities of different porous aerogel samples and γ is the percolation coefficient characterizing the aerogel structure. For porous metals, the power law for the sound velocity and the percolation coefficient were determined in [17]. The revealed linear dependence of the sound velocity in the aerogel on its density confirms a power dependence of the sound velocity in the aerogel on its porosity and allows us to directly determine the percolation coefficient, which was found to be equal to 3. The measured coefficient was close to the value $\gamma = 3.2$ utilized in [9] in the numerical hydrodynamic simulation of an aerogel exposed to intense irradiation.

NUMERICAL SIMULATION

In order to determine the induced electrization of highly porous aerogels, we numerically calculated the interaction of the electron beam from the Kal'mar accelerator with aerogels.

When an electron beam is absorbed by an aerogel, strong electric fields arise in it, leading to its breakdown and a charge flow from the volume of the energy-release zone to the aerogel surface. These electric fields may significantly distort the electron energy-release profile [8, 9]. To correctly determine the effect of these fields on the formation of the energy-release zone requires an allowance for the high-energy conductivity [14, 15] of dielectrics, which is brought about during the absorption of electron radiation.

The high-energy conductivity in wide-gap dielectrics is determined by the fact that, when electrons are

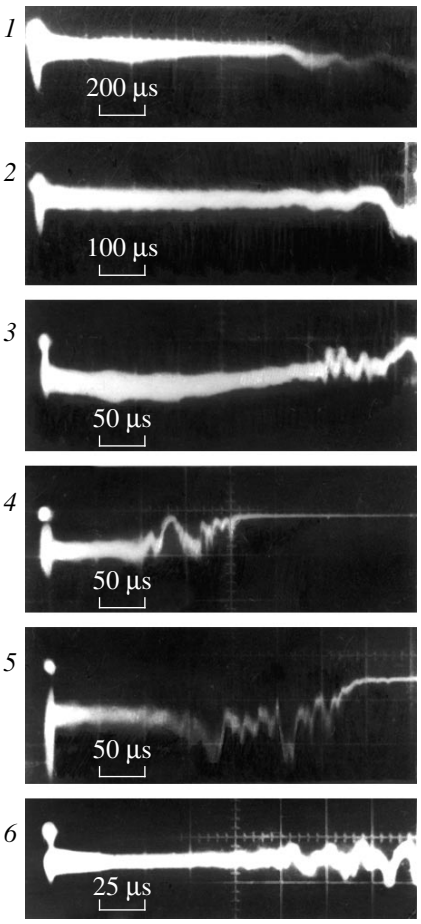

Fig. 6. Interferograms illustrating the propagation velocity of an elastic disturbance in aerogels of various densities.

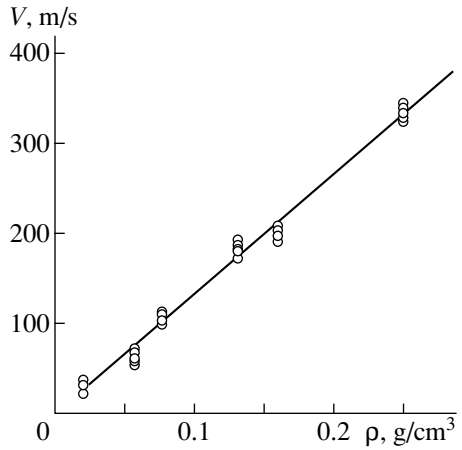

Fig. 7. Elastic disturbance velocity in an aerogel as a function of its density.

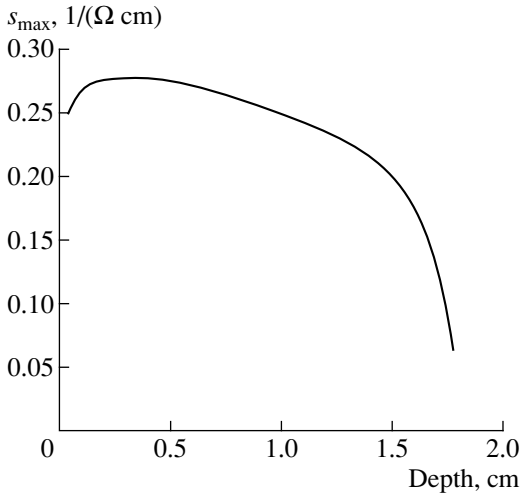

Fig. 8. Profile of the maximum induced conductivity during aerogel irradiation.

cooled to an energy $\varepsilon \approx 1.5\varepsilon_g$ of the order of magnitude of the forbidden zone $\varepsilon_g \approx$ 10–20 eV, the energy loss rate abruptly falls (by a factor of 1000), because it becomes impossible to continue exciting electrons from the forbidden zone to the conduction band. The main cooling channel [14, 15] for electrons with energies ε in a range $\{T, h\omega\} < \varepsilon < 1.5\varepsilon_g$ is the interaction with optical phonons and with electrons thermalized at the temperature T with the energy loss rates

$$Q_{d0} \approx \mu\omega_0 h\omega_0(\varepsilon/h\omega_0)^{1/2}$$

$$Q_T \approx \omega_0/\mu^5(N_T a^3)h\omega_0(h\omega_0/\varepsilon)^{1/2},$$

respectively.

Here, ω_0 is the optical phonon frequency; $(N_T a^3) \approx 10^{-11}W\{(x, t)T^{3/2}(x, t)\}^{1/2}$ is the number of thermalized electrons in an elementary cell a^3 determined by binary collisions; $W(x, t)$ [J/(cm^3 ns)] is the energy-release rate of the electron beam at a depth x and moment t; and $\mu = (m/M)^{1/4} \approx 0.1$ is the series expansion parameter [15]. The electron heating power in the induced electrostatic field E in the prebreakdown regime is evaluated as

$$Q_E \approx eE(2e/m_e)^{1/2},$$

where m_e is the electron mass.

With further electron cooling, $\varepsilon < h\omega_0$, the emission of optical phonons becomes impossible and only the interaction of electrons with acoustic phonons and traps (defects of the crystal lattice) is efficient. The latter effect depends heavily on the dielectric features and determines the slow charge relaxation after the irradiation is completed [14, 15]. Since the experimentally measured time lag of the slow glow component in the aerogel is rather large, we neglect this low-energy conductivity.

Thus, the high-energy conductivity is

$$\sigma \approx \frac{e^2}{m_e}\int_{\max\{T,\,\eta\omega_0\}}^{1.5\varepsilon_g} F(\varepsilon)\tau_\perp(\varepsilon)d\varepsilon,$$

where $\tau_\perp \approx \tau_{d0} \approx \mu\omega_0(T/\eta\omega_0)(\varepsilon/\eta\omega_0)^{1/2}$ is the relaxation time of an electron pulse and $F(\varepsilon)$ is the nonequilibrium distribution function for high-energy electrons, which can be estimated from the energy balance

$$\{Q_{d0}(\varepsilon) + Q_T(\varepsilon) - Q_E(\varepsilon)\}F(\varepsilon) = G(x, t)[1 - (\varepsilon/1.5\varepsilon_g)^{3/2}],$$

where $G(x, t) \approx W(x, t)/1.5\varepsilon_g$ is the volumetric generation rate for high-energy electrons and the expression in the square brackets approximately describes the density of energy states.

The $F(\varepsilon)$ singularity (zeroing of the expression in the braces) corresponds to the high-energy breakdown that develops at the breakdown field E_{br} [8],

$$E_{\rm br} \approx \mu(\omega_0/e)(m_e\eta\omega_0)^{1/2}[1 + (\eta\omega_0/\varepsilon^*)^{1/2} \times (N_T a^3/\mu^6)]/(1 + \Pi)^{1/3} \le 200/(1 + \Pi)^{1/3}\ [\text{kV/cm}],$$

which is several orders of magnitude lower than the equilibrium value. Here, we take into account that $(\varepsilon^*/\eta\omega_0) < (\varepsilon_g/\eta\omega_0) \approx \mu^{-2}$ and $(1 + \Pi)^{1/3}$ is the correction for the material porosity (discontinuity) Π.

The specific energy release of the electron beam as a function of the Lagrangian coordinate of the absorption depth and irradiation time was calculated in the diffusion approximation [18] taking into account the quasistationary generation of electric fields, as well as actual oscillograms of the current and voltage of the Kal'mar accelerator and the dependence of the electron path depth on the electron energy taken from [19].

Numerical calculations have shown that, at an irradiation power J_0 = 15 kA/cm^2, U = 300 keV, the high-energy breakdown intensity $E_{\rm br}$ = (70–80) kV/cm is reached at the moment of termination of the irradiation in almost the entire energy-release zone. In highly porous aerogels with a depth $R \approx 2$ cm of the energy-release zone, the electrostatic energy becomes comparable with the energy of primary electrons, thus strongly affecting the formation of the energy-release zone [8, 9] in an aerogel with a density of 0.03 g/cm^3. The calculated profile of the maximum conductivity, which is induced during irradiation, corresponding to this regime is shown in Fig. 8.

CONCLUSIONS

(1) The spatial glow of an aerogel irradiated by a high-intensity pulse electron beam is studied experimentally.

(2) Along with the classical glow of a transparent dielectric medium exposed to an electron beam, a slow glow component ($\approx 2 \times 10^{-5}$ s) is revealed, which coincides with the pattern of dynamic aerogel rarefaction—with a compression wave propagating deep into the aerogel.

(3) The origin of the slow glow component is evidently due to the significant volumetric electrization of a highly porous aerogel arising under its irradiation by an electron beam.

(4) Experiments with layered targets have confirmed the existence of internal rarefaction waves from aerogel inhomogeneities.

(5) Direct experiments have confirmed a power dependence of the sound velocity in the aerogel on its density and helped determine the percolation coefficient, the value of which ($\gamma = 3$) agrees satisfactorily with the value $\gamma = 3.2$ utilized in previous calculations.

ACKNOWLEDGMENTS

We are grateful to the staff members at the Institute of Catalysis (Russian Academy of Sciences, Novosibirsk) for helping us prepare aerogel samples and to B.A. Bryunetkin for helping us record the optical spectrum of the aerogel emission.

This work was supported by the Russian Foundation for Basic Research, project no. 97-02-16729a.

REFERENCES

1. M. Burchell and R. Thomson, Bull. Am. Phys. Soc. **40**, 1409 (1995).
2. G. Yu. Gus'kov, N. V. Zmitrenko, and V. G. Rozanov, Pis'ma Zh. Éksp. Teor. Fiz. **108**, 548 (1995) [JETP **81**, 296 (1995)].
3. Ya. B. Zel'dovich and Yu. P. Raizer, *Physics of Shock Waves and High-Temperature Hydrodynamic Phenomena* (Nauka, Moscow, 1966, 2nd ed.; Academic, New York, 1966, 1967).
4. A. I. Funtikov, Teplofiz. Vys. Temp. **36**, 405 (1998).
5. G. I. Kanel', S. V. Razorenov, A. V. Utkin, and V. E. Fortov, *Impact–Wave Phenomena in Condensed Media* (Yanus-K, Moscow, 1996).
6. I. I. Zalyubovskiĭ, A. I. Kalinichenko, and V. T. Lazurik, *Introduction to Radiation Acoustics* (Vishcha Shkola, Kharkov, 1986).
7. B. A. Demidov, V. P. Efremov, I. A. Ivonin, *et al.*, Zh. Tekh. Fiz. **67** (11), 19 (1997) [Tech. Phys. **42**, 1258 (1997)].
8. B. A. Demidov, V. P. Efremov, I. A. Ivonin, *et al.*, Zh. Tekh. Fiz. **68** (10), 112 (1998) [Tech. Phys. **43**, 1239 (1998)].
9. B. A. Demidov, V. P. Efremov, I. A. Ivonin, *et al.*, Zh. Tekh. Fiz. **69** (12), 18 (1999) [Tech. Phys. **44**, 1413 (1999)].
10. A. É. Bugrov, I. N. Burdonskiĭ, V. V. Gavrilov, *et al.*, Zh. Éksp. Teor. Fiz. **111**, 903 (1997) [JETP **84**, 497 (1997)].
11. J. Lindl, Phys. Plasmas **2**, 3933 (1995).
12. G. Yu. Gus'kov, N. V. Zmitrenko, and V. G. Rozanov, Pis'ma Zh. Éksp. Teor. Fiz. **66**, 521 (1997) [JETP Lett. **66**, 555 (1997)].
13. V. E. Fortov, A. S. Filimonov, V. K. Gryaznov, *et al.*, in *Proceedings of the International Conference on Physics of Strong Coupled Plasmas*, Ed. by W. D. Kraft (World Scientific, Singapore, 1996), pp. 317–321.
14. D. I. Vaĭsburd, *High-Energy Solid-State Electronics* (Novosibirsk, 1982).
15. V. F. Gantmakher and I. B. Levinson, *Scattering of Current Carriers in Metals and Semiconductors* (Nauka, Moscow, 1984).
16. I. M. Sokolov, Usp. Fiz. Nauk **150** (2), 221 (1986) [Sov. Phys. Usp. **29**, 924 (1986)].
17. Yu. A. Krysanov and S. A. Novikov, Prikl. Mekh. Tekh. Fiz., No. 6, 57 (198).
18. K. Kanaya and S. Okadama, J. Phys. D **5** (1), 43 (1972).
19. V. F. Baranov, *Electron Radiation Dosimetry* (Atomizdat, Moscow, 1974).

Translated by A. Seferov

Technical Physics, Vol. 45, No. 7, 2000, pp. 878–882. Translated from Zhurnal Tekhnicheskoĭ Fiziki, Vol. 70, No. 7, 2000, pp. 65–69.

On the Theory of Space–Time Polarization Holography

B. N. Kilosanidze and E. Sh. Kakichashvili

Institute of Cybernetics, Academy of Sciences of Georgia, Tbilisi, 380086 Georgia

Received July 26, 1999

Abstract—Polarization holographic recording and the reconstruction of the field of a nonstationary object wave are considered theoretically. Expressions for the nondiffracted beam, as well as the virtual and real images, formed by a space–time polarization hologram are analyzed. It is shown that, under certain conditions imposed on the isotropic, anisotropic, and gyrotropic responses of a polarization-sensitive medium, one can adequately reconstruct the space structure, time waveform, and polarization characteristics of the field of a nonstationary object in the virtual image. *© 2000 MAIK "Nauka/Interperiodica".*

Recently evolved so-called time holography, extending the holographic method to recording and reconstructing the time behavior of nonstationary wave processes, has attracted considerable interest. This direction represents a great heuristic contribution to completing the construction of holography fundamentals [1, 2]. The concept of holographic recording and reconstruction of nonstationary wave fields was first put forward in [3]. It is based on the unambiguous relation between the time waveform of a nonstationary process and its frequency spectrum [4, 5]. A rigorous theoretical substantiation of space–time holography for the scalar description of nonstationary waves was given in [6].

In this work, the developed theoretical approach is extended to the case when the state and degree of polarization of nonstationary electromagnetic wave fields are treated rigorously. Earlier, in order to prove the feasibility of recording and reconstructing the state and degree of polarization of arbitrary electromagnetic waves, the holographic method was modified for stationary wave fields [7–9].

We represent the field from a nonstationary object in the paraxial approximation of the Kirchhoff vector diffraction integral modified for the case of nonstationary wave fields [10]:

$$\mathbf{E}_{\text{ob}}(x, y, z, \omega, t) \approx \frac{i}{2\pi c}\int\limits_{S_0}\int\limits_{T_0}\frac{\omega}{r}\mathbf{E}_{\text{ob}}(x_0, y_0, z_0, t_0) \times \exp i\omega\left[(t-t_0)-\frac{1}{c}r\right]dt_0 dS_0, \quad (1)$$

where c is the velocity of light; ω is the frequency; (x_0, y_0, z_0, t_0) and (x, y, z, t) are the space and time coordinates of object and observation points, respectively; r is the distance between these points; S_0 and T_0 are the space and time intervals occupied by the object; and $dS_0 = dx_0 dy_0$.

In (1), $\mathbf{E}_{\text{ob}}(x_0, y_0, z_0, t_0)$ is the field immediately behind the object. It is formed when a totally polarized monochromatic wave of frequency ω_0 with the Jones vector [11]

$$\mathbf{E}_0 = \hat{E}_{0x}\exp-\frac{i\omega_0 z}{c}\begin{pmatrix}1\\ i\varepsilon\end{pmatrix}, \quad 0 \le \varepsilon = \frac{E_{0y}}{E_{0x}} \le 1 \quad (2)$$

propagates along the z axis through a nonstationary object with the Jones matrix [11]

$$M_{\text{ob}}(x_0, y_0, z_0, t_0) = \begin{pmatrix}\hat{m}_{11}(x_0, y_0, z_0, t_0) & \hat{m}_{12}(x_0, y_0, z_0, t_0)\\ \hat{m}_{21}(x_0, y_0, z_0, t_0) & \hat{m}_{22}(x_0, y_0, z_0, t_0)\end{pmatrix}.$$

In the following, the properties of the nonstationary object are assumed to be independent of the frequency of illuminating light; that is, $\hat{m}_{ij}(x_0, y_0, z_0, t_0) \neq f(\omega_0)$. Such a limitation, not being fundamental, makes it possible to substantially simplify subsequent calculations. Clearly, for actual media, the condition of object independence of the light frequency is an approximation similar to the "black screen" approximation used in [12, 13].

The nonstationary object depolarizes the illuminating monochromatic wave, which is assumed to be initially totally polarized. In the general case, the wave transmitted through the object is partially elliptically polarized. The modified Jones vector for the transmitted wave immediately behind the object can be represented in the form of partially coherent elliptically polarized orthogonal components [14]:

$$\mathbf{E}_{\text{ob}}(x_0, y_0, z_0, t_0) = \left[\hat{E}_{Ax}M_{\text{ob}}(x_0, y_0, z_0, t_0)\begin{pmatrix}1\\ i\varepsilon\end{pmatrix} \oplus \hat{E}_{By}M_{\text{ob}}(x_0, y_0, z_0, t_0)\begin{pmatrix}i\varepsilon\\ 1\end{pmatrix}\right]\exp i\omega t_0, \quad (3)$$

where $\varepsilon = E_{Ay}/E_{Ax} = E_{Bx}/E_{By}$; $0 \le \varepsilon \le 1$; $\oplus$ is the symbol designating noncoherent summation of amplitudes (it was introduced in [14], where the Jones vector–matrix method was formally extended to partially polarized light); $\hat{E}_A$ is the complex amplitude of a component of basis A; and $\hat{E}_B$ is the complex amplitude of a component of basis B orthogonal and noncoherent to basis A.

For the reference illuminating wave, we use a wave passed through an infinitely narrow time gate with a δ-shaped transmission. It is known that the interruption of a wave train changes the wave frequency: an initially monochromatic train becomes nonmonochromatic after passing the gate. In this case, according to the definition of the δ function, the passed wave has a continuous spectrum, with the spectral density constant over the entire frequency range [15]. In addition, the gate totally depolarizes an initially polarized wave. Then, the modified Jones vector of the reference wave can be represented as an orthogonal basis of elliptically polarized components [14]:

$$\mathbf{E}_{\text{or}} = \left[E_{0x}\exp i\varphi\begin{pmatrix}1\\ i\varepsilon\end{pmatrix} \oplus E_{0x}\exp i\left(\Psi-\frac{\pi}{2}\right)\begin{pmatrix}i\varepsilon\\ 1\end{pmatrix}\right] \times \exp i\omega\left(t-\frac{1}{c}z\right) \tag{4}$$

where $\varepsilon = E_{0y}/E_{0x}$ and E_{0x}, E_{0y} and φ, Ψ are the respective amplitudes and initial phases of two mutually noncoherent components.

In polarization holographic recording, mutually coherent components of the orthogonal basis of the reference and object waves independently interfere with each other at corresponding frequencies and the resulting fields are summed up noncoherently (additively). The net field in the hologram plane has the form

$$\begin{aligned}\mathbf{E}_\Sigma(x, y, z, t) = \mathbf{E}_{\text{or}} + \mathbf{E}_{\text{ob}} = &\left\{E_{0x}\exp i\varphi\exp i\omega\left(t-\frac{1}{c}z\right)\right.\\ &+\frac{i}{2\pi c}\int\!\!\int_{S_0T_0}\frac{\omega}{r}\hat{E}_{Ax}M_{\text{ob}}(x_0, y_0, z_0, t_0)\\ &\left.\times\exp i\omega\left[(t-t_0)-\frac{1}{c}r\right]dS_0dt_0\right\}\begin{pmatrix}1\\ i\varepsilon\end{pmatrix}\\ &\oplus\left\{E_{0x}\exp i\left(\Psi-\frac{\pi}{2}\right)\exp i\omega\left(t-\frac{1}{c}z\right)\right.\\ &+\frac{i}{2\pi c}\int\!\!\int_{S_0T_0}\frac{\omega}{r}\hat{E}_{By}M_{\text{ob}}(x_0, y_0, z_0, t_0)\\ &\left.\times\exp i\omega\left[(t-t_0)-\frac{1}{c}r\right]dS_0dt_0\right\}\begin{pmatrix}i\varepsilon\\ 1\end{pmatrix}.\end{aligned} \tag{5}$$

The intensity of the electric vector of the net wave is described by the real part of expression (5) [16]:

$$\mathrm{Re}(\mathbf{E}_\Sigma) = \mathbf{p}\cos\omega t + \mathbf{q}\sin\omega t, \tag{6}$$

where the parameters $\mathbf{p}$ and $\mathbf{q}$ of the net ellipse are determined in terms of polarization ellipse components for the bases A and B according to the rules [14]

$$\begin{aligned}\mathbf{p} &= \mathrm{Re}(\mathbf{E}_\Sigma)_A \oplus \mathrm{Re}(\mathbf{E}_\Sigma)_B = \mathbf{p}_A \oplus \mathbf{p}_B,\\ \mathbf{q} &= \mathrm{Im}(\mathbf{E}_\Sigma)_A \oplus \mathrm{Im}(\mathbf{E}_\Sigma)_B = \mathbf{q}_A \oplus \mathbf{q}_B.\end{aligned} \tag{7}$$

In order to record net wave (5), we use a polarization-sensitive medium [17, 18]. We assume that both the recording medium and the nonstationary object are spectrum-nonselective in the entire frequency range.

The photoanisotropy and photogyrotropy induced in the photosensitive recording medium are related to the polarization characteristics of the inducing light via the relationship obtained in [19, 20]. This relationship contains complex coefficients of the light-induced elliptical birefringence; and the vector photoresponse of the polarization-sensitive medium is described by the functions of isotropic, $\hat{s}$, anisotropic, $\hat{\nu}_L$, and gyrotropic, $\hat{\nu}_G$ responses. In our work, we assume that the functions $\hat{s}$, $\hat{\nu}_L$, and $\hat{\nu}_G$ do not depend on the frequency of incident radiation.

The light-induced anisotropy and gyrotropy of the polarization-sensitive medium can be described by Jones matrices [8, 11]. In [20], rules of constructing the Jones matrix for a polarization-sensitive medium were formulated for the case of partially polarized inducing radiation. With these rules and the relationship obtained in [20], we come to the resulting expression for the Jones matrix:

$$M = \exp(-2i\kappa d\hat{n}_0)\begin{pmatrix}M_{11} & M_{12}\\ M_{21} & M_{22}\end{pmatrix}, \tag{8}$$

where

$$\begin{aligned}M_{11,22} &= 1-\frac{i\kappa d}{2\hat{n}_0}[\hat{s}(I_1+I_2)_A + \hat{s}(I_1+I_2)_B\\ &\pm\hat{\nu}_L\cos 2\Theta_A(I_1-I_2)_A \pm \hat{\nu}_L\cos 2\Theta_B(I_1-I_2)_B],\\ M_{12,21} &= -\frac{i\kappa d}{2\hat{n}_0}[\hat{\nu}_L\sin 2\Theta_A(I_1-I_2)_A\\ &+\hat{\nu}_L\sin 2\Theta_B(I_1-I_2)_B \mp i\hat{\nu}_G(I_\pm - I_\mp)_A\\ &\mp i\hat{\nu}_G(I_\pm - I_\mp)_B].\end{aligned}$$

In formula (8), $\kappa = 2\pi/\lambda$; λ is the wavelength of the initial illuminating wave; d is the thickness of the recording medium; $\hat{n}_0$ is the complex refractive index

of the medium in the initial (unilluminated) state; $(I_1 + I_2)_A$ and $(I_1 + I_2)_B$ are the first Stokes parameters, $(I_1 - I_2)_A$ and $(I_1 - I_2)_B$ are the second Stokes parameters, and $(I_\pm - I_\mp)_A$ and $(I_\pm - I_\mp)_B$ are the fourth Stokes parameters for A and B components, respectively; and Θ_A and Θ_B are the orientation angles (measured counterclockwise from the x axis) of the major axis of the polarization ellipse for A and B components, respectively.

Expressing the Stokes parameters appearing in (8) in terms of the parameters $\mathbf{p}_A$, $\mathbf{p}_B$, $\mathbf{q}_A$, and $\mathbf{q}_B$ [8], we obtain the formula for the holographic matrix represented as the sum of three matrices in the entire frequency range:

$$M = M_0 + M_{-1} + M_{+1}. \tag{9}$$

Here, M_0 is the matrix responsible for the undiffracted beam,

$$M_0 \approx \exp(-2i\kappa d\hat{n}_0)\left[1 - \frac{i\kappa d\hat{s}}{\hat{n}_0}(1+\varepsilon^2)E_{0x}^2\right]\begin{pmatrix} 1 & 0 \\ 0 & 1 \end{pmatrix}; \tag{10}$$

M_{-1} is the matrix responsible for the virtual image,

$$M_{-1} \approx \frac{\kappa d}{4\pi c\hat{n}_0}\exp(-2i\kappa d\hat{n}_0)\begin{pmatrix} (M_{-1})_{11} & (M_{-1})_{12} \\ (M_{-1})_{21} & (M_{-1})_{22} \end{pmatrix} \tag{11}$$

with matrix elements

$$(M_{-1})_{11,22} = \iiint\limits_{S_0 T_0 \Omega}\frac{\omega}{r}\{\hat{E}_{Ax}[(\hat{s} \pm \hat{v}_L)(\hat{m}_{11} + i\varepsilon\hat{m}_{12}) - i\varepsilon(\hat{s} \mp \hat{v}_L)(\hat{m}_{21} + i\varepsilon\hat{m}_{22})]E_{0x}\exp -i\varphi + \hat{E}_{By} \times [(\hat{s} \mp \hat{v}_L)(\hat{m}_{22} + i\varepsilon\hat{m}_{21}) - i\varepsilon(\hat{s} \pm \hat{v}_L)(\hat{m}_{12} + i\varepsilon\hat{m}_{11})] \times E_{0x}\exp -i\left(\Psi - \frac{\pi}{2}\right)\Big\}\exp i\frac{\omega}{c}z \times \exp -i\omega\left(t_0 + \frac{1}{c}r\right)d\omega dt_0 dS_0,$$

$$(M_{-1})_{12,21} = \iiint\limits_{S_0 T_0 \Omega}\frac{\omega}{r}\{\hat{E}_{Ax}[(\hat{v}_L \pm \hat{v}_G)(\hat{m}_{21} + i\varepsilon\hat{m}_{22}) - i\varepsilon(\hat{v}_L \mp \hat{v}_G)(\hat{m}_{11} + i\varepsilon\hat{m}_{12})]E_{0x}\exp -i\varphi + \hat{E}_{By} \times [(\hat{v}_L \mp \hat{v}_G)(\hat{m}_{12} + i\varepsilon\hat{m}_{11}) - i\varepsilon(\hat{v}_L \pm \hat{v}_G)(\hat{m}_{22} + i\varepsilon\hat{m}_{21})]E_{0x}\exp -i\left(\Psi - \frac{\pi}{2}\right)\Big\} \times \exp i\frac{\omega}{c}z\exp -i\omega\left(t_0 + \frac{1}{c}r\right)d\omega dt_0 dS_0;$$

and M_{+1} is the matrix responsible for the real image,

$$M_{+1} \approx -\frac{\kappa d}{4\pi c\hat{n}_0}\exp(-2i\kappa d\hat{n}_0)\begin{pmatrix} (M_{+1})_{11} & (M_{+1})_{12} \\ (M_{+1})_{21} & (M_{+1})_{22} \end{pmatrix} \tag{12}$$

with matrix elements

$$(M_{+1})_{11,22} = \iiint\limits_{S_0 T_0 \Omega}\frac{\omega}{r}\Big\{\hat{E}_{Ax}^*[(\hat{s} \pm \hat{v}_L)(\hat{m}_{11}^* - i\varepsilon\hat{m}_{12}^*) + i\varepsilon(\hat{s} \mp \hat{v}_L)(\hat{m}_{21}^* - i\varepsilon\hat{m}_{22}^*)]E_{0x}\exp i\varphi + \hat{E}_{By}^* \times [(\hat{s} \mp \hat{v}_L)(\hat{m}_{22}^* - i\varepsilon\hat{m}_{21}^*) + i\varepsilon(\hat{s} \pm \hat{v}_L)(\hat{m}_{12}^* - i\varepsilon\hat{m}_{11}^*)] \times E_{0x}\exp i\left(\Psi - \frac{\pi}{2}\right)\Big\}\exp -i\frac{\omega}{c}z\exp i\omega\left(t_0 + \frac{1}{c}r\right) \times d\omega dt_0 dS_0,$$

$$(M_{+1})_{12,21} = \iiint\limits_{S_0 T_0 \Omega}\frac{\omega}{r}\Big\{\hat{E}_{Ax}^*[(\hat{v}_L \pm \hat{v}_G)(\hat{m}_{21}^* - i\varepsilon\hat{m}_{22}^*) + i\varepsilon(\hat{v}_L \pm \hat{v}_G)(\hat{m}_{11}^* - i\varepsilon\hat{m}_{12}^*)]E_{0x}\exp i\varphi + \hat{E}_{By}^* \times [(\hat{v}_L \pm \hat{v}_G)(\hat{m}_{12}^* - i\varepsilon\hat{m}_{11}) + i\varepsilon(\hat{v}_L \mp \hat{v}_G)(\hat{m}_{22}^* - i\varepsilon\hat{m}_{21}^*)]E_{0x}\exp i\left(\Psi - \frac{\pi}{2}\right)\Big\} \times \exp -i\frac{\omega}{c}z\exp i\omega\left(t_0 + \frac{1}{c}r\right)d\omega dt_0 dS_0.$$

In the above formulas, $\hat{m}_{ij} \equiv \hat{m}_{ij}(x_0, y_0, z_0, t_0)$ are the coordinate- and time-dependent elements of the two-dimensional matrix of the nonstationary object. In this work, we do not analyze convolutions. Under certain relationships between the response functions, namely, for

$$\hat{s} = \hat{v}_L, \quad \hat{v}_L = -\hat{v}_G, \tag{13}$$

expressions (11) and (12) are simplified. It should be noted that conditions (13) are satisfied with a high accuracy for many polarization-sensitive media [8].

Then the matrices M_{-1} and M_{+1} are given by

$$M_{-1} \approx \frac{\kappa d\hat{v}_L}{2\pi c\hat{n}_0}\exp(-2i\kappa d\hat{n}_0)\iiint\limits_{S_0 T_0 \Omega}\frac{\omega}{r}M_{ob}P \times \exp -i\omega\left[t_0 + \frac{1}{c}(r - z)\right]d\omega dt_0 dS_0, \tag{14}$$

$$M_{+1} \approx -\frac{\kappa d\hat{\nu}_L}{2\pi c\hat{n}_0}\exp(-2i\kappa d\hat{n}_0)\int\limits_{S_0T_0\Omega}\int\int\frac{\omega}{r}P^*M_{\text{ob}}^* \times \exp i\omega\left[t_0+\frac{1}{c}(r-z)\right]d\omega dt_0 dS_0. \quad (15)$$

Expressions (14) and (15) involve the object matrix M_{ob} and matrix P, which is

$$P = \begin{pmatrix} \hat{a}+\varepsilon^2\hat{b} & -i\varepsilon(\hat{a}-\hat{b}) \\ i\varepsilon(\hat{a}-\hat{b}) & \varepsilon^2\hat{a}+\hat{b} \end{pmatrix},$$

where

$$\hat{a} = \hat{E}_{Ax}E_{0x}\exp -i\varphi, \quad \hat{b} = \hat{E}_{By}E_{0x}\exp -i\left(\Psi-\frac{\pi}{2}\right)$$

and P^* and M_{ob}^* are Hermitian conjugates.

Let us illuminate the obtained hologram by a reconstructing nonpolarized wave with complex amplitudes $E'_{0x}\exp i\varphi'$ and $E_{0y}\exp i\Psi'$ ($\varepsilon' = E'_{0y}/E'_{0x}$) and a frequency ω':

$$\mathbf{E}_{\text{rec}} = \left[E'_{0x}\exp i\varphi'\begin{pmatrix}1\\ i\varepsilon'\end{pmatrix} \oplus E'_{0x}\exp i\left(\Psi'-\frac{\pi}{2}\right)\begin{pmatrix}i\varepsilon'\\ 1\end{pmatrix}\right] \times \exp i\omega'\left(t'-\frac{1}{c}z\right). \quad (16)$$

The transmitted wave takes the form

$$\mathbf{E}(x', y', z', t') = \frac{i}{2\pi c}\int\limits_S\frac{\omega'}{r'}M\mathbf{E}_{\text{rec}}\exp -i\frac{\omega'}{c}r'dS, \quad (17)$$

where S is the hologram area and r' is the distance between a point on the hologram surface and the observation point.

Sequentially substituting expressions (10), (14), and (15) into formula (17), we determine the nondiffracted beam and the virtual and real images formed by the hologram. Now it is necessary to determine which wave should be used to reconstruct the object field in the virtual image. Evidently, this requires the determination of the eigenvectors (and their related eigenvalues) of the matrix P. It has been found that, correct to a constant factor, the eigenvectors of the matrix P are $\begin{pmatrix}1\\ i\varepsilon\end{pmatrix}$ and $\begin{pmatrix}i\varepsilon\\ 1\end{pmatrix}$ and the eigenvalues are $(1+\varepsilon^2)\hat{a}$ and $(1+\varepsilon^2)\hat{b}$. This implies that the reconstructing wave should be identical to the reference wave used in recording.

For the nondiffracted wave, we obtain

$$\mathbf{E}_0 \approx \exp(-2i\kappa d\hat{n}_0)\left[1-\frac{i\kappa d\hat{s}}{\hat{n}_0}(1+\varepsilon^2)E_{0x}^2\right] \times \left[E_{0x}\exp i\varphi\begin{pmatrix}1\\ i\varepsilon\end{pmatrix} \oplus E_{0x}\exp i\left(\Psi-\frac{\pi}{2}\right)\begin{pmatrix}i\varepsilon\\ 1\end{pmatrix}\right] \times \exp i\omega\left(t'-\frac{1}{c}z'\right), \quad (18)$$

and the virtual and real images are given, respectively, by

$$\mathbf{E}_{-1}(x', y', z', t') \approx \frac{i\kappa d\hat{\nu}_L}{(2\pi c)^2\hat{n}_0}\exp(-2i\kappa d\hat{n}_0)E_{0x}^2(1+\varepsilon^2) \times \int\limits_{SS_0T_0\Omega}\int\int\int\int\frac{\omega^2}{r'r}\left[\hat{E}_{Ax}M_{\text{ob}}(x_0, y_0, z_0, t_0)\begin{pmatrix}1\\ i\varepsilon\end{pmatrix} \oplus \hat{E}_{By}M_{\text{ob}}(x_0, y_0, z_0, t_0)\begin{pmatrix}i\varepsilon\\ 1\end{pmatrix}\right]\exp i\omega \times \left[(t'-t_0)-\frac{1}{c}(r'+r)\right]d\omega dt_0 dS_0 dS \quad (19)$$

and

$$\mathbf{E}_{+1}(x', y', z', t') \approx -\frac{i\kappa d\hat{\nu}_L}{(2\pi c)^2\hat{n}_0}\exp(-2i\kappa d\hat{n}_0)E_{0x}^2 \times \int\limits_{SS_0T_0\Omega}\int\int\int\int\frac{\omega^2}{r'r}\left[P_A^*M_{\text{ob}}^*(x_0, y_0, z_0, t_0)\begin{pmatrix}1\\ i\varepsilon\end{pmatrix} \oplus P_B^*M_{\text{ob}}^*(x_0, y_0, z_0, t_0)\begin{pmatrix}i\varepsilon\\ 1\end{pmatrix}\right]\exp i\omega \times \left[(t'+t_0)-\frac{1}{c}(r'-r+2z)\right]d\omega dt_0 dS_0 dS, \quad (20)$$

where

$$P_A^* = \exp i\varphi P^*, \quad P_B^* = \exp i\left(\Psi-\frac{\pi}{2}\right)P^*.$$

The integrals in formulas (19) and (20) will be taken in the linear approximation for distances r and r' and infinitely large domains of integration S, S_0, T_0, and Ω. The integrals over the domains S and Ω are essentially space and time δ functions. Calculations similar to those performed in [6] lead to the final expressions for the images formed by the space–time polarization hologram.

For the virtual image, we obtain from (19) at $z' = z_0$

$$\mathbf{E}_{-1}(x', y', z', t') \approx -\frac{2\pi i\kappa d\hat{\mathbf{v}}_L}{\hat{n}_0}\exp(-2i\kappa d\hat{n}_0)E_{0x}^2(1+\varepsilon^2) \times\left[\hat{E}_{Ax}M_{\text{ob}}(x', y', z', t')\begin{pmatrix}1\\ i\varepsilon\end{pmatrix}\oplus\hat{E}_{By}M_{\text{ob}}(x', y', z', t')\begin{pmatrix}i\varepsilon\\ 1\end{pmatrix}\right]. \quad (21)$$

It follows from formula (21) that this expression, correct to a constant factor, describes the complete reconstruction of both the space–time structure and polarization characteristics of the nonstationary object wave field.

For the real image, we obtain from (20) at $z' = 2z - z_0$

$$\mathbf{E}_{+1}(x', y', z', t') \approx -\frac{2\pi i\kappa d\hat{\mathbf{v}}_L}{\hat{n}_0}\exp(-2i\kappa d\hat{n}_0)E_{0x}^2 \times\left[P_A^* M_{\text{ob}}^*\left(x', y', z', \frac{2z}{c}-t'\right)\begin{pmatrix}1\\ i\varepsilon\end{pmatrix}\right. \quad (22)$$
$$\left.\oplus\ P_B^* M_{\text{ob}}^*\left(x', y', z', \frac{2z}{c}-t'\right)\begin{pmatrix}i\varepsilon\\ 1\end{pmatrix}\right].$$

One can see from formula (22) that, at the distance $z' = 2x - z_0$, the image with the pseudoscopic spatial structure of the object field is formed symmetrically to the virtual image about the hologram plane. It has an inverted time waveform with a time delay due to passing the distance $2z = z' + z_0$ from the observation point to the real image. Its polarization state is transformed according to the matrices P_A^* and P_B^*.

In conclusion, the capability of the polarization holographic method to reconstruct the spatial structure, time waveform, and polarization state of the initial field of a nonstationary object ultimately extends the potentialities of the holographic method.

ACKNOWLEDGMENTS

We are grateful to Sh.D. Kakichashvili for the statement of the problem and helpful discussions.

REFERENCES

1. D. Gabor, Proc. R. Soc. London, Ser. A **197**, 454 (1949).
2. Yu. N. Denisyuk, Dokl. Akad. Nauk SSSR **144**, 1275 (1962) [Sov. Phys. Dokl. **7**, 543 (1962)].
3. V. A. Zubov, A. V. Kraĭskiĭ, and T. I. Kuznetsova, Pis'ma Zh. Éksp. Teor. Fiz. **13**, 443 (1971) [JETP Lett. **13**, 307 (1971)].
4. V. A. Zuĭkov, V. V. Samartsev, and R. G. Usmanov, Pis'ma Zh. Éksp. Teor. Fiz. **32**, 293 (1980) [JETP Lett. **32**, 270 (1980)].
5. P. M. Saari, R. K. Kaarli, and A. K. Rebane, Kvantovaya Élektron. (Moscow) **12**, 672 (1985).
6. Sh. D. Kakichashvili and E. Sh. Kakichashvili, Pis'ma Zh. Tekh. Fiz. **24** (11), 76 (1998) [Tech. Phys. Lett. **24**, 446 (1998)].
7. Sh. D. Kakichashvili, Opt. Spektrosk. **33**, 324 (1972).
8. Sh. D. Kakichashvili, *Polarization Holography* (Leningrad, 1989).
9. Sh. D. Kakichashvili and B. N. Kilosanidze, Zh. Tekh. Fiz. **67** (6), 136 (1997) [Tech. Phys. **42,** 709 (1997)].
10. Sh. D. Kakichashvili, Pis'ma Zh. Tekh. Fiz. **20** (22), 78 (1994) [Tech. Phys. Lett. **20**, 925 (1994)].
11. R. C. Jones, J. Opt. Soc. Am. **31**, 488 (1941).
12. G. R. Kirchhoff, *Selected Works* (Moscow, 1988).
13. F. Kottler, Prog. Opt. **4**, 283 (1965).
14. Sh. D. Kakichashvili, Zh. Tekh. Fiz. **65** (7), 200 (1995) [Tech. Phys. **40**, 743 (1995)].
15. A. A. Kharkevich, *Spectra and Analysis* (Moscow, 1962).
16. M. Born and É. Wolf, *Principles of Optics* (Pergamon, Oxford, 1969; Nauka, Moscow, 1973).
17. F. Weigert, Verh. Dtsch. Phys. Ges. **21**, 479 (1919).
18. H. Zocher and K. Coper, Z. Phys. Chem. **132**, 313 (1928).
19. Sh. D. Kakichashvili, Opt. Spektrosk. **52**, 317 (1982) [Opt. Spectrosc. **52**, 191 (1982)].
20. Sh. D. Kakichashvili and B. N. Kilosanidze, Pis'ma Zh. Tekh. Fiz. **21** (23), 6 (1995) [Tech. Phys. Lett. **21**, 951 (1995)].

Translated by A. Kondrat'ev

Technical Physics, Vol. 45, No. 7, 2000, pp. 883–886. Translated from Zhurnal Tekhnicheskoĭ Fiziki, Vol. 70, No. 7, 2000, pp. 70–73.

RADIOPHYSICS

Relativistic Microwave Devices with Postacceleration of an Electron Beam in the Interaction Space

É. B. Abubakirov and A. V. Savel'ev

Institute of Applied Physics, Russian Academy of Sciences, ul. Ul'yanova 46, Nizhni Novgorod, 603600 Russia

E-mail: edward@appl.sci-nonv.ru

Received December 1, 1998; in final form, November 11, 1999

Abstract—We analyzed the possibility of improving the efficiency of microwave devices operating with relativistic electron beams in systems with particle postacceleration in the interaction space. The fundamental feature of this approach is the formation of the accelerating-potential profile with the inherent electric field of a high-current electron beam. It is shown that the use of the space-variant beam-potential sag helps raise the estimated efficiencies of relativistic Cherenkov TWT and BWO up to values of about 50%. © *2000 MAIK "Nauka/Interperiodica".*

Facilities with postacceleration of an electron beam in the interaction space are a promising version of powerful RF devices. This kind of acceleration helps increase the average energy of previously formed electron bunches, as in Reltron [1], simultaneously reducing the relative energy spread, and thus effectively achieve a high output RF power. Applying an accelerating electric field to the electrons captured by a synchronous electromagnetic wave also provides the mode of their adiabatic deceleration [2, 3]. In this case, the electron-beam potential energy in the accelerating static field is actually converted to RF radiation.

Note that, as a rule, electron postacceleration is performed by introducing supplementary high-voltage electrodes which need intricate and bulky insulation and are unsuitable for transporting the electron beam. At the same time, for high-current electron beams focused by a longitudinal magnetic field, the particle energy is likely to be controlled by the beam-inherent fields. Powerful relativistic microwave devices are conventionally used when the electron currents account for an appreciable fraction of the limiting vacuum value. The inherent fields of this electron flux are rather strong, and, therefore, the potential difference between the beam and the transport-channel wall ΔU is large. In this connection, the particle energy in the beam $E = e(U_a - \Delta U)$ may noticeably differ from the peak energy determined by the anode (accelerating) voltage U_a. The drop of potential ΔU depends on the beam current, its configuration, and position in the transport channel. For example, for a circular cross section of the drift channel and a narrow tubular (circular) electron beam, we have

$$\Delta U = \frac{2J\ln(R/r)}{\nu}, \qquad (1)$$

where J is the beam current, ν is the electron velocity, and R and r are the anode and electron-beam radii.

One can easily see that, as the ratio R/r changes, i.e., as the beam approaches or recedes from the transport-channel wall, the electron energy in the beam may vary within wide margins. This control of the beam position can be attained by creating the required configuration of the lines of force of the static magnetic field focusing the high-current electron beam. For instance, diverging field lines (magnetic field decreasing along the channel) maintain a constant electron acceleration.

Let us estimate the possibilities of controlling the particle energy under changes of the "beam-potential sag." The electron energy in the stationary beam is minimum $E_{\min} = mc^2(\gamma_a^{1/3} - 1)$ when the current has the limiting value for this transport channel

$$J_{\lim} = \frac{mc^3(\gamma_a^{2/3} - 1)^{3/2}}{2e\ln(R/r)}, \qquad (2)$$

where e and m are the electron charge and mass, $\gamma_a = 1 + eU_a/mc^2$, and U_a is the accelerating voltage. If the electron energy in the initial beam state is close to the minimum value, the possible relative increment in their kinetic energy is $(eU_a - E_{\min})/E_{\min} = \gamma_a^{1/3}(\gamma_a^{1/3} + 1)$. It is evident that the particle energy in the transport channels can be increased three times even for slightly relativistic ($\gamma_a \longrightarrow 1$) flows. This acceleration technique seems to be best suited to relativistic-electron beams, whose potential profile, defined by relation (1), is virtually unchanged during their interaction with the RF field because of the weak energy dependence of the relativistic particle velocity.

Now we analyze the usability of electron-beam postacceleration for specific tasks. By way of example,

1063-7842/00/4507-0883$20.00

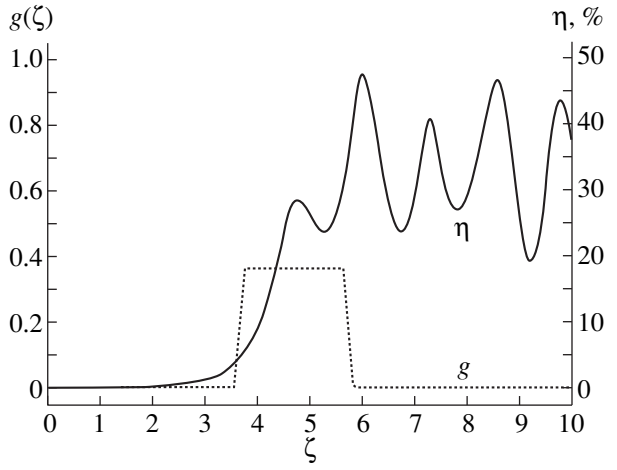

Fig. 1. The efficiency and the effective accelerating force versus the longitudinal coordinates in the TWT with electron postacceleration.

consider the relativistic Cherenkov traveling-wave tube (TWT) and the backward-wave oscillator (BWO). For simplicity, we use a one-dimensional TWT (BWO) simulation in which the particle acceleration is taken into account by means of an additional force that is dependent on the longitudinal coordinate. Electron trajectories are assumed to coincide with the lines of the guiding magnetic field. This approximation is valid if the radius and pitch of the Larmor electron spiral in the magnetic field are small with respect to the characteristic scale of the focusing-field-strength variation. Under these assumptions, the force acting on the electron that moves along the field line of force $r(z)$ is defined with relation (1):

$$G(z) = e\frac{dU}{dr}\sin\varphi \approx \frac{2eJ}{\nu}\frac{1}{r}\frac{dr}{dz}. \qquad (3)$$

where $\varphi = \arctan(H_r/H_z) \ll 1$ and H_r and H_z are the vector components of the focusing-magnetic-field strength. The interaction of an ultrarelativistic electron beam ($\gamma = E/mc^2 \gg 1$) with a synchronous wave is described by a system of nonlinear equations [4], supplemented with the accelerating force $G(z)$:

$$\frac{dw}{d\zeta} = \mathrm{Re}\left\{\left(\alpha F + i\sigma\int_0^{2\pi} e^{i\vartheta}d\vartheta_0\right)e^{-i\vartheta}\right\} + g(\zeta),$$
$$\frac{d\vartheta}{d\zeta} = \frac{1}{w^2} - \delta, \quad \frac{dF}{d\zeta} = \mp\alpha I\int_0^{2\pi} e^{i\vartheta}d\vartheta_0. \qquad (4)$$

Here, $w = \gamma/\gamma_0$ is the electron energy normalized by the initial value; $\gamma = (1 - \nu^2/c^2)^{-1/2}$ is the relativistic mass factor; $\vartheta = \omega t - kz$ is the particle phase with respect to the synchronous wave; $F = 2e\gamma_0 E_z/mc\omega\alpha$; $g = 2\gamma_0 G/mc\omega$; $\zeta = kz/2\gamma_0^2$; $k = \omega/c$; $\delta = 2\gamma_0^2(h/k - 1)$ is the initial detuning of synchronism; $I = (\gamma_0^3 eJ/\pi\omega^2 mP)|E_z/\alpha|^2$; $\alpha^2 = |E_z|^2/2h^2P$ is the coupling resistance of electrons with the wave; P is the power transferred by the wave; h is its longitudinal wave number; $\sigma = 4\gamma_0 T(eJ/mc^3)/\pi(\gamma_0^2 - 1)^{3/2}$ is the coefficient of space charge; T is the depression coefficient; e and m are the electron charge and mass.

To give specific expressions to the dependences $\alpha(\zeta)$ and $\sigma(\zeta)$, we assume that the electrodynamic systems of the TWT and BWO are circular corrugated waveguides. In this case, $\alpha = \alpha_0 I_0(\chi r)/I_0(\chi r_0)$; $\sigma = \sigma_0 T(r)/T(r_0)$, where r_0 is the initial beam radius; χ is the transverse wave number of the synchronous harmonic; $T(r) = I_0(pr)[I_0(pR)K_0(pr) - I_0(pr)K_0(pR)]/I_0(pR)$; I_0 and K_0 are the modified zero-order Bessel function; and $p = k/\sqrt{\gamma_0^2 - 1}$. Sign (–) in expressions (4) corresponds to the case when the electrons and the energy in the wave (TWT) move in the same direction, and the sign (+) corresponds to their counterpropagation (BWO). If the beam entering the interaction space is not modulated, the boundary conditions in (4) are written as follows:

$$w(0) = 1, \quad \vartheta(0) = \vartheta_0 \in [0, 2\pi],$$
$$F(0) = F_0(\mathrm{TWT}) \quad \text{or} \quad F(\zeta_k) = 0(\mathrm{BWO}), \qquad (5)$$

where ξ_k is the dimensionless length of the interaction space.

While simulating the TWT, the configuration of the guiding-magnetic-field lines was selected so that the electrons were postaccelerated in the region where a compact bunch of electrons had already been formed. For simplicity, the accelerating force was assumed to be constant in this region and a specific dependence $r(\zeta)$, needed for evaluating $\alpha(\zeta)$ and $\sigma(\zeta)$, was found from (3). Note that the beam radius should be varied adiabatically smoothly in order to avoid a significant loss of electrons from the bunch produced. A solution of Eqs. (4) is shown in Fig. 1 as the interaction efficiency versus the longitudinal coordinate

$$\eta = 1 - \frac{1}{2\pi}\frac{\int_0^{2\pi} w(\zeta)d\vartheta_0}{1 + \int_0^{\zeta} g(\zeta')d\zeta'}. \qquad (6)$$

Simultaneously with the postacceleration, an increase in the beam radius causes the coupling coefficients and the space charges to change (Fig. 2). In this case, the relative change in the kinetic energy of electrons due to postacceleration is $\Delta E/E_0 = 0.75$. The peak efficiency achieved in this case is nearly 50%.

In high-current devices, the space charge significantly affects the electron-bunching process in the

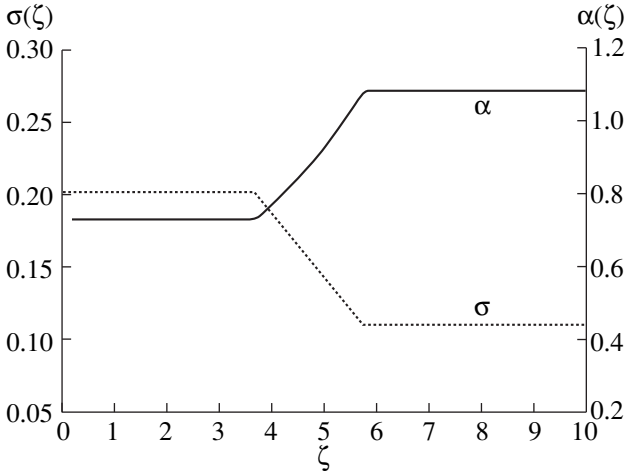

Fig. 2. Variations in the coupling and space-charge coefficients in the TWT with postacceleration of the electron beam.

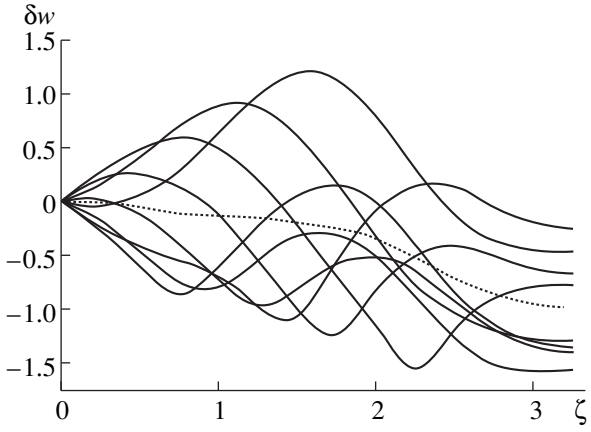

Fig. 3. Variations of the normalized energy $\delta w = w(\zeta) - \int_0^\zeta g(\zeta')d\zeta' - 1$ of electrons with various initial phases (solid lines) and their average energy (dashed line) in the BWO with electron postacceleration along the interaction space.

field of a synchronous wave, preventing the formation of a compact bunch. The advantage of the postacceleration scheme in question is that the beam broadening results in the attenuation of the space charge and reduction of the repulsive forces, favoring formation of a dense electron bunch. Moreover, bringing the beam closer to the walls of the waveguiding system in Cherenkov devices is accompanied by an increase in the synchronous-harmonic amplitude, which provides more effective deceleration of the electron bunch by the wave.

The feasibility of beam postacceleration in the BWO was similarly analyzed. It is interesting to compare these results for the BWO with the coupling-resistance jump [5]. As in [5], the interaction space in the BWO with postacceleration can be functionally divided into two parts. The electron bunching predominantly occurs in the part with reduced coupling resistance and relatively low electron energy; in the other BWO part, energy is taken up from the bunched flow. Analyzing the electron phase distribution, we see that the bunch is not formed until $\zeta \approx 1.5$ and the average electron energy slightly changes up to this moment (Fig. 3). The electrons then reach the region of stronger coupling with the field, where the bunch gives up most of its energy to the wave. In contrast to [5], the coupling of the electrons with the wave varies smoothly and is accompanied by the postacceleration of the electron bunch. When $\alpha(\zeta_k)/\alpha(0) = 3$, $\zeta_k = 3.25$, and $\Delta E/E_0 = 1$, this BWO has an efficiency of 48.2%. It is important that, without the postacceleration, this drop of the coupling resistance provides a significantly lower efficiency (18.4%) of the BWO with the given parameters.

Now we discuss the features in using the method with finite magnetic fields, when particles may move across the magnetic-field lines of force. Note that, when implementing the postacceleration principle, the configuration of the static magnetic field confining the electron beam corresponds to beam decompression, which helps maintain the microwave-device efficiency for finite values of the magnetic field [6]; therefore, similar estimates are used. The longitudinal motion is assumed to govern until $v_\perp \ll c\gamma^{-1}$, where $v_\perp$ is the transverse electron velocity [4]. When a coaxial diode with magnetic insulation is used to form the electron beam, those particles emitted by the cathode side have the maximum transverse velocity; their Larmor radius is defined by the relation $R_{\perp 0} = v_\perp/\omega_{Hc} = (mc^2/e)E_c/H_c$, where $v_\perp$ corresponds to the drift velocity in the crossed radial electric field at the cathode side E_c and focusing magnetic field close to the cathode H_c. As the magnetic field changes, the peak-to-peak amplitude of transverse oscillations increases as $R_\perp \approx R_{\perp 0}\sqrt{H_c/H}$; hence, $v_\perp \approx \omega_H R_\perp = (c/\gamma)E_c/\sqrt{H_c H}$. Therefore, the transverse velocities are small when $E_c \ll \sqrt{H_c H}$. Naturally, this condition is more stringent than that with a homogeneous magnetic field which is equal to the field at the cathode; however, the difference is only $\sqrt{H_c H}$ times.

Thus, the calculations corroborate the feasibility of using particle postacceleration to increase the sensitivity of microwave devices with relativistic electron beams. The advantage of the postacceleration scheme is that the longitudinal distribution of potential required for its implementation is formed by the electron beam itself. In addition, the space charge of the beam decreases, and the coupling between electrons and the wave increases during the interaction. However, it is important that just imparting additional kinetic energy

to electrons, i.e., postacceleration, plays the decisive role in raising the device sensitivity.

REFERENCES

1. R. B. Miller, W. F. McCullough, K. T. Lankaster, and C. A. Muehlenweg, IEEE Trans. Plasma Sci. **20**, 332 (1992).
2. E. D. Belyavskiĭ, Radiotekh. Élektron. (Moscow) **16**, 208 (1971).
3. N. S. Ginzburg, I. A. Man'kin, V. E. Polyak, *et al.*, *Relativistic High-Frequency Electronics* (IPF AN SSSR, Gorki, 1985), Vol. 7, p. 37.
4. N. F. Kovalev, M. I. Petelin, M. D. Raĭzer, and A. V. Smorgonskiĭ, *Relativistic High-Frequency Electronics* (IPF AN SSSR, Gorki, 1979), p. 76.
5. N. F. Kovalev and V. I. Petrukhina, Élektronika SVCh, No. 7, 102 (1977).
6. E. B. Abubakirov, M. I. Fuchs, N. G. Kolganov, *et al.*, in *Proceedings of the 3rd Int. Workshop "Strong Microwave in Plasmas," Nizhni Novgorod, Institute of Applied Physics, 1996*, vol. 2, pp. 810–828.

Translated by N. Goryacheva

Technical Physics, Vol. 45, No. 7, 2000, pp. 887–895. Translated from Zhurnal Tekhnicheskoĭ Fiziki, Vol. 70, No. 7, 2000, pp. 74–82.

ELECTRON AND ION BEAMS, ACCELERATORS

Dispersion Dilution of the Beam Emittance in Linear High-Energy Electron Accelerators

V. M. Tsakanov

Erevan Institute of Physics, Erevan, 375036 Armenia

E-mail: tsakanov@jerewan1.yerphi.am

Received February 12, 1999

Abstract—Dispersion dilution of the beam emittance in a linear accelerator due to the initial uncorrelated spread of the particle energy in a bunch is considered. Both coherent beam oscillations and the case of the disturbed central trajectory and its local correction are treated. Emphasis is given to the analytic description of the dispersion dilution of the beam emittance. Exact analytic expressions derived for the emittance evolution along the accelerator are strengthened by the numerical simulation of particle tracks in the main linear accelerator of the future electron–positron collider. *© 2000 MAIK "Nauka/Interperiodica".*

INTRODUCTION

The achievement of ultimately small electron (positron) beam emittances in the future electron–positron collider is a key challenge in obtaining high luminosity at the collision site [1–3]. In the main linear accelerator of the collider, where particles are accelerated from several GeV to several hundred GeV, the natural emittance, in the ideal case, must shrink as much as possible because of the adiabatic damping of transverse particle oscillations. Actually, however, the trajectories of the particles are disturbed because of tolerances imposed on elements of the electron–optic system of the accelerator and transverse wake fields arising in accelerating sections [4, 5]. In addition, a bunch has an energy spread both correlated with the particle longitudinal coordinate (because of the interaction with the accelerating structure) and uncorrelated (because of beam preforming). The Balakin–Novokhatsky–Smirnov method [6] allows one to suppress an increase in the emittance due to the correlated energy spread and wake fields within a bunch if so-called particle autophasing conditions are met [7, 8]. However, the remaining uncorrelated energy spread causes beam emittance dispersion dilution (BEDD). This poses major problems for obtaining energetic beams with ultimately small lateral and vertical emittances.

An increase in the emittance of a beam with an initial energy spread is associated both with coherent betatron oscillations of a beam with nonzero initial amplitudes (deflection and angle of deflection) of its center of gravity and with the disturbed central trajectory. The disturbance of the trajectory stems from quadrupole lens misarrangement. When passing through the focusing system of the accelerator, particles having different energies acquire a phase incursion of betatron oscillations and, if the central trajectory is nonzero, separate on the phase plane, resulting in BEDD. In this case, the Liouville theorem is invalid and the beam emittance is defined statistically as the root-mean-square (rms) spread of particles over the phase plane of transverse oscillations.

BEDD has been treated from various standpoints [9–17]. Both the analytic characterization of the phenomenon and numerical simulation of particle trajectories in a linear accelerator have been performed. Physically, BEDD in linear accelerators is well understood (see, e.g., [9, 13, 15]); however, the unified approach to the problem that makes possible the rigorous analytic characterization of the beam emittance in the presence of an initial spread of the particle energies is lacking in the literature. Let us consider in detail two important issues.

First, the two-particle model of bunch is obviously inappropriate for the analytic description of BEDD when the spread of the particles is large. Indeed, if the relative phase incursion of betatron oscillations of a nonequilibrium particle is 2π (one turn of the nonequilibrium particle about the phase ellipse with respect to an equilibrium particle), the rms emittance goes to zero. In reality, however, as the particles spread, the entire phase ellipse of the transverse betatron oscillations of the center of gravity of a beam becomes occupied by particles with nonequilibrium energies. Therefore, in the analytic description of BEDD, one should rely on the actual energy distribution of the particles in a bunch.

The second remark concerns BEDD numerical simulation when the central trajectory is disturbed and associated corrections are made. Note that lens misarrangement can be taken into account only by specifying the offsets of the quadrupole lenses relative to the accelerator axis. The offsets are presented as a random set of uncorrelated displacements with a known rms

1063-7842/00/4507-0887$20.00

alignment precision. However, the disturbed central trajectory may significantly (by several orders of magnitude) differ for two sets [18, 19]; hence, it is necessary to average the BEDD effects over many sets of the displacements of focusing components from the zero trajectory. As shown in [20], by introducing the rms area of the disturbed machine phase ellipse, one can rigorously describe the rms disturbance of the central trajectory (along the accelerator) to which particle tracks converge when averaged over many sets of lens misarrangements. Virtually, the analytic description provides the exact averaging of the rms beam parameters over all possible trajectories of particles in a bunch.

In this work, we study the BEDD effect in linear accelerators that is due to the uncorrelated initial particle energy spread in a bunch. First, we will consider coherent betatron oscillations with the central trajectory disturbed because of quadrupole lens misarrangement. Then, the case when a dipole corrector in each of the quadrupole lenses compensates for central trajectory distortions by determining the position of the center of gravity of a beam will be discussed. Results for FODO (F, focusing lens; O, open gap; D, defocusing lens) periodicity cells for various phase incursion vs. particle energy dependences along the accelerator [8, 21] will be presented. Analytic expressions for rms beam emittance are compared with simulations of particle trajectories in the main accelerator to be used in the SBLC thermal linear collider (accelerating field frequency 3 GHz) and the TESLA superconducting linear collider (accelerating field frequency 1.3 GHz) [22].

EQUATIONS OF MOTION AND PHASE DISPERSION OF BETATRON OSCILLATIONS

As usual, we assume that the focusing system of an accelerator consists of many FODO cells (periods), each having two accelerating sections. Particles in a bunch experience the same acceleration with a constant gradient γ', so that the equilibrium energy of the particles varies linearly along the accelerator: $\gamma(z) = \gamma_0 + \gamma' z$, where γ_0 and $\gamma(z)$ are, respectively, the initial and instantaneous Lorenz factors of an equilibrium particle and z is the particle position γ. It is assumed that the phase incursion of betatron oscillations per cell varies with energy as [8]

$$\tan\frac{\mu_n}{2} = \frac{1}{4}K_n L_q(\beta_{n\max} - \beta_{n\min}) = \tan\frac{\mu_1}{2}g_n^{\alpha}, \quad (1)$$

where μ_n is the phase incursion in the nth cell, $g_n = \gamma_0/\gamma_n$, $\gamma_n = \gamma_0 + (n-1)\Delta\gamma$ is the energy of a particle entering the nth cell, $\Delta\gamma$ is the energy gain per FODO cell, $K_n = ec(\partial B/\partial x)/E$ is the normalized strength of quadrupole lenses, e is the electron charge, c is the speed of light, $\partial B/\partial x$ is the gradient of the lens magnetic field, E is the instantaneous energy of an equilibrium particle, and L_q is the quadrupole lens length.

Note that the above formula is nothing else than the cell chromaticity, which defines a relative change in the phase incursion of betatron oscillations per period for a nonequilibrium particle. The parameter α specifies the law of phase variation with particle acceleration (energy). Thus, the phase incursion μ_1 during the first period and parameter α uniquely characterize the focusing systems of an accelerator and linear optics of an electron beam if it is assumed that lateral and vertical oscillations are uncoupled. Such an approach is applicable to all possible beam trajectories. As shown below, the BEDD effect to a great extent depends on the phase incursion at the beginning of an accelerator and its variation along the accelerator. It is significant [8] that, with the focusing system defined in such a way, the particle autophasing conditions are met and the exponent α in formula (1) equals 0.5.

The linearized equation for transverse motion of a nonequilibrium particle in a linear accelerator where quadrupole lenses are displaced from the axis has the form

$$x'' + \frac{\gamma'}{\gamma} + K_x(1-\delta)(x - x_q) = 0, \quad (2)$$

where x is the transverse (vertical or lateral) displacement of the particle, $x_0 = x(0, \delta_0)$ and $x_0' = x'(0, \delta_0)$ are the initial amplitudes, $\delta(z) = \delta_0\gamma_0/\gamma(z)$ is an acceleration-dependent change in the uncorrelated relative energy deviation, $\delta_0 = \Delta E/E_0$ ($\delta_0 \ll 1$) is the initial uncorrelated energy deviation, K_x is the lens strength, and $x_q(z) = x_{qk}$ are random displacements of the quadrupole lenses from the axis. The derivative is taken with respect to the coordinate z along the accelerator axis.

The general solution of the equation of motion is represented as the sum of betatron oscillations x_b and the disturbed trajectory x_d:

$$x(z, \delta) = x_b(z, \delta) + x_d(z, \delta). \quad (3)$$

The explicit form of these solutions is found by applying Twiss matrix formalism [23–25]:

$$x_b(z, \delta) = a_b\left(\frac{\gamma_0}{\gamma(z)}\bar{\beta}(z)\right)^{1/2}\cos[\bar{\mu}(z) + \vartheta_b], \quad (4)$$

$$x_d(z, \delta) = \int_0^z M_{12}^{\delta}(z', z)K_x(z')dz', \quad (5)$$

where the M_{12}^{δ} element of the Twiss matrix for a nonequilibrium particle is given by

$$M_{12}^{\delta}(z', z) = \sqrt{\bar{\beta}(z')\bar{\beta}(z)}\left(\frac{\gamma(z')}{\gamma(z)}\right)^{1/2}\sin[\bar{\mu}(z) - \bar{\mu}(z')]. \quad (6)$$

Here, $\bar{\beta} = \beta + \Delta\beta$ and $\bar{\mu} = \mu + \Delta\mu$ are the amplitude β function and phase of betatron oscillations for the particle, respectively; $\Delta\beta$ and $\Delta\mu$ are their changes relative

to the equilibrium values β and μ; and a_b and ϑ_b are the initial transverse deflection and angle of deflection (at the exit to the accelerator), respectively. It can be shown that $\Delta\beta$ and $\Delta\mu$ are expressed through the parameters of the focusing system as [23, 24]

$$\Delta\beta(z) = \int_0^z \delta(z')\beta(z')K_x(z')\sin[2\mu(z) - 2\mu(z')]dz', \quad (7)$$

$$\Delta\mu(z) = -\int_0^z \delta(z')\beta(z')K_x(z')\sin^2[\mu(z) - \mu(z')]dz'. \quad (8)$$

Thus, the mean change in the amplitude function in linear accelerators can be ignored, unlike magnetic resonance accelerators [24]; on the other hand, the mean increase in the phase incursion causes beam spreading on the phase plane and, hence, an increase in the rms beam emittance. The current emittance ε is defined statistically as the rms spread of particles on the phase plane of transverse oscillations [26]:

$$\varepsilon = \sqrt{\langle \Delta x^2\rangle \langle \Delta x'^2\rangle - \langle \Delta x \Delta x'\rangle^2}, \quad (9)$$

where $\Delta x = x - \bar{x}$; $\Delta x' = x' - \bar{x}'$, and $\bar{x}$ and $\bar{x}'$ are the position and angular coordinate of the center of gravity of a beam.

Averaging is accomplished over all particles in a bunch. We are interested in the averaged (over the instantaneous phases of betatron oscillations) emittance along the accelerator. Then, $\varepsilon = \langle \Delta x^2\rangle/\beta$ if the dispersion of the betatron function is absent.

The uncorrelated particle energy spread in a bunch is observed when the bunch is injected into the main linear accelerator. The spread is the consequence of the beam forming history (storage ring and bunch compressor). If all of the particles have the same acceleration in a given cross section of the bunch, the spread is inversely proportional to the energy of an equilibrium particle. Then, in the thin-lens approximation, the mean change in the phase incursion for a nonequilibrium particle that has the relative initial energy deviation δ_0 is given as the sum over periodicity cells:

$$\Delta\mu = -\frac{1}{2}\delta_0 \sum_n g_n K_n L_{qn}(\beta_{n\,\max} - \beta_{n\,\min}). \quad (10)$$

For our representation of the focusing system, this formula is recast as

$$\Delta\mu = -2\delta_0 \tan\frac{\mu_1}{2}\frac{1}{\Delta\gamma}\sum_n g_n^{\alpha+1}\Delta\gamma, \quad (11)$$

which is the energy integral at a slow energy variation along the accelerator ($\Delta\gamma/\gamma \ll 1$). In terms of the accelerator parameters, it is given by

$$\Delta\mu = -2\delta_0 \tan\frac{\mu_1}{2}\frac{\gamma_0}{\Delta\gamma}\frac{1}{\alpha}(1 - g^\alpha). \quad (12)$$

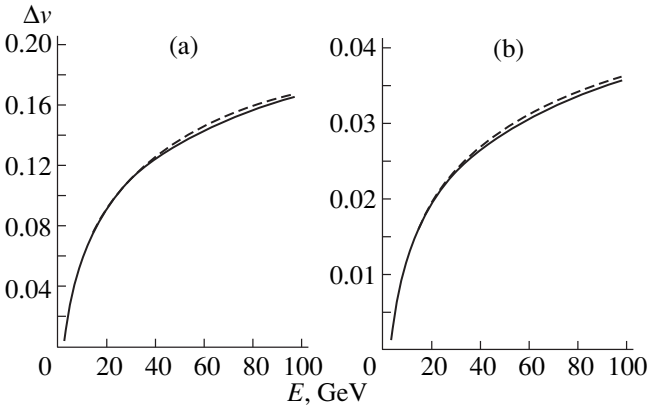

Fig. 1. Beam chromaticity vs. particle energy in the main accelerator of the (a) SBLC ($\delta_0 = 0.01$) and (b) TESLA ($\delta_0 = 0.014$) colliders.

An important parameter of the machine is its chromaticity ξ. For linear high-energy accelerators, it can be defined as a change in the number of betatron oscillations of a nonequilibrium particle with the rms energy deviation σ_ϵ from the equilibrium energy after a single transit of a bunch through the accelerator: $\xi = \Delta\mu_s/2\pi$. In linear accelerators, chromaticity is virtually responsible for beam spreading on the phase plane of transverse betatron oscillations. The beam spread, as evidenced by the foregoing, depends on the initial rms energy deviation in the beam, energy gain per cell, phase incursion in the first cell, and a variation of phase incursion along the accelerator.

Figure 1 shows the growth of the chromaticity along the main accelerator in the SBLC thermal and TESLA superconducting colliders with constant betatron phase incursions per period ($\alpha = 0$) of $\pi/2$ and $\pi/3$, respectively [22]. Notice that the small phase incursion per period of the focusing system and the relatively large particle energy gain per period (~900 MeV) in the TESLA design are key factors that specify the small chromaticity of the machine. This, as demonstrated below, is significant for retaining the natural beam emittance in the main linear accelerator.

COHERENT OSCILLATIONS OF THE BEAM

To begin with, we will consider the dynamics of particles in a bunch with an uncorrelated initial Gaussian energy spread of coherent betatron oscillations entering into a linear accelerator (x_0 and x_0' are the initial transverse amplitudes). The focusing system is assumed to be perfectly arranged with respect to the accelerator axis. With the amplitude dispersion ignored, betatron

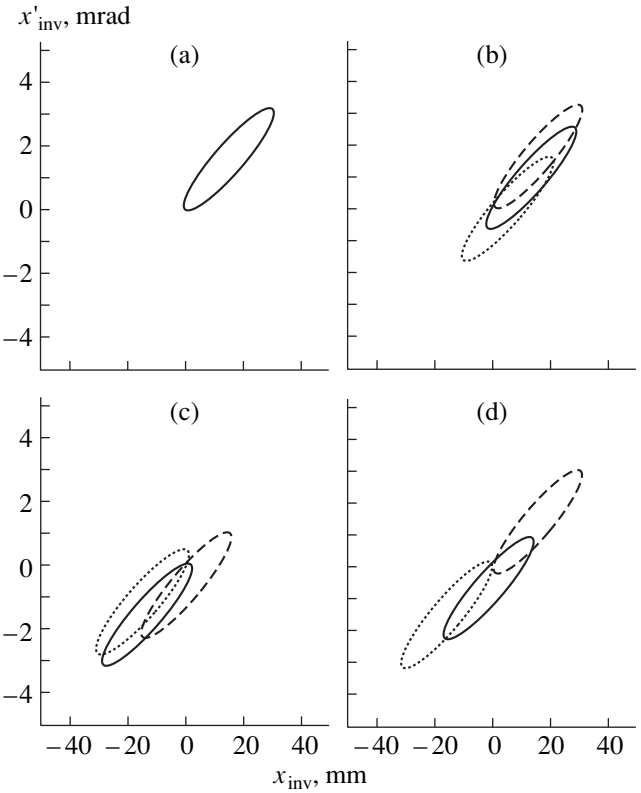

Fig. 2. Phase ellipse splitting in the invariant phase plane (x, x') for beam coherent betatron oscillations in the main accelerator of the SBLC. The phase ellipses of equilibrium-energy particles (solid line) and those with higher (dashed line) and lower (dotted line) energies are shown. E = (a) 3.15, (b) 25, (c) 100, and (d) 250 GeV.

oscillations of a particle with a small initial relative energy deviation δ_0 from the equilibrium value [the term x_b in (3)] can be written as

$$x(z, \delta) = x_c(z, \delta) + x_\beta(x, \delta), \tag{13}$$

where

$$x_{c,\beta}(z, \delta) = a_{0,\beta}\left(\beta(z)\frac{\gamma_0}{\gamma(z)}\right)^{1/2} \times \cos[\mu(z) + \Delta\mu(z, \delta) - \vartheta_{0,\beta}]. \tag{14}$$

Here, a_0 and ϑ_0 define the initial position of the center of gravity of the bunch on the phase plane (x, x') and a_β and ϑ_β define the initial position of the particle relative to the center of the bunch.

Then, the instantaneous center of gravity $\bar{x}$ and rms size $\sigma_x = \langle \Delta x^2 \rangle^{1/2}$ of the bunch are defined as the means over energy spread and initial coordinates of the particles in the bunch:

$$\bar{x}(z) = \int_{-\infty}^{\infty} P_0(\delta) \langle x(z, \delta) \rangle_{a_\beta, \vartheta_\beta} d\delta, \tag{15}$$

$$\sigma_x^2(z) = \int_{-\infty}^{\infty} P_0(\delta) \langle x^2(z, \delta) - \bar{x}^2(z) \rangle_{a_\beta, \vartheta_\beta} d\delta, \tag{16}$$

where $P_0(\delta)$ is the initial uncorrelated particle energy distribution. Let it be Gaussian with the rms deviation σ_ϵ.

Averaging yields the expression that locates the center of gravity of a beam in the accelerator:

$$\bar{x}(z) = a_0\left(\beta(z)\frac{\gamma_0}{\gamma(z)}\right)^{1/2} \times \exp(-\Delta\mu_s^2/2)\cos[\mu(z) - \vartheta_0], \tag{17}$$

where $\Delta\mu_s$ is the mean shift of the betatron phase of a nonequilibrium particle for the initial rms energy deviation σ_ϵ [see (12)].

The rms size of the bunch is found similarly:

$$\sigma_x^2 = \frac{\gamma_0}{\gamma}\sigma_\beta^2 + \frac{a_0^2}{2}\frac{\gamma_0}{\gamma}\{1 - [\cos^2(\mu - \vartheta_0) - \cos(2\mu - 2\vartheta_0)]\exp(-\Delta\mu_s^2)\}, \tag{18}$$

where σ_β is the initial rms transverse size of the bunch.

The mean contribution to the increase in the rms emittance is determined by averaging the obtained expression over the instantaneous phase of betatron oscillations μ within $(0, 2\pi)$. Ignoring the dispersion of the amplitude betatron function, we will have for the dispersion dilution of the bunch emittance:

$$\Delta\varepsilon = \varepsilon - \varepsilon_\beta = \frac{a_0^2}{2}\frac{\gamma_0}{\gamma}[1 - \exp(-\Delta\mu_s^2)], \tag{19}$$

where ε_β and ε are the natural and rms instantaneous beam emittances.

If it is taken into account that a_0^2 is the area of the initial central phase ellipse, the emittance dilution is limited by the half-area of the ellipse of coherent betatron oscillations of the beam:

$$\Delta\varepsilon_{max} = \frac{1}{2}\frac{\gamma_0}{\gamma}(\gamma_x x_0^2 + 2\alpha_x x_0 x_0' + \beta_x x_0'^2), \tag{20}$$

where α_x, β_x, and γ_x are the Twiss matrix parameters at the exit to the accelerator.

Note that the BEDD effect does not depend on the natural emittance. At a high beam spread, the effect becomes a crucial factor if the vertical emittance is small, since the machine ellipse may considerably exceed the beam natural emittance. Hereafter, it will be supposed that the initial phase ellipse of coherent betatron oscillations coincides with the natural phase ellipse, or, in other words, that the initial amplitudes (deflection and angle) of the center of gravity lie on the one-sigma contour ($a_0^2 = \varepsilon_{\beta 0}$). Figure 2 shows the evo-

lution of the normalized phase ellipses of particles with different energies in the main linear accelerator of the SBLC collider. As the particles are accelerated, the ellipses in the phase plane are split so that low-energy particles are ahead of equilibrium particles in phase, while high-energy ones lag behind. Bunch particles tend to occupy the machine phase ellipse of coherent betatron oscillations irrespectively of the initial oscillation phase (Fig. 3). Of importance here is that the center of gravity of the beam approaches the accelerator axis and the coherent betatron oscillation amplitude exponentially drops with increasing BEDD, which is associated with Landau collisionless damping [5]. For an uncorrelated initial Gaussian particle energy spread in a bunch, the expression for Landau damping parameter follows from formulas (12) and (17):

$$\alpha_L(z) = \frac{1}{2}\Delta\mu_s^2 = \frac{1}{8}\left[\sigma_\epsilon \tan\frac{\mu_1}{2}\frac{\gamma_0}{\Delta\gamma}\frac{1}{\alpha}(1-g^\alpha)\right]^2. \quad (21)$$

At small beam spreads ($\xi \ll 1$), the BEDD effect can be approximated as

$$\frac{\Delta\varepsilon}{\varepsilon} \approx 2\sigma_\epsilon^2 \tan^2\frac{\mu_1}{2}\left(\frac{\gamma_0}{\Delta\gamma}\right)^2\frac{1}{\alpha^2}(1-g^\alpha)^2. \quad (22)$$

The BEDD evolution along the main linear accelerator in the SBLC and TESLA colliders [see (19)] are shown in Fig. 4 (dashed line). The solid line stands for the BEDD numerical simulation in the accelerator. The analysis and numerical simulation are seen to be in good agreement. The same is also true for the variation of the Landau damping parameter with particle acceleration. Thus, the derived formulas can be thought of as the rigorous analytic description of uncorrelated BEED for the case of coherent betatron oscillations in linear accelerators. Note that, if the autophasing condition ($\alpha = 0.5$) [8] is met, the uncorrelated BEDD is markedly suppressed, as follows from the data for the SBLC design (Fig. 4, dotted line). It is also worthy to notice that the BEDD effect at coherent oscillations is reversible. As shown in [17], an increase in the emittance can be almost totally avoided if particles on the phase plane are redistributed in a dispersionless positive-chromaticity arc that is placed in the injection stage.

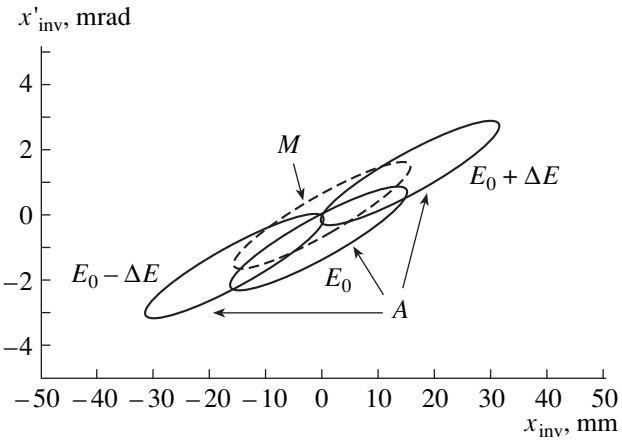

Fig. 3. Machine phase ellipse (*M*) and actual phase portrait (*A*) of a beam after particle spreading in the phase plane at beam coherent oscillations in the SBLC linear accelerator. E = 250 GeV.

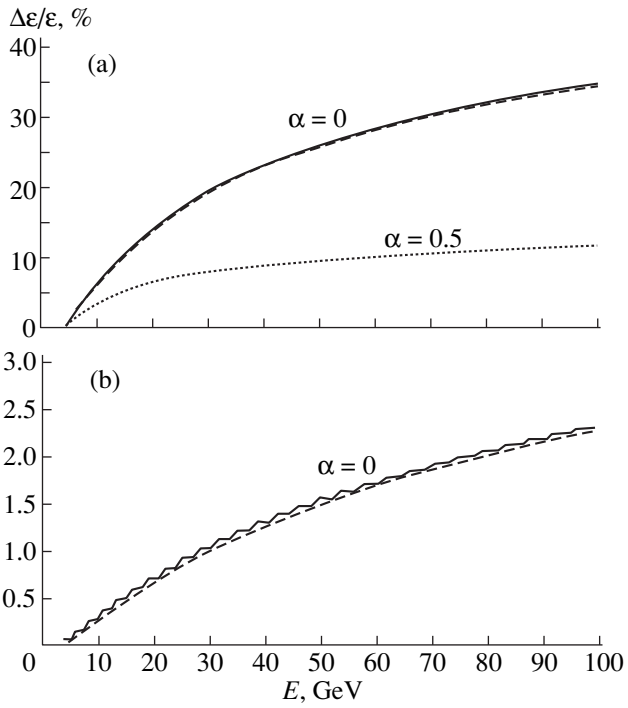

Fig. 4. Relative dilution of the rms emittance of a bunch at beam coherent oscillations. Solid line, particle tracing; dashed line, analytic description. (a) SBLC ($\delta_0 = 0.01$) and (b) TESLA ($\delta_0 = 0.014$).

DISTURBANCE AND CORRECTION OF THE CENTRAL TRAJECTORY

We now proceed to a study of the disturbance term in the equation of motion. Recall that disturbance is due to lens misarrangement. Let us first consider the disturbance of the central trajectory with regard for random lens offsets from the accelerator axis. In view of (3), (5), and (6), the partial solution (of the equation of motion) that corresponds to the disturbed central trajectory ($\delta_0 = 0$, $x_0 = 0$, $x_0' = 0$) can be represented in the form

$$x_d(z) = \sqrt{\frac{\beta(z)}{\gamma(z)}}\sum_k K_k L_{qk} x_{qk}\sqrt{\beta_k\gamma_k}\sin[\mu(z)-\mu(z_k)], \quad (23)$$

where quantities with the subscript k refer to the corresponding values in the kth quadrupole lens.

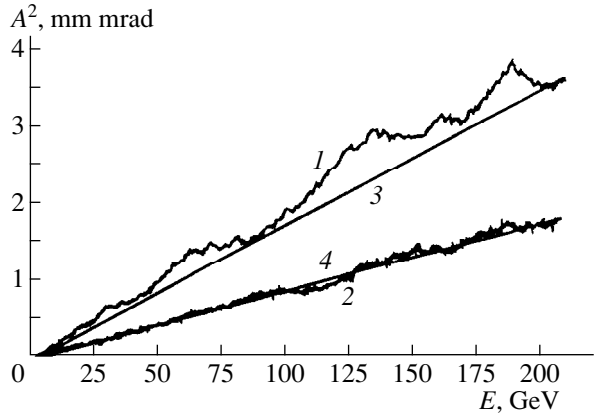

Fig. 5. Area variation for the rms disturbed machine ellipse along the accelerator (particle tracing). Averaging over 100 sets of random lens displacements from the axis. The rms deviation is (*1*) 0.1 (SBLC) and (*2*) 0.5 mm (TESLA). (*3*, *4*) analytic description.

The random lens offsets are assumed to be mutually uncorrelated; hence, cross terms make no contribution to the rms displacement of the central trajectory ($\langle x_{qk}x_{ql}\rangle = 0$ at $k \neq l$). As for free betatron oscillations, we introduce the rms disturbed instantaneous phase ellipse of the beam [20]:

$$\gamma_x\langle x_d^2\rangle + 2\alpha_x\langle x_d x_d'\rangle + \beta_x\langle x_d'^2\rangle = A^2. \qquad (24)$$

The area of the disturbed ellipse (divided by 2π) is given by

$$A^2 = 16\frac{\langle x_q^2\rangle}{L_c\gamma(z)}\sum_n \gamma_n \tan\frac{\mu_n}{2}$$
$$= 16\frac{\langle x_q^2\rangle}{L_c^2}\frac{\gamma_0}{\Delta\gamma}\tan\frac{\mu_1}{2}\frac{1}{2-\alpha}\frac{\gamma_0}{\gamma}\left[\left(\frac{\gamma}{\gamma_0}\right)^{2-\alpha} - 1\right]. \qquad (25)$$

Here, α_x, β_x, and γ_x are instantaneous Twiss matrix parameters and L_c is the FODO cell length. In deriving (25), we made use of the following relationships for the amplitude functions of a symmetric FODO cell [25]:

$$\beta_{\max} + \beta_{\min} = \frac{2L_c}{\sin\mu}, \quad KL_qL_c = 4\sin\frac{\mu}{2}. \qquad (26)$$

Notice that the rms displacement of the lens and tolerance a_q are related through the relationship $a_q^2 = 3\langle x_q^2\rangle$. As shown in [20], expression (25), which relates the area of the rms disturbed phase ellipse to the key accelerator parameters, yields the exact rms disturbance of the central trajectory for uncorrelated random lens offsets. The variation of the disturbed phase ellipse area along the main accelerator in the SBLC and TESLA designs is depicted in Fig. 5. The rms phase ellipse areas converge to the exact solution after averaging the particle track over 100 or more sets of random lens offsets.

In the presence of an initial uncorrelated particle energy spread in a bunch, nonequilibrium particles will tend to occupy the disturbed phase ellipse of the accelerator. For a nonequilibrium particle with an initial energy deviation δ_0, its trajectory will then be defined by the expression

$$x_d(z, \delta) = \sqrt{\frac{\beta(z)}{\gamma(z)}}\sum_k K_k L_{qk} x_{qk}\sqrt{\beta_k\gamma_k}$$
$$\times \sin[\mu(z) - \mu(z_k) + \Delta\mu(z_k, z)] + x_\beta(z, \delta), \qquad (27)$$

where

$$\Delta\mu(z_k, z) = -2\delta_0\frac{\gamma_0}{\Delta\gamma}\tan\frac{\mu_1}{2}\frac{1}{\alpha}\left[1 - \left(\frac{\gamma_k}{\gamma}\right)^\alpha\right] \qquad (28)$$

is the phase shift of the betatron oscillations for the nonequilibrium particle under the action of the *k*th quadrupole lens.

Assuming, as before, the Gaussian initial particle energy distribution and performing averaging over particle energies and positions, we will obtain the expression for the rms transverse beam size:

$$\sigma_x^2(z) = \frac{1}{2}\langle x_q^2\rangle\frac{\beta(z)}{\gamma(z)}\sum_k K_k^2 L_{qk}^2\beta_k\gamma_k$$
$$\times[1 - \exp(-\Delta\hat{\mu}_k^2)] + \sigma_\beta^2(z), \qquad (29)$$

where $\Delta\hat{\mu}_k$ is now the phase shift of the betatron oscillations for the nonequilibrium particle with the rms energy deviation.

In deriving the rms beam size, averaging was also performed over the instantaneous phase $\mu(z)$ within $(0; 2\pi)$. On averaging, account was taken of the fact that the undisturbed trajectory averaged over the initial amplitudes (a_β, ϑ_β) goes to zero and the rms deviation is coincident with the instantaneous undisturbed rms beam size $\langle x_\beta^2\rangle = \sigma_\beta^2$. Supposing that a single cell makes a negligible contribution to the phase shift (which is justified for $\Delta\gamma/\gamma \ll 1$), the rms beam size can be represented as the sum over the periodicity cells:

$$\sigma_x^2(z) = 8\frac{\langle x_q^2\rangle}{L_c}\frac{\beta(z)}{\gamma(z)}\tan\frac{\mu_1}{2}\sum_n\left(\frac{\gamma_0}{\gamma_n}\right)^\alpha\gamma_n$$
$$\times[1 - \exp(-\Delta\hat{\mu}_n^2)] + \sigma_\beta^2(z). \qquad (30)$$

Passing from the sum to the energy integral, one obtains the fairly good approximation for an increase in

the admittance (provided that the beam spread is small):

$$\frac{\Delta\varepsilon}{\varepsilon_\beta} \approx 32\frac{\langle x_q^2\rangle}{\varepsilon_0 L_c}\sigma_\epsilon^2\left(\frac{\gamma_0}{\Delta\gamma}\right)^3 \times \tan^3\frac{\mu_1}{2}\frac{1}{4-\alpha^2}\left[\left(\frac{\gamma}{\gamma_0}\right)^{2-\alpha}-1\right]. \quad (31)$$

Note the very strong dependence of the BEDD on the phase incursion per period of the focusing system μ_1 and the energy gain per periodicity cell $\Delta\gamma$. Figure 6 compares the relative emittance increase along the main accelerator for the SBLC and TESLA colliders. The rms beam sizes were averaged over 100 sets of lens offsets. Clearly, the central trajectory of the beam needs correction.

Let us correct the central trajectory by measuring the position of the center of gravity of the beam and find the rms BEDD. We assume that beam position monitors are embedded in each of the quadrupole lenses with a misarrangement b_k relative to the center of the kth lens. Let the kth lens be randomly displaced by x_{qk} from the accelerator axis. The misarrangements of the accelerator components are assumed to be constant. Once the center of gravity in the kth lens has been determined, the trajectory of subsequent bunches is corrected toward the lens center by previous dipole correctors with a resolution d_k. In so doing, the central trajectory remains disturbed, but the disturbance does not grow along the accelerator. The center-of-gravity displacement in the kth quadrupole lens after correction, x_{ck}, is given by

$$x_{ck} = x_{qk} + b_k + d_k. \quad (32)$$

Note that all of the quantities are random and mutually uncorrelated. The rms deviation of the center of gravity along the accelerator is expressed as

$$\langle x_c^2\rangle = \langle x_q^2\rangle + \langle x_{\mathrm{BPM}}^2\rangle + \langle x_{\mathrm{RES}}^2\rangle, \quad (33)$$

where $\langle x_q^2\rangle^{1/2}$ is the rms deviation of the lenses from the accelerator axis, $\langle x_{\mathrm{BPM}}^2\rangle^{1/2}$ is the rms deviation of the beam position monitors from the centers of the lenses, and $\langle x_{\mathrm{RES}}^2\rangle^{1/2}$ is the rms resolution of the monitors.

It is easy to check that, correct to the first order in energy deviation ($\delta_0 \ll 1$), the displacement of a nonequilibrium particle from the disturbed central trajectory, $\Delta x = x_\delta - x_c$, satisfies the equation

$$\Delta x'' + \frac{\gamma'}{\gamma}\Delta x' + K_x(1-\delta)\Delta x = \delta K_x(x_c - x_q) - \delta G_x(z), \quad (34)$$

where $G_x(z) = ecB(z)/E = 1/\rho_s(z)$ is the instantaneous curvature of the central trajectory disturbed by the dipole correctors.

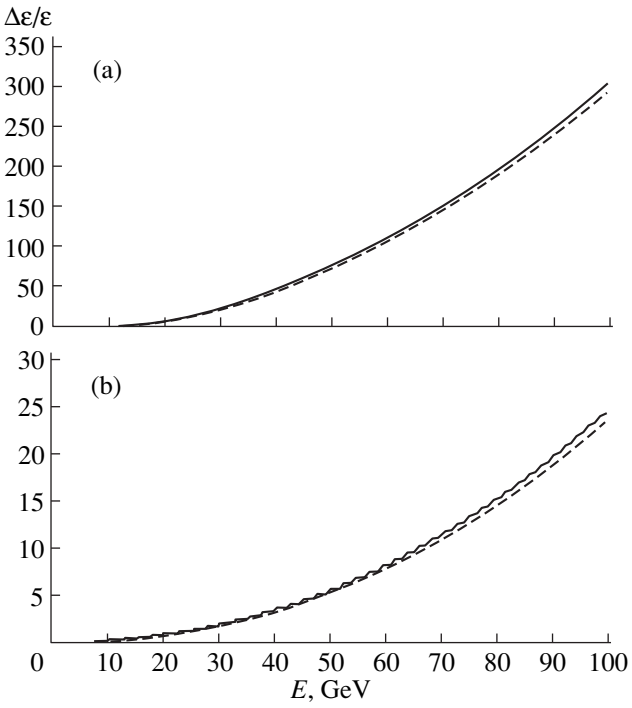

Fig. 6. BEDD in the case of the disturbed central trajectory (solid line). Dashed line, analytic curve. (a) SBLC (δ_0 = 0.01, $\mu = \pi/2$) and (b) TESLA (δ_0 = 0.014, $\mu = \pi/3$).

As usual, we will assume that the additional dispersion function due to dipole correctors goes to zero at the end of the accelerator and does not contribute to the rms beam emittance. Then, the solution of (34) using the Twiss matrix element M_{12} [see (6)] appears as

$$\Delta x(z) = \delta_0\int_0^z \frac{\gamma_0}{\gamma(z')}K_x(z')[x_c(z') - x_q(z')]M_{12}^\delta(z', z)dz'. \quad (35)$$

With the above correcting technique, the BEDD exact value can be found if, for any given set of random quantities x_{qk}, b_k, and d_k along the accelerator, the disturbed central trajectory $x_c(z)$ is represented as a smooth function of coordinate z, $F(z)$, with the extension $F(z_k) = x_{ck}$. The square of the relative displacement of a nonequilibrium particle averaged over instantaneous phases and energy deviations is then given by

$$\langle\Delta x^2(z)\rangle = \frac{1}{2}\langle x_B^2\rangle\sigma_\epsilon^2\beta(z)\frac{\gamma_0}{\gamma(z)} \times \sum_n \frac{\gamma_0}{\gamma_n}K_n^2 L_{qn}^2(\beta_{n\max} + \beta_{n\min}), \quad (36)$$

where the quantity $\langle x_B^2\rangle = \langle x_{\mathrm{BPM}}^2\rangle + \langle x_{\mathrm{RES}}^2\rangle$ depends only on the arrangement accuracy of the correctors and their resolution.

Passing to integration in view of formulas (26) for the amplitude functions, we come to the expression for

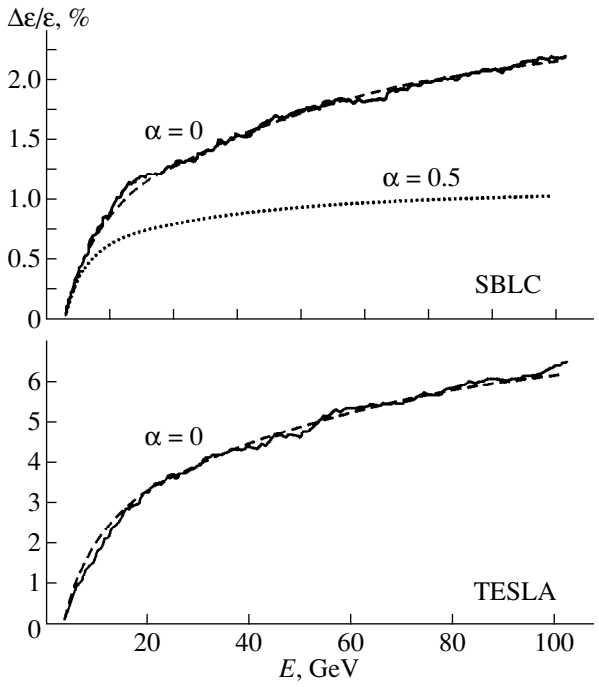

Fig. 7. BEDD in the linear accelerator for the corrected central trajectory. Averaging over 100 sets of monitor displacements from the lens centers and their resolutions (solid line). The rms deviations for the monitor displacements and resolutions are, respectively, 0.1 and 0.01 mm for the SBLC and 0.5 and 0.05 mm for the TESLA. Dashed line, analytic curve.

the relative dilution of the emittance along the accelerator:

$$\frac{\Delta\varepsilon}{\varepsilon} = 8\sigma_\epsilon^2 \frac{\langle x_B^2 \rangle}{\varepsilon_0 L_c} \frac{\gamma_0}{\Delta\gamma} \tan\frac{\mu_1}{2} \frac{1}{\alpha}\left[1 - \left(\frac{\gamma_0}{\gamma}\right)^\alpha\right]. \qquad (37)$$

Note that the correction of the central trajectory considerably diminishes its smearing even in comparison with free betatron oscillations of a beam. Figure 7 shows the relative dilution of the beam lateral emittance for the SBLC and TESLA designs after such a correction. Again, the results of particle tracing are averaged over 100 sets of center-of-gravity random displacements from the accelerator axis. Since the vertical emittance is, as a rule, markedly smaller than the lateral, the accuracy of arrangement of the lenses and correcting system in the vertical plane must be much higher. With the autophasing condition fulfilled ($\alpha = 0.5$) and the same correcting system used, the uncorrelated BEDD considerably decreases, as before (the dashed line for the SBLC design).

CONCLUSION

The exact analytic expressions for BEDD in high-energy linear accelerators were derived for the case when the betatron oscillation phase randomly varies with the equilibrium particle energy. Free coherent betatron oscillations, the disturbance of the central trajectory, and the correction of the disturbed trajectory were investigated. The obtained expressions allow researchers to precisely estimate the beam quality and predict its behavior in high-energy linear accelerators, as well as to optimize the focusing and correcting systems. Under the conditions of the energy-dependent betatron phase incursion, autophasing was shown to considerably suppress the uncorrelated BEDD.

ACKNOWLEDGMENTS

The author thanks R. Brinkmann, J. Rossbach, and R. Wanzenberg for the support and valuable remarks.

Special thanks to É. Gazazyan for the fruitful comments and discussion.

REFERENCES

1. A. Skrinsky, in *Proceedings of the 12th International Conference on High Energy Accel., Fermilab, Batavia, IL, 1983*, pp. 104–108.
2. J. T. Seeman, SLAC-PUB-4886 (1989), p. 5.
3. N. Holtcamp, in *Proceedings of the 15th International Conference on High Energy Accel., Hamburg, 1993*, pp. 770–776.
4. K. Bane, SLAC-PUB-4169 (1986), p. 44.
5. A. Chao, *Physics of Collective Beam Instabilities in High Energy Accelerators* (Wiley, New York, 1993), p. 286.
6. V. Balakin, A. Novokhatsky, and V. Smirnov, in *Proceedings of the 12th International Conference on High Energy Accel, Fermilab, Batavia, IL, 1983*, pp. 119–120.
7. V. Balakin, Preprint No.88-100, IYaF (Budker Institute of Nuclear Physics, Siberian Division, Russian Academy of Sciences, Novosibirsk, 1988).
8. V. M. Tsakanov, Phys. Rev. ST Accel. Beams **1**, 041001 (1998).
9. I. M. Kapchinskiĭ, Usp. Fiz. Nauk **132**, 639 (1980) [Sov. Phys. Usp. **23** (4), 835 (1980)].
10. I. M. Kapchinskiĭ, *The Theory of Linear Resonant Amplifiers* (Énergoizdat, Moscow, 1982), p. 240.
11. *Linear Accelerators of Ions*, Ed. by B. P. Murin (Atomizdat, Moscow, 1978), Vol. 1, p. 264.
12. V. Balakin, A. Novokhatsky, and V. Smirnov, in *Proceedings of the 12th International Conference on High Energy Accel., Fermilab, Batavia, IL, 1983*, p. 121.
13. R. D. Ruth, SLAC-PUB-4436 (1987), p. 22.
14. R. D. Ruth, in *Proceedings of 1991 Part. Accel. Conference, San Francisco, 1991*, p. 2037.
15. T. Raubenheimer, SLAC-387 (1991), p. 111.
16. M. Drevlak, M. Timm, and T. Weiland, in *Proceedings of the 18th International Lingc Conference, Geneva, 1996*, p. 621.
17. V. M. Tsakanov, Nucl. Instrum. Methods Phys. Res. A **421**, 423 (1999).

18. A. Mosnier and A. Zakharian, in *Proceedings of the 4th European Part. Accel. Conference, London, 1994*, p. 1111.
19. M. Drevlac, DESY 95-225 (1995), p. 148.
20. V. M. Tsakanov, Zh. Tekh. Fiz. **69** (7), 95 (1999) [Tech. Phys. **44**, 825 (1999)].
21. G. Guignard, in *Proceedings of 1993 Part. Accel. Conference, New York, APS, 1993*, p. 3600.
22. *Conceptual Design of a 500 GeV e^+ e^- Linear Collider with Integrated X-ray Laser Facility*, Ed. by R. Brinkmann, G. Materlik, J. Rossbach, and A. Wagner (DESY, Hamburg, 1997), Vols. I and II, p. 275.
23. E. D. Courant and H. S. Snyder, Ann. Phys. (N.Y.) **3**, 1 (1958).
24. M. Sands, *The Physics of Electron Storage Rings*, SLAC-121 (1971), p. 172.
25. J. Rossbach and P. Schmuser, in *Proceedings of the CERN Accelerator School, CERN 94-01, 1994*, p. 17.
26. J. Buon, in *Proceedings of the CERN Accelerator School, CERN 94-01, 1994*, p. 89.

Translated by V. Isaakyan

Technical Physics, Vol. 45, No. 7, 2000, pp. 896–904. Translated from Zhurnal Tekhnicheskoĭ Fiziki, Vol. 70, No. 7, 2000, pp. 83–91.

Dynamical Chaos in a Charged-Particle Flow Produced by a Magnetron Injection Gun: Numerical Simulation and Experiment

Yu. A. Kalinin, V. N. Kozhevnikov, A. G. Lazerson, G. I. Aleksandrov, and E. E. Zhelezovskiĭ

Chernyshevsky State University, Saratov, 410026 Russia

E-mail: trubnicov@sgu.ssu.runnet.ru

Received March 4, 1998; in final form, July 2, 1999

Abstract—A theoretical and experimental study of spatial and temporal current oscillations in a magnetron injection gun is presented. Basic features of the device operation are ascertained. Complicated system dynamics, namely transitions from regular to chaotic oscillations in response to changing the system parameters, is revealed. The conclusions are drawn based on the analysis of the computed electron trajectories and output-current waveforms and spectra. Experimentally, the spectra of the beam-current oscillations, noise-intensity spectral density, etc., are obtained. Strong broadband microwave oscillations of the output current are observed for a wide range of the lengths of the emitting and the nonemitting portions of the cathode. © *2000 MAIK "Nauka/Interperiodica".*

INTRODUCTION

Complicated dynamical phenomena (particularly, dynamical chaos) in nonlinear oscillators have attracted considerable interest for many years due to their significance for both basic research and various applications. Nevertheless, among a large number of papers devoted to numerical and experimental investigations of chaos, only few studies concern the dynamics of systems with distributed parameters or many degrees of freedom. This fact stems from serious difficulties faced by anyone who tries to construct realistic models of such systems under the conditions where they behave in a complicated fashion. By now, a lot of papers have been devoted to the dynamical chaos of oscillations in electron flows without a magnetic field (O-type tubes); however, there are few papers in which analogous phenomena were studied in the presence of the crossed electric and magnetic fields (M-type tubes). As early as in [1, 2], it was noted that M-type tubes can produce intense internal noise, which makes them promising for practical applications.

The reason for an anomalously high noise level in M-type tubes is still poorly understood. For M-type diodes and guns, an attempt to explain the internal noise in terms of the complicated dynamics of an electron stream in crossed fields has been made in [3]. Here, we extend this approach to the magnetron injection gun (MIG), which may be useful for designing high-power microwave noise sources [4].

DESCRIPTION OF THE MODEL AND THE CONDITIONS OF THE NUMERICAL SIMULATION

A schematic of a MIG is shown in Fig. 1. It is seen that a real MIG is a fairly complicated device; therefore, the studying of the processes occurring in it is a rather intricate problem. Hence, when modeling the dynamics of the electron flow in such a device, we will use a simplified model shown in Fig. 2. We consider a plane-electrode diode in a magnetic field; the dimensions of the cathode and the anode in the *x*- and *z*-directions are assumed to be much larger than the interelectrode spacing. Our numerical analysis of the electron motion employs a version of a particle method (see, e.g., [5]) in which we allow for the forces acting on a

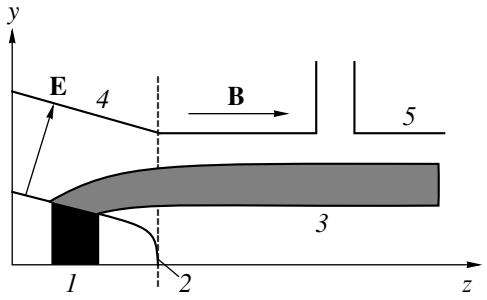

Fig. 1. Schematic of the magnetron injection gun: (*1*) cathode (the dashed line shows the boundary of the emitting region), (*2*) injection region, (*3*) helical electron beam, (*4*) control electrode, and (*5*) anode.

1063-7842/00/4507-0896$20.00 © 2000 MAIK "Nauka/Interperiodica"

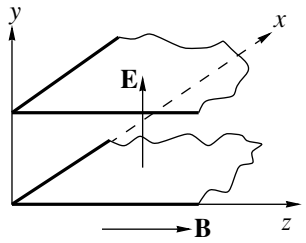

Fig. 2. Plane-electrode diode (a simplified model of a real device).

particle in the *y*- and the *z*-directions only. The only *y*-component of the space charge field is taken into account. The general concept of the model was formulated in [5], and its application to the problem of dynamical chaos was reported in [3]. Neglecting the edge effects, the configuration under study implies the following structure of the fields. The alternating electric field has the E_z component. In the *z*-direction, a drawing field E_z is also applied, whose amplitude depends on *y* as $E_z = Py$ and is constant along the *z*-direction. The magnetic field is uniform and has only one component $B_z = B_0$. Thus, the crossed static fields E_y and B_0 govern the motion of emitted electrons in the (x, y) plane, whereas the drawing electric field controls the electron motion along the *z*-axis.

With allowance for the above assumptions, the equations of electron motion in a M-type MIG [3] must be supplemented with the equation of motion along the *z*-axis:

$$\ddot{z} = Py, \tag{1}$$

where *z* and *y* are dimensionless coordinates and *P* is the ratio between the amplitudes of the longitudinal and transverse components of the electrostatic field.

Computer simulations of the complicated electron dynamics in an MIG involved the following control parameters: the emission current, the cathode length, the drift length (i.e., the length of the nonemitting portion of the cathode), and the parameter $P = E_s/E_a$ (the ratio between the longitudinal, E_s, and transverse, E_a, components of the electric field). The fixed parameters were the magnetic induction, the initial electron velocity, the interelectrode spacing, etc. Note that such parameters as the emission current, the cathode length, and the drift length are also used in the models of a magnetic diode and an M-type gun.

The numerical simulation yielded graphic representations of electron trajectories, waveforms of the output and induced currents, and spectral charts (Figs. 3–6).

RESULTS OF NUMERICAL SIMULATIONS

Numerical simulations revealed transitions to intense chaotic electron motion, which resembles turbulence and manifests itself in chaotic noiselike oscillations of the output current. The parameters of these oscillations are very sensitive to the above control

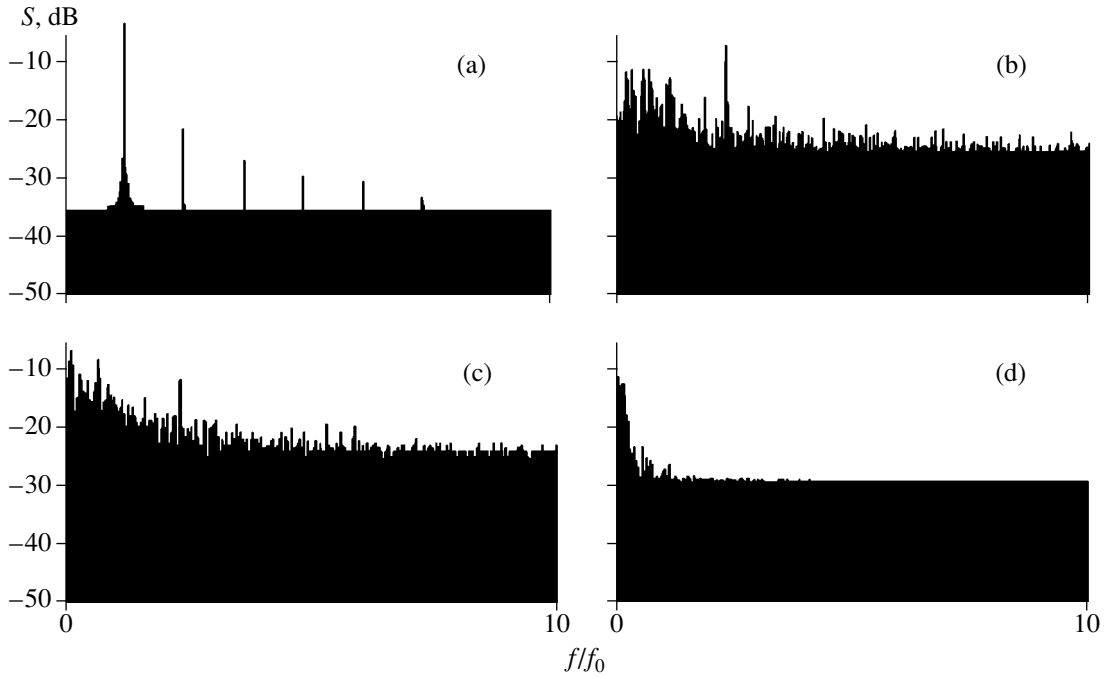

Fig. 3. Numerical simulation: the MIG output-current spectrum at a small emission current ($\omega_p/\omega_c = 0.16$) for the cathode length L_c = (a) 1, (b) 2, (c) 5, and (d) 10 mm.

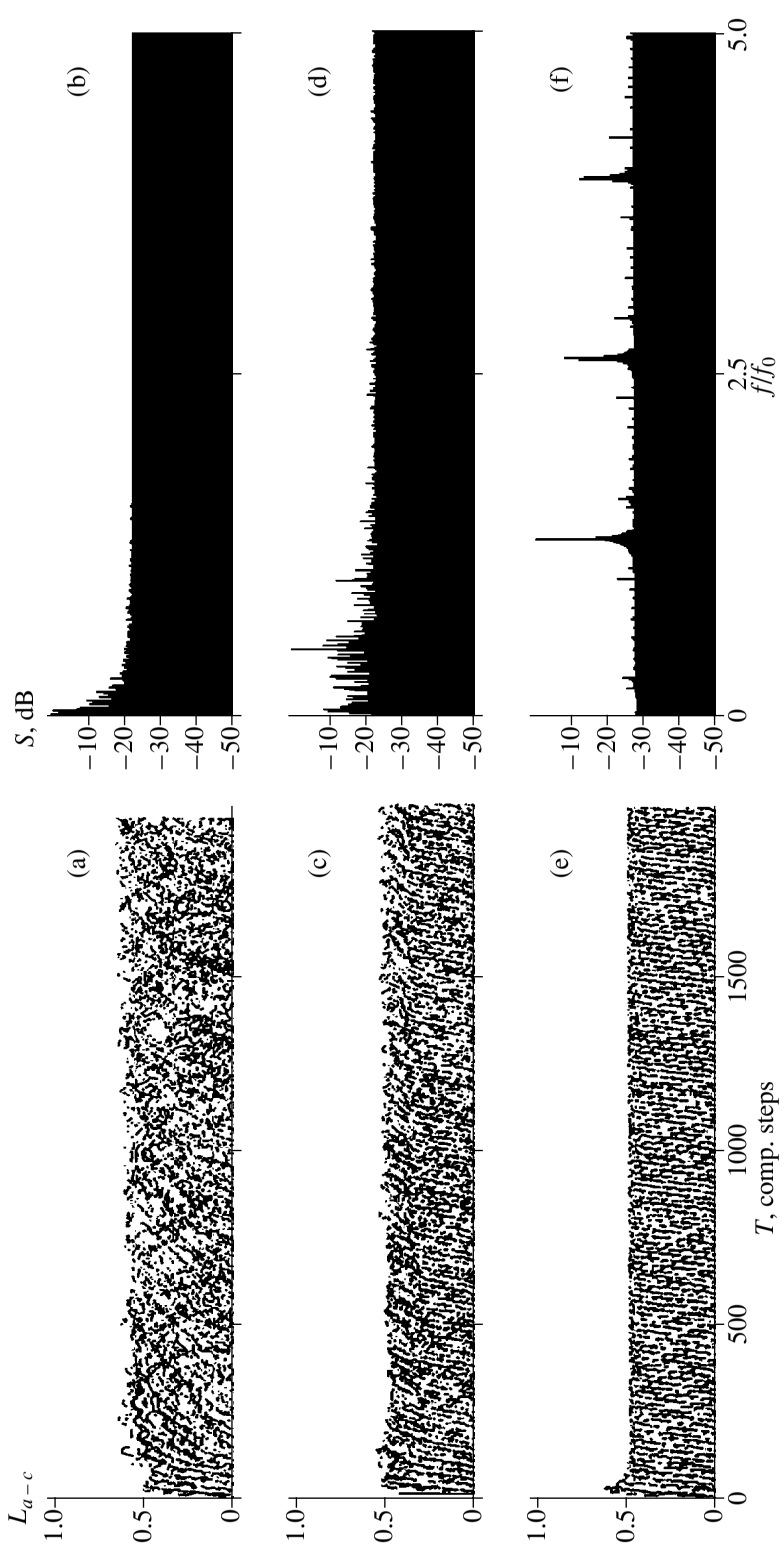

Fig. 4. Numerical simulation: (a, c, e) the electron trajectories and (b, d, f) the output spectrum for P = (a, b) 0.01, (c, d) 0.25, and (e, f) 2.0; L_{a-c} is the distance between the anode and the cathode.

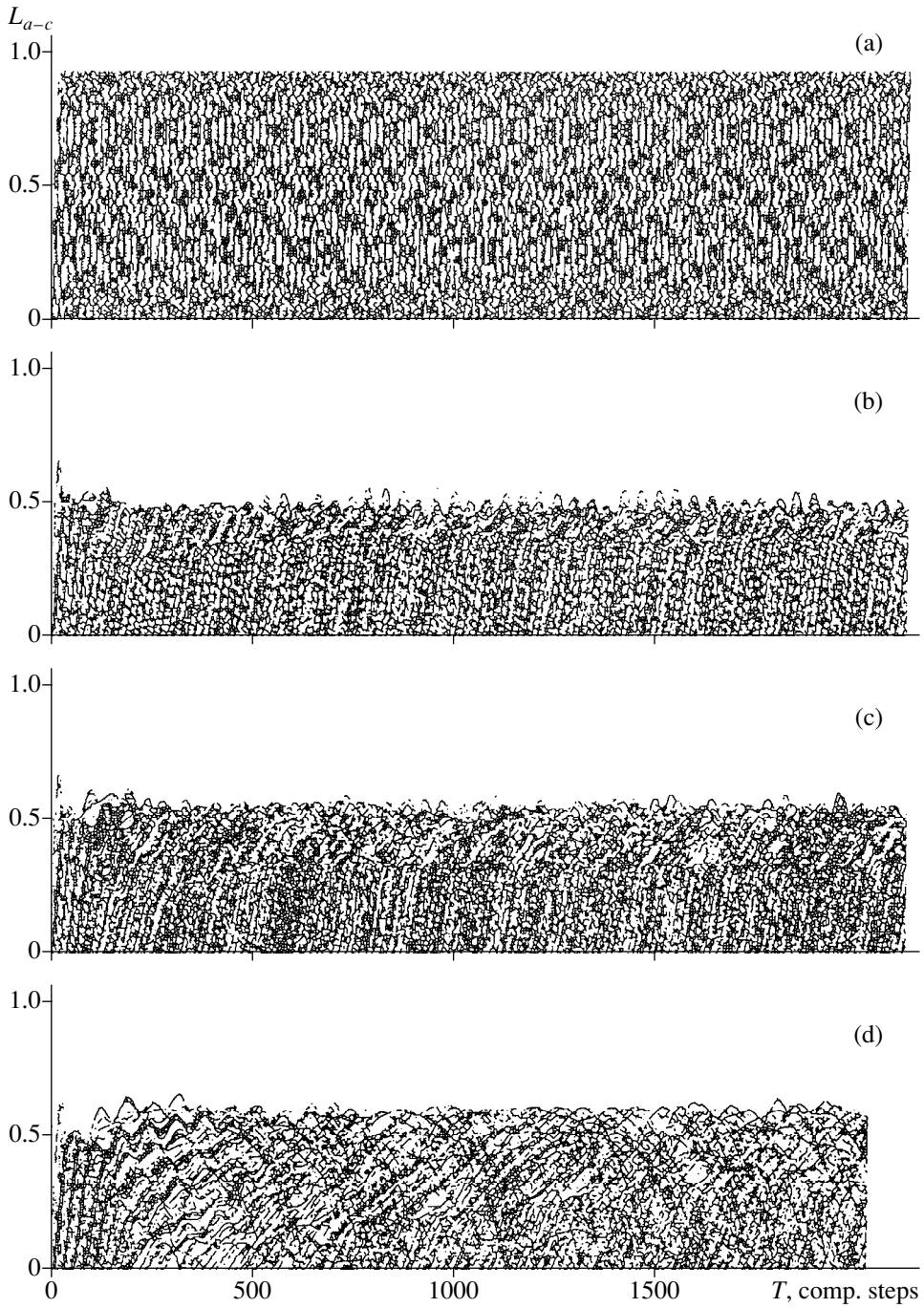

Fig. 5. Numerical simulation: electron trajectories for different values of the cathode length.

parameters: I_0 (the maximum emission current), L_c (the cathode length), L_{dr} (the drift length), and P.

The scenario of the transition to chaos is very similar to those for a magnetic diode and an M-type gun [3] but is quite different from those for systems with few degrees of freedom.

For small values of the emission current, a transition to the chaotic regime of electron motion occurs and the oscillations of the output current appear with an increase in the cathode length or/and a decrease in the parameter $P = E_s/E_a$. Figure 3 displays the normalized noise spectral density (NSD) as a function of the frequency (normalized to the cyclotron frequency) for different values of the cathode length. Figure 4 shows how the electron trajectories and NSD vary as the parameter P increases.

Figure 3 demonstrates that an originally excited periodic oscillation becomes quasi-periodic and then

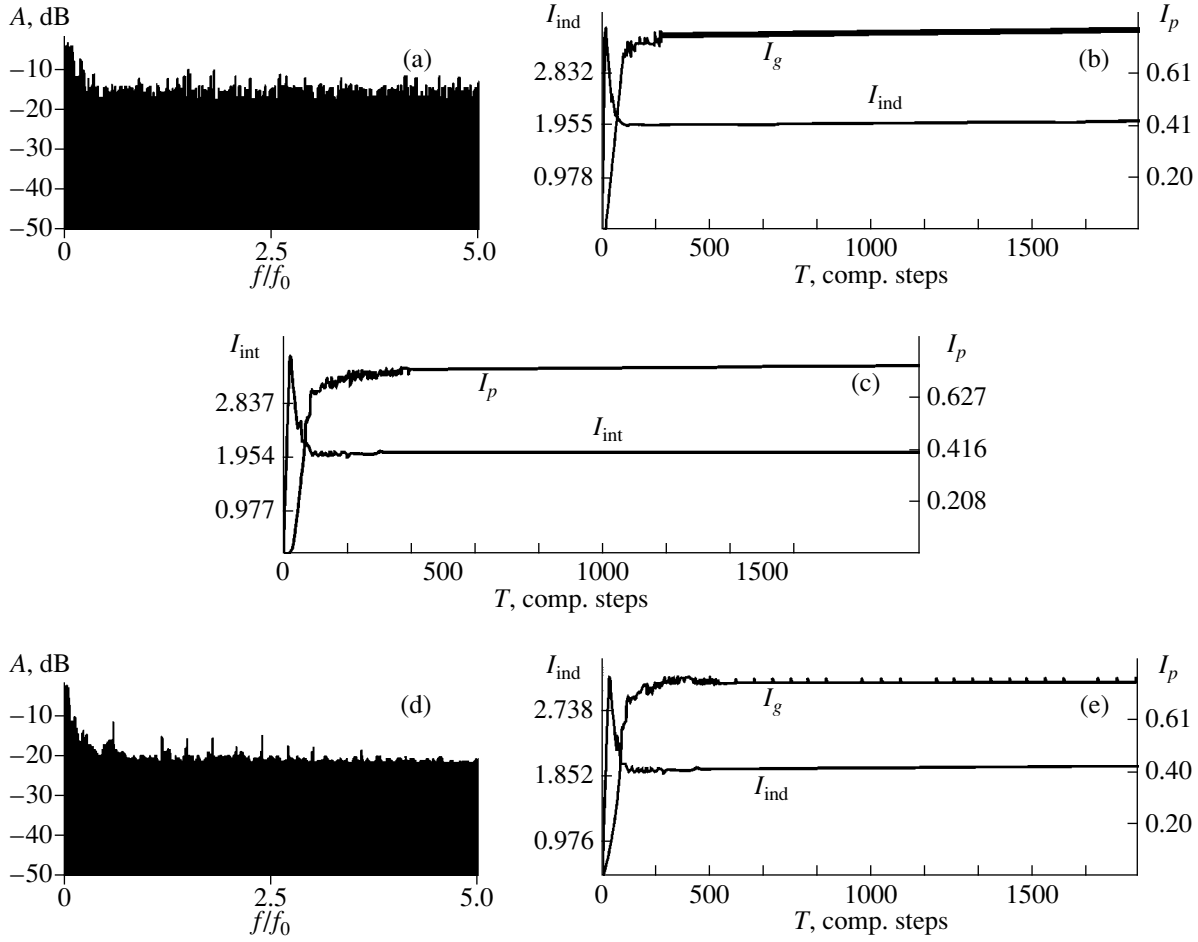

Fig. 6. Numerical simulation: (a, d) the output oscillation spectra and (b, c, e) waveforms of the gun current (I_g) and induced current (I_{ind}) for I_0 = (a, b) 1.442 (c) 1.443–1.449, and (d, e) 1.450 A.

chaotic. Note that the energy of chaotic oscillations concentrates in the lower frequency region. The excitation and development of this type of oscillation stem primarily from the oscillations of the beam boundary due to the modulation of the time required for different groups of electrons to reach this boundary. The beam boundary is formed by the groups of electrons (each group consisting of large number of particles) simultaneously occurring in this spatial region. Figure 5 shows the evolution of the electron motion with an increase in the cathode length. One can see the onset of chaotic oscillations of the beam boundary (Figs. 5a, 5b), the expansion of chaos (Fig. 5c), and the eventual establishment of turbulence in the entire interelectrode space (Fig. 5d).

As the emission current increases ($\omega_p/\omega_c > 0.5$, where ω_p and ω_c are the plasma frequency and the cyclotron frequency, respectively), the output current exhibits oscillations due to the development of turbulence in the electron flow (Fig. 5d). Starting from a certain value of the emission current, the electron trajectories begin to drift as a whole in the longitudinal direction under the action of an accumulated space charge, their behavior is transformed completely, and a kind of fluid turbulence arises in a fraction of the electron flow; there is a drift motion of a jet, on which a disordered motion of each of the other individual jets is superimposed. The spectrum of such oscillations is fairly wide, and their intensity concentrates in the lower frequency region (Fig. 3d). As the emission current increases further, chaos sets in at smaller drift lengths, appearing as a strong and broadband output current oscillations (Fig. 6a).

The transition to chaos resemble Landau's scenario for the onset of turbulence. However, there is some difference. At certain values of the parameters, the MIG produces a stationary current. As some parameter varies, quasi-periodic (sometime, single-frequency) oscillations are excited. As the parameter is varied further, the number of spectral components increases (the noise appears). The further variation in the parameter leads to a decrease in the number of spectral components; then, the noise level increases again, and so on. Finally, the transition to the regime of strong turbulence occurs. We also revealed that, at certain intermediate values of the parameter, the oscillations of the MIG current may dis-

appear completely so that the output current becomes time independent. This occurs in a narrow parameter range. After some time, quasi-stationary oscillations appear again; further, they may transform into turbulence and then terminate. Such a termination (quenching) of oscillations may recur several times (Fig. 6). For the fixed parameters, we observed up to three quenchings.

Under fully developed chaos, the NSD in an MIG was found to exceed the spectral density of the Schottky noise in electron guns by six to seven orders of magnitude (Fig. 7).

We also carried out the stability analysis of the solutions for different ranges of the control-parameter values. In particular, we studied the dependence of the normalized bandwidth on the step size (expressed in fractions of π) and on the number of the layers between any two successively extracted layers (Figs. 8, 9). It was found that the solution is the most stable if the layers are extracted at each step (or at least every fifth or sixth step) and if the step size (expressed in fractions of π) is 15–30 (an optimum value is 25). Such a large step size was dictated by computational problems.

EXPERIMENTAL RESULTS

The experiments were carried out with a model MIG schematically shown in Fig. 10. The device includes a conic cathode with a 1.5-mm-wide porous metallic thermionic emitter, control electrodes, and an anode. The anode–collector spacing is 3 mm. The angle of the cathode face with the axis is 15°.

The NSD in the MIG beam was measured with an analyzer, which was a segment of a slow-wave helix attached to a shield by means of ceramic rods and matched with an output coupler. Behind the analyzer, there was an electron collector (microwave probe), which was connected to the output coupler via a matching unit. The collector was designed as a segment of coaxial cable, which allowed us to measure the NSD. The MIG was placed into a demountable vacuum assembly under continuous evacuation [6]. The magnetic field was produced by permanent magnets; the maximum magnetic field strength was 2000 Oe.

The setup scheme allowed us to move the magnetic focusing system in both the longitudinal and transverse directions. The measurements were carried out in a pulsed regime (anode modulation). The other electrodes were connected to dc voltage sources. The signals from the probes (the helix and the collector) were examined with an S4-60 spectrum analyzer, which operates in the range 200 MHz to 19 GHz, and with a high-frequency S1-74 spectrum analyzer. The analyzers were exploited in conjunction with high-Q filters (the passband being 2 to 4 MHz), which offer the 1- to 2-GHz and 2- to 4-GHz tuning ranges; the detected output signals were recorded by an EPP-09 recorder.

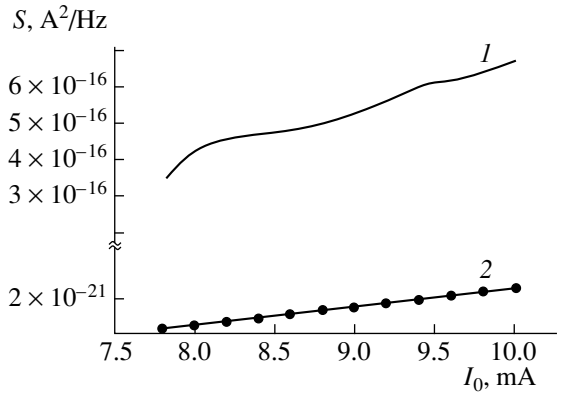

Fig. 7. Numerical simulation: the noise spectral density S vs. the maximum emission current I_0 for (*1*) fully-developed chaos and (*2*) Schottky noise.

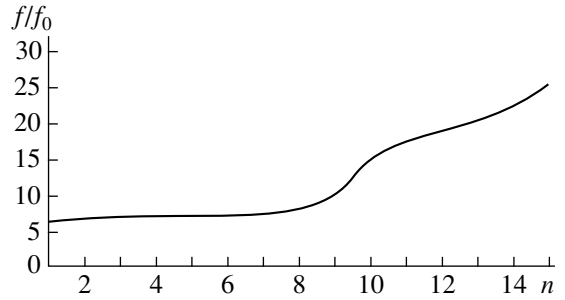

Fig. 8. Numerical simulation: the normalized bandwidth f/f_0 vs. the number n of layers between any two successively withdrawn layers.

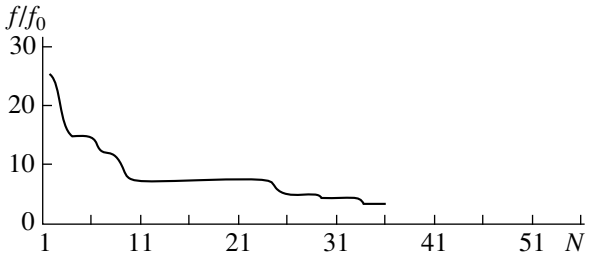

Fig. 9. Numerical simulation: normalized bandwidth f/f_0 vs. the step size (expressed in fractions of π).

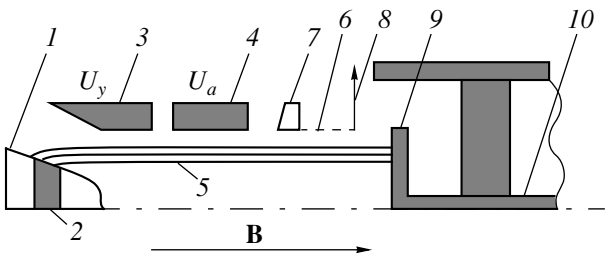

Fig. 10. Schematic of the model gyrotron MIG: (*1*) cathode, (*2*) emitter, (*3*) control electrode, (*4*) anode, (*5*) electron beam, (*6*) slow-wave helix, (*7*) absorber, (*8*) output coupler, (*9*) high-frequency probe (collector), and (*10*) inner conductor of the collector.

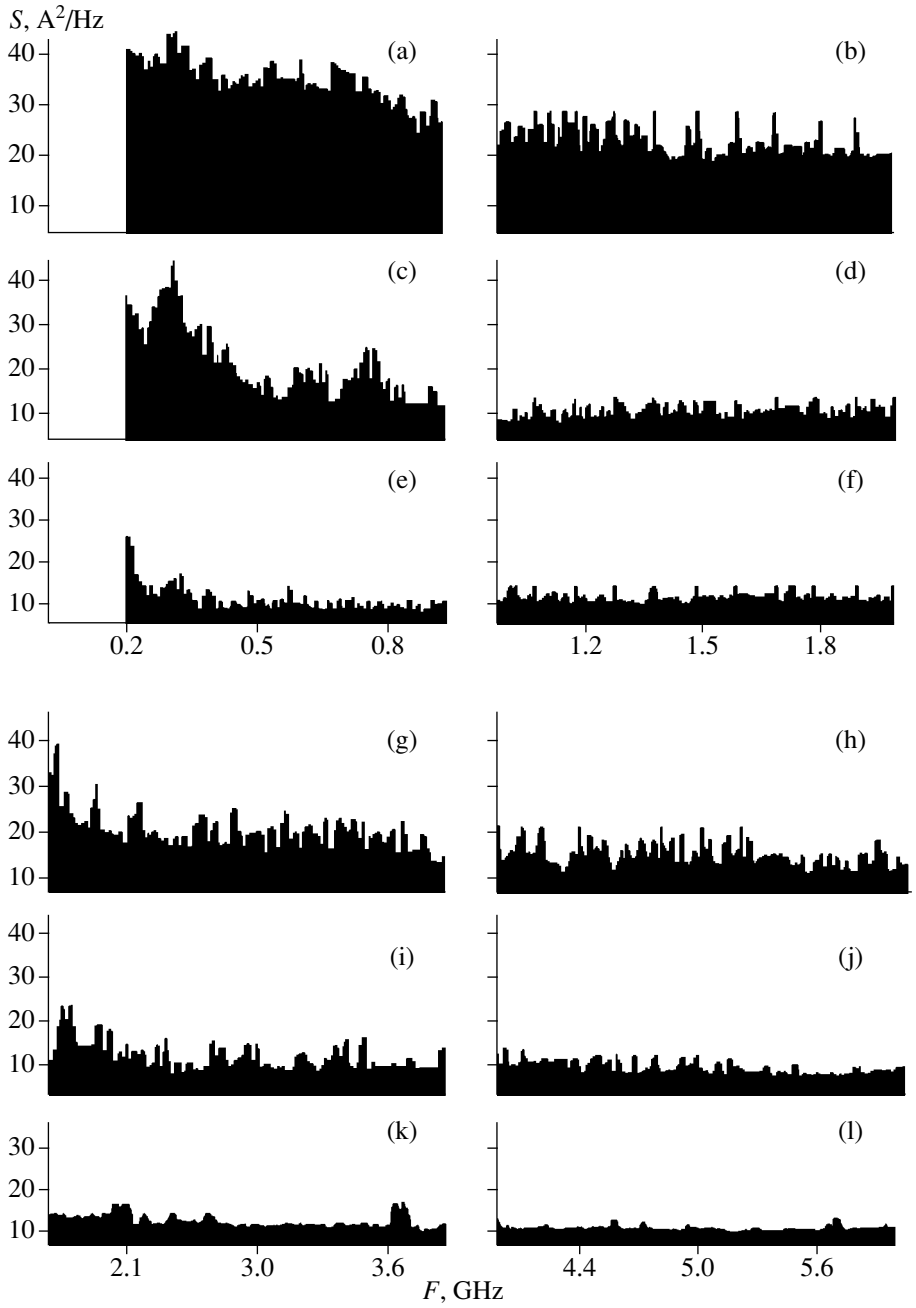

Fig. 11. Experiment: the oscillation spectra of the electron beam for (a, b, g, h) $U/U_0 = 1.0$ and $I/I_0 = 1.0$, (c, d, i, j) $U/U_0 = 0.57$ and $I/I_0 = 0.43$, and (e, f, k, l) $U/U_0 = 0.33$ and $I/I_0 = 0.11$. Panels (a–f) refer to $0.2 < F < 2.0$ GHz, and panels (g–l) refer to $2.0 < F < 6.0$ GHz.

Figure 11 presents typical spectra of stochastic oscillations in the beam, measured in the 200 MHz to 6 GHz range in different operating regimes. It is seen that the intensity of oscillations is the highest at lower frequencies (400–500 MHz). The higher frequency components grow with an increase in the accelerating voltage and the beam current.

Figure 12 displays the chaotic spectra for different values of the beam current, the latter being varied via the change in the heater voltage. Note that, by varying the heater voltage, we could change the structure of the oscillation spectrum and vary the amplitude of oscillations in a wide range.

Thus, chaotic oscillations may arise in a high-current beam produced by an MIG. The chaos stems from the presence of virtual cathodes. The properties of the excited oscillations can be controlled via the voltages applied to the electrodes, the magnitude and distribu-

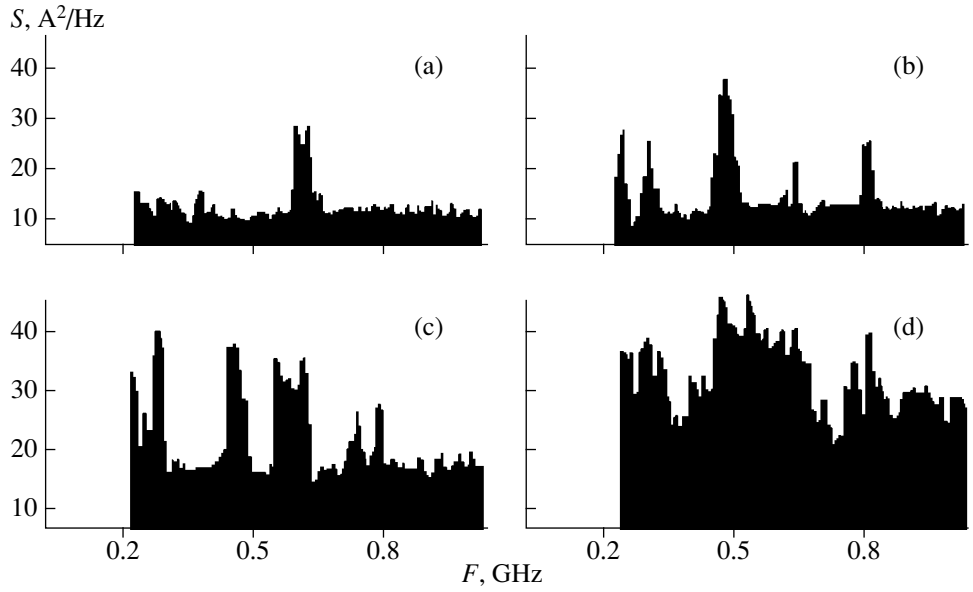

Fig. 12. Experiment: the oscillation spectra of the electron beam for different values of the heater voltage: (a) $U/U_h = 0.39$ with $I/I_0 = 0.11$, (b) $U/U_h = 0.47$ with $I/I_0 = 0.35$, (c) $U/U_h = 0.72$ with $I/I_0 = 0.71$, and (d) $U/U_h = 1.0$ with $I/I_0 = 1.0$.

tion of the magnetic field, and the magnitude and harmonic content of an external signal (single-frequency, multifrequency, or noise-like signal) that comes from a microwave source or from the output of the slow-wave helix through a feedback loop.

DISCUSSION

Figure 13 shows the NSD at frequencies of $f = 5$ and 10 GHz versus the normalized heater voltage $U_h = U_{h0}$, where U_{h0} is the heater voltage corresponding to the space-charge–limited current. The figure also shows the spectral density $S(U_h/U_{h0})$ of Schottky noise. It is seen that the intensity of oscillations at the output of the anode is much higher than the intensity of Schottky noise (by six to seven orders of magnitude) and does not fall and even rises at the heater voltages higher than U_{h0}.

Note that the variations in the heater voltage U_h and the accelerating voltage U_0 in the experiment correspond to the variations in the emission current I_0 and the parameter P in numerical simulations. Therefore, we can point out a qualitative agreement between the behaviors of the experimental and computed spectra when the relevant parameters are varied. We also note that, in both the experiment and numerical simulations, the NSD in the MIG current is higher by six to eight orders of magnitude than the intensity of Schottky noise.

The measured dependences of the spectra of chaotic current-density oscillations on the electric and magnetic parameters in MIG-based systems allowed us to reveal the mechanism for the excitation and sustaining of oscillations in the MIG beams and explain why the measured noise level is higher than the theoretical one. Specifically, two factors should be highlighted. The first factor is the formation of a virtual cathode (a minimum of the potential) near the MIG cathode; the influence of this factor increases with an increase in the width of the emitting belt at the cathode. The second factor is the formation of a magnetic mirror in the region where the magnetic field increases. A substantial radial component of the magnetic field in this region gives rise to a second virtual cathode. The chaotic oscillations in high-current MIG beams result from a decreased drift velocity of electrons and a significant scatter in the beam electron

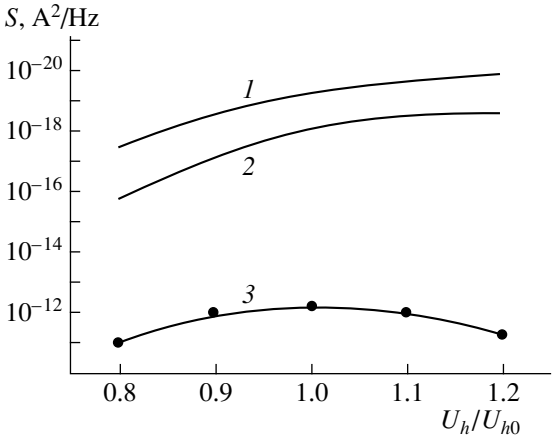

Fig. 13. Experiment: the NSD at the output of the anode vs. the normalized heater voltage at frequencies of (*1*) 5 and (*2*) 10 GHz; curve *3* refers to Schottky noise.

velocity as well as from oscillations of the parameters of the virtual cathodes.

CONCLUSIONS

The results of numerical and experimental studies show that, in an MIG, chaotic oscillations whose spectral intensity is higher than the intensity of Schottky noise can arise. The numerical and experimental results are in good qualitative agreement. Thus, the theoretical model presented can adequately describe the processes occurring in real devices. Quantitative discrepancies between the theory and the experiment (including a higher noise level measured) may be attributed to the assumptions of the model (such as replacing a realistic gun configuration with a plane-electrode diode and neglecting the cycloidal motion of electrons).

Finally, the results obtained allow us to infer that the anomalously high noise level observed previously (see, e.g., [3]) has a dynamical nature. We think that such MIGs could serve as high-power sources of broadband signals.

REFERENCES

1. G. Baneman, in *Crossed-Field Microwave Devices*, Ed. by E. Okress (Academic, New York, 1961; Innostrannaya Literatura, Moscow, 1961), Vol. 1.
2. B. L. Usherovich, *Electronics Reviews, Ser.: Microwave Electronics* (1969), Vol. 7.
3. E. E. Zhelezovskiĭ, A. G. Lazerson, and B. L. Usherovich, Pis'ma Zh. Tekh. Fiz. **21** (18), 12 (1995) [Tech. Phys. Lett. **21**, 730 (1995)].
4. E. E. Zhelezovskiĭ, USSR Inventor's Certificate No. 788993 (Moscow, 1980).
5. L. M. Lagranskiĭ and B. L. Usherovich, Voprosy Radioélektron., Ser. I: Élektron. **1**, 3 (1964).
6. Yu. A. Kalinin and A. D. Essin, *Experimental Methods and Tools in Vacuum Microwave Electronics* (Saratov, 1991), Part 1.

Translated by A.A. Sharshakov

Technical Physics, Vol. 45, No. 7, 2000, pp. 905–908. Translated from Zhurnal Tekhnicheskoĭ Fiziki, Vol. 70, No. 7, 2000, pp. 92–95.

Effect of Thermal Annealing on Spectral Properties of Electrodeposited Carbon Films

V. P. Dymont, M. P. Samtsov, and E. M. Nekrashevich

Institute of Solid-State Physics and Semiconductors, Academy of Sciences of Belarus, Minsk, 220072 Belarus
E-mail: ryzkov@ifttp.bas-net.by

Received April 7, 1999

Abstract—The effect of thermal annealing on properties of carbon films deposited on nickel electrodes by the electrodeposition method was studied. It has been shown that annealing at a temperature of 300°C results in the formation of nanosize diamond clusters. With an increase in the annealing temperature, the size of diamond clusters diminishes. At an annealing temperature of 900°C, all of the carbon enters into reaction with nickel, thus forming nickel carbide. *© 2000 MAIK "Nauka/Interperiodica".*

INTRODUCTION

A number of properties of diamond-like films (transparency in the visible and infrared spectral ranges, chemical stability, high hardness and good heat conduction) make them an attractive material for use in various technological fields. Characteristics of the diamond-like carbon films largely depend on the method and conditions of growth. Earlier, we developed a new technique of producing diamond-like carbon films using the electrolytic process. Description of this method and some properties of the obtained coatings are given in [1, 2]. In this work, results of studies of the electrodeposited films annealed at various temperatures by the methods of Raman scattering, infrared absorption, and Auger spectroscopy are presented.

SAMPLE PREPARATION AND MEASUREMENT TECHNIQUES

The films were prepared by the electrolytic method at a low (–40°C) temperature. As an electrolyte, acetylene solution in liquid ammonia was used. The electrolysis was carried out at a voltage of 10 V for 15 h. The film deposition technique is described in more detail elsewhere [2]. Under these conditions, fairly thick (1–2 μm) smooth light-brown high-ohmic films were obtained. Properties of as-deposited films and films annealed at 300, 600, and 900°C were studied. The annealing was carried out for 1 h in quartz ampoules pumped out to pressures not higher than 10^{-4} Pa. Raman scattering spectra in the range of 1000–1800 cm^{-1} at room temperature were registered using the RAMALOG-44 spectrometer (wavelength of incident radiation λ = 514.5 nm). IR spectra in the range 1000–4000 cm^{-1} were taken with the PERKIN-ELMER 180 instrument in reflection geometry at room temperature. Auger spectra were registered with the PERKIN-ELMER PHI-660 spectrometer.

EXPERIMENTAL RESULTS

A vacuum anneal of carbon films results in visually detectable modifications of the surface. A film annealed at 300°C changes in color from light-brown to almost black and remains physically intact. Annealing at 600°C makes the film still darker: it becomes black and glassy. After annealing at 900°C, the film becomes transparent. For all samples of the Raman scattering (RS) spectra, infrared (IR) spectra and spectra of Auger electrons were taken.

(a) As-deposited film. An RS spectrum of the as-deposited film with a broad asymmetric band in the frequency range 1200–1700 cm^{-1} is shown in Fig. 1. In Fig. 2, an IR absorption spectrum of the same film fea-

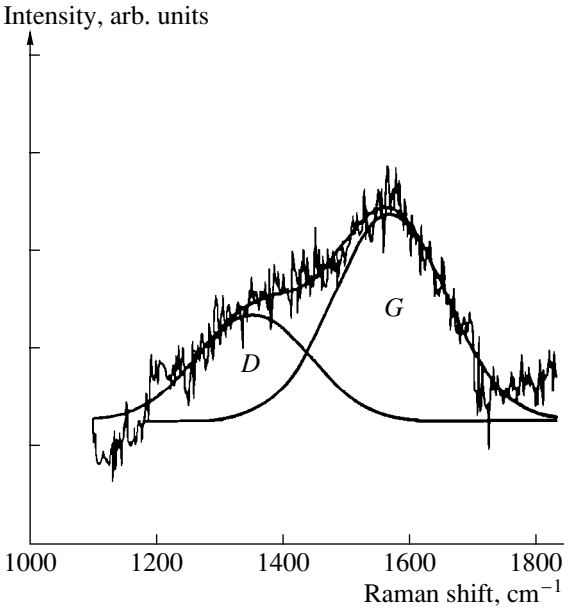

Fig. 1. Raman spectrum of the as-deposited film.

1063-7842/00/4507-0905$20.00 © 2000 MAIK "Nauka/Interperiodica"

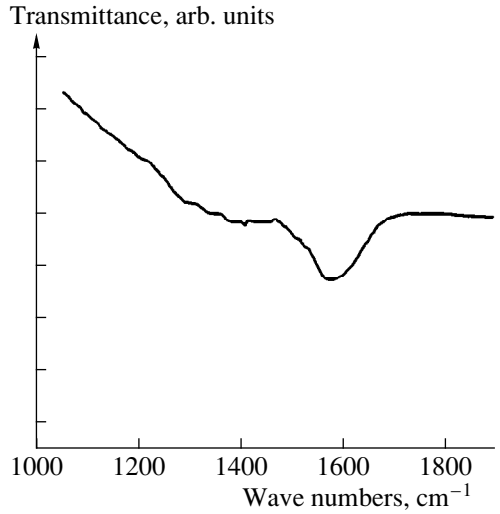

Fig. 2. IR absorption spectrum of the as-deposited film.

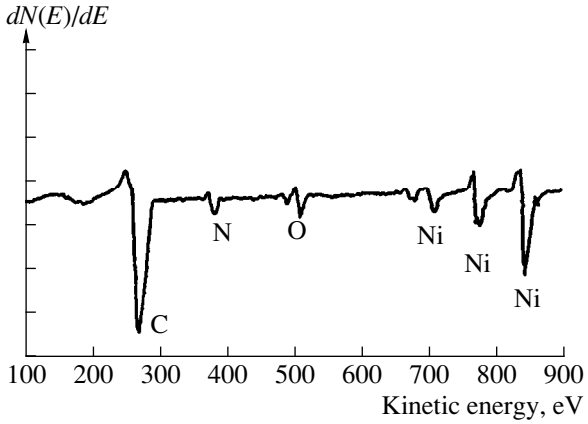

Fig. 3. Auger spectrum of the as-deposited film.

turing two broad absorption bands peaking at 1580 and 1350 cm^{-1} is shown. In an Auger spectrum of the film in Fig. 3, besides the carbon peak, peaks due to nitrogen, oxygen, and nickel are present.

(b) Film annealed at 300°C. An RS spectrum of this film is shown in Fig. 4. It is generally similar to the spectrum of the previous sample, except for some enhancement of the scattering intensity at lower frequencies. The IR spectrum of the annealed film differs only slightly from that of the as-deposited film. There are also no significant differences in the Auger spectra of these samples.

(c) Film annealed at 600°C. In the Raman spectra of this film (Fig. 5), further enhancement of the relative intensity of the scattering band in the vicinity of 1350 cm^{-1} can be seen. The Auger and IR spectra of the samples remain practically unchanged.

(d) Film annealed at 900°C. Spectral characteristics of the film annealed at this temperature show considerable transformations. In the RS spectrum, the scattering bands in the 1000–1800 cm^{-1} range disappear. Considerable changes are seen in the Auger spectra as well (Fig. 6). The lines due to nitrogen are missing and, besides, significant changes are found in the shape of the low-energy part of the carbon peak (inset in Fig. 6).

DISCUSSION

Raman spectra of the two known crystalline forms of carbon, graphite (sp^2 hybridization), and diamond (sp^3 hybridization) have been considered in detail in [3]. For monocrystalline and polycrystalline diamond, only one peak at a frequency of 1332 cm^{-1} is observed. The spectrum of monocrystallyne graphite also consists of a line in the 1590–1600 cm^{-1} range. The Raman spectrum of polycrystalline graphite consists of two bands. A *G*-line (graphite line) is localized around 1600 cm^{-1} and a *D*-line (disordered graphite) in the vicinity of 1355 cm^{-1}. The *D*-line in the scattering spectrum is due to the presence of small-sized crystallites of graphite which causes the violation of the selection rules. The ratio of integrated intensities of the *D*- and *G*-lines (I_D/I_G) is inversely proportional to the size of crystallites [3]. The Raman spectra of carbon films containing carbon in sp^2 hybridization are similar to spectra of finely crystalline carbon [4]. The absence in the RS spectra of the diamond line, even in those cases where X-ray diffraction analysis indicates the presence of diamond, is usually explained by the fact that the efficiency of Raman scattering for diamond is lower by a factor of 55 than for graphite. Therefore, the quantity of the sp^3-hybridized carbon is judged by indirect evidence. Therefore, the spectral position of the *G*-line gives an indication of the ratio of carbon in sp^2 and sp^3 hybridization states in a sample [5]. Contributions to the profile of the RS line of a carbon film may come from other vibrations related to sp^3 hybridization carbon. For example, the spectrum may contain the following lines: a line due to disordered sp^3-bonded carbon at 1140 cm^{-1}; a line due to distorted sp^3-bonded carbon at 1488 cm^{-1}; and a line due to hexagonal modification of diamond (lonsdaleite) at 1305 cm^{-1} [6].

Thus, RS spectra of carbon films can be represented as a superposition of Gaussian curves, with peak positions, integrated intensities, and halfwidths as fitting parameters. By comparing the obtained results with published data, one can make judgments about the types of chemical bonds in the compounds comprising the films under study, their relative content, as well as the degree of perfection of the crystalline structure.

The experimental spectra could be approximated in most cases by four Gaussian curves under the assumption that two of the curves are related to sp^2- and two more, to sp^3-hybridized carbon. The spectrum of the film prior to annealing is best described with two Gaussian curves centered at 1352 cm^{-1} (*D*-line) and 1568 cm^{-1} (*G*-line). This shift of the *G*-line from the

asymptotic position for graphite at 1600 cm^{-1} towards smaller wave numbers may be caused by the presence of sp^3-hybridized carbon. According to [7], the position of the *G*-line at 1568 cm^{-1} corresponds to a 70%-content of sp^3-hybridized carbon. The ratio of integrated intensities of the *D*- and *G*-lines is equal to 0.5. This value is characteristic of hydrogenated amorphous silicon films (usually in the range 0.3–3.0), and its change is due to the difference in the number and/or size of the graphite clusters. The halfwidth of the *D*- and *G*-lines is equal to 180 cm^{-1}. The same value is characteristic of carbon films containing small graphite clusters.

The presence in the IR absorption spectrum of bands in the region from 1350 to 1600 cm^{-1} suggests that part of the carbon atoms has been replaced by nitrogen. This conclusion is based on an observation that, in the IR range, vibrations related to sp^2-bonded carbon are inactive. Substitution of nitrogen for part of the carbon lifts this prohibition [8]. The presence of nitrogen in the film is confirmed by the nitrogen line in the Auger spectra. Regrettably, qualitative determination of nitrogen in the film from available data is not possible. It can only be hypothesized that the nitrogen content does not exceed 5–10 at. %.

It is highly probable that, at room temperature, the film consists of small graphite clusters doped with nitrogen and uniformly distributed in the matrix of amorphous hydrogenated carbon.

After annealing at 300°C, the *D*- and *G*-components of the Raman scattering spectrum become narrower and shift towards positions asymptotic for graphite (Fig. 4), which is evidence of the structural ordering of sp^2-hybridized forms of carbon. The number and size of the graphite clusters do not change because the ratio of integrated intensities I_D/I_G remains equal to about 0.5. Besides, components related to the sp^3-hybridized carbon appear in the film spectrum; a broad line centered at 1320 cm^{-1} (curve *1* in Figs. 4, 5), which can be related to finely dispersed diamond, and a line centered at 1440 cm^{-1} (curve *2* in Figs. 4, 5), which can be related to distorted sp^3-hybridized carbon [6]. The formation of the diamond form of carbon in the films at atmospheric pressure does not run counter to the generally accepted view of the stability of allotropic modifications of carbon (graphite and diamond) in the ultradisperse state. For example, according to estimates in [10], carbon clusters with size $\ll$10 nm at room temperature and normal pressure are stable in diamond modification, whereas the bulk material representing the stable phase under these conditions is graphite.

The RS spectrum of the film annealed at 600°C is also composed of four Gaussian curves (Fig. 5). The lines centered at 1350 cm^{-1} (*D*) and 1593 cm^{-1} (*G*) can be ascribed to polycrystalline graphite; the line centered at 1480 cm^{-1} (curve *2*) to distorted sp^3-hybridized carbon; and the line at 1280 cm^{-1} (curve *1*) to finely dispersed diamond. The ratio (I_D/I_G) at this temperature also remains equal to 0.5. Halfwidths of the lines *D* and *G* decrease considerably, down to 90 cm^{-1} and 70 cm^{-1}, respectively. Also, the position of the *G*-line is close to the asymptotic position for graphite. This indicates the greater perfection of the structure of existing graphite clusters. The observed shift of the position of the "diamond" line (curve *1*) towards smaller wave numbers and the simultaneous increase of the integrated intensity and the halfwidth of the line relating to the distorted sp^3-hybridized carbon (curve *2*) indicate that the size of diamond clusters decreases as the temperature is raised.

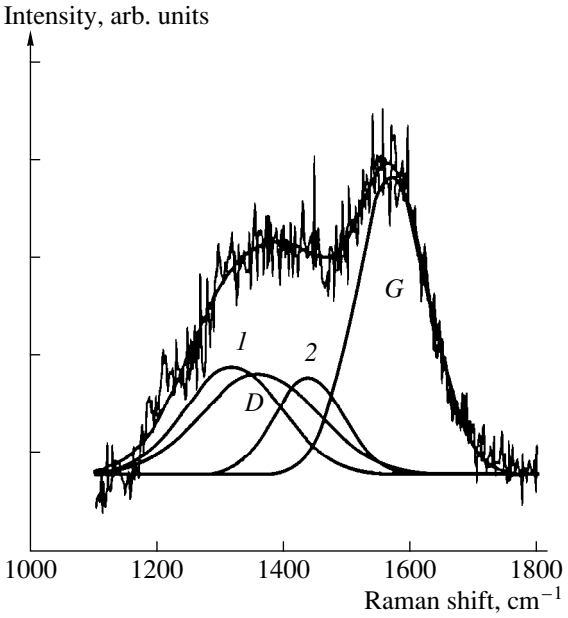

Fig. 4. Raman spectrum of the film annealed at 300°C.

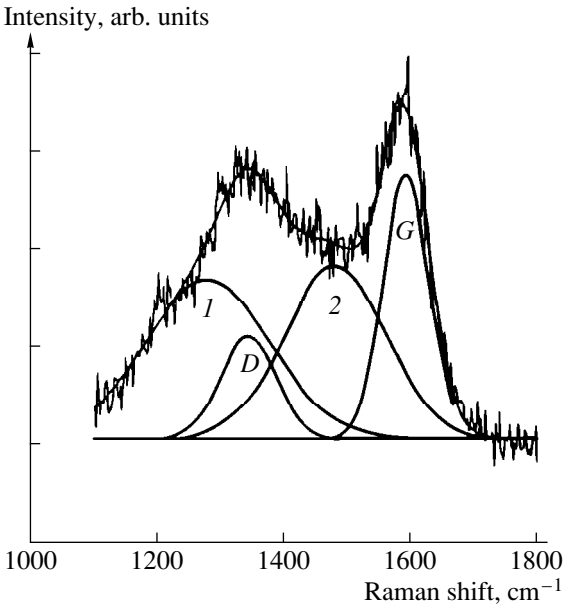

Fig. 5. Same as Fig. 4, at 600°C.

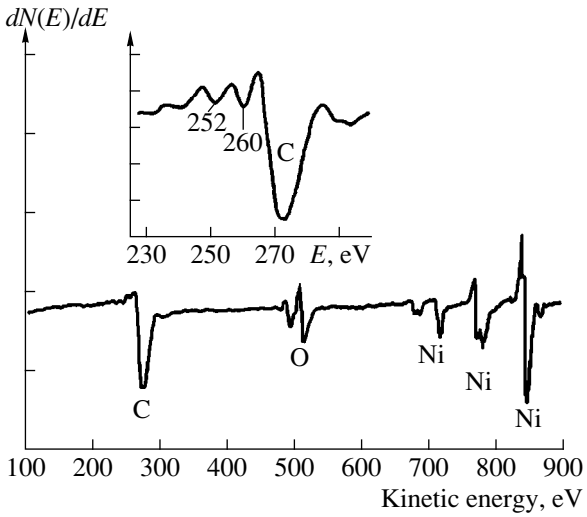

Fig. 6. Auger spectrum of the film annealed at 900°C.

It is very likely that during the annealing of the film at 900°C, the interaction of carbon with finely dispersed nickel, present in the film bulk, takes place. As a result of this interaction, nickel carbide is formed. An Auger spectrum of such a film shown in the inset in Fig. 6 is very much like that of the pure nickel carbide.

CONCLUSIONS

Analysis of the obtained data warrants a conclusion that the film that is not subjected to heat treatment consists of nanosize graphite clusters uniformly distributed in a matrix of hydrogenated amorphous carbon in which a part of the carbon atoms has been replaced by nitrogen atoms. It has been established that quite a large quantity of nickel and some oxygen are present in the film. Therefore, the electrolytic method under given conditions yielded films of rather complex composition containing 70–80 at. % of carbon. Analysis of the Raman spectra suggests that annealing at 300°C, besides producing a higher degree of order in the film, causes the formation of nanosize diamond clusters. With a further increase of the annealing temperature, the crystal structure of the graphite clusters becomes more perfect, and the size of diamond clusters diminishes. At temperatures above 600°C, the interaction of carbon with nickel in the film bulk takes place. As a result, all carbon reacts with nickel thus forming nickel carbide.

The work was supported by the Foundation for Basic Research of the Republic of Belarus. One of the authors acknowledges financial support from the Ministry of Education of the Republic of Belarus.

REFERENCES

1. V. P. Novikov and V. P. Dymont, Pis'ma Zh. Tekh. Fiz. **22** (7), 39 (1996) [Tech. Phys. Lett. **22**, 283 (1996)].
2. V. P. Novikov and V. P. Dymont, Appl. Phys. Lett. **70**, 200 (1997).
3. F. Tuinstra and J. L. Koenig, J. Chem. Phys. **53**, 1126 (1970).
4. V. D. Andreev, T. A. Nachal'naya, Yu. I. Sozin, and V. A. Semenovich, Tekh. Sredstvo Svyazi, Ser. Tekhnol. Proizvodstva Oborudovanie, No. 4, 18 (1991).
5. R. O. Dillon, J. A. Woollam, and V. Katkanat, Phys. Rev. B **29**, 3482 (1984).
6. L. C. Nistor, J. V. Landuyt, V. G. Ralchenko, *et al.*, Diamond Relat. Mater., No. 6, 159 (1997).
7. S. Prawer, K. W. Nugent, Y. Lifshitz, *et al.*, Diamond Relat. Mater., No. 5, 433 (1996).
8. J. H. Kaufman, S. Metin, and Saperstein, Phys. Rev. B **39**, 13053 (1989).
9. M. M. Lacerda, D. F. Franceschini, F. L. Freire, *et al.*, J. Vac. Sci. Technol. A **15**, 1970 (1997).
10. M. Y. Gamarnik, Nanostruct. Mater. **7**, 651 (1996).

Translated by B. Kalinin

Technical Physics, Vol. 45, No. 7, 2000, pp. 909–914. Translated from Zhurnal Tekhnicheskoĭ Fiziki, Vol. 70, No. 7, 2000, pp. 96–101.

Deformation of the Contact Area and Adhesive Friction between a Scanning Frictional Microscope Probe and the Atomic-Flat Surface

G. V. Dedkov and M. B. Dyshekov

Kabardino-Balkar State University, ul. Chernyshevskogo 173, Nalchik, 360004 Russia

E-mail: gv dedkov@mail.ru

Received November 22, 1999

Abstract—The determination of the equilibrium atomic structure of a nanotribocontact, formed by a hard probe to be viewed as a paraboloid of revolution and subjected to an external load, with the soft surface modeled by a set of parallel atomic planes is considered. Structural, energy, and load characteristics are calculated. In addition, dissipative static adhesive friction as a function of the normal load and the radius of probe curvature for the diamond–graphite system is derived. A number of approximations of the interatomic potentials is used. It is shown that an allowance for the deformation of the contact area causes the adhesive frictional force in the tensile (negative) load range to decrease. For positive loads in a range of 0–80 nN, the variation of the frictional force (when deformation is taken into account) depends on the radius of the probe curvature and the used approximation of the interaction potential. The dependence of friction on the radius of the probe curvature is close to a direct proportionality. The calculated results are compared with the available experimental data. *© 2000 MAIK "Nauka/Interperiodica".*

The achievements of scanning probe microscopy have stimulated the advent and development of the novel promising fields of research in physics, such as nanotribology and nanolithography [1–3], that makes it necessary to detail the nanostructure friction mechanisms. According to present-day concepts, the frictional force involves deformation and adhesive components, the latter being theoretically described in the most difficult manner. There are two main approaches to solving this problem. They are based on the macroscopic contact theory [4–6] and molecular-dynamics methods [7–11]. In the first case, the theory uses the values of elastic characteristics known at the macrolevel and a semiempirical relationship of Bowden and Tabor for the frictional force [4]

$$F = \tau A,$$

where τ is the shear strength and A is the actual contact area. Generally speaking, both quantities lose their meaning on the atomic scale; therefore, the results derived by means of the contact theory must be treated critically. In this case, in addition, the physical mechanism of friction-related irreversible energy losses is not revealed. Numerical simulations have shortcomings as well, since one has, first of all, to limit the number of particles involved in the process of the dynamical relaxation that makes it difficult to evaluate the fraction of the energy dissipated into the heat. This is especially the case if a "thermal" model of the system is initially considered. In molecular-dynamics calculations, inevitably, it is necessary to consider only the finite number of atoms of both the nanoprobe and surface; therefore, during the dynamical relaxation, the energy is "trapped" in the contact area, whereas it must be actually dissipated into the bulk of the contacting bodies via vibrational modes. As a result, when loading a contact, the response of the simulated system may significantly differ from that of an actual one. There are certain difficulties in a qualitative determination of the contribution of the "internal" and "external" frictions [9–11], which are associated with energy dissipation into the bulk of the rubbing bodies and governed by the dissipative component of lateral forces. Finally, the temporal and velocity scales for the numerical experiments (typical values are 1–1000 m/s) significantly differ from the scanning velocities in the probe microscopy (10^{-4}–10^{-7} m/s). In [12], we suggested a "quasistatic" adhesive friction model for the nanoprobe slipping along the atomically flat surface, in which each elementary slipping act ("microslip") is accompanied by a drastic disruption of existing adhesion bonds between atoms of the tip and surface and, on the other hand, by the avalanche-like process of creating new bonds. The residual potential atomic energy of disrupting and new arising bonds is further transformed into the heat via vibrational modes. According to this model, we have the following expression for a dissipative static (velocity-independent) adhesive frictional force

$$F = \frac{\sum_m |\Delta w_m|}{\Delta x}, \qquad (2)$$

1063-7842/00/4507-0909$20.00

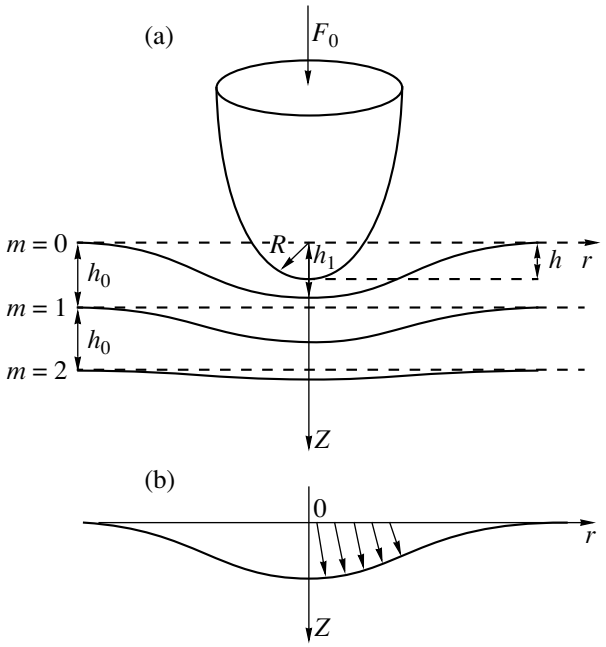

Fig. 1. (a) Schematic diagram of the contact area between the tip of a probe microscope and the surface and (b) the shift directions of atoms of the top atomic plane of a material due to deformation.

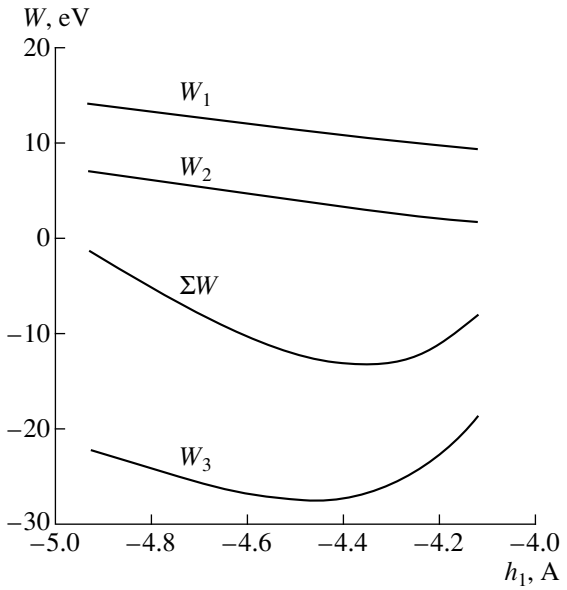

Fig. 2. The single contributions and the total contact energy for a diamond–graphite system for the probe with $R = 15$ nm as a function of the vertical shift of the top graphite plane, h_1. The height of the probe with respect to the non-shifted position of the top plane is $h = -0.2$ nm.

where Δw_m is the change in energy of the mth bond due to a microslip and Δx is the corresponding travel of the probe. The initial position of the nanoprobe corresponds to the minimum of the tribosystem energy. The experiments performed with frictional microscopes demonstrate that a typical travel Δx is approximately equal to the surface lattice constant independently of dimensions of the contact area. In the framework of the model under consideration, this fact has a simple geometric explanation, since the total number of the adhesive bonds and the probe–surface interaction energy quantitatively display the periodicity of the surface atomic structure for a lateral travel of the probe apex, and its equilibrium position corresponds to the minimum of the tribosystem energy and is separated by a spacing equal to the lattice period from other neighboring positions. To overcome the corresponding potential barrier, each microslip needs an "activation energy" accumulated in the form of the elastic deformation energy in the cantilever–probe–surface system as the movable part of the microscope scans along the surface.

In [12], we considered a simplified contact model regardless of the deformation of the contact area, which is justified only for fairly large distances of the probe apex from the surface. In this study, we take the deformation into consideration by means of a geometric model allowing us to find the form of the contact area and the arrangement of atoms in it by minimizing the energy of the system. Further, we calculate the frictional force using formula (2). The particular numerical calculations are performed for the contact between a hard diamond probe and a (0001) graphite surface. The choice of this system is governed by simplicity (identical atoms) and the possibility of applying the rather simple approximations of interatomic potentials. In addition, the graphite was used as a standard test-object in nanoprobe microscopy.

The diamond probe is assumed to have the form of a paraboloid of revolution with a radius of curvature R. It is oriented by the symmetry axis [111] along the normal to the surface, which is modeled by a set of atomic planes separated by a spacing h_0. Figure 1a shows an approximate deformation of the surface, when an external normal force P is applied to the probe. The shift directions of atoms of a single atomic plane (initial atom sites are shown by the dashes) are given in Fig. 1b. We assume that the shape of the deformed atomic layers replicates the axial probe symmetry and may be defined by a model function $z(r)$. In specific calculations, we used the functions

$$z(r) = \frac{b^4}{2R(r^2 + b^2 a^{2m})}, \qquad (3)$$

where R is the radius of the probe curvature, m is the serial number of the atomic plane (counting inward of the sample), and a and b are the variational parameters.

Equation (3) automatically takes into account the fact that the radius of curvature of the top atomic plane at $r = 0$ is R and with rising m (at $a > 1$), the planes become more and more "smooth." The suggestion about the radius of curvature, however, is not basically

important. With allowance for the above suggestions, the relation between the (x, y) coordinates of an atom on the nondeformed plane and $(x', y', z'(\sqrt{x'^2 + y'^2}))$ on the deformed one is given by equation (3), in which the (x, y) coordinates are replaced by the "primed" ones, and the formulas

$$r = r' - \frac{2A^2 r'}{(r'^2 + B^2)^3}, \quad r = \sqrt{x^2 + y^2}, \qquad r' = \sqrt{x'^2 + y'^2}, \quad x/y = x'/y', \tag{4}$$

where $A = b^4/2R$ and $B = ba^m$.

Let us represent the contact energy as the sum of three main contributions

$$W = W_1 + W_2 + W_3, \tag{5}$$

where W_1 is the change in the energy of planes due to deformation of the covalent bonds, W_2 is the change in the coupling energy between planes, and W_3 is the probe–surface coupling energy.

For the covalent carbon bond energy in the planes, we used the Morze approximation

$$\varepsilon(d) = -U_0(\exp(-2a(d - d_0)) - 2\exp(-\alpha(d - d_0))), \tag{6}$$

where $d_0 = 0.142$ nm is the equilibrium bond length, $U_0 = 3.68$ eV, and $\alpha = 3.093/d_0$. The small bond deformation energy for this choice of constants is $35.2(d - d_0)^2/d_0^2$ eV in agreement with [13]. The probe–surface coupling and the interaction of carbon atoms of different planes were calculated in the approximation of the pairwise interactions using the *C–C* potential evaluated by means of the electron gas model [12] and with the Lennard–Jones potential in the form

$$U(r) = -C_6(r^{-6} - (r_0^6/2)r^{-12}), \tag{7}$$

where $C_6 = 3.745 \times 10^{-18} JA^6$ is the dispersive coupling constant for carbon atoms in their nonvalent states and $r_0 = 3.81$ A. A combined potential was also applied, which coincides with the electron gas model at $r < 0.25$ nm and smoothly changes to the potential (7) at $r > 0.25$ nm. In this case, both the short-range repulsion and long-range attraction are taken into account more correctly. The corresponding approximations to the potentials are numbered by the indices 1, 2, and 3.

The equilibrium characteristics of the contact were calculated by minimizing the energy W over the parameters a and b at fixed values of R and h for each particular lateral position of the probe apex with respect to the surface (Fig. 1a). The value of h was assumed to be positive if the probe was shifted upwards with respect to the top nondeformed graphite plane; otherwise, it was negative. The load P of the contact and the normal contact hardness were found by differentiation of the energy (minimized over parameters a and b) with respect to h. The friction was evaluated with formula (2) at given values of a, b, and h.

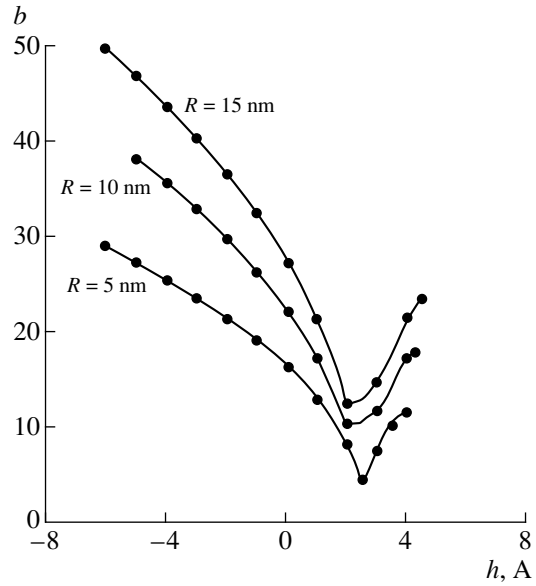

Fig. 3. The dependence of the parameter b on the height h of the probe apex above the top nonshifted graphite plane for several radii of the probe curvature corresponding to the energy minimum of the probe–surface system. Calculated curves correspond to the potential 3. For positive h, the surface of graphite determined by equation (3) is "heaved" upwards, tending to form a connective neck with the probe.

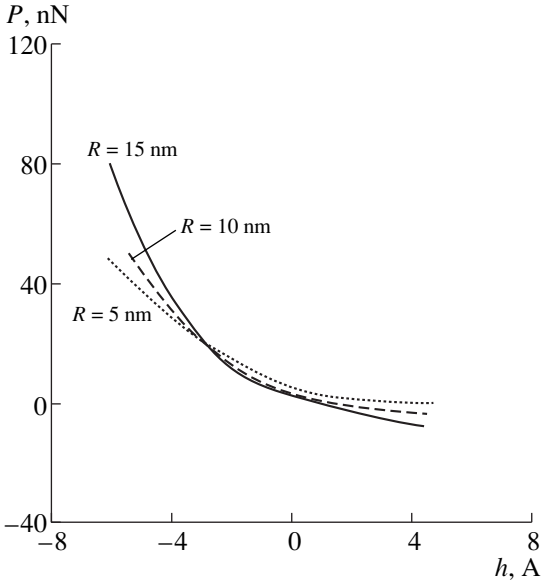

Fig. 4. The dependence of the normal load at the contact on the apex height for several probe radii. The calculations correspond to the potential 3.

Figure 2 shows generic dependences of individual contributions and the total contact energy on the vertical shift of the top atomic plane, h_1, at the point $r = 0$

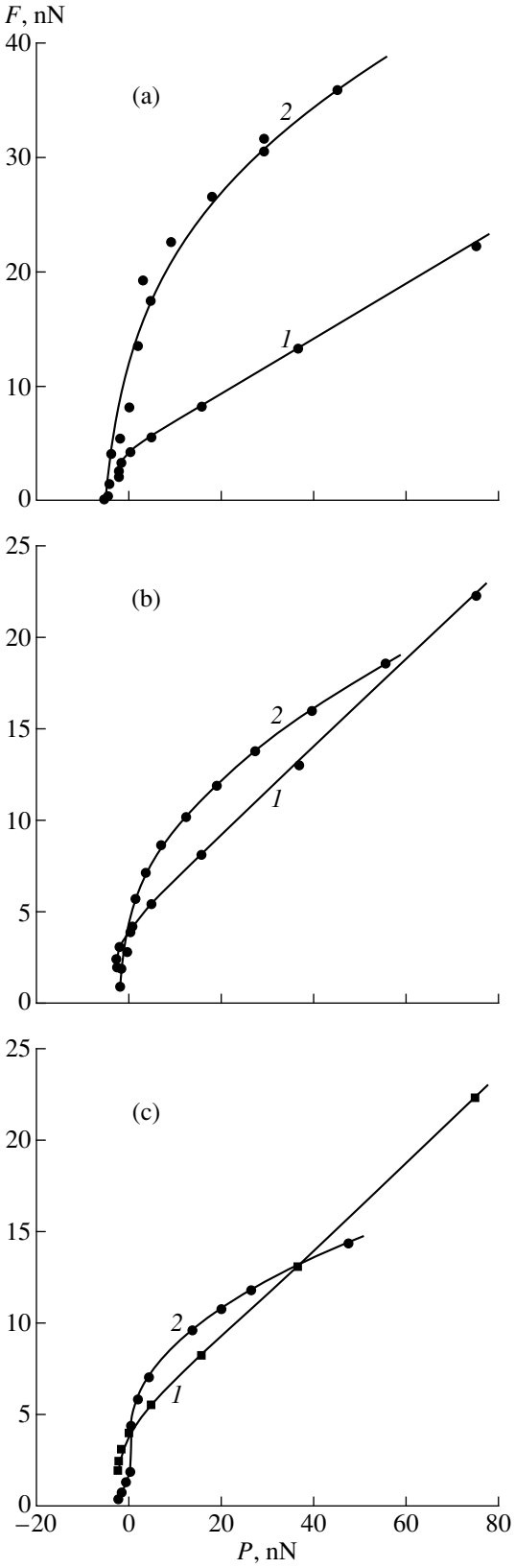

Fig. 5. The friction–load dependences for the potentials (a) 1, (b) 2, and (c) 3. The radius of the probe curvature is 5 nm. Curves *1* and *2* are plotted without and with allowance for the contact deformation, respectively.

(Fig. 1a). In this case, the probe apex height (R = 15 nm) above the upper nondeformed graphite plane was equal to –0.2 nm. The parameters b and h_1 are connected by the relationship $b = \sqrt{2R|h_1|}$. It is seen that the dependence $W_3(h_1)$ follows the dependence of the pairwise interaction potential r; i. e., it has a minimum, a sharp rise at $h_1 \longrightarrow 0$, and a smoother increase with the zero asymptotic at $h_1 \longrightarrow -\infty$. The sum of energies $W_1 + W_2$, on the contrary, changes monotonically, since the deformation of atomic planes and their excess interactions increase with the rise in b. As a result, the total energy W always possesses the pronounced minimum if we take into account the limitation $|h| \le |h_1|$, at which the probe does not actually "puncture" the nearest plane shifted downwards.

The parameter a characterizes the degree of relaxation of the atomic layer displacements with the distance inward of the sample. The minimum over a is more flattened and depends slightly on the probe radius and distance h. In our evaluations, a = 1.054 was obtained. The amplitude of the vertical plane shifts was decreased by a factor of 10 at m = 22.

Figure 3 shows the dependences $b(h)$ for the energy minimum of the contact for different radii of the nanoprobe. In Fig. 4, the dependences of the normal load P on h are given. The range of positive values of h corresponds to the separation of the probe in its lifting from the surface. In Figs. 5a and 5b are shown the calculated friction-force dependences on the normal load for the potentials 1 and 2 (corresponding to the approximations of the electron gas model and Lennard-Jones, respectively) with and without allowance for the deformation of the contact area. For both cases, the radius of curvature was equal to 5 nm. The nonmonotonic character of the calculated points in the range of small loads is determined by the discreteness of an atomic structure. In this case, the dependence $W(a, b)$ reveals a variety of fairly close minima, making it difficult to determine the most probable structure, since even a small probe shift in the vertical direction may give rise to a nonmonotonic variation in the coupling energy. Thus, as a whole, the approximation *1* leads to higher values of the friction force as compared with the approximation *2*. In addition, the allowance for deformation of the contact area causes the frictional force to increase. For the potential 1, this increase is several times in the range of positive loads. For the potential 2, it lies in the interval between 0 and 50% within a load range of 0 to 60 nN. For negative loads, the potential 2 with the allowance for the deformation gives somewhat smaller values of the pulloff probe forces (in magnitude) than in the opposite case.

Figures 6a and 6b show the friction–load dependences for the nanoprobes with radii of 5, 10, and 15 nm using combined potential 3. A comparison of the corresponding curves in Figs. 6a and 6b for the probe with a radius of curvature of 5 nm shows that, for loads

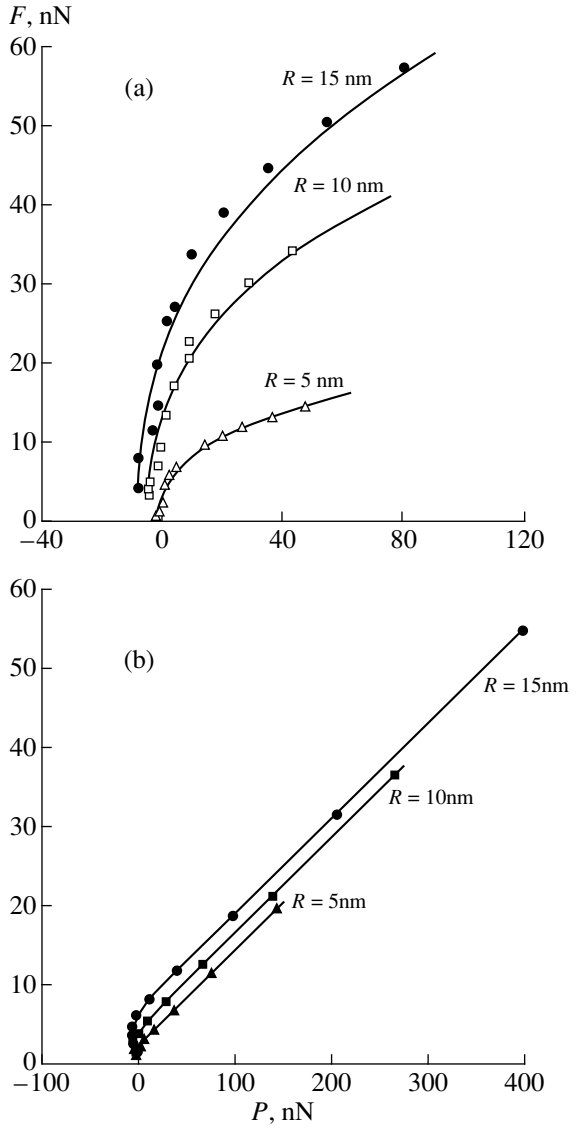

Fig. 6. The friction–load dependences for the probes of various radii. The calculated curves are obtained for the potential 3 in two cases: (a) without and (b) with allowance for deformation of the contact area.

of 0–80 nN, the regard for deformation gives rise to somewhat lesser values of the frictional force than in the opposite case. Conversely, for a larger probe radius, the frictional force is greater when deformation is taken into account. The calculation results also indicate that the frictional force is approximately proportional to the radius of probe curvature.

Unfortunately, the lack of information makes it impossible to compare in detail our results with experimental ones. Among the known studies devoted to measuring "dry" adhesive friction in a vacuum by means of a scanning frictional microscope, one can notice papers [14–16] in which the friction–load dependences for a number of contacts are given. These are Si (probe)—$NbSe_2$ (the radii of the probe curvature are 12 and 48 nm), diamond (probe)—tungsten carbide (the radius of the probe curvature is 110 nm), and Pt (probe)—mica (the radius of the probe curvature is 140 nm).

In analyzing the dependences given in these studies, one can, as is in our calculations, note an irregular character of the experimental points for small loads. These irregularities are more pronounced at a small probe radius when the discreteness of the structure is more strongly exhibited. Note that in the absence of the contact area deformation, the theoretical dependences are smooth (compare *a* and *b* in Fig. 6). The results of our calculations at R = 10 nm and the data from [15] for Si–$NbSe_2$ at R = 12 nm are close qualitatively. In the quantitative respect, our values of frictional forces are two to three times greater. The discrepancy may be caused by a different kind of interacting atoms and, correspondingly, load characteristics of tribosystems, by an error of formula (2), and (or) experimental data.

The conclusion about the proportionality of the frictional force to the radius of the probe curvature is confirmed by the comparison of the experimental data from [14, 15] with each other, since the friction for the Pt–mica contact (R = 140 nm) in [14] is higher by an order of magnitude than that for the Si–$NbSe_2$ contact (R = 12 nm). In [16], however, the values of the frictional force are anomalously small for the large probe radius (110 nm), and, therefore, too small for such a stiff contact shear stress value (238 MPa) calculated in the Derjaguin–Muller–Toporov contact approximation [6]. Since the probe profile was uncontrolled, the results may be explained by the fact that the probe tip in actuality was considerably smaller (provided that the friction was the same). It is possible that the radius of the tip curvature was about 10 nm.

REFERENCES

1. C. M. Mate, G. M. McClelland, R. Erlandsson, and S. Chiang, Phys. Rev. Lett. **59**, 1942 (1987).
2. *Fundamentals of Friction: Macroscopic and Microscopic Processes*, Ed. by G. L. Singer and H. M. Pollock (Cluwer, Dordrecht, 1991).
3. B. Bhushan, Tribol. Int. **28**, 85 (1995).
4. F. P. Bowden and D. F. Tabor, *The Friction and Lubrication of Solids* (Clarendon Press, Oxford, 1964).
5. K. L. Johnson, K. Kendall, and A. D. Roberts, Proc. R. Soc. London, Ser. A **324**, 301 (1971).
6. B. V. Derjaguin, V. M. Muller, and Y. P. Toporov, J. Colloid Interface Sci. **53**, 314 (1975).
7. D. J. Maugis, J. Colloid Interface Sci. **150**, 243 (1992).
8. U. Landman, M. D. Luedtke, and M. W. Ribarsky, J. Vac. Sci. Technol. **7**, 2829 (1989).
9. U. Landman and M. D. Luedtke, *Fundamentals of Friction: Macroscopic and Microscopic Processes*, Ed. by G. L. Singer and H. M. Pollock (Cluwer, Dordrecht, 1991), p. 463.
10. A. V. Pokropivnyĭ, V. V. Pokropivnyĭ, and V. V. Skorokhod, Pis'ma Zh. Tekh. Fiz. **22** (2), 1 (1996) [Tech.

Phys. Lett. **22**, 46 (1996)]; V. V. Pokropivnyĭ, V. V. Skorokhod, and A. V. Pokropivnyĭ, Trenie i Iznos **17**, 579 (1996).

11. A. Buldum, S. Ciraci, and I. P. Batra, Phys. Rev. B **57**, 2468 (1998).
12. G. V. Dedkov, in *Proceedings of the 8th International Conference on Tribology, NORDTRIB'98, Aarhus, Denmark, DTI Tribology Centre, 1998*, Vol. 1, p. 47; Pis'ma Zh. Tekh. Fiz. **24** (19), 44 (1998) [Tech. Phys. Lett. **24**, 766 (1998)]; Mater. Lett. **38**, 360 (1999); Wear **232** (2), 145 (1999).
13. W. A. Harrison, *Electronic Structure and the Properties of Solids: The Physics of the Chemical Bond* (Freeman, San Francisco, 1980; Mir, Moscow, 1983).
14. R. W. Carpick, N. Agrait, D. F. Ogletree, and M. Salmeron, Langmuir **12**, 3334 (1996).
15. M. A. Lanz, S. J. O'Shea, M. E. Welland, and K. L. Johnson, Phys. Rev. B **55**, 10776 (1997).
16. M. Enashescu, R. J. A. van den Oetelaar, R. W. Carpick, *et al.*, Phys. Rev. Lett. **81**, 1877 (1998).

Translated by Yu. Vishnyakov

Technical Physics, Vol. 45, No. 7, 2000, pp. 915–921. Translated from Zhurnal Tekhnicheskoĭ Fiziki, Vol. 70, No. 7, 2000, pp. 102–108.

EXPERIMENTAL INSTRUMENTS AND TECHNIQUES

Kinetics of Radiation Cooling of Fullerenes

A. A. Vostrikov, A. A. Agarkov, and D. Yu. Dubov

Kutateladze Institute of Thermophysics, Siberian Branch,
Russian Academy of Sciences, Novosibirsk, 630090 Russia
E-mail: vostrikov@itp.nsc.ru

Received March 10, 1999; in final form June 29, 1999.

Abstract—Emission from fullerene molecules excited by means of electron impact in crossed beams under conditions of single collisions between electrons and C_{60} molecules in a kinetic energy range E_e from 25 to 100 eV was studied experimentally. Emission spectra in a wavelength range from 300 to 800 nm; the emission excitation functions and the temperature of emitting molecules as a function of E_e were measured with a resolution of 1.6–3.2 nm. The contribution to emission from ionized C_{60}^{+*} molecules has been determined and data on the emissivity of the C_{60}^{+*} ion have been obtained. It has been shown that the emission spectra can be well approximated with the spectral distribution of thermal emission from a black body (Planck's formula), taking into account the lowering of emissivity for a small particle. The emission can be observed starting with electron energy of about 27 eV; the emission excitation function is of a nonresonant form, peaking at an energy of $E_e \approx$ 70 eV. As E_e is increased, the temperature of emitting particles rises and reaches its maximum value of 3100–3200 K at $E_e \approx 47$ eV. © *2000 MAIK "Nauka/Interperiodica".*

INTRODUCTION

In previous investigations at our laboratory, emission from microparticles of condensed matter (clusters of molecular gases $(CO_2)_n$, $(N_2O)_n$, $(H_2O)_n$, and $(N_2)_n$ formed in supersonic jets under excitation by means of electron impact) was studied [1–3]. It was found that the energy of vibrational [1] and electronic [2, 3] excitations is quickly dissipated through the heating of the cluster. The rate of return from excited states back to the ground states rises dramatically with the cluster size, and the emission spectrum corresponds to emission from electron-excited states of molecules ejected from the cluster. A similar picture was observed under the laser excitation of vibrational degrees of freedom of SF_6 molecules in clusters [4]. Thus, the ejection of molecules in excited states and the evaporation are the major cooling channels in weakly bound clusters [5], and the effect of radiation cooling is not observed. Still, there is indirect evidence that radiation cooling in molecular systems plays an important part, for example, in gas-phase ion-molecular processes [6]. Correspondingly, ion-molecular processes in clusters can also proceed with the participation of radiation cooling.

Tightly bound clusters (clusters of less volatile substances) were found to display radiation cooling with a continuous emission spectrum similar to Planck's spectrum [7, 8]. The temperature of emitting clusters, as in the case of tungsten clusters W_n with $n > 200$, could be as high as 3800 K [8]. The clusters were heated by means of an oxidation reaction (Nb_n clusters in [7]) or by laser irradiation (Nb_n, W_n, and Hf_n clusters [8]).

The discovery in 1985 of fullerenes possessing a unique stability with respect to fragmentation stimulated investigations of highly-excited fullerene molecules in the gas phase [9–17], in particular of electron-induced processes [10, 11, 14, 17]. It has been found that the primary excitation of fullerene molecules, like that of other complex molecules and clusters, initiates cascades of secondary processes, while the complex energy spectrum of the excited states (including collective excitations) facilitates the rapid dissipation of the primary excitation and attainment of partial or complete thermalization. However, the basic distinction between fullerenes and most other microsystems lies in the extreme stability of the carbon cage [8]. Because of this high stability, fragmentation, which is the dominant cooling channel of an excited "excessive" complex system (it is monomolecular disintegration in the case of a molecule and evaporation of structural units in the case of a cluster), is impeded by the relaxation of the excited fullerene. As a consequence, competing (not evaporating) molecule cooling processes of comparable intensity come to the foreground, namely, electron and photon emission (analogues of macroscopic processes of thermionic emission and thermal emission, respectively). For example, in [13, 14], a continuous emission spectrum was registered in the visible range from a flux of C_{60} molecules heated in various ways. The molecules were either vaporized from a solid sample by laser radiation [13] or excited by an electron impact [14].

In this study, thermal emission from fullerenes was excited in crossing beams of C_{60} and low-energy elec-

1063-7842/00/4507-0915$20.00

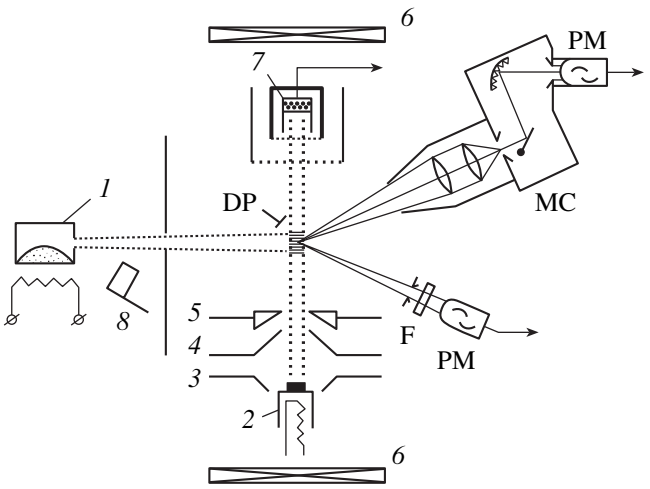

Fig. 1. Schematic of the experimental setup.

trons. A continuous emission spectrum was observed after excitation by means of electron impact in a wavelength range from 300 to 800 nm (the results given here were obtained with spectral resolution $\Delta\lambda = 3.2$ nm; check measurements at $\Delta\lambda = 1.6$ nm yielded identical spectra). The spectrum could be described by Planck's formula for emission from a sphere of much smaller diameter than the emission wavelength, $d \ll \lambda$ [19].

EXPERIMENTAL TECHNIQUE

The procedure and the experimental setup for the generation of the molecular beam and excitation of C_{60} by electrons was identical to the ones used in experiments on the measurement of the absolute cross sections of C_{60}^- and C_{60}^+ [11, 17, 20]. For emission registration, the setup was equipped with an optical system. The schematic of the experiment is shown in Fig. 1.

The effusion molecular beam was formed by vaporizing fullerenes from source *1* heated to $T_0 = 800$ K and intersected by an electron beam at an angle of 90°. The beam of electrons emitted from oxide cathode *2* was formed by a system of apertures *3–5*, collimated with the magnetic field (300 G) of magnets *6* and registered at collector *7* of the Faraday cup type. The current of electrons did not exceed 60 μA and the density of molecules in the region of crossing of the beams was of the order of 10^{10} cm^{-3}. In this way, a pairwise interaction of electrons and molecules was ensured. The energy of electrons in the beam E_e varied in the range from 0 to 100 eV.

The emission from the intersection region of the two beams was collected at right angles to the electron beam; the angle with the molecular beam direction was 40°. A system of short-focus lenses imaged the emission onto the entrance slit of an MUM monochromator (MC) (200–800 nm, reciprocal dispersion 3.2 nm/mm) and, following spectral dispersion, it was registered with an FEU-79 photomultiplier (PM). The spectral sensitivity of the system of optical diagnosis was calibrated using a CI 10–300 lamp as a standard emitter. In order to determine the flux of photons $I(\lambda)$, the registered spectra were normalized using a curve of relative spectral sensitivity $\eta/(\lambda)$. The integrated intensity was registered by a photomultiplier, with the monochromator replaced by a ZS-8 broad-band filter (F). Under these conditions, the integrated spectral sensitivity curve had a maximum at 500 nm and a halfwidth of 150 nm. The spatial resolution of the detecting system (the size of the spot from which the emission was collected) was determined using a point radiation source.

To isolate the contribution from C_{60}^{+*} ions to the total emission, an electric field was applied to the region of beam crossing which was produced by two deflecting plates (DP) placed along the axes of molecular and electron beams. With increasing electric field strength ξ between the plates, the time spent by the ions in the field of view diminished. Because of the magnetic collimation of electrons, there was no distortion of the electron beam by the field ξ. To verify this, we measured in the same setup the emission due to short-lived states of N_2^+ ($B^2\Sigma_u^+$, $\lambda = 391$ nm) and found that their emission intensity did not depend on the strength of the pulling electric field.

Generally speaking, contributions to emission may also come from fragments, both neutral, C_{60-2n}^*, and charged, C_{60-2n}^{+*}. But the threshold for fragmentation under electron impact suffers a significant kinetic shift, being observed at 42–44 eV, and at $E_e < 100$ eV, the fraction of fragments does not exceed 5–7% [10, 12]. Taking this into account and also considering the character of $I(E_e)$ plots obtained in this work, we conclude that the emission is due mainly to unfragmented fullerene molecules.

Contributions to emission from other sources was eliminated in the following ways. The electron-induced emission from the background gas and other possible sources was measured while the beam source aperture was closed with shutter *8*. The contribution to the signal of thermal radiation from heated parts of the fullerene source was eliminated by modulating the electron beam; it was chopped at a frequency of 80 Hz, and the photomultiplier signal was measured in the lock mode at the chopping frequency.

RESULTS AND DISCUSSION

In Fig. 2, typical spectra are shown (curves *1*) of emission, generated as a result of electron impact on the fullerene molecule in crossing beams at electron energies 66 (a) and 30 eV (b). In order to obtain these curves, the contribution of the background gas was subtracted from the total PM signal (curve *2*); then the dif-

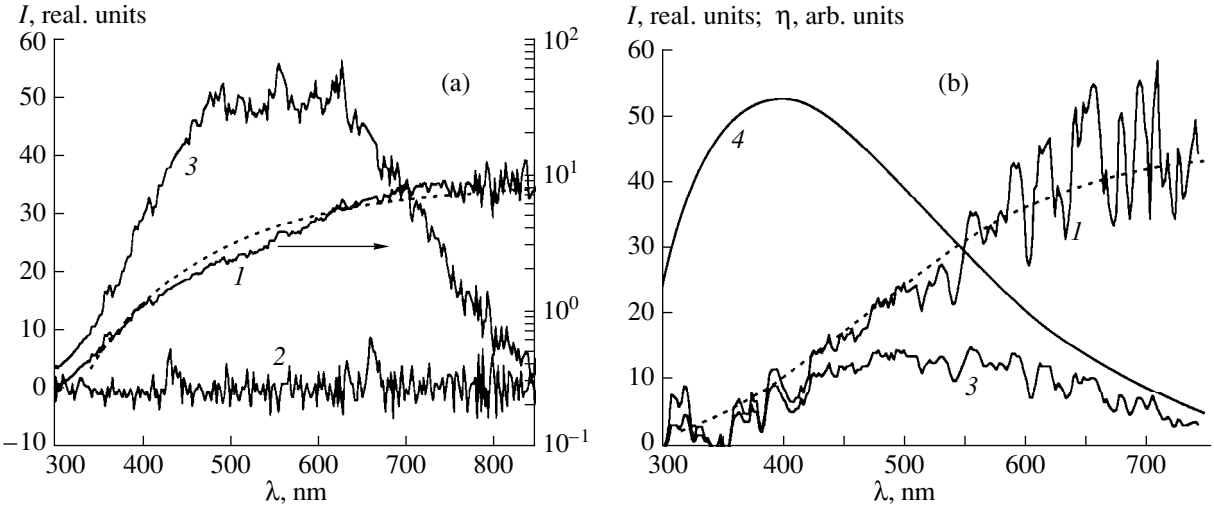

Fig. 2. Electron-induced radiation spectra. Dashed line is an approximation of the experimental data by formula (1).

ference signal (desired signal, curve *3*) was corrected for the spectral sensitivity of the optical system (curve *4*).

Let us compare this spectrum with the one that is due to the thermal emission of a small spherical particle heated to a temperature *T*. The rate of photon emission I_{th} in the wavelength range $[\lambda, \lambda + \Delta\lambda]$ from a heated body is described by Planck's formula

$$I_{th}(\lambda, T) = 2\pi c S \Delta\lambda \varepsilon(\lambda, T) / \left[\lambda^4 \left(\exp\left(\frac{hc}{\lambda kT}\right) - 1\right)\right], \quad (1)$$

where *S* is the emitting area and $\varepsilon(\lambda, T)$ is the emissivity of a solid. It follows from the emission theory for small particles [19] that the emissivity of a sphere of diameter $d \ll \lambda$ is $\varepsilon(\lambda) \propto d/\lambda$ (because photon emission comes from the bulk of the particles instead of their surface). The C_{60} molecule is spherically symmetrical and hollow; for this geometry, the function $\varepsilon(\lambda) \propto \lambda^{-1}$ will obviously be valid. The outer diameter of the electron shell of a molecule is $d \approx 1$ nm. Below we assume

$$\varepsilon(\lambda) = \varepsilon_0 \frac{d}{\lambda}, \quad (2)$$

where ε_0 is a numerical constant.

In order to derive the internal energy E_v of a fullerene molecule corresponding to the temperature of emitting molecules, we calculated, following [13], the vibrational energy in the approximation of harmonic intramolecular vibrations of C_{60}. Contributions of all the 46 vibrational modes were summed up, taking into account their degree of degeneration. The results of calculations with the use of data on frequencies presented in [21] practically coincided with calculations in [12]. At $T > 1500$ K, the curve of $E_v(T)$ is well approximated by a linear function $E_v(\text{eV}) \cong 13.9 + 0.0143(T - 1500)$.

Figure 3 shows the measured emission intensity of the fullerene as a function of energy E_e. Here curve *1* is an integrated emission (measured in "filter + photomultiplier" scheme); curve *2* is the emission at a wavelength $\lambda = 540$ nm, $\Delta\lambda = 3.2$ nm. Curve *3* in Fig. 3 is the dependence of the temperature of emitting particles $T(E_e)$ obtained by fitting the spectral data with formula (1) using the least squares method. It can be seen that as E_e is increased to about 47 eV, the temperature *T* rises in proportion to E_e. At $E_e > 47$ eV, the temperature of emitting particles rises to a maximum value of $T^* \approx$ 3100–3200 K corresponding to the internal energy of the C_{60} molecule $E_v \cong 36$ eV. Taking into account that

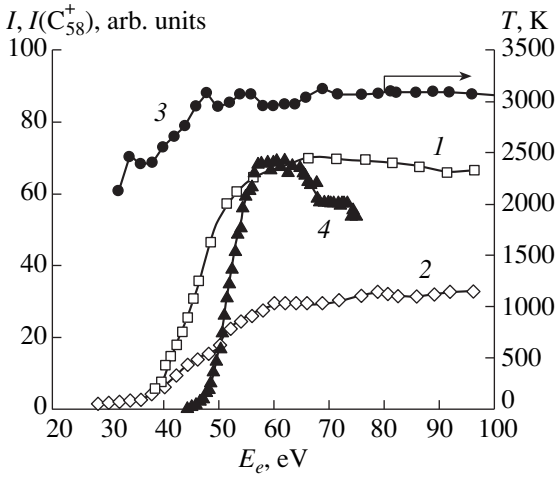

Fig. 3. Plots of the emission intensity (*1*, *2*), the temperature of emitting molecules (*3*) and the current of C_{58}^+ fragments (*4*) [10] versus electron energy.

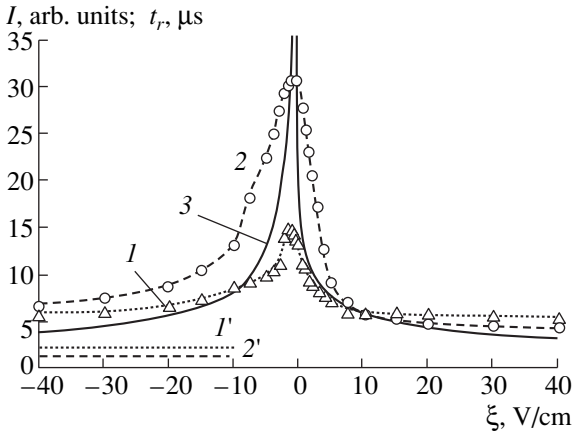

Fig. 4. Plots of the emission intensity (*1*, *2*) and the calculated ion transit time (*3*) versus the electric field strength.

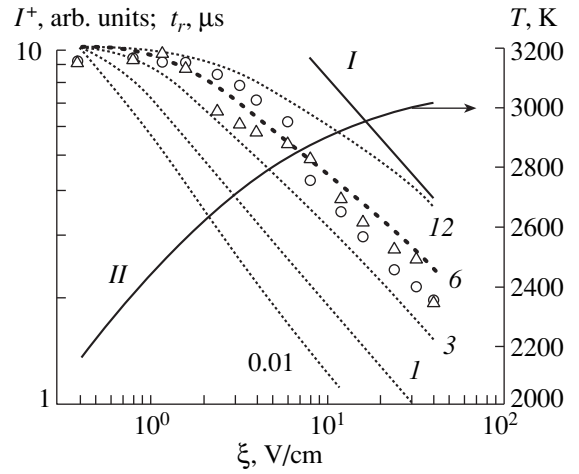

Fig. 5. Experimental (○, △) and calculated (dashed lines) plots of the emission intensity of molecules, ion transit time (*I*) and their ultimate temperature (*II*) against the electric field strength (values of ε_0 are indicated at the curves).

the main emission source is the ionized molecule (ionization potential U_i = 7.6 eV [11, 18]) and that the thermal energy of the C_{60} molecule in the effusion beam $E_{v,0} = E_v(T_0) \cong 4.6$ eV, we obtain that the energy transferred to the molecule by an electron ($E_v + U_i - E_{v,0}$) amounts to 39 eV. Thus, the primary and secondary electrons take away only 8 eV. The transfer of such a great amount of energy to the C_{60} molecule implies a multielectron excitation process.

The existence of a limit for the temperature increase of the C_{60}^{+*} molecule can be explained by competition between the radiation cooling of the molecule heated by an electron and an alternative cooling process by evaporation of C_2 through the process $C_{60}^{+*} \longrightarrow C_{60-2n}^{+*} + nC_2$, the rate constant of which has a stronger temperature dependence [9]. Note, at this point, that the sum $kT^* + U_f$, where U_f is the ionization potential of C_{58}, turned out to be close to the threshold energy E_e for the dissociative ionization [10, 12, 18].

Shown in Fig. 3 (curve *4*) is the dependence [10] of the current due to C_{58}^+ ions generated as a result of the metastable fragmentation of C_{60}^{+*} during the time interval 7.7–31.2 μs lapsed after interaction with an electron for an initial thermal energy of the molecule $E_{v,0} \approx$ 4.5 eV. It is seen that the threshold for the generation of the fragments is indeed close to the energy E_e, at which the temperature rise of emitters ceases, i.e., hotter molecules, apparently, rapidly loose energy through the evaporation of C_2.

Heating the C_{60} molecule causes not only its fragmentation but also the thermal emission of an electron, which is a faster process [9]. Therefore, the main emission source at $E_e \geq 40$ eV, as shown earlier by the present authors [22], is provided by the ionized C_{60}^{+*} molecules. In Fig. 4, the integrated intensity *I* is plotted as a function of the strength ξ and polarity of the electric field between the deflecting plates at energies E_e = 40 (curve *1*) and 65 eV (curve *2*). Also shown in this figure is the time of stay of a C_{60}^{+*} ion in the emission region under observation (curve *3*) calculated for an ion produced in the center of electron beam and having the starting velocity equal to the velocity of a C_{60} molecule in the effusion beam. The asymmetry of the curves is related to the fact that the optical axis and the molecule velocity are not collinear (the angle between them is 40°).

It can be easily shown that, at strong pulling fields, the time of stay of the ions in the region under observation t_r and, consequently, their emission intensities I^+ are proportional to $\xi^{-1/2}$. By plotting $I(\xi)$ in coordinates $I(\xi) - \xi^{-1/2}$ and extrapolating to the origin of the coordinates, we find that the contribution to emission from neutral particles does not exceed 16 and 4% for E_e = 40 and 65 eV, respectively. These values are shown in Fig. 4 by horizontal lines *1*' and *2*'.

Data in Fig. 4 allow estimates to be made of the emissivity of C_{60}^{+*}. For this purpose, we subtracted from the total emission *I* the contribution of neutral particles. In Fig. 5, the symbols correspond to data for the ion emission $I^+(\xi)$ derived from the left-hand branches of curves *1* and *2* in Fig. 4. The calculated dependence of time t_r on ξ is shown in Fig. 5, curve *I*.

The emission at small ξ (corresponding to large values of time t_r) does not vary in proportion to t_r. We relate this behavior of $I^+(\xi)$ to the radiation cooling of the C_{60}^{+*} ion during its stay in the region under observation. In order to derive the dependence of the emission

intensity on the cooling rate, we integrate the emission flux energy $q = (hc/\lambda)I_{th}$ with respect to λ. Taking $\varepsilon(\lambda)$ in the form of (2), we get, as a result of integration, an expression similar to the Stephan–Boltzmann formula for a small particle

$$q = \varepsilon_0 \sigma_c T^5 \tag{3}$$

where $\sigma_c = 24.888\ 2\pi hc^2 Sd(k/hc)^5$.

Making use of

$$qdt = -CdT, \tag{4}$$

and integrating (4), we get variation with time of the temperature of C_{60}^{+*}

$$T(t, T_i) = T_i\{1 + t[4\varepsilon_0 \sigma_c T_i^4]/C\}^{-1/4}, \tag{5}$$

where T_i is the initial ion temperature.

Substituting (5) into (1), we get an expression for the ion emission intensity I_{th}^+ as a function of the time in transit t and the initial temperature T_i. The integral of $I_{th}^+(t)$ over the ion trajectory with account taken of the spatial variation of the sensitivity of the optical system $\eta(r)$

$$N^+ = \int_0^\infty I_{th}^+ \eta(r(t))dt \tag{6}$$

represents the number of photons registered by the optical system per one emitting C_{60}^{+*} ion. As the rate of formation of C_{60}^{+*} ions does not depend on the field ξ, the $N^+(\xi)$ dependence to within a constant A coincides with the measured signal $I^+(\xi)$.

Depicted by a dashed line in Fig. 5 are the calculation results for $N^+(\xi)$ at $T_i = 3150$ K and $\lambda = 540$ nm for several values of the constant ε_0. For illustration purposes, the calculated $N^+(\xi)$ curves have been normalized at their maxima in the region of large times t_r. In comparing the experimental data points for $I^+(\xi)$ with calculated $N^+(\xi)$ curves, the differences between N^+ and I^+ values were minimized using the least squares method with constants A and ε as fitting parameters. It was found that the best agreement with the model is observed at $\varepsilon_0 = 5.7$ for $E_e = 40$ eV (triangles) and $\varepsilon_0 = 6$ for $E_e = 65$ eV (open circles). The final temperature T_f of C_{60}^{+*} ions exiting the region under observation for $\varepsilon_0 = 6$ is shown by curve *II* in Fig. 5.

A qualitative confirmation of the temperature variation of the quantity $T(C_{60}^{+*})$ has been obtained from measurements of the emitting region profiles along the direction perpendicular to the optical observation axis and the axis of the electron beam for emission from

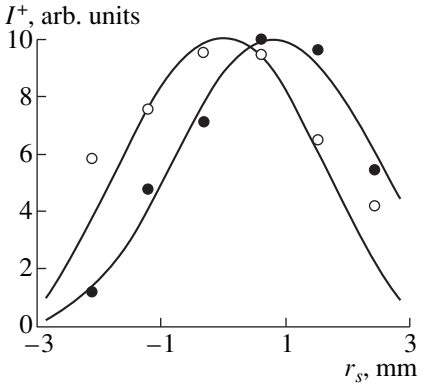

Fig. 6. Transverse profiles of the electron-induced emission ($E_e = 70$ eV) from nitrogen ions (open circles) and fullerene molecules (solid circles). Symbols show the experimental results, and solid curves show the results of calculations.

nitrogen ions $N_2^+(B^2\Sigma_u^+, \lambda = 391$ nm) and C_{60}^{+*} ions. The obtained distributions of the emission intensity are shown in Fig. 6. Maxima of I^+ curves in Fig. 6 have been made equal. Note that in these measurements, nitrogen was leaked in the chamber to a pressure of 10^{-4} Pa. The lifetime of the state is $B^2\Sigma_u^+ \sim 0.1$ μs; i.e., the thermal motion of the excited N_2^+ ions during a radiative lifetime can be neglected. In this case, the measured emission intensity is given to within a device constant by the integral

$$I_n(r_s) = \int_{P(r),\ \eta(r)\neq 0} d^3 r \eta(r - r_s)P(r). \tag{7}$$

Here, $|r_s|$ is the distance from the optical axis to the electron beam axis, and the integration is carried out over the region where both the excitation level $P(r)$ and the sensitivity of the registration system $\eta(r)$ are nonzero. For a fullerene, taking into account the radiation cooling, we get

$$I_f(r_s) = \int_{P(r_0)\neq 0} d^3 r_0 P(r_0) \times \int_{\eta(r)\neq 0} d^3 r \eta(r - r_s) I_{th}(t(r - r_0)), \tag{8}$$

where $t(r - r_0) = |r - r_0|/|v_0|$ is the time of ion transit and v_0 is the starting velocity vector (measurements were carried out at $\xi = 0$).

The emission profile of N_2^+ calculated by formula (7) and the emission profile of the fullerene derived using formulas (1), (5), and (8) at $\varepsilon_0 = 6$ are shown in Fig. 6 as solid curves. It can be seen that the shift of the fullerene emission profile relative to that of nitrogen is

Emissivity of fullerenes

Emitting particle	Coefficient ε	Process considered	References
C_{60}^{*}	$0.5–1.2 \times 10^{-4}$	Cooling of heated molecules in a beam	[5]
C_{60-2n}^{+*}	$2–4.4 \times 10^{-2}$	Metastable fragmentation	[8]
C_{60}^{-*}	$\sim 1.2 \times 10^{-4}$	Thermionic emission	[9]
C_{60}^{+*}	$1.0–1.1 \times 10^{-2}$	Optical emission	This study

well described by our model of the radiation cooling of C_{60}^{+*}.

Previously [12, 15, 16], in studies of relaxation processes in a gaseous fullerene, estimates of emissivity have been made. However, in analyzing these data, the following points should be taken into consideration. Firstly, indirect estimates of the radiation cooling constant are strongly influenced by the choice of the rate constants of competing processes, mechanisms of which are not quite well understood. Secondly, in [12, 15, 16], experimental determinations were carried out of the loss rates of the internal energy q in different temperature ranges and the ε values were "recovered" under certain assumptions differing from those adopted in this work. For example, the dependence of ε on λ was ignored [12, 15], and it was assumed [16] that $q \propto T^{7.6}$ or $\varepsilon(\lambda) \propto (d/\lambda)^{3.6}$. In view of the above, we have used the data of [12, 15, 16] for the rate of radiative energy loss $q(T)$ and recovered the values of ε using formulas (2) and (3). Values of ε for λ = 540 nm and d = 1 nm are given in the table.

Note that our values of ε are much higher than those of indirect estimations. This is probably due to the difference in temperatures (in [12, 16] the temperature of particles did not exceed 1800 K), which can have a twofold effect. Firstly, as the temperature is increased, the cooling rate of C_{60}^{+*} can rise because of the evaporation of C_2. However, this effect appears to be not strong enough because the observed cooling rates are the same at energies 40 and 65 eV, whereas fragmentation at 40 eV is practically zero (curve *4* in Fig. 3; see also [10, 12]). Secondly, the possibility that ε depends on T cannot be excluded. In our calculations above, this dependence was neglected because of a rather small temperature drop observed during crossing by the C_{60}^{**} ion of the region under observation (curve *II* in Fig. 5).

The most complicated issue is the formation mechanism of the Planck's emission spectrum of a nanoparticle. In ordinary media, the continuous thermal emission spectrum is formed as a result of the transfer of resonant emission under conditions of photon reabsorption [23]. It is evident that because of the low density of C_{60} molecules in the beam, the reabsorption does not take place. The absorption spectrum of unexcited C_{60} displays a resonant character typical of molecular spectra [24] and showing that, in this place, the number of optically active states is small. The continuous character of the electron-induced emission of highly excited fullerene molecules can possibly be explained by optical transitions between electron-excited states whose density is high [25]. The shape of the observed C_{60}^{**} emission spectra indicates that the highly excited fullerene molecule is large enough for complete thermal equilibrium between emission modes to be achieved.

CONCLUSIONS

In this work, the emission of fullerene molecules excited by electron impact in crossing beams under conditions of single inelastic collisions $C_{60} + e^{-}$ in the range of collision energies from 25 to 100 eV was studied, and the following results have been obtained.

Collisions between C_{60} and electrons produce emission from C_{60}^{*} molecules and C_{60}^{+*} ions at electron energies starting from ≈27 eV. The major contribution to the emission comes from C_{60}^{+*} ions, which form after the fast thermal emission of electron.

The emission excitation function $I(E_e)$ has been derived. The function has a nonresonant character and reaches a maximum at an energy $E_e \approx 70$ eV.

It has been found that the spectrum of electron-induced emission of fullerene molecules is described by Planck's formula for radiation from small particles of sizes much smaller than the radiation wavelength. The temperature of molecules determined from emission spectra rises in proportion to E_e as the electron energy is increased to ≈47 eV and then stays constant at $T \approx 3150$ K. Considering the distribution of temperatures of the molecules, the heating can be as high as $T_m \approx 3800$ K.

The kinetics of radiation cooling of C_{60}^{+*} has been investigated and the emissivity value obtained: $\varepsilon \approx 10^{-2}$ at λ = 540 nm and d = 1 nm. The results of works [7, 8, 13, 14] and of this study show that the method of excitation of metal clusters and C_{60} molecules has no effect

on the emission spectrum; metal particles and fullerene molecules produce Planck's spectrum for thermal emission. This is probably the common property of tightly bound clusters and molecules.

ACKNOWLEDGMENTS

The authors are grateful to S. V. Drozdov for his assistance.

The work was supported by the Russian Foundation for Basic Research (grant nos. 97-02-17804 and 98-02-17804) and a grant from the Ministry of Education of the Russian Federation.

REFERENCES

1. A. A. Vostrikov and S. G. Mironov, Chem. Phys. Lett. **101**, 583 (1983).
2. A. A. Vostrikov, D. Yu. Dubov, and V. P. Gilyova, Z. Phys. D **20**, 205 (1991).
3. A. A. Vostrikov and V. P. Gileva, Pis'ma Zh. Tekh. Fiz. **20** (15), 40 (1994) [Tech. Phys. Lett. **20**, 625 (1994)].
4. I. M. Beterov, Yu. V. Brzhazovskiĭ, A. A. Vostrikov, *et al.*, Kvantovaya Élektron. (Moscow) **7**, 2443 (1980).
5. A. A. Vostrikov, D. Yu. Dubov, and V. P. Gileva, Zh. Tekh. Fiz. **59** (8), 52 (1989) [Sov. Phys. Tech. Phys. **34**, 872 (1989)].
6. R. C. Dunbar, Int. J. Mass Spectrom. Ion Processes **100**, 423 (1990).
7. U. Frenzel, A. Roggenkamp, and D. Kreisle, Chem. Phys. Lett. **240**, 109 (1995).
8. U. Frenzel, U. Hammer, H. Westje, *et al.*, Z. Phys. D **40**, 108 (1997).
9. Z. Wan, J. F. Christian, Y. Basir, *et al.*, J. Chem. Phys. **99**, 5858 (1993).
10. M. Foltin, M. Lezius, P. Scheier, *et al.*, J. Chem. Phys. **98**, 9624 (1993).
11. A. A. Vostrikov, D. Yu. Dubov, and A. A. Agarkov, Pis'ma Zh. Tekh. Fiz. **21** (17), 73 (1995) [Tech. Phys. Lett. **21**, 715 (1995)].
12. E. Kolodney, B. Tsipinyuk, and A. Budrevich, J. Chem. Phys. **102**, 9263 (1995).
13. R. Mitzner and E. E. B. Campbell, J. Chem. Phys. **103**, 2445 (1995).
14. A. A. Vostrikov, D. Yu. Dubov, and A. A. Agarkov, Pis'ma Zh. Éksp. Teor. Fiz. **63**, 915 (1996) [JETP Lett. **63**, 963 (1996)].
15. K. Hansen and E. E. B. Campbell, J. Chem. Phys. **104**, 5012 (1996).
16. J. U. Andersen, C. Brink, P. Hvelplund, *et al.*, Phys. Rev. Lett. **77**, 3991 (1996).
17. A. A. Vostrikov, D. Yu. Dubov, A. A. Agarkov, *et al.*, Mol. Mater. **20**, 255 (1998).
18. C. Lifchitz, Mass Spectrom. Rev. **12**, 261 (1993).
19. C. F. Bohren and D. R. Huffman, *Absorption and Scattering of Light by Small Particles* (Wiley, New York, 1983; Mir, Moscow, 1986).
20. A. A. Vostrikov, D. Yu. Dubov, and A. A. Agarkov, Pis'ma Zh. Tekh. Fiz. **21** (13), 55 (1995) [Tech. Phys. Lett. **21**, 517 (1995)].
21. R. A. Jishi, R. M. Mirie, and M. S. Dresselhaus, Phys. Rev. B **45**, 13685 (1992).
22. A. A. Agarkov, D. Yu. Dubov, and A. A. Vostrikov, in *Proceedings of the 17th International Symposium on Molecular Beams, France, 1997*, pp. 399–402.
23. Yu. K. Zemtsov, A. Yu. Sechin, A. N. Starostin, *et al.*, Zh. Éksp. Teor. Fiz. **114**, 135 (1998) [JETP **87**, 76 (1998)].
24. P. F. Coheur, M. Carleer, and R. Colin, J. Phys. B **29**, 4987 (1996).
25. W. A. Chupka and C. E. Klots, Int. J. Mass Spectrom. Ion Processes **167–168**, 595 (1997).

Translated by B. Kalinin

Technical Physics, Vol. 45, No. 7, 2000, pp. 922–927. Translated from Zhurnal Tekhnicheskoĭ Fiziki, Vol. 70, No. 7, 2000, pp. 109–114.

EXPERIMENTAL INSTRUMENTS AND TECHNIQUES

Discharge Leader Self-Organization on the Water Surface

V. P. Belosheev

Vavilov State Optical Institute, All-Russia Research Center,
ul. Babushkina 36/1, St. Petersburg, 199034 Russia

Received May 20, 1999

Abstract—Experimental studies on the self-organization of dissipative dynamic systems have shown that this property is inherent to the structure of the discharge leader. *© 2000 MAIK "Nauka/Interperiodica".*

In recent years, interest in studying the self-organization phenomenon in living and physical systems has quickened. The latter are especially promising in this respect because of their simplicity and the availability of well-developed experimental methods and tools. At present, few systems where self-organization is known to take place are the objects of investigation. A wider coverage of dissimilar systems would be of great value for the in-depth analysis of the self-organization mechanisms and properties.

In this work, the self-organization of the discharge leader on the water surface (LOW) was discovered. This study is an extension of [1], where an arc discharge initiated on the water surface was used as a source of UV radiation to deactivate microorganisms [2].

When a cylindrical cathode was partially immersed in water (vertically) and the anode tip was above the water surface at a distance of 1–3 cm from the cathode [1], the formation of the leader was found to shunt the water resistance in the gap and cause nonlinear current feedback (between the gap voltage and resistance) to occur. In other words, if the LOW is initiated by a capacitor, an $R(t)C$ discharge arises in the circuit and an exponential current and voltage decay is not observed.

Further studies of LOW [3, 4] under creeping discharge conditions (Fig. 1) have shown that the LOW may be quasi-one- or quasi-two-dimensional depending on whether the cathode is one- or two-dimensional (Fig. 2). The leader core is driven by the potential difference between it and the water surface in front of it. The leader structure forms by repeatedly splitting the core because of its flattening. The LOW structure thus obtained is fractal with the fractal dimension $D = 0.96$ and 1.85 for quasi-one- and quasi-two-dimensional discharges, respectively. Their evolution is self-consistent [4, 5].

Here, we report additional information that provides a deeper insight into the role of a corona in the leader evolution. Based on these data and also in view of self-organization signs [3–5] found in nonequilibrium dynamic dissipative systems [6, 7], we establish the fact of LOW self-organization. The self-organization signs are, specifically, the spontaneous and threshold character of structuring and structure breakdown, as well as the relation between the dissipated power and structuring.

CONDITIONS FOR LOW STRUCTURING

LOW structuring is demonstrated more distinctly with the two-dimensional LOW [4]. The setup for LOW study (Fig. 1) is essentially a 1.5-cm-high cylindrical glass cuvette *1* of diameter 9 cm, two-thirds full of tap water *2* with a conductivity of $\cong 1 \times 10^{-4}\ \Omega^{-1}\ \text{cm}^{-1}$. Cathode *3*, an 0.05-cm-thick brass disk 7 cm in diameter was placed concentrically to the cuvette 0.3 cm below the water surface. The end of a stainless steel wire 7.5×10^{-3} cm in diameter served as anode *4*. The anode was 0.1–0.3 cm above the water surface at the center of the cuvette.

In experiments, we used 0.1-μF-storage capacitor *5*, which was charged to the initial voltage $U_0 = 3$–6 kV. A discharge was initiated by shortening air gap *6*. Oscillograms of the capacitor voltage U_c and discharge current i (Fig. 3) were obtained using resistive voltage divider *7* and shunt *8*. The discharge was photographed with camera *9*. The experimental conditions were detailed in [3, 4].

At the initial voltage $U_0 = 3$–6 kV (positive anode *1* in Fig. 4), cone-shaped corona *3* was initiated in air gap *2*. As soon as the corona cone base reached the water surface, from three to six initial leaders *4* began

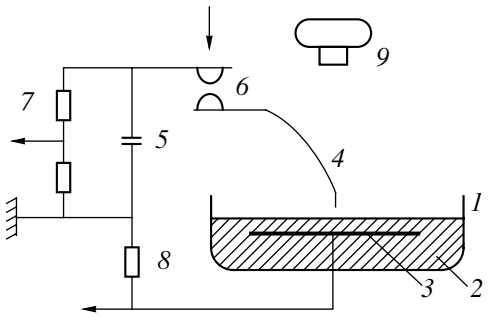

Fig. 1. Experimental setup.

1063-7842/00/4507-0922$20.00

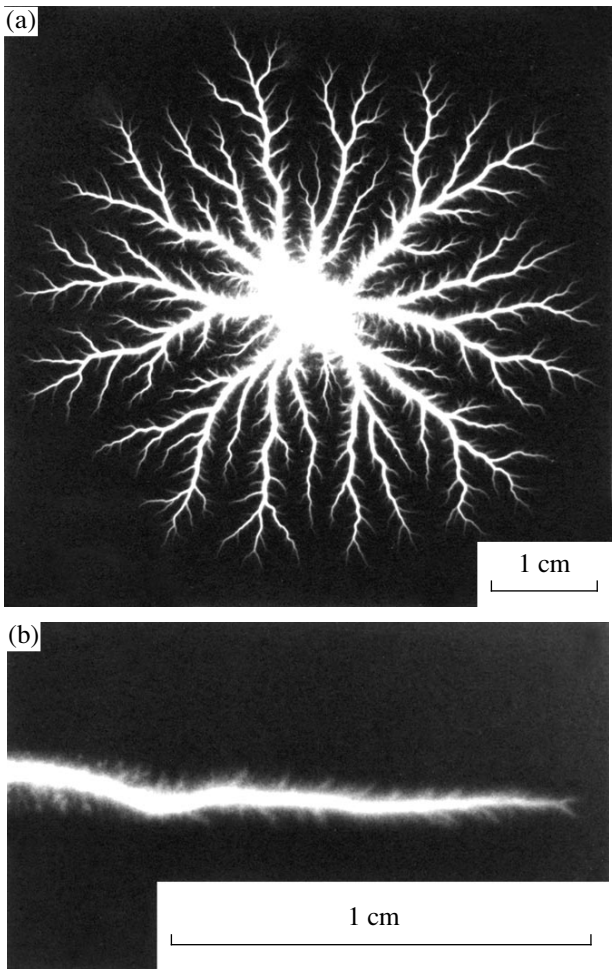

Fig. 2. (a) Two-dimensional discharge and (b) the end of a one-dimensional discharge.

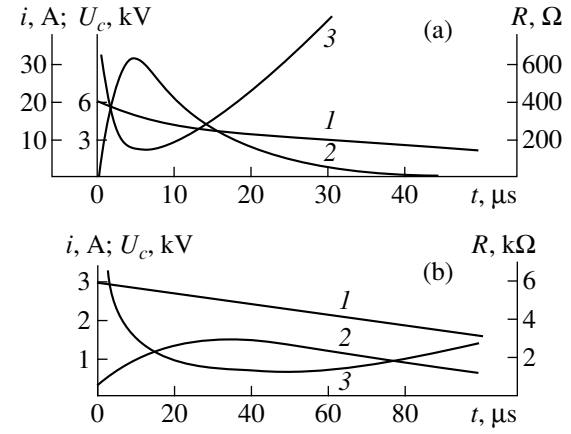

Fig. 3. Time dependences (oscillograms) of the (*1*) capacitor voltage, (*2*) discharge current, and (*3*) discharge circuit resistance. U_0 = (a) 6 and (b) 3 kV.

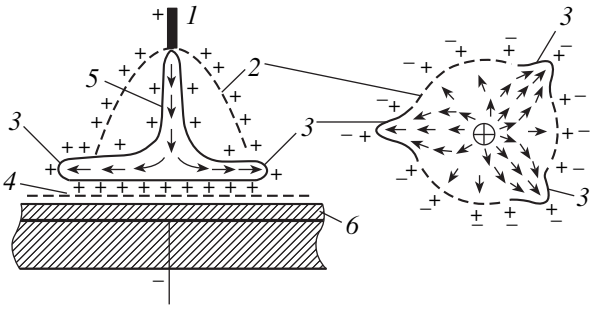

Fig. 4. Corona (dashed lines) and contracted (continuous lines) discharges in the anode–water gap. Pluses and minuses are charges on the plasma and water surfaces; arrows, current streams.

to develop over it. The onset of the discharge in the gap was indicated by the current passing through the discharge circuit. Its value increased from that typical of coronas to i_0 = 3 A (U_0 = 6 kV) (Fig. 3, curve *2*). The final value was set after the corona cone had touched the water surface. During this stage (≈100 ns), cathode layer *5* (Fig. 4), necessary for passing the conduction current, formed in the anode–water gap near the water and the initial corona was successively changed to glow, abnormal glow, and arc discharges *6*. The current value i_0 equals U_0/R_0, where R_0 is the discharge circuit resistance, which includes the plasma resistance in the anode–water gap and the resistance of the water layer between the cathode and corona cone. A further increase in the current is due to the LOW evolution, specifically, an increase in the leader area and water layer under the leader structure. This water layer defines the discharge circuit resistance at this stage of the discharge [4].

In [3], the structure of a quasi-one-dimensional leader was represented as consisting of a channel, arms, and branches. Streamers at the leader core, though expected, were absent in the photograph of the entire leader. According to [8], it was assumed that they are comparable in size with the core radius and remained unresolved. However, in the photograph taken with a greater magnification from a one-dimensional leader developed in the gap (Fig. 2b), filament-like formations against the diffuse background are seen in the last centimeter of the channel on both of its sides. Away from the core, branches are observed. The filaments were observed most distinctly in a microscope with a 16× magnification. The filament length increased from 150 μm at the core to 400 μm at 1 cm from it. The spacing between the filaments was 100 and 30 μm, respectively. The filament diameter was found to be 20–30 μm throughout the channel. The angle between the channel and filaments increases from 20° at the core of the leader to 80° at its end. However, streamers ahead of the leader were not observed either in the photograph or in the microscope. Here, it should be taken into consideration that the photograph of the entire leader is identical to the original only at the end part of the stopped leader. Away from the core, the image of the leader,

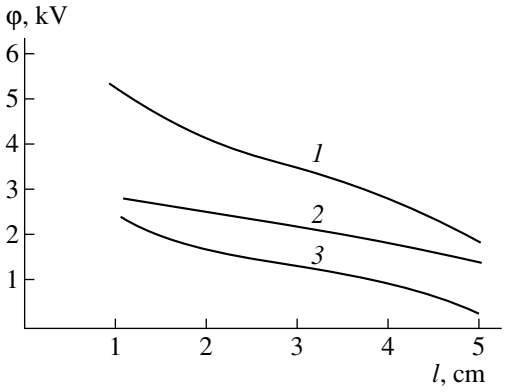

Fig. 5. (*1*) Core potential, (*2*) water surface potential, and (*3*) core–water potential difference vs. the leader length.

including that observed in the microscope, is the continuous superposition of its previous images.

With regard for data for pulse coronas [8, 9], one may suppose that the observed filaments are streamers arising when the moving core displays corona.

The leader core is driven by the Coulomb force, which is proportional to the potential difference between the core and water surface in front of it, $U = \varphi_c - \varphi_w$ (Fig. 5). In addition, the core motion is closely related to a plasma generated at the core front. It has been suggested [3] that the plasma is generated largely in the cathode layer, the voltage drop across which is 0.3–0.4 kV. Therefore, the core stops when $\Delta U = 0$.

However, the observed corona of the core and the coincidence (within the experimental error) of the corona threshold voltage in air (2.3 kV [10]) with the potential of the core at the instant it stops (2 kV) for any of the initial voltages in the range 3–6 kV strongly suggests that the corona discharge significantly contributes to plasma generation. On the other hand, it follows from the above that streamers would arise only ahead of the moving core if its potential exceeds 2.3 kV. Hence the absence of streamers in front of the stopped core in the photograph.

The major role of the core corona in the evolution of the leader is also strengthened by the decrease in the core velocity from $(1–2) \times 10^5$ to $(1–2) \times 10^4$ cm/s when the core potential drops to ≈3 kV (Fig. 5). This is also the threshold potential for the evolution of the leader, this threshold being of synergistic nature. The necessary value of the anode potential is the sum of the threshold potential for the corona discharge initiated from the tip, 2.3 kV, and the threshold voltage drop across the cathode layer, 0.3–0.4 kV. The core moves with a velocity of $(1–2) \times 10^4$ cm/s ($\Delta U \geq 0.4$ kV) also because of plasma generation in the cathode layer. Only when this layer breaks down ($\Delta U \leq 0.3$ kV) does the core stop. Note that, when the leader core stops, the rest of the channel may continue to display corona and, accordingly, the surrounding cathode layer may remain intact, since the channel potential near the anode is still relatively high. However, as the capacitor and anode voltages drop, the leader core moves towards the anode and the leader shortens.

Thus, the LOW evolution proceeds at two levels. It begins in the plasma of the corona cone near the water surface (the microlevel), where initial leaders, early macroelements, start to form (Fig. 4). However, the evolution of the macrostructure through the movement of the cores and their splitting are also provided by microprocesses taking place in the corona and cathode layer. The appearance of the corona and cathode layer has a threshold character. Hence, LOW structuring also has the voltage threshold.

LOW STRUCTURE AND POWER DISSIPATION IN THE DISCHARGE CIRCUIT

The other sign of true self-organization in dynamic dissipative systems is the growth of dissipated power during self-organization. As noted, the LOW structure develops from three to six initial leaders by repeatedly splitting their cores.

Each of the cores in the LOW structure moves through the interaction with the net field of polarization charges on the water surface and with elements surrounding the water. Therefore, the leading cores at the periphery of the structure move in the radial direction, while those lagging behind and being at the center of the structure move according to the randomly directed local field of the structure.

A combination of the determinate (radial) and random movements of the core makes the structure spatially stochastic and fractal [5]. The fractal dimension D of the structure does not depend on the number of initial leaders and on the initial voltage in the 4–6 kV range (the range being studied). The fractal dimension of the structure is related to the full length L of its elements in a given radius r; namely, $L \sim r^D$. In our case, the radius of the structure equals the length of the leaders l, $l \sim t^{1/2}$ [3, 4]; hence, $L \sim t^{D/2}$. At the same time, the discharge circuit resistance is defined by that of the water layer under the structure, that is, depends on the structure size and element density. Eventually, $R \sim 1/L \sim t^{-D/2}$. As the structure develops, the voltage across the capacitor reduces insignificantly (Fig. 3); therefore, the current in the circuit $i = U_0/R \sim t^{D/2}$, and the power dissipated in the discharge circuit is $P \sim i^2R \sim t^{D/2}$. That is, the power dissipated in the circuit at the stage of current growth is proportional to the full length of the structure elements.

As stated above, when the corona ceases, the core slows down, and when its potential becomes equal to that of the water, the core stops. The current ceases to grow, the power balance in the channel is violated, the plasma in the core breaks down, and the structure shrinks. This, in turn, causes the current, and hence,

power in the discharge circuit to decrease further, etc. [3].

The analysis of the origination and evolution of the LOW structure, as well as its relation to the power dissipated in the discharge circuit, allows us to argue, by analogy with self-organization in nonequilibrium dynamic dissipative systems [6, 7], that the LOW structure evolution represents one more example of dissipative system self-organization.

STRUCTURE SELF-ORGANIZATION

Once the fact of self-organization is established, it makes sense to treat this phenomenon at length. We proceed from the assumption that system elements provide necessary conditions for structuring and structure evolution.

By elements of the well-developed LOW structure, we will mean leader channels in the region from the corona cone to the most remote (along the radius) core, side arms emerging from the channels or larger arms to the core most remote from them, and arms emerging from the last bifurcations together with their cores. The role of branches in LOW self-organization is insignificant, and they will be excluded from consideration. A specific feature of LOW structure self-organization is that these structure elements appear immediately during LOW evolution and self-organization.

As noted, at the early stage of structuring, areas with an elevated charge density, which give rise to cores, appear in the boundary layer of the corona nonequilibrium plasma. These areas move, because the charged plasma is unstable in the electric field. When moving, the cores leave behind them a conducting plasma channel, which transfers the corona cone potential to the cores. The resulting core–channel plasma formation is the initial macrostructure element, a leader nucleus. Its further development implies core splitting and the emergence of side arms, which are new structure elements. As the number of structure elements grows and the system becomes unstable, self-organization at the macrolevel starts. Here, the early channels become the first (basic) ordering parameters. The side arms and branches of leaders set up the final hierarchy of ordering parameters in LOW structuring.

Leader core splitting is certainly the key process in LOW structuring. In [5], core splitting was associated with a like residual charge present in front of a core. As the core moves, the charge builds up, so that the core front flattens at points where it touches the channel envelope. It appears, however, that the residual charge may not be a decisive factor in core splitting. Indeed, a streamer core is not split, as a rule, but retains its shape (self-sharpens) [11]. This self-consistent process can be explained by a decrease in the energy density in the streamer channel with distance from the core; accordingly, the rate of ionization drops, and the channel narrows. On the contrary, a leader channel expands with distance away from the core; hence, the core must flatten on its axis. One can argue, in this case, that the plasma formation (a cylindrical channel and a hemispheric core) cannot be dynamically stable. According to the type of core–electrode coupling, the formation will necessarily be converted either to a streamer with a narrowing channel or to an expanding leader. Therefore, analysis of streamer or leader evolution within the cylindrical model will inevitably cause errors.

Generally, self-organization in a system occurs when it is necessary to enhance the energy flux through it from an external source with a growing gradient at the system boundaries. Under such conditions, a mechanism of energy transfer through the system changes to a higher-rate one. In liquids, for example, heat conduction changes to Benard cellular convection, and in lasers, spontaneous lasing changes to induced lasing. In our case, the system cannot enhance the energy flux by locally increasing the process rate, since the water conductivity remains unchanged. Here, the energy flux grows owing to the extensive development of the system in the form of LOW structuring. Remarkably, not only LOW structure elements are produced but also the nonlinear interaction of the entire system with the energy source to sustain structure instability is provided.

It is known that positive feedback (PF) arising in a system is a sign of its instability. In our case, it shows up (at the stage of current growth) as a continuously maintained unambiguous correspondence between the length of a leader and the current through it (*l–i* correspondence) [3], i.e., between the radius of the structure and the current through it. This correspondence reflects the relation between the leader core potential and the anode (corona cone) potential. This relation sets in through the channel, whose conductivity depends on the passing current. Note that PF is inherent in leader evolution and can be considered as an immanent property in developing each of the structure elements.

As the cores are split, the number of structure elements increases and so does the charge interaction between them. This interaction appears as negative feedback (NF), which is inherent in the entire structure.

It is obvious that the PF prevails early in structuring; therefore, the number of structure elements doubles within 0.2 cm (Fig. 6). Then, NF comes into play, and the rate of element production diminishes. Subsequently, the partial contributions of NF and PF to the overall process presumably vary, as follows from the varying number of elements (Fig. 6, curve *1*). This combined action continues until all structure elements develop over the entire structure area and depends on the element position in the structure. It is responsible for the competitive growth of the elements and their selection by formation rate and, hence, length. Eventually, the structure becomes hierarchically self-similar, i.e., fractal [5].

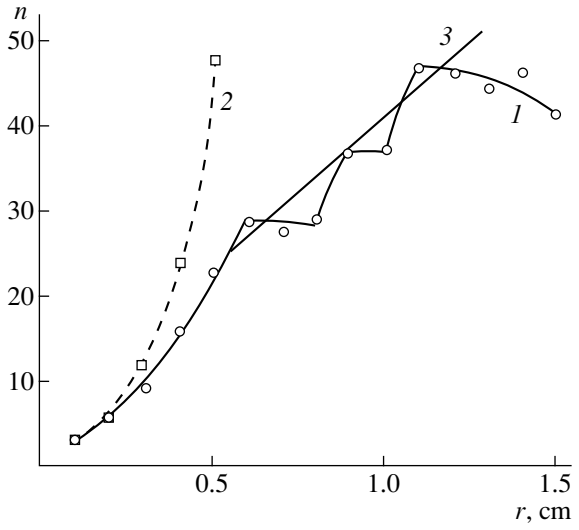

Fig. 6. Number of elements vs. radius: (*1*) actual structure, (*2*) doubled number, and (*3*) averaged curve to calculate *D*.

However, the space–time characteristics of the structure also depend on other factors. Since each of the elements is subjected to the determinate and random fields and the element position specifies their combined action on it during the structure evolution, the LOW structure exhibits time-variant stochasticity. On the other hand, the nonstationarity of the energy source and the absence of limits for structuring make the system spatially irregular, unlike Benard cells and laser modes, i.e., space-stochastic.

In the foregoing, LOW self-organization after the appearance of several initial leaders was considered. However, a mechanism of their appearance, i.e., processes in the plasma layer at the water surface, is also of great interest. This nonequilibrium plasma layer forms when the corona cone base comes in contact with the water surface. The diameter of the layer is close to that of the cone base (0.1–0.3 cm, depending on U_0), and its thickness is comparable to the core diameter, $\approx 10^{-2}$ cm. As the current through the layer grows when contracted along the anode–water gap axis, so does (within ≈100 ns) the energy flux through the layer. This may induce ionic–acoustic vibrations in the plasma layer. Charge density crests at the layer periphery may initiate the nucleation of initial leaders.

Another possible initiation mechanism is the occurrence of a planar double electric layer at the instant when the positively charged cone base touches the negatively charged water surface (Fig. 4). Further, this layer serves as the cathode layer to provide a discharge in the anode–water gap. Its diameter and thickness are 0.1–0.3 and $\approx 10^{-3}$ cm, respectively [10]. With regard for the planar geometry of the cathode layer, oppositely moving electrons and ions in it, and a drastic increase in the energy flux when the current contracts, a current structure of Benard cell type may form in this layer. Current stratification observed in the cathode layer of a glow discharge [10] and cathode spot ordering [12] are indirect evidence for this supposition. In this case, the current structure in the cathode layer will modulate the charge density in the plasma layer adjacent to it on the anode side (Fig. 4), and the crests of the charge density at the boundary of this layer will give rise to initial leaders.

In both mechanisms, the charge density varies in a regular manner, including in the periphery of the layer, which provides the symmetric arrangement of initial leaders. Note that the symmetry is also a necessary condition for the resulting structure to be electrically stable.

The nucleation of initial leaders may follow the third possible scenario. Since the *l–i* correspondence, acting as PF, is universally present in the system, radial charge-density microfluctuations in the corona plasma layer at the water surface may be brought to the macrolevel. The competition between (and eventually the selection of) macrofluctuations will cause radial splitting (contraction) of the current into several channels (Fig. 4), and the charge interaction between the macrofluctuations will provide the electrical stability of the channels.

Obviously, the above scenarios are not mutually exclusive and may coexist during self-organization at the microlevel. The early stage of LOW structuring calls for further investigation. It would be useful for finding determinateness limits at the early stage of self-organization in any system. In our opinion, the phenomenon of LOW structuring offers a greater scope for experimentation than other physical systems.

Our studies of LOW structuring and structure evolution [3–5] can be summarized as follows.

(1) LOW structuring exhibits all of the signs of self-organization in nonequilibrium dynamic dissipative systems [6, 7].

(2) LOW self-organization proceeds in two stages. First, the radial charge-density structure forms in the disk-shaped layer of the nonequilibrium plasma near the water surface; then, the LOW current channels evolve from the charge density structure.

(3) The evolution and self-organization of the LOW structure impose limits on the specific power (power per element) dissipated in the system. This leads to a rise in the number of structure elements by splitting and, hence, the total dissipated power; in other words, the self-organization proceeds in the extensively developing system.

(4) A structure element moves because of the movement of its core, which is driven by the source potential. The source potential is transferred to the core through the channel. Hence, the cores and channels fulfil different functions during the process.

(5) The self-organization of the structure is governed by a combined action of PF, the immanent prop-

erty of each of the elements, and NF, the immanent property of the structure as a whole. This leads to the competition between structure elements, their selection, and the fractality of the structure. In addition, dynamic self-consistency between the structure and power source is provided.

(6) The nonstationarity of the power source and the unrestrictedness of LOW structuring are responsible for the space–time stochasticity of the structure.

(7) Based on items 1–4, LOW self-organization can be considered as a universal evolutionary model.

REFERENCES

1. V. P. Belosheev, Zh. Tekh. Fiz. **66** (8), 50 (1996) [Tech. Phys. **41**, 773 (1996)].
2. V. P. Belosheev, RF Patent No. 2042641 (May 14, 1992).
3. V. P. Belosheev, Zh. Tekh. Fiz. **68** (7), 44 (1998) [Tech. Phys. **43**, 783 (1998)].
4. V. P. Belosheev, Zh. Tekh. Fiz. **68** (11), 63 (1998) [Tech. Phys. **43**, 1329 (1998)].
5. V. P. Belosheev, Zh. Tekh. Fiz. **69** (4), 35 (1999) [Tech. Phys. **44**, 381 (1999)].
6. I. P. Prigozhin, Usp. Fiz. Nauk **131** (2), 189 (1980).
7. H. Haken, *Synergetics: an Introduction* (Springer-Verlag, Berlin, 1977; Mir, Moscow, 1980).
8. É. M. Bazelyan and I. M. Razhanskiĭ, *Spark Discharge in Air* (Nauka, Novosibirsk, 1988).
9. I. S. Stekol'nikov, *The Nature of Long Spark* (Akad. Nauk SSSR, Moscow, 1960), p. 55.
10. Yu. P. Raĭzer, *The Physics of Gas Discharge* (Nauka, Moscow, 1987).
11. Yu. P. Raĭzer and A. N. Simakov, Fiz. Plazmy **24**, 754 (1998) [Plasma Phys. Rep. **24**, 700 (1998)].
12. Yu. D. Korolev and G. A. Mesyats, *The Physics of Pulse Breakdown* (Nauka, Moscow, 1991).

Translated by V. Isaakyan

Technical Physics, Vol. 45, No. 7, 2000, pp. 928–930. Translated from Zhurnal Tekhnicheskoĭ Fiziki, Vol. 70, No. 7, 2000, pp. 115–117.

EXPERIMENTAL INSTRUMENTS AND TECHNIQUES

Melting of Aluminum Nitride at Atmospheric Nitrogen Pressure

L. G. D'yachkov, L. A. Zhilyakov, and A. V. Kostanovskiĭ

Joint Institute for High Temperatures, Russian Academy of Sciences, Moscow, 127412 Russia

E-mail: dyachkov@theor.termo.msk.ru

Received August 19, 1998; in final form August 26, 1999

Abstract—Experimental results on the melting of aluminum nitride heated by an electric arc burning in a nitrogen atmosphere at a pressure of 0.2–0.3 MPa are presented. A qualitative explanation of the dissociation suppression mechanism under arc heating is proposed. It has been shown that the suppression is possible at atmospheric pressure due to the photoactivation of aluminum on the sample surface by resonant radiation of aluminum vapors present in the electric arc. © *2000 MAIK "Nauka/Interperiodica".*

INTRODUCTION

Aluminum nitride (AlN) is a promising material possessing a combination of properties valuable for practical use [1]. Their full utilization is possible for mono- or polycrystalline AlN. Dense crystalline aluminum nitride can be obtained either by gas-phase growth [2] or by crystallization from melt [3, 4]. The latter method is more productive but its implementation is extremely difficult. Heating of aluminum nitride at atmospheric pressure results in intensive dissociation and complete destruction of the sample (transition from solid to gas phase) already at 2400–2700 K, which is much lower than its melting point $T_m = 3070 \pm 100$ K [5]. Therefore, to determine the melting parameters of aluminum nitride and produce it in polycrystalline form, growth from melt at elevated nitrogen pressure is used in order to suppress the thermal dissociation of AlN. For example, laser melting requires a nitrogen pressure not lower than 10 MPa [3], while in a container melting, it is 0.5 MPa [4].

In [6] an experiment on heating a porous AlN ceramics by an ac electric arc at nitrogen pressures 0.2–0.3 MPa was carried out. The arc was initiated under the AlN sample and the current was 60–80 A. Indications of aluminum nitride melting were observed.

The choice of the alternating current arc as a heater, the porous ceramics as an AlN sample, and the scheme of heating from the bottom is not accidental. The alternating field confines Al^+ ions [7] and having the arc under the sample reduces the carry-over of aluminum vapor forming as a result of AlN dissociation from the reaction zone by convection currents. However, heating from the bottom poses the problem of melt confinement. The porous sample structure through the capillary enables a sufficient amount of molten AlN phase to be accumulated for unambiguous instrumental proof of the fact of melting. In these conditions, samples have been obtained with a clearly distinguishable remelted surface layer having properties differing from those of the starting material and possessing high hardness. X-ray phase analysis has shown that the dominant phase (up to 99%) in the molten layer is a perfectly crystallized aluminum nitride. Detailed description of the experiment as well as of the preceding studies has been given in [6].

This paper considers the suppression mechanism of AlN dissociation as well as the specific conditions of the electric arc heating favoring the AlN melting. The possibility of melting aluminum nitride at atmospheric pressure has been shown.

DISSOCIATION SUPPRESSION MECHANISM

Suppose that the surface of an AlN sample is heated to melting point T_m. However, for the melting really to occur, it is necessary that a dynamic equilibrium between the condensed aluminum nitride and the gas phase products of its decomposition be established according to the reaction

$$\mathrm{AlN}c \longleftrightarrow \mathrm{Al} + 1/2\mathrm{N}_2 \qquad (1)$$

(c denotes the condensed state). Otherwise, if the partial pressures of nitrogen and aluminum vapors are too low, instead of melting, an intensive dissociation will take place. The constant of reaction (1) given by

$$K = P(\mathrm{Al})P^{1/2}(\mathrm{N}_2) \qquad (2)$$

at thermodynamic equilibrium can be expressed, for example, in terms of constants of the reactions $\mathrm{AlN}(c) \longleftrightarrow \mathrm{Al} + \mathrm{N}$ and $\mathrm{N}_2 \longleftrightarrow 2N$, which can be found in [8]; at $T \cong 3000$ K, it is equal to 0.12 $\mathrm{MPa}^{3/2}$. This means that at a partial nitrogen pressure $P(\mathrm{N}_2)$ of, say, 0.1 MPa, the equilibrium pressure of aluminum vapors should be 0.38 MPa, which is impossible since the saturated vapor pressure of aluminum at this tem-

1063-7842/00/4507-0928$20.00

perature is only 0.24 MPa [8]. If $P(\mathrm{Al}) = 0.24$ MPa, the equilibrium nitrogen pressure will be equal to $P(\mathrm{N_2}) = 0.25$ MPa as it follows from (2).

Thus, the aluminum nitride can be melted only at nitrogen pressures of no less than 0.25 MPa. In this case, if $P(\mathrm{N_2})$ is not too high, the aluminum vapor should be close to saturation, which is difficult to provide technically since, in the absence of the hermeticity of the heated volume, the vapor will intensively diffuse to colder regions and condense there. To reduce $P(\mathrm{Al})$ by a factor of n while maintaining the equilibrium of process (1), it is necessary to increase the nitrogen pressure by a factor of n^2. Therefore, the melting of AlN can be achieved only at pressures that are high enough.

The conclusion made above is true for the conditions of thermal excitation of aluminum atoms. In the process of AlN dissociation, excited aluminum atoms Al* are released, presumably to the first excited state $4s(^2S)$ with energy $E^* = 3.14$ eV [9]. Therefore, the reaction that is actually taking place is

$$\mathrm{AlN}(c) \longleftrightarrow \mathrm{Al}^* + 1/2\mathrm{N_2}, \tag{3}$$

and the reaction constant can be written in the following form

$$K^* = P(\mathrm{Al}^*)P^{1/2}(\mathrm{N_2}), \tag{4}$$

where $P(\mathrm{Al}^*)$ is the partial pressure of aluminum atoms in the $4s(^2S)$ state.

At $T = 3000$ K, the equilibrium pressure of excited atoms is

$$\begin{aligned} P(\mathrm{Al}^*) &= P(\mathrm{Al})\frac{g^*}{\Sigma(T)}\exp\left(-\frac{E^*}{kT}\right) \\ &= 1.77\times 10^{-6}P(\mathrm{Al}). \end{aligned} \tag{5}$$

Here $g^* = 2$ is the statistical weight of the excited state; Σ is the statistical sum of an atom, which at a specified temperature is actually equal to the statistical weight $g = 6$ of the ground state $3p(^2P)$. As a result, we obtain $K^* = 210\mathrm{Pa}^{3/2}$; that is, at atmospheric nitrogen pressure, $P(\mathrm{Al}^*) = 0.7$ Pa.

After dissociation by (3), aluminum atoms pass to the ground state and an equilibrium between the ground and excited states sets up. Only then, if excitation/deexcitation of the atoms in the near-surface gas layers results from collision processes, the direct and reverse reactions (3) (as well as (1)) may come to an equilibrium making the melting possible. This will occur at the extremely high equilibrium gas phase pressures specified above, although the vast majority of aluminum atoms in the ground state are not involved in the processes (3). In this case, the number of excited aluminum atoms arriving at a sample surface element ds in time dt and maintaining equilibrium in (3) is determined by the expression

$$dN = \frac{P(\mathrm{Al}^*)}{\sqrt{2\pi MkT_m}}dsdt, \tag{6}$$

where M is the mass of the aluminum atom. It is assumed that in the near-surface gas layer of a thickness of the order of the atom free path, the temperature is close to the surface temperature T_m.

If the occupation of the excited states is governed by some nonthermal process and is in excess of that given by (5), only the equilibrium in (3) (but not in (1)) is of importance. In that case, the melting is possible at lower gas phase pressures.

When a sample is heated by arc, the excitation of aluminum atoms at the surface can be caused by radiation from the arc. Then, the condition for equilibrium in (3) and therefore, the possibility of melting, can be described as follows. After dissociation by (3), aluminum atoms pass to the ground state and escape to the arc plasma. The density of aluminum vapors in the arc plasma increases until the intensity of radiation from the arc due to the aluminum resonant transition $4s(^2S) \longrightarrow 3p(^2P)$ becomes high enough for excitation of such a number of aluminum atoms at the sample surface that an equilibrium between the direct and reverse reactions in (3) is established. To estimate the minimum required aluminum vapor density in the arc, the number of resonant photons arriving at the sample surface should be no less than that given by (6). Expressing $P(\mathrm{Al}^*)$ from (4) and substituting into (6), we obtain that the flux density of resonant photons emitted by the arc should be no less than

$$j = \frac{K^*(T_m)}{\sqrt{2\pi MkT_m P(\mathrm{N_2}, T_m)}}. \tag{7}$$

At the same time, the flux density of aluminum atoms coming to the sample surface should be no less than the value given by (7), and all these atoms can be considered to be in the ground state. For this to occur, the aluminum vapor pressure in the near-surface layer should be no less than the equilibrium partial pressure of excited atoms at the melting temperature, which is given by equation (4).

The flux density of photons at an emission wavelength λ is

$$j_a = \frac{lN_a^*A}{4\pi} = \frac{2\pi e^2}{mc}\frac{lN_a gf}{\lambda^2\Sigma(T_a)}\exp\left(-\frac{E^*}{kT_a}\right), \tag{8}$$

where A is the transition probability (Einstein coefficient); f is the oscillator strength; and N_a^* and N_a are the densities of excited atoms and the total density of aluminum atoms in the radiating plasma layer of thickness l at a temperature T_a, respectively.

For the transition under consideration, $f = 0.12$ [10]. To make an estimation, assume that the temperature T_a and electron density n_e in the arc are independent of the aluminum vapor density; that is, the desired minimum density N_a is low enough. We take $T_a = 12000$ K and $n_e = 10^{17}$ cm^{-3} [11]. Thus, it is assumed that the density of aluminum ions is less than 10^{17} cm^{-3}. Assume also that the arc plasma is transparent for the resonant radiation; i.e., the characteristic transverse dimension of the arc l can be taken equal to ≈0.5 cm.

Based on the assumptions made and equating (7) and (8), we obtain

$$N_a \approx \frac{2 \times 10^{15}}{\sqrt{P(\mathrm{N}_2, T_m)}},$$

where the nitrogen pressure is measured in Pa and the aluminum atom density, in cm^{-3}.

From the Saha equation, it is easy to determine that the aluminum ion density is $N_i \approx 30N_a$. At atmospheric nitrogen pressure, $N_a \approx 6 \times 10^{12}$ cm^{-3} and $N_i \approx 2 \times 10^{14}$ cm^{-3} < 10^{17} cm^{-3}, as was assumed. In the conditions under consideration, the broadening of spectral lines is of the Stark type and the resonance line has a Lorenz contour with a halfwidth $\Delta\lambda = 0.016$ nm [12]. For the Lorenz contour, the adsorption coefficient at the center of the line is

$$k_\lambda = \frac{e^2\lambda^2 N_a f}{mc^2\Delta\lambda}$$

and at nitrogen pressures approaching the atmospheric pressure, the optical thickness $k_\lambda l \sim 0.1$; that is, for the resonance aluminum line, the arc plasma is transparent. Therefore, the assumptions made are valid.

At an aluminum vapor density $N_a + N_i \approx 2 \times 10^{14}$ cm^{-3}, the respective partial pressure in the arc is about 30 Pa. Taking into account that aluminum comes from the AlN dissociation at the sample surface and the fact that, with heating from the bottom, convective currents return the aluminum vapors to the sample surface, it can be assumed that, near the surface, the vapor pressure will be not lower than in the arc. The latter exceeds the equilibrium partial pressure of excited atoms at $T_m = 3000$ K, which is of the order of 1 Pa as follows from (5). Therefore, the second condition for suppressing the dissociation will be fulfilled as well.

CONCLUSIONS

In [6], it has been experimentally shown that it is possible to suppress the dissociation of aluminum nitride and melt it by an electric arc in a nitrogen environment at pressures close to the atmospheric pressure. In this study, relying on the analysis of the dissociation mechanism, it has been shown that, even at aluminum vapor partial pressure in the arc of the order of 10–100 Pa, the conditions for the photoactivation of the number of Al atoms necessary to suppress the AlN dissociation are ensured and the melting of aluminum nitride at atmospheric nitrogen pressure is made possible. This is a result of aluminum photoactivation at the AlN sample surface at the melting temperature by resonant radiation of the aluminum vapor from the hot zone of the arc. It is important, therefore, that the arc be positioned under the AlN sample; otherwise the convective currents would carry aluminum vapors away from its surface and the necessary vapor density may not be attained.

The method considered can also be successfully applied in melting other easily dissociating high-melting-temperature nonmetallic nitrides, like nitrides of boron, silicon, and others.

REFERENCES

1. G. V. Samsonov, *Nitrides* (Naukova Dumka, Kiev, 1969).
2. G. A. Slack and T. F. McNelly, J. Cryst. Growth **42**, 560 (1977).
3. A. V. Kostanovskiĭ, Teplofiz. Vys. Temp. **32**, 742 (1994).
4. A. V. Kostanovskii and A. V. Kirillin, in *Proceedings of the International Symposium on Nitrides, Saint-Malo, France, 1996*, Vol. B28.
5. V. L. Vinogradov, A. V. Kostanovskii, and A. V. Kirillin, High Temp.–High Press. **23**, 685 (1991).
6. L. A. Zhilyakov and A. V. Kostanovskiĭ, Teplofiz. Vys. Temp. **37**, 71 (1999).
7. D. A. Zhilyakov, D. N. Gerasimov, and A. V. Kostanovskiĭ, Teplofiz. Vys. Temp. **35**, 147 (1997).
8. L. V. Gurvich, I. V. Veĭts, V. A. Medvedev, *et al.*, *Thermodynamic Properties of Substances* (Nauka, Moscow, 1978–1982), Vols. 1–4.
9. L. A. Zhilyakov, A. V. Kostanovskiĭ, and A. V. Kirillin, Dokl. Akad. Nauk SSSR **35**, 606 (1994).
10. A. A. Radtsig and B. M. Smirnov, *Reference Data on Atoms, Molecules, and Ions* (Énergoatomizdat, Moscow, 1986; Springer-Verlag, Berlin, 1985).
11. É. I. Asinovskiĭ, A. V. Kirillin, and V. L. Nizovskiĭ, *Sustained Electric Arcs and Their Application in Thermal Physical Experiment* (Nauka, Moscow, 1992).
12. H. R. Griem, *Spectral Line Broadening by Plasmas* (Academic Press, New York, 1974; Mir, Moscow, 1978).

Translated by M. Lebedev

Technical Physics, Vol. 45, No. 7, 2000, pp. 931–936. Translated from Zhurnal Tekhnicheskoĭ Fiziki, Vol. 70, No. 7, 2000, pp. 118–124.

EXPERIMENTAL INSTRUMENTS AND TECHNIQUES

A New Model of a Quantum Magnetometer: A Single-Cell Cs–K Tandem Based on Four-Quantum Resonance in ^{39}K Atoms

E. B. Aleksandrov, M. V. Balabas, A. K. Vershovskiĭ, and A. S. Pazgalev

Vavilov State Optical Institute, All-Russia Research Center, ul. Babushkina 36/1, St. Petersburg, 199034 Russia

E-mail: balabas@soi.spb.ru

Received September 3, 1999

Abstract—A new model of a quantum magnetometer based on the principle of Cs–K tandem was developed and experimentally tested. The specific features of the magnetometer are a single absorption cell containing Cs and K vapors, digital synthesis of the potassium resonance frequency by multiplying the cesium resonance frequency by a conversion factor (the ratio of the atomic constants), and the use of four-quantum resonance in potassium atoms. Device readings were found to be insensitive (within 10 pT) to variations of the main operating parameters even if the variations go far beyond the normal service variability. © *2000 MAIK "Nauka/Interperiodica".*

INTRODUCTION

Since the late 1950s, the absolute values of magnetic fields falling into the geophysical range have been usually measured with optically pumped quantum magnetometers. Optically pumped magnetometers (OPMs) are significantly more sensitive and faster than conventional proton (precession) magnetometers [1–3]. In addition, the recently developed OPM models provide a higher accuracy of measurement than the proton instruments. Many OPM models of different measuring accuracy, resolving power, speed, working range, power consumption, weight, dimensions, price, etc., have been described in the literature. In view of a wide variety of OPM applications, it is hardly probable that they will ever be covered by one unified multipurpose OPM design. Therefore, the development of new OPM models best suited to specific types of measurement remains a topical problem.

The goal of this work is to describe a new OPM model intended largely for observatory measurements of the magnetic field magnitude in the geomagnetic range. The model is distinguished by high speed (0–100 Hz band) and high resolution (~10 pT/Hz$^{1/2}$) in combination with the record-breaking long-term stability (reading variations within 10 pT) and a strictly linear dependence of the resonance frequency on magnetic induction. Although such good characteristics have previously been achieved in some other types of OPMs, the model under consideration is the first to combine all of these advantages. Note also that, in the field of metrology, it is always worthwhile to develop a device based on an essentially new approach even if its metrological performance is not superior to that of previous models.

PRINCIPLE OF OPERATION

In metrology, the problem of combining high accuracy with high speed is usually solved by integrating two different measuring devices into a single system so that the readings of a high-speed device are corrected with a slower-speed but high-precision device. This principle is used, for example, in modern time-keeping systems and was proposed to be applied in precise measurements of the magnetic induction magnitude [4]. A magnetometer built around this principle is often called tandem. It consists of OPMs of two types: a spin generator with the output frequency proportional to the external magnetic induction (M_x–OPM) and a passive radio spectrometer where a feedback loop is employed for holding a selected resolved magnetic resonance line (M_z-OPM). The latter OPM provides a higher accuracy of resonance frequency measurement, whereas M_x-OPM oscillates near the center of gravity of a group of unresolved lines and, therefore, is prone to large systematic errors.

In the early tandem model, the atomic vapor of the rubidium isotope ^{87}Rb was used in both components. However, ^{87}Rb proved to be a poor choice, because its magnetic resonance spectrum contains a group of lines the spacing between which in the slightly disturbed magnetic field of the Earth is only several times larger than their widths. A Cs–K tandem [5] (cesium is used in the M_x component; and potassium, in the M_z component), developed many years after its Rb counterpart, is free from this disadvantage, because the magnetic resonance spectrum of potassium is completely resolved in the whole range of the earth's magnetic fields. This prevents the interference of adjacent spectral lines.

1063-7842/00/4507-0931$20.00

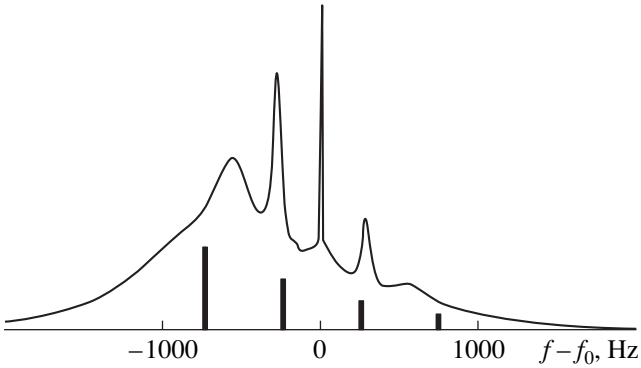

Fig. 1. Calculated dependence of the pump light absorption by ^{39}K vapors on the frequency f of RF field $H_1(f)$.

The distinguishing features of the OPM tandem described in this work are as follows: (1) the absorption cell, containing a mixture of Cs and K vapors, is shared by the component magnetometers and (2) the potassium M_z-OPM uses the four-quantum (4Q) magnetic resonance line corresponding to the transition between the sublevels $|F = 2, m_F = 2\rangle \Leftrightarrow |F = 2, m_F = -2\rangle$.

The common absorption cell by both magnetometers eliminates the systematic error caused by a difference in the magnetic fields in two separate cells. In addition, this reduces the size of the device. The use of four-quantum magnetic resonance allows the device resolution to be increased many times. Another advantage is that the dependence of the four-quantum resonance frequency on the magnetic induction is strictly linear. As shown in [6, 7], the high-order resonance line $n = 2F$ is prominent in the spectrum of n-quantum transitions like $\Delta F = 0$, $\Delta m_F = |n|$. The frequency of this resonance is almost independent of the alternating magnetic field intensity H_1. Moreover, this resonance line is the narrowest and has the highest intensity. In the case of potassium, the maximum value of the total angular momentum F equals 2. Therefore, the multiplicity of the high-order resonance is 4. At optimum values of the magnetic field intensity H_1, the four-quantum resonance width can be as small as several hertz, whereas the other resonance lines are significantly broadened. This allows the problem of searching and holding the required resonance line (the total number of resonance lines is 10) to be easily solved. An example of the potassium magnetic resonance spectrum calculated for the case of pumping with circularly polarized D_1-line light is shown in Fig. 1. The curve represents the superposition of multiquantum resonances of multiplicity 1–4 in a strong magnetic field H_1. The underlying discrete spectrum shows four single-quantum resonances in a weak field H_1. The abscissa is $f - f_0$, where f is the frequency of the radio-frequency (RF) alternating magnetic field applied and f_0 is the four-quantum resonance frequency. The continuous spectrum was calculated for the static magnetic field 50 μT and the relatively high amplitude of the alternating magnetic field H_1 ($\gamma H_1 = 200\Gamma_0$, where $\gamma = 7$ Hz/nT is the gyromagnetic ratio and Γ_0 is the width of the single-quantum resonance line). The (discrete) spectrum of slightly excited potassium atoms is calculated for the weak alternating magnetic field H_1 such that $\gamma H_1 = \Gamma_0$. This spectrum consists of four almost equidistant lines corresponding to $m_F \Leftrightarrow m_F + 1$ transitions for $F = 2$. Their width is far less than the distance between them and cannot be resolved in the scale of the figure. It is seen that the two spectra diverge significantly. That of potassium excited by the strong magnetic field is characterized by the extraordinarily narrow four-quantum resonance line and resonance lines of multiplicity n = 1–3, broadened by the magnetic field.

The block diagram of the device is shown in Fig. 2. The detector of the magnetometer incorporates an evacuated spherical glass bulb 80 mm in diameter. The inner surface of the bulb is covered by a paraffin film. The bulb has an extension containing a globule of the cesium–potassium alloy. Thus, at a temperature of about 50°C, the densities of Cs and K vapors inside the bulb are kept close to each other.

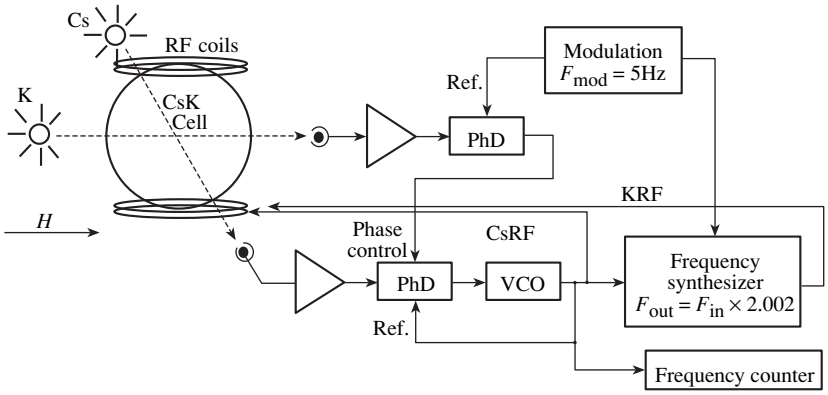

Fig. 2. Simplified functional diagram of the Cs–4QK tandem.

The bulb is illuminated by beams of circularly polarized light from cesium- and potassium-discharge lamps. Only the D_1 lines of resonance doublets are used. The potassium light is aligned with the static magnetic field, whereas the cesium beam makes an angle of ~45° with the field direction. After passing through the cell, both beams are detected with silicon photodiodes. The resulting photocurrents are amplified and applied to the inputs of two phase detectors (PhDs). The cesium spin generator is based on the principle of self-tuning of the voltage-controlled oscillator (VCO) frequency to the cesium resonance frequency. For this purpose, the signal from the cesium beam photodetector is applied to one of the inputs of the phase detector. The reference signal is generated by the VCO. If the frequency of the VCO, feeding the RF induction coil, is close to the cesium resonance frequency, the pump beam, having passed the bulb, becomes amplitude-modulated at the VCO frequency. The modulation phase depends on how close the VCO frequency is to the resonance frequency. The signal from the VCO is applied to the second input of the phase detector. In turn, the VCO frequency is controlled by the output voltage of the phase detector. In this manner, the VCO is tuned to the resonance frequency.

The cesium resonance frequency is a rough measure of the external magnetic field intensity. However, its value needs correction because of significant systematic errors. The correction is performed by bringing an additional loop for controlling the VCO frequency in the device circuit through the signal of four-quantum potassium resonance. The doubled frequency of cesium resonance deviates only by 0.1% from the four-quantum potassium resonance frequency throughout the range of geomagnetic fields. This allows the potassium resonance frequency to be synthesized by merely multiplying the VCO frequency by a constant factor of 2.002395 …. Along with the frequency multiplication, provision is made for a slow (at a frequency of 5 Hz) frequency modulation of the VCO signal. The signal induced by the potassium beam is synchronously detected at the modulation frequency. This allows the error signal for correcting the VCO frequency (f_{VCO}) to be obtained (provided that f_{VCO} lies within the cesium resonance line width). Thus, the output frequency dynamics is measured using the fast cesium magnetometer; then, the obtained data are corrected with regard for the narrow potassium resonance frequency measured with the slower potassium magnetometer.

The frequency f_K of four-quantum resonance in potassium atoms depends on the magnetic field intensity H as

$$f_K = H\mu_B(g_j + 3g_i)/(4h), \quad (1)$$

where μ_B is the Bohr magneton; g_j and g_i are the electron and nuclear g factors for potassium, respectively; and h is Planck's constant.

METROLOGICAL PERFORMANCE OF THE MAGNETOMETER

The absolute values of the constants involved in equation (1) are known with an accuracy to ~10^{-7}. Taking the values of g_j and g_i for the potassium isotopes ^{39}K and ^{41}K from [8]:

$$g_f = 2.00229421(24),$$

$$^{39}g_i = -1.14193489(12) \times 10^{-4},$$

$$^{41}g_i = -0.7790600(8) \times 10^{-4}$$

and that of μ_B/h from the CODATA Recommendations, (1997):

$$\mu_B/h = 13.99624677(94)\ \text{Hz/nT},$$

we obtain for proportionality factor f_K/H

$$f_K/H = 7.00466137(58)\ \text{Hz/nT}. \quad (2)$$

Formally, the absolute accuracy of the tandem is limited by an error involved in scaling factor f_K/H (2). However, in terms of reproducibility of device readings, the absolute accuracy of the tandem can go beyond these limits. Equation (1) relates the output frequency of the magnetometer to the magnetic field intensity through the atomic and fundamental constants and, therefore, imposes no limitations on the reproducibility. The limitations occur when the parametric dependence of the four-quantum resonance frequency on the following factors is taken into account: the spectral composition and intensity of the pump light, the amplitude of the resonance-inducing alternating magnetic field, the density of potassium vapors, and the static magnetic field intensity. Magnetization of magnetometer parts and an imperfect procedure for determining the resonance peak position can also contribute to systematic errors.

In four-quantum resonance OPMs, the systematic errors are expected to be lower than in conventional single-quantum resonance instruments because of a smaller resonance width and higher resolution. The resolution may, however, be increased at the expense of reproducibility due to reduced pump light intensity. It is well known that pumping causes optical shifts of the resonance frequency. These are of two types [9]. One occurs when RF coherence is transferred from the atomic ground state to the excited state [10]. An optical shift of this type is not observed in the case of four-quantum resonance, since the coherence cannot be transferred to the excited state at single-quantum optical excitation. The second component of the optical shift is the Stark shift [11]. It is typical of four-quantum resonance but can be linearly decreased by reducing the pump light intensity or even completely eliminated by selecting the appropriate spectrum of pump light.

Experimental study of the long-term stability of the magnetometer is extremely difficult because of the lack

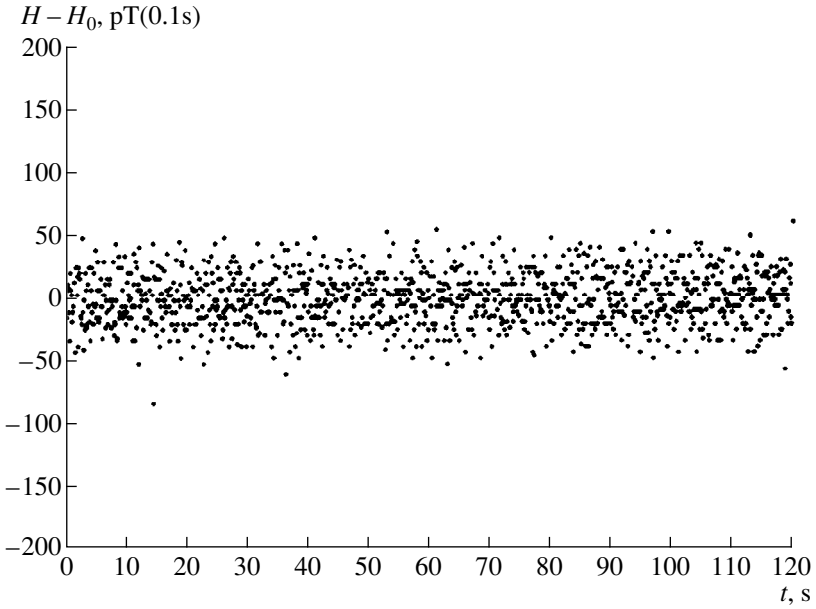

Fig. 3. Cs–K tandem resolution. H_0 = 49574.500 nT, σ (0.1 s) = 18 pT.

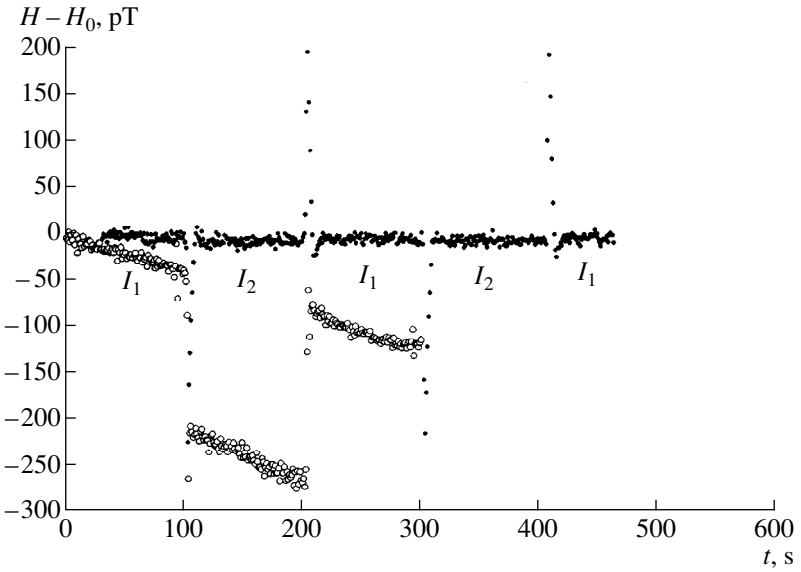

Fig. 4. Effect of variations in the cesium lamp intensity on the readings of the Cs–K tandem (filled circles) and cesium magnetometer (open circles). H_0 = 49574.470 nT, I_1 = 3.0 μA, and I_2 = 1.5 μA.

of standards of the desired accuracy. Also, it is hard to produce a sufficiently stable magnetic field. To tackle the problem, we placed the magnetometer into the stabilized magnetic field and measured changes in its readings induced by variations in pump light intensity, RF-field strength, operating cell temperature, and phase modulation parameters. These variations can be made sufficiently fast, so that the drift of the magnetic field intensity can be neglected.

The magnetometer resolution is basically limited by the performance of the cesium spin generator. In the experiments, however, the magnetometer sensitivity was limited by a number of other factors, including the magnetic field stability. Hence, the obtained value is merely the lower limit of sensitivity. Figure 3, characterizing the device resolution, shows the scatter in the device readings at a rate of 10 counts per second in a stabilized magnetic field of about 0.5 Oe. The dispersion of counts is 18 pT. Averaging over one second decreases the dispersion almost tenfold. This means that the shot noise of the photocurrent does not limit the device sensitivity (i.e., theoretically, the sensitivity can be increased).

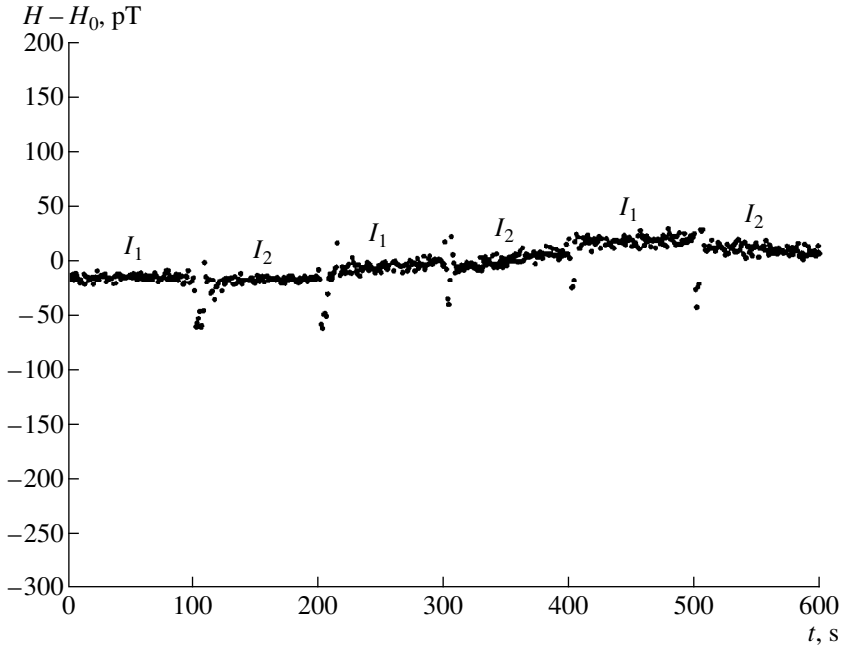

Fig. 5. Effect of variations in the potassium lamp intensity on the readings of the Cs–K tandem. H_0 = 49574.470 nT, I_1 = 7.6 μA, and I_2 = 4.6 μA.

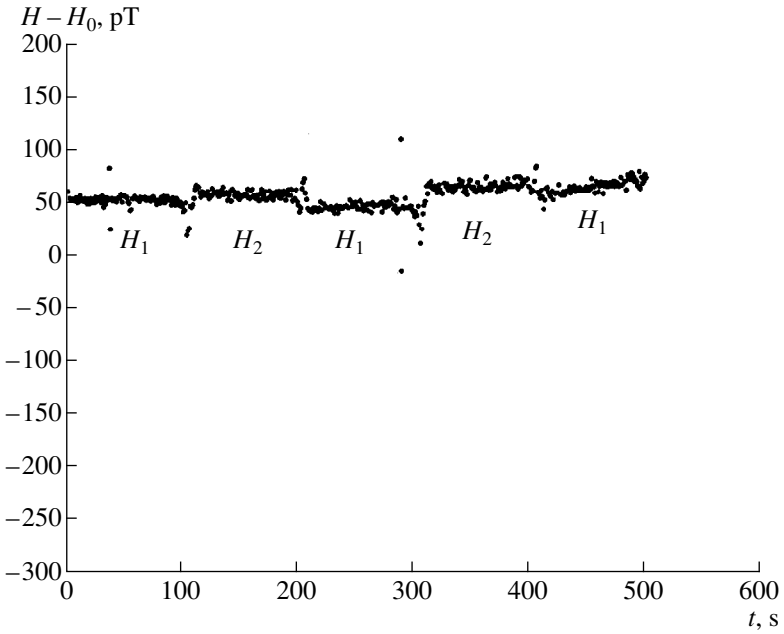

Fig. 6. Dependence of the Cs–K tandem readings on the amplitude of the RF field inducing resonance in potassium atoms. H_0 = 49574.470 nT and $H_2 = 2H_1$.

The effect of variations in the cesium lamp intensity on OPM readings is shown in Fig. 4 (filled circles indicate the tandem readings; open circles, readings of the cesium magnetometer decoupled from the potassium magnetometer). The intensity of the cesium lamp was subjected to stepwise twofold variations (alternate twofold increase and decrease). For the tandem, no effect on its readings was expected. It can be seen that they remain unchanged within a random error of about 10 pT (abrupt changing in the light intensity causes transient overshoots). On the contrary, the readings of the cesium spin generator alone drift with time and change abruptly by approximately 0.2 nT in response to the changes in the intensity of the cesium lamp.

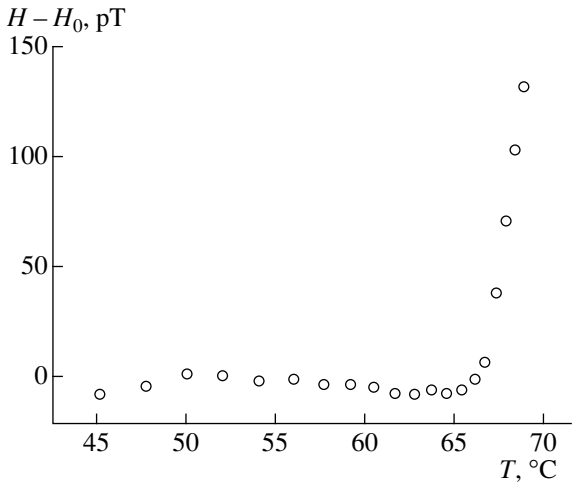

Fig. 7. Dependence of the Cs–K tandem readings on the absorption cell temperature. H_0 = 49573.870 nT.

The variations in the potassium lamp intensity were expected to bring about small changes in the tandem readings. The experimental curve is shown in Fig. 5. It is hard to perceive any systematic variation in the tandem readings (within the limits of 10 pT) against the background of noise and drift, which is caused, in all probability, by the imperfect magnetic field stabilizer.

A more pronounced effect on the tandem readings is exerted by variations in the RF field inducing four-quantum resonance in potassium atoms (Fig. 6). It can be seen that a 1.5-fold increase in the RF-field amplitude makes the device readings larger by 10–20 pT. As expected, the RF-field variations had no effect on the device readings in the case of cesium resonance.

Generally, OPM readings strongly depend on the absorption cell temperature. The temperature dependence of the tandem readings is shown in Fig. 7. The device readings remain constant within 10 pT within an uncommonly wide temperature range of 45–65°C. At higher temperatures, potassium resonance is not observed.

High absolute accuracy of the new magnetometer is especially difficult to verify by experiment. To do this requires a sufficiently stable and uniform magnetic field and a high-precision reference instrument. In our experiments, a certified alkali–helium magnetometer [12] was used for this purpose. Within the magnetic induction range 30–60 μT, the discrepancy between the readings of the tandem and alkali-helium magnetometer did not exceed 0.5 nT.

CONCLUSION

Testing of the Cs–K tandem supported its high metrological performance. It was found that, within the limits of about 10 pT, the device readings were virtually independent of the pump light intensity, RF-field strength, and absorption cell temperature, even if changes in these parameters went far beyond the normal service variability. The most pronounced effect on the tandem readings was found to be exerted by the variations in the RF field inducing four-quantum resonance in potassium atoms. In this connection, it is recommended to use the instrument as a stationary measuring device. In this case, the (normal) projection of the alternating magnetic field H_1 on the direction of the magnetic field H_0 to be measured is relatively easy to maintain at a constant level.

REFERENCES

1. E. B. Aleksandrov, Opt.-Mekh. Prom–st. **55** (12), 27 (1988).
2. E. B. Alexandrov and V. A. Bonch-Bruevich, Opt. Eng. **31**, 711 (1992).
3. E. B. Aleksandrov, V. A. Bonch-Bruevich, and N. N. Yakobson, Opt. Zh., No. 11, 17 (1993).
4. A. H. Allen and P. L. Bender, J. Geomagn. Geoelectr. **24** (1), 105 (1972).
5. E. Pulz, H.-J. Linthe, and A. Best, in *Proceedings of the VI Workshop on Geomagnetic Observatory Instruments, Data Acquisition, and Processing, Dourbes, Belgium, 1994*, pp. 7–13.
6. E. B. Aleksandrov and A. S. Pazgalev, Opt. Spektrosk. **80**, 534 (1996) [Opt. Spectrosc. **80**, 473 (1996)].
7. E. B. Alexandrov, A. S. Pazgalev, and J. L. Rasson, Opt. Spektrosk. **82**, 14 (1997) [Opt. Spectrosc. **82**, 10 (1997)].
8. A. Beckmann, K. D. Boeklen, and D. Elke, Z. Phys. **270**, 173 (1974).
9. C. Cohen-Tannoudji and A. Kastler, Prog. Opt. **5**, 3 (1966).
10. B. S. Mathur, H. Tang, and W. Happer, Phys. Rev. **171**, 11 (1968).
11. B. R. Bulos, A. Marshall, and W. Happer, Phys. Rev. A **4**, 51 (1971).
12. E. V. Blinov, R. A. Zhitnikov, and P. P. Kuleshov, Zh. Tekh. Fiz. **49**, 588 (1979) [Sov. Phys.–Tech. Phys. **24**, 336 (1979)].

Translated by K. Chamorovskiĭ

Technical Physics, Vol. 45, No. 7, 2000, pp. 937–938. Translated from Zhurnal Tekhnicheskoĭ Fiziki, Vol. 70, No. 7, 2000, pp. 125–126.

BRIEF COMMUNICATIONS

The Threshold Current of a Balanced Double-Contact Low-Inductance Interferometer

I. N. Askerzade

Institute of Physics, Academy of Sciences of Azerbaijan, pr. Dzhavida 33, Baku, 370143 Azerbaijan

E-mail: solcdphs@lan.ab.az

Received May 13, 1999

Abstract—The dependence of the threshold current of a double-contact low-inductance interferometer on the capacitance of a Josephson contact and geometric inductance was found. © *2000 MAIK "Nauka/Interperiodica".*

The miniaturization of electrodes and striplines in superconducting electron devices is known to increase the circuit impedance. Therefore, the design of low-current switches is of great importance. Interference devices, which offer higher sensitivity to a magnetic field than isolated Josephson contacts, seem to be the most appropriate in this respect. Also, interference devices made by advanced submicron technology allow for a considerable decrease in the contact capacitance [1].

A double-contact interferometer is the simplest device whose critical current depends on an applied magnetic field [2]. Memory cells on isolated contacts with the use of double-contact interferometers were and remain to be the best candidates for superconducting computers. Double-contact interferometers are also the basis for high-speed parallel analog-to-digital converters. A variety of nonlinear properties inherent in double-contact interferometers makes possible the creation of other pulse [3] and digital [4] devices. In [3], for example, a double-contact interferometer was used as a short strobe driver.

In double-contact interferometers, switching between various states strongly depends on the external (supply) current I_e, the capacitance parameter β of a Josephson contact, and the geometric inductance l. Here, $\beta = 2\pi I_c R_N^2 C/\Phi_0$ (C is the capacitance; R_N is the resistance in the normal state; and Φ_0 is a magnetic flux quantum, $\Phi_0 = \hbar/2e$), and $l = 2\pi L I_c/\Phi_0$. As was noted [2], there always exists the threshold current I_Q of the interferometer (which depends on l, β, and critical current ratio I_{c_1}/I_{c_2}) such that, at $I_e > I_Q$, the system is switched into the resistive (R) state. At $I_e < I_Q$, the system passes to the superconducting (S) state.

In spite of the considerable progress into fabricating Josephson-contact circuits with double-contact interferometers, a dependence of the threshold current I_Q on l and β still remains unclear. In our opinion, this problem is also closely related to the problem of nondestructive data readout [5] and the need for using external clocked power supplies in pulse-actuated circuits [6, 7]. With this in mind, we evaluated the threshold current in a balanced double-contact interferometer in the low-inductance approximation.

It is known that, in the low-conductance limit, a balanced double-contact interferometer behaves as a single Josephson contact with a critical current

$$I_M = 2I_c \cos\frac{\varphi_1 - \varphi_2}{2}$$

and an effective phase $\varphi = (\varphi_1 + \varphi_2)/2$. For closedness, the equation for total magnetic flux,

$$\varphi_1 - \varphi_2 = \varphi_e - l\sin\frac{\varphi_e}{2}\cos\varphi, \qquad (1)$$

where $\varphi_e = 2\pi\Phi_e/\Phi_0$, must be added.

At low l's ($l \ll 1$) and in view of (1), the supply current (in terms of contact critical current) within the resistive model is given by

$$i_e = \frac{I_e}{I_c} = 2\cos\frac{\varphi_e}{2}\sin\varphi + \frac{l}{2}\sin^2\frac{\varphi_e}{2}\sin 2\varphi. \qquad (2)$$

In deriving an analytic dependence of the threshold current on l and β, we ignore a similar dependence for the supply current, since it is negligible in comparison with the desired one. We will also ignore decay in the contacts, assuming β^{-1} to be a small parameter. With these assumptions met, the transition free energy is expressed as

$$E = E_c = \left\{\frac{\beta\dot{\varphi}^2}{2} + 2\cos\frac{\varphi_e}{2}(1-\cos\varphi) + \frac{l}{4}\sin^2\frac{\varphi_e}{2}(1-\cos 2\varphi)\right\}, \qquad (3)$$

where $E_c = \Phi_0 I_c/2\pi$.

1063-7842/00/4507-0937$20.00

Resistive losses in energy per cycle (2π) are calculated by the formula

$$W_i = E_c \int_0^{2\pi} \dot{\varphi}(\varphi) d\varphi. \quad (4)$$

The expression for $\dot{\varphi}(\varphi)$ is found from (3):

$$\dot{\varphi} = \left(\frac{2}{\beta}\right)^{1/2} \left\{ e - 2\cos\frac{\varphi_e}{2}(1-\cos\varphi) - \frac{l}{4}\sin^2\frac{\varphi_e}{2}(1-\cos 2\varphi) \right\}^{1/2}, \quad (5)$$

where $e = E/E_c$.

The infinite phase variation is possible only if $e \geq 4\cos(\varphi_e/2)$. At a fixed current, the energy delivered from the power source is found as

$$W_e = E_c \int_0^{2\pi} i_e d\varphi = 2\pi E_c i_e. \quad (6)$$

The mean voltage ($\bar{\dot{\varphi}} = \vartheta$) is determined by equating energies (4) and (6). The supply current at which Josephson oscillation ceases is found from the limit of (5) at $e = 4\cos(\varphi_e/2)$:

$$i_e = \frac{1}{2\pi} \int_0^{2\pi} \dot{\varphi} d\varphi. \quad (7)$$

In this case, integral (4) is calculated by expanding (5) in the small parameter l; eventually, we obtain

$$\frac{I_Q}{2I_c} = \frac{4}{\pi\sqrt{\beta}} \left|\cos(\varphi_e/2)\right|^{1/2} \left\{ 1 - \frac{l\sin^2(\varphi_e/2)}{6\cos(\varphi_e/2)} \right\}. \quad (8)$$

It follows from (8) that the value of $I_Q/2I_c$ decreases at $l = 0$ and $\varphi_e = 0$, as in the case of the recovery current for a single contact [2]. Along with the critical current, the threshold current of a balanced double-contact interferometer turns out to be modulated by an external magnetic field. With the inductance l fixed, the threshold current vanishes at some flux Φ_e. This means that, for $I_e \neq 0$ and large β's, the system will always change over to the R state.

REFERENCES

1. K. K. Likharev, A. B. Zorin, and V. K. Semenov, *New Horizons for Superconductor Electronics* (Moscow, 1988), Vol. 1.
2. K. K. Likharev, *Introduction to the Dynamics of Josephson Contacts* (Nauka, Moscow, 1985).
3. P. Wolf, B. J. van Zeghbroeck, and U. Deutsch, IEEE Trans. Magn. **21**, 226 (1985).
4. C. A. Hamilton and F. L. Lloyd, IEEE Trans. Magn. **19**, 1259 (1983).
5. R. E. Harris, C. A. Hamilton, and F. L. Lloyd, Appl. Phys. Lett. **35**, 720 (1979).
6. S. R. Whiteley, G. K. G. Hohenwarter, and S. M. Faris, IEEE Trans. Magn. **23**, 899 (1987).
7. I. N. Askerzade, Zh. Tekh. Fiz. **70** (1), 68 (2000) [Tech. Phys. **45**, 66 (2000)].

Translated by V. Isaakyan

Technical Physics, Vol. 45, No. 7, 2000, pp. 939–941. Translated from Zhurnal Tekhnicheskoĭ Fiziki, Vol. 70, No. 7, 2000, pp. 127–129.

BRIEF COMMUNICATIONS

Dependence of the Transverse Dynamics of the Plasma Electrons in the Ion Focus Regime on the Ratio of the Radius of a Relativistic Electron Beam to the Radius of the Ion Channel

E. K. Kolesnikov and A. S. Manuĭlov

Smirnov Research Institute of Mathematics and Mechanics, St. Petersburg State University, St. Petersburg, 198904 Russia

Received May 28, 1999

Abstract—A study is made of the effect of the magnetic self-field of a relativistic electron beam propagating in the ion focus regime on the transverse dynamics of plasma electrons. For Gaussian radial profiles of the beam and the ion density in the channel, the maximum deviation of the plasma electrons from the axis of the beam–plasma system is determined as a function of the space-charge neutralization fraction, the ratio of the characteristic beam radius to the channel radius, and the net beam current. © *2000 MAIK "Nauka/Interperiodica".*

Recently, much attention has been devoted to the problem of the propagation of a relativistic electron beam (REB) in the ion focus regime (IFR) [1–8]. The IFR arises when the ion line density N_i in the plasma channel is lower than the line beam density N_b. At the entrance to a preformed plasma channel, the electric self-field of the beam front expels the plasma electrons from the channel, so that the ions remaining in the channel focus and guide the beam, thereby preventing its transverse dispersion.

The main onset condition of the IFR implies a sufficiently low pressure of the background gas–plasma medium. In this case, the electrons that are produced in a preformed plasma channel or a channel created directly by the electron-beam ionization of a gas and are pushed away from the beam path by the transverse component of the collective electric field cause no additional ionization of the background plasma. This situation occurs under the condition

$$\lambda_i \gg R_b, \tag{1}$$

where λ_i is the characteristic scale length on which the avalanche ionization develops and R_b is the characteristic beam radius.

For the space charge of an REB to be neutralized in the IFR, the transverse component of the electric field of the beam front should rapidly expel the background electrons away from the beam path. However, the process of charge neutralization can also be affected by the magnetic self-field of the beam, which may, to a substantial extent, prevent the background electrons from leaving the beam region.

In this paper, assuming that the radial profiles of the beam and the ion density in the channel are Gaussian in shape, we investigate how the parameter $\eta = R_b/R_i$ (where R_b and R_i are the characteristic radii of the beam and ion channel, respectively) influences the transverse collisionless dynamics of the plasma electrons in the process of charge neutralization at the beam front in the IFR. In considering situations with different η values, we also study how the escape of plasma electrons away from the beam region is affected by the magnetic self-field of the beam with a current in the range I_b = 5–50 kA. Note that the case $\eta = 1$ was examined by Briggs and Yu [4] for a Bennet beam and a Bennet profile of the ion density in the channel.

We consider a paraxial monoenergetic REB guided with a preformed plasma channel in the IFR. We direct the z-axis of the cylindrical coordinate system (r, θ, z) along the channel axis and assume that the electron and ion densities in the channel obey Gaussian distributions,

$$n_{b,i} = \frac{N_{b,i}}{\pi R_{b,i}} \exp\left(-\frac{r^2}{R_{b,i}^2}\right), \tag{2}$$

where the subscripts b and i stand for the parameters of the beam and ion channel, respectively, and N_b and N_i are the line densities of the beam electrons and the ions in the channel.

We also assume that the z-component of the collective electric field, E_z, is small, the net beam current I_b is time independent, and the electron motion in the channel is collisionless. Under all the above assumptions, the energy equation yields

$$\frac{d\gamma}{dt} = \left(\frac{eV_r}{\beta mc^3}\right)\frac{2I_b}{r}\left[\left(1 - \exp\left(-\frac{r^2}{R_b^2}\right)\right) - f_c\left(1 - \exp\left(-\frac{r^2}{R_i^2}\right)\right)\right], \tag{3}$$

1063-7842/00/4507-0939$20.00

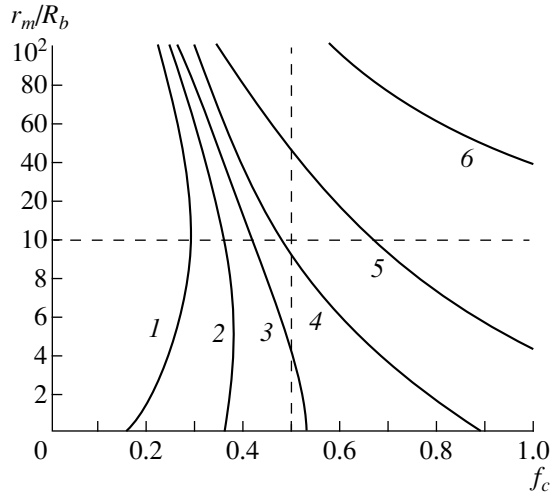

Fig. 1. Dependence of r_m/R_b on f_c for $\eta = R_b/R_i$ = (*1*) 5, (*2*) 2, (*3*) 1.5, (*4*) 1, (*5*) 0.5, and (*6*) 0.1.

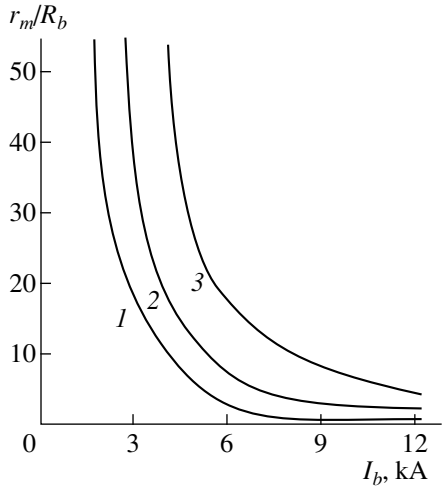

Fig. 2. Dependence of r_m/R_b on I_b for η = (*1*) 1.5, (*2*) 1, and (*3*) 0.5.

where m and e are the mass and charge of an electron, $\beta = v_z/c$, v_r and v_z are the radial component and the z-component of the beam electron velocity, I_b is the net beam current, c is the speed of light, $f_c = N_i/N_b$ is the effective space-charge neutralization fraction, γ is the Lorentz factor, and t is the time.

Note that the right-hand side of (3) incorporates the contribution of the radial component E_r of the electric field of both the beam electrons and the ions in the channel.

Assuming that the plasma electrons are initially immobile, from (3) we obtain

$$\gamma - 1 = \frac{I_b}{I_A^*}[\Re(r, r_0, R_b) - f_c\Re(r, r_0, R_i)], \qquad (4)$$

where $I_A^* = 17\beta$ [kA] is the Alfvén current for $\gamma = 1$ and $r_0 = r$ at $t = 0$, $E_1(z) = \int_z^\infty d\mu \exp(-\mu)/\mu$ is the integral exponential function, and

$$\Re(r, r_0, \xi) = \ln\left(\frac{r}{r_0}\right)^2 - E_1\left(\frac{r_0^2}{\xi^2}\right) + E_1\left(\frac{r^2}{\xi^2}\right). \qquad (5)$$

On the other hand, taking into account the paraxial character of the beam, we turn to formula (2) and the z-component of the equation of motion of a plasma electron to obtain

$$\frac{\gamma v_z}{c} = \frac{I_b}{I_A^*}\Re(r, r_0, R_b). \qquad (6)$$

Note that the right-hand side of (6) incorporates the contribution of the θ-component of the magnetic self-field of the beam. With allowance for the relationship

$$\left(\gamma\frac{v_r}{c}\right)^2 = \gamma^2 - \left(\gamma\frac{v_z}{c}\right)^2 - 1, \qquad (7)$$

from (5) we find

$$\left(\gamma\frac{v_r}{c}\right)^2 = 2\tilde{I}_b\Big[\Re(R_b) - f_c\Re(R_i) - f_c\tilde{I}_b\Re(R_b)\Re(R_i) + \frac{f_c^2}{2}\tilde{I}_b\Re^2(R_i)\Big], \qquad (8)$$

where $\tilde{I}_b = I_b/I_A^*$ and the notation $\Re(\xi) = \Re(r, r_0, \xi)$ is introduced for brevity.

The maximum deviation of a plasma electron from the axis of the beam–plasma system is defined as the distance r_m between the electron stopping point ($v_r = 0$) and the axis and can be found from the equation

$$\Re(R_b) = \frac{f_c\Re(R_i)[2 - f_c\Re(R_i)\tilde{I}_b]}{2(1 - f_c\Re(R_i)\tilde{I}_b)}. \qquad (9)$$

Figure 1 shows the dependence of r_m/R_b on f_c for different values of $\eta = R_b/R_i$ at $I_b = 5$ kA and $r_0/R_b = 0.1$. Note that a curve analogous to curve *4* was obtained by Briggs and Yu [4] for Bennet profiles n_b and n_i of the beam and the ion density in the channel. Figure 2 shows the dependence of r_m/R_b on I_b for $\eta = 0.5$, 1, and 1.5 at $f_c = 0.5$. From Fig. 1, we can see that the divergence of the ion channel ($\eta < 1$) has a significant impact on the escape of plasma electrons from the beam region. In particular, for $\eta = 0.1$, the maximum deviation of the plasma electrons from the system axis in the neutralization phase (up to $f_c \simeq 0.6$) is $r_m/R_b > 10^2$. For larger values of the parameter η ($\eta > 1$), in the range $f_c > 0.2$, the maximum deviation r_m is much smaller. A comparison

of curves *1–3* with curve *4* ($\eta = 1$) confirms the qualitative conclusion that the beams with larger radii more efficiently prevent the escape of plasma electrons in the radial direction. That is why, for the same value of f_c, curves *1–3* lie below curve *4*. It is seen from Fig. 2 that the magnetic self-field of the beam, B_θ, which is proportional to the net beam current I_b, may, to a substantial extent, prevent the background electrons from leaving the beam region.

REFERENCES

1. H. L. Buchanan, Phys. Fluids **30**, 221 (1987).
2. R. F. Fernsler, R. F. Hubbard, and S. P. Slinker, Phys. Fluids B **4**, 4153 (1992).
3. J. Krall, K. Nguyen, and G. Joyce, Phys. Fluids B **1**, 2099 (1989).
4. R. J. Briggs and S. S. Yu, Rep. No. UCID-19399 (Lawrence Livermore National Laboratory, Livermore, CA, 1982), p. 47.
5. V. B. Vladyko and Yu. V. Rudyak, Fiz. Plazmy **19**, 1444 (1993) [Plasma Phys. Rep. **19**, 760 (1993)].
6. E. K. Kolesnikov and A. S. Manuĭlov, Radiotekh. Élektron. (Moscow) **37**, 694 (1992).
7. E. K. Kolesnikov and A. D. Savkin, Pis'ma Zh. Tekh. Fiz. **20** (1), 54 (1994) [Tech. Phys. Lett. **20**, 26 (1994)].
8. E. K. Kolesnikov and A. G. Zelenskiĭ, Zh. Tekh. Fiz. **65** (5), 188 (1995) [Tech. Phys. **40**, 510 (1995)].

Translated by G.V. Shepekina

Technical Physics, Vol. 45, No. 7, 2000, pp. 942–944. Translated from Zhurnal Tekhnicheskoĭ Fiziki, Vol. 70, No. 7, 2000, pp. 130–132.

BRIEF COMMUNICATIONS

Effect of Multiple Scattering and the External Magnetic Field on the Resistive Sausage Instability of a Relativistic Electron Beam

E. K. Kolesnikov and A. S. Manuĭlov

Smirnov Research Institute of Mathematics and Mechanics, St. Petersburg State University, St. Petersburg, 198904 Russia

Received May 28, 1999

Abstract—The problem is studied of how multiple Coulomb scattering and the external longitudinal magnetic field affect the resistive sausage instability of a relativistic electron beam propagating in a gas–plasma medium with nonzero ohmic conductivity. It is shown that these factors significantly reduce the amplitude of the sausage mode. *© 2000 MAIK "Nauka/Interperiodica".*

In recent years, much attention has been paid to the dynamics of relativistic electron beams (REBs) propagating in gas–plasma media [1–12]. Among the problems associated with the guiding of REBs, of special interest is that of investigating the large-scale resistive instabilities of the beams. Along with the resistive firehose instability (the mode with the azimuthal wave number $m = 1$), an important role is played by the resistive sausage instability (the mode with the azimuthal wave number $m = 0$), which manifests itself as axisymmetric perturbations of the beam radius. Physically, the mechanism for the onset of the resistive sausage instability (RSI) is governed by the phase delay between the eddy currents induced by these perturbations and the oscillating component of the beam current density. The RSI of an REB was studied in a number of papers [3–5, 9, 10], which, however, did not treat the often encountered effects of multiple Coulomb scattering of the beam electrons by the atoms and molecules of the background gas and did not take into account the external longitudinal magnetic field.

In this paper, we use analytic methods to derive the perturbed beam radius as a function of the background gas density and the strength of the external longitudinal magnetic field.

We consider an axisymmetric paraxial REB propagating along the z-axis of the cylindrical coordinate system (r, θ, z) in a scattering gas–plasma medium with a high ohmic conductivity σ such that $4\pi\sigma R_b/c \gg 1$, where R_b is the characteristic beam radius and c is the speed of light. We assume that the beam is completely charge-neutralized and that the magnetic self-field of the beam (or, in other words, the beam current) is neutralized only partially, the degree of neutralization being f_m. We also assume that the beam propagates along a steady-state external uniform magnetic field of strength B_0.

The transverse dynamics of such an REB is described by the following equations for the doubled root-mean-square beam radius R^2 and the root-mean-square beam emittance E^2 [1, 3, 5]

$$\frac{\partial^2 R}{\partial z^2} + \frac{2U}{R} + \frac{k_c^2 R}{4} = \frac{4E^2}{R^3} + \frac{4P_\theta^2}{R^3}, \tag{1}$$

$$\frac{\partial E^2}{\partial z} = -\alpha_{ph}\frac{R^3 U}{E}\frac{\partial^2 R}{\partial z^2} + 2\sigma_1 n_g R^2. \tag{2}$$

Here, $U = \langle k_\beta^2 r^2 \rangle$ is the generalized perveance of the beam (where the angle brackets stand for averaging over the radial profile of the beam current density); k_β^2 is the squared betatron wavenumber of the beam electrons; $k_c^2 = eB_0/\gamma mc^3$ is the cyclotron wavenumber of the beam electrons in a longitudinal magnetic field of strength B_0 (where e and m are the charge and mass of an electron and γ is the Lorentz factor); P_θ is the θ-component of the generalized momentum of the beam electrons in the beam segment under consideration; α_{ph} is the phase-mixing coefficient of the beam electrons [8]; σ_1 is the transport cross section for multiple scattering of the beam electrons by the background gas atoms; and n_g is the density of gas atoms.

Assuming that, in the linear stage of the RSI, the perturbed quantities are small (in particular, $\delta R = R - R_0 \ll 1$, where R_0 is the doubled equilibrium beam radius), from (1) and (2) we find

$$\frac{\partial^2 \delta R}{\partial z^2} + \frac{4U_0}{R_0^2}\delta R + k_c^2 \delta R + \frac{2\delta U}{R_0} = \frac{4\delta E^2}{R_0^3}, \tag{3}$$

$$\frac{\partial \delta E^2}{\partial z} = -\frac{\alpha_{ph} R_0^3 U_0}{4 E_0} \frac{\partial^2 \delta R}{\partial z^2} + 2 R_0 \delta R \sigma_1 n_g, \quad (4)$$

where the zero subscript denotes unperturbed parameter values.

Assuming that, during the RSI, the perturbations of the beam radius are self-similar, we can obtain

$$\delta U = \frac{\delta R}{R_0} 2\Psi (1 - f_m) U_0, \quad (5)$$

where

$$\Psi = \frac{4\pi^2}{I_b^2} \int_0^\infty dr r^3 J_b^2(r), \quad (6)$$

I_b is the net beam current, and $J_b(r)$ is the radial profile of the beam current density.

We will work under the condition

$$\frac{L_{z0}}{L_{z1}} \gg 1, \quad (7)$$

where

$$L_{z0} = \frac{R_0}{\partial R_0 / \partial z}, \quad L_{z1} = \frac{\delta R}{\partial \delta R / \partial z}. \quad (8)$$

Condition (7), which implies that, in the positive direction along the z-axis, the equilibrium root-mean-square beam radius changes much more gradually than the perturbed beam radius δR, allows us to solve equations (3) and (4) over distances of $z \le L_{z0}$ by taking the Laplace transform

$$\Delta F = \int_0^\infty dz \exp(i\Omega z) F(z), \quad (9)$$

where F is a function of z.

In this way, equations (3) and (4) yield

$$\Delta R = \frac{F(\Omega)}{D(\Omega)}. \quad (10)$$

Here,

$$F(\Omega) = \left(1 + \frac{i\alpha_{ph} U_0}{\Omega E_0}\right)\left[\frac{\partial \delta R}{\partial z}(0) - i\Omega \delta R(0)\right], \quad (11)$$

$$D(\Omega) = \Omega_0^2 - \Omega^2 - \frac{i\alpha_{ph} \Omega U_0}{E_0} - \frac{4iS}{\Omega R_0^2}, \quad (12)$$

where $S = 2\sigma_1 n_g$, $U_0 = I_b / I_A$, I_A is the limiting Alfvén current, and

$$\Omega_0^2 = \frac{4U_0}{R_0^2}(1 - f_m + \Psi) + k_c^2 \quad (13)$$

with f_m as the degree of current neutralization and Ψ as the form-factor defined in (6). Taking the inverse Laplace transform and assuming $\partial \delta R / \partial z(0) = 0$, we obtain

$$\delta R(z) = \frac{\delta R(0)}{2\pi i} \int_{-\infty}^{\infty} d\Omega \exp(-i\Omega z) \times \frac{(\Omega + i\alpha_{ph} \mathcal{R})\Omega}{(\Omega\Omega_0^2 - \Omega^3 - i\alpha_{ph} \mathcal{R} \Omega^2 - i\Lambda_{sc})}, \quad (14)$$

where i is the imaginary unit, $\Lambda_{sc} = 4S / R_0^2$, and $\mathcal{R} = U_0 / E_0$.

Clearly, the integral over Ω in (14) can be evaluated by the method of residues. In the particular case with no scattering ($\Lambda_{sc} = 0$), we readily obtain

$$\delta R(z) = \delta R(0) \exp\left(\frac{-\alpha_{ph} \mathcal{R} z}{2}\right) \times \left[\cos(z\Psi_1) + \frac{\alpha_{ph} \mathcal{R}}{2\Psi_1} \sin(z\Psi_1)\right], \quad (15)$$

where Ω_0 is defined by (13) and

$$\Psi_1 = \left(\Omega_0^2 - \frac{\alpha_{ph}^2 \mathcal{R}^2}{4}\right)^{1/2}. \quad (16)$$

Expression (15) is a generalization of the analogous expression derived by Lee [5] to the case $B_0 \neq 0$. From (15), we can easily see that the processes of phase mixing partially suppress the RSI on the spatial scale $L_{ph} \sim 2E_0 / (\alpha_{ph} U_0)$.

With allowance for multiple Coulomb scattering ($\Lambda_{sc} \neq 0$), the poles of the integrand in (14) can only be found by solving the cubic equation

$$\Omega^3 + i\alpha_{ph} \mathcal{R} \Omega^2 - \Omega\Omega_0^2 + i\Lambda_{sc} = 0. \quad (17)$$

Again, applying the method of residues and per-

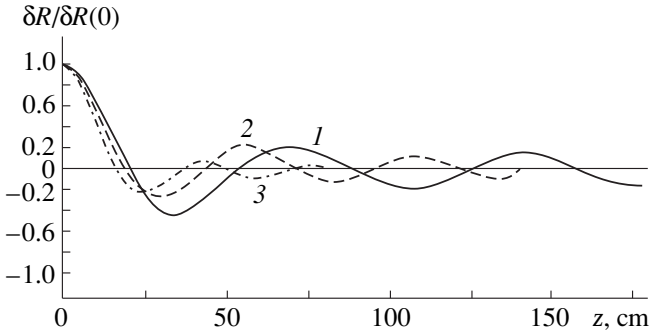

Radial perturbation $\delta R / \delta R(0)$ vs. z for (*1*) case (25), (*2*) case (26), and (*3*) case (27).

forming laborious manipulations, we obtain

$$\delta R(z) = \delta R(0)\exp[-(b/3+T/2)z]\frac{2}{(4A+9T^2)} \times\left\{(2A+2B-3T\Psi_1)\cos(\sqrt{A}z) + \frac{[2A\Psi_1+3T(A+B)]}{\sqrt{A}}\sin(\sqrt{A}z)\right\} + \exp[-(b/3-T)z]\frac{4(T^2+bT/3+2b^2/9)}{(4A+9T^2)}, \quad (18)$$

where

$$T = (M-(P)^{1/2})^{1/3}+(M+(P)^{1/2})^{1/3}, \quad (19)$$

$$M = T_1+\frac{\Lambda_{sc}}{4}, \quad b = \alpha_{ph}\frac{U_0}{E_0}, \quad (20)$$

$$T_1 = \frac{b\Omega_0^2}{6}-\frac{b^3}{2}7+\frac{\Lambda_{sc}}{4}, \quad (21)$$

$$P = \frac{\Omega_0^4}{27}\left(\Omega_0^2-\frac{b^2}{4}\right)+\Lambda_{sc}T_1, \quad (22)$$

$$A = \Omega_0^2-\frac{b^2}{3}+\frac{3}{4}T^2, \quad (23)$$

$$B = \left(\frac{b}{3}+\frac{T}{2}\right)\left(\frac{2b}{3}-\frac{T}{2}\right). \quad (24)$$

In order to illustrate the results obtained, we consider an REB with a Bennet radial current-density profile truncated at $r = R_b$ ($\alpha_{ph} = 0.62$). The figure shows the z-profiles of δR obtained from formula (18) for the cases

$$k_c = 0, \quad \Lambda_{sc} = 0, \quad (25)$$

$$k_c^2 = 3.6\times10^{-3}, \quad \Lambda_{sc} = 0, \quad (26)$$

$$k_c = 0, \quad \Lambda_{sc} = 2.3\times10^{-3}\ \text{cm}^{-3} \quad (27)$$

under the conditions $R_0 = 1$ cm and $U_0 = 2\times10^{-3}$. The value $\Lambda_{sc} = 2.3\times10^{-3}$ cm^{-3} in (27) corresponds to the case in which the scattering gas is nitrogen at atmospheric pressure, the beam particle energy being $E = 5$ MeV. The value of k_c^2 in (26) corresponds to $B_0 = 100$ G at $\gamma = 10$.

From the figure, we can see that the external longitudinal magnetic field and the processes of multiple scattering and phase mixing all act to suppress the radial perturbations of the beam during the RSI. This conclusion agrees with the results of experiments, in which no undamped axisymmetric perturbations of the beam radius were observed.

REFERENCES

1. E. P. Lee, Phys. Fluids **19**, 60 (1976).
2. E. P. Lee, Phys. Fluids **21**, 1327 (1978).
3. E. P. Lee and R. K. Cooper, Part. Accel. **7**, 83 (1976).
4. E. P. Lee and S. S. Yu, Rep. No. UCID-18330 (Lawrence Livermore National Laboratory, Livermore, CA, 1979), p. 23.
5. E. P. Lee, Rep. No. UCID-18940 (Lawrence Livermore National Laboratory, Livermore, CA, 1981), p. 34.
6. R. F. Fernsler, R. F. Hubbard, and M. Lampe, J. Appl. Phys. **75**, 3278 (1994).
7. E. R. Nadezhdin and G. A. Sorokin, Fiz. Plazmy **14**, 619 (1988) [Sov. J. Plasma Phys. **14**, 365 (1988)].
8. W. A. Barletta, E. P. Lee, and S. S. Yu, Nucl. Fusion **21**, 961 (1981).
9. M. Lampe and G. Joyce, Phys. Fluids **26**, 3371 (1983).
10. E. K. Kolesnikov and A. S. Manuĭlov, Pis'ma Zh. Tekh. Fiz. **17** (3), 46 (1991) [Sov. Tech. Phys. Lett. **17**, 96 (1991)].
11. E. K. Kolesnikov and A. S. Manuĭlov, Zh. Tekh. Fiz. **62** (9), 55 (1992) [Sov. Phys. Tech. Phys. **37**, 924 (1992)].
12. E. K. Kolesnikov and A. S. Manuĭlov, Zh. Tekh. Fiz. **67** (7), 108 (1997) [Tech. Phys. **42**, 819 (1997)].

Translated by G.V. Shepekina

Technical Physics, Vol. 45, No. 7, 2000, pp. 945–947. Translated from Zhurnal Tekhnicheskoĭ Fiziki, Vol. 70, No. 7, 2000, pp. 133–135.

BRIEF COMMUNICATIONS

Cooperative Mechanism of Self-Diffusion in Metals

V. G. Chudinov

Physicotechnical Institute, Ural Division, Russian Academy of Sciences, Izhevsk, 426001 Russia;
E-mail: uufti@fti.udmurtia.su

Received June 1, 1999

Abstract—The atomic mechanism of self-diffusion in a face-centered cubic structure (exemplified by aluminum) is simulated by the molecular-dynamics method without resorting to *a priori* information. No confirmation of vacancy-jump mechanisms of diffusion has been obtained. The cooperative mechanism of diffusion suggested previously by Khait and Klinger and based on the assumption of possible local melting near vacancies (within one–two nearest coordination shells) appears to be valid. As a result, the preexponential factor proves to depend on the temperature and heat of melting, and the exponential factor depends on the heat of melting and the current temperature. © *2000 MAIK "Nauka/Interperiodica".*

1. Atomic diffusion in solids is one of the fundamental phenomena which is a base for understanding a lot of effects. But, strange as it may seem, there is no unified point of view on the diffusion mechanisms that were devoid of internal contradictions. The quantities entering into the equations for diffusion parameters become meaningful only when the atomic mechanism of the process is known. As a rule, some conclusions on these quantities can be made by measuring the energies controlling the process. For simple metals far from the melting point, such a parameter is the energy of vacancy self-diffusion, which counts in favor (but by no means proves) of the widely used model of diffusion through vacancy jumps. As other possible mechanisms, the following are usually listed: direct exchange, cyclic exchange (ring mechanism), simple interstitial mechanism, interstitialcy mechanism, crowdion mechanism, etc. [1]. "First-principles" calculations based on these models underestimate the diffusion rates by tens and even hundred of times and have a rather heuristic significance. The inconsistencies appearing in such an "individual" description of diffusion phenomena led Frenkel' [2] to the idea that in a self-consistent diffusion theory, the interacting particles had to be considered as a coherent system, like in the Debye theory of heat capacity.

An attempt to build such a theory was undertaken by Khait [3]. In his opinion, the application of the standard theory of fluctuations has been unsuccessful because of the incorrect consideration of thermal-energy fluctuations as small corrections to the equilibrium distribution function in spite of the correct estimations of macroscopic parameters. The thing is in that although the short-lived fluctuations that involve a limited number of particles give a negligible contribution to the averaged equilibrium parameters, they nevertheless may play an important part in some kinetic processes. In application to diffusion through the vacancy mechanism, this means the following. A diffusion jump may occur when a fluctuation in the atomic distribution appears around a vacancy. After relaxation of the given fluctuation, one of the atoms surrounding the vacancy may occupy the vacancy position.

A similar approach was developed, e.g., by Klinger [4]. In his opinion, the temperature in some region around a vacancy may exceed, due to a fluctuation, the melting (more correctly, quasimelting) temperature of the crystal. Upon the subsequent solidification, the vacancy may occupy another site of the restored crystal lattice. It is very important that Klinger obtained an expression for the diffusion coefficient as a function of the temperature and heat of melting

$$D = \frac{1}{6}\nu d^2 \exp\left(\frac{k\lambda_m - \alpha\sigma_{ls}^0 (V_L n)^{2/3}}{kT_m}\right)\exp\left(-\frac{n\lambda_m}{kT}\right), \quad (1)$$

where ν is the mean frequency of atomic vibrations; d is the length of a diffusion jump; T_m, the melting temperature; λ_m, the heat of melting; n, the number of atoms of the second phase; σ_{ls}^0, the surface tension at the liquid–crystal interface; V_L, the volume per atom in the liquid phase; and k, the Boltzmann constant.

Agreement with experiment for simple metals is obtained when n = 12–20, i.e., at local disordering within 1–2 coordination shells. This agrees with the generalized coordinate relation for the self-diffusion energy $E = 15\lambda_m$ [1].

In this work, we used the molecular-dynamics method (MDM) to qualitatively test the ideas developed in [1–4]. The method consists in a numerical solution of the Newton equations of motion when pairwise interaction potentials (PIP) are known. Its main advantage is the minimum of physical information taken *a priori* [5].

1063-7842/00/4507-0945$20.00

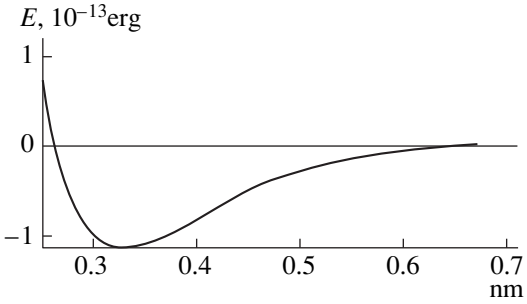

Fig. 1. Pairwise interaction potential for aluminum.

It should be noted that the work requires a lot of computer time, since diffusion processes are very slow on the MDM scale.

2. Several approaches are used in MDM to study diffusion phenomena.

1. Determining diffusion coefficients by calculating mean-square displacements

$$D = \frac{1}{6}\frac{\left\langle \sum_j [x_j(\tau) - x_j(0)]^2 \right\rangle}{\tau}, \qquad (2)$$

where $x_j(\tau)$ is jth coordinate of an atom at the time moment τ and $\langle\rangle$ stands for averaging over all atoms. The method is integral and does not allow one to determine the atomic mechanism of diffusion.

2. Determining the diffusion barrier by "squeezing" a diffusing atom through a fixed lens of atoms in the direction toward a vacancy.

3. The same as in 2, but with atomic relaxation.

4. The same as in 2, but with "shooting" the diffusing atom through the lens.

In the last three methods, the model of diffusion is actually specified. The corresponding energies differ in a ratio of 1 : 0.1 : 0.3, respectively.

We propose a substantially different approach. At a fixed temperature, we construct a crystallite with this or that defect. Then, we let the atoms in the equilibrium state perform free vibrations and jumps and fix their coordinates in the computer memory after certain time periods. After executing an elementary diffusion act, a return to the preceding time moment was made, and the process was repeated with a more detailed analysis of the parameters of atoms surrounding the defect (kinetic and potential energies, velocity vectors of atoms in the structure, etc.). Thus, no model assumptions on the mechanism of the diffusion act is done in the computer experiment, except for specifying the interatomic interaction.

We used a PIP of the Morse type for aluminum cut at 0.7 nm (Fig. 1), which provided stability of the face-centered cubic lattice, and an MDM20 computer code [5]. A crystallite with cyclic boundary conditions was formed having the face-centered cubic (fcc) lattice and containing ~1500 sites (one of which was vacant). At first, all of the atoms were given the same velocity (corresponding to a given temperature) with random directions. After that, no intervention to the system was made. After a period of $\sim 10^{-12}$ s, an equilibrium state with a Maxwell distribution of velocities was reached. The criterion of a jump was an atomic translation to another Wigner–Seitz cell constructed for the ideal lattice. Obviously, some of the jumps were reversible and did not contribute to the diffusion. These jumps were not taken into account. All the atoms were numbered and their positions were traced in time. The average jump time was $\sim 10^{-13}$ s. About 100 jumps occurring according to a common scheme were observed. The melting temperature for a given PIP was ~1100 K. One could hardly expect better agreement when using a model potential. We believe that the main purpose when using the MDM should be the investigation of atomic mechanisms of diffusion (at least qualitatively) rather than fitting numeric results to experimental data.

3. The temperature in the experiment was 900 K. This choice was accounted for by two reasons: (a) at lower temperatures, there were no jumps at all or their numbers for the time periods used (10^{-11} s) were insufficient for reliable statistical analysis; (b) at higher temperatures, double and triple jumps took place along with common single jumps, which led to deviations from the Arrenius law.

By assuming that an elementary act of vacancy diffusion occurs as the overcoming of a potential barrier by one of the surrounding atoms and the subsequent relaxation of this fluctuation of thermal energy, we can expect the existence of some characteristic jump frequency and a uniform distribution of jumps in time. However, they proved to occur as series consisting of 5–10 acts for 10^{-12} s. This agrees with the estimations of the theory of short-lived large-energy fluctuations (SLEF) [3, 4].

Analysis of velocity vectors and kinetic and potential energies of diffusing atoms revealed that there is neither increase in the velocity in the vacancy direction before a jump, nor a pronounced potential barrier to be overcome when moving away from the four-atomic lens.

Figure 2 displays the kinetic and potential energies before and after a single diffusion act for two nearest-neighbor coordination shells around a vacancy. One can see that the kinetic energy increases by a factor of ~4, but the potential energy varies within the range of common fluctuations. The atomic structure around a vacancy is typical of liquid. The vacancy location cannot be identified reliably. The fluctuation disappears for $\sim 10^{-12}$ s, and the vacancy may occupy any site of the crystal lattice after the solidification of the "quasimolten" region. So, a cooperative mechanism of diffusion is realized, in which the number of atom jumps, includ-

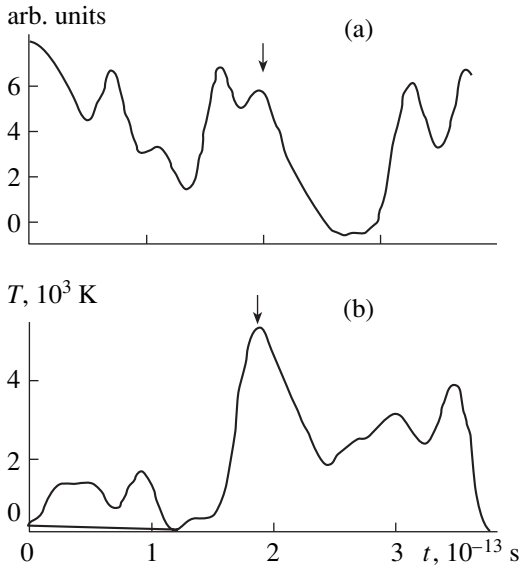

Fig. 2. Dependence of (*a*) the kinetic and (*b*) the potential energies (in temperature units) per atom near a vacancy (1st coordination shell) before and after jump. The conditional moment of the jump occurrence is indicated by an arrow.

ing nonreversible ones, is much more that in the traditional theory.

4. In conclusion, we would like to notice that the whole body of the results obtained suggest that a cooperative mechanism of diffusion is preferable. It can be interpreted as the quasimelting of the nearest surroundings of a vacancy due to rather small kinetic energy fluctuations (with 20–100 atoms being involved in the process). Then, diffusion according to a nonbarrier mechanism, close to the diffusion mechanism in liquid, takes place; i.e., this is an anharmonic process in which the peculiarities of interatomic interaction become a decisive factor [5].

ACKNOWLEDGMENTS

The author would like to thank E.I. Salamatov for fruitful discussion and useful remarks.

REFERENCES

1. B. S. Bokshteĭn, *Diffusion in Metals* [in Russian] (Metallurgiya, Moscow, 1978).
2. Ya. D. Frenkel', *Introduction to the Theory of Metals* (Fizmatgiz, Moscow, 1958).
3. Y. L. Khait, Physica A (Amsterdam) **103**, 1 (1980).
4. M. M. Klinger, Metallofizika (Kiev) **6** (5), 11 (1984).
5. V. M. Dyadin and V. G. Chudinov, Available from VINITI, No. 1537-V 91 (1991).

Translated by M. Astrov

Technical Physics, Vol. 45, No. 7, 2000, pp. 948–949. Translated from Zhurnal Tekhnicheskoĭ Fiziki, Vol. 70, No. 7, 2000, pp. 136–137.

BRIEF COMMUNICATIONS

On the Influence of Ionization Density in a Fast Charged Particle Track on the Light Output of Scintillations

V. K. Lyapidevskiĭ and M. I. Ryazanov

Moscow State Engineering Physics Institute (Technical University), Kashirskoe sh. 31, Moscow, 115409 Russia

Received June 4, 1999; in final form, September 6, 1999

Abstract—It is shown that ionization density due to a fast charged particle influences the light output of a scintillator through the relaxation transition of an electron from an impurity atom to a host-material ion. © *2000 MAIK "Nauka/Interperiodica".*

(1) In organic scintillators, regardless of their nature, the ratio of light outputs due to α particles and electrons (α/β ratio) is known to be about 0.1 [1, 2]. The same has also been observed in inorganic scintillators [3]. The independence of the α/β ratio on the scintillation material and impurity type suggests that this effect is related to general, rather than specific, properties of scintillators. Hence, the explanation of the α/β ratio uniqueness must rely on general scintillation laws and mechanisms. A uniqueness mechanism for the α/β ratio was not considered earlier; however, the effect has been supposed to be associated with molecule–molecule and molecule–ion interactions [4].

(2) When exposed both to electrons and to α particles, organic scintillators in the pure state scintillate weakly and the scintillation intensities are close to each other. This indicates that the α/β ratio depends on the states taken by scintillation impurities under the action of electrons and α particles. The effects fast electrons and heavy α particles have on a material differ in that a heavy particle passing through the substance creates a much higher ionization density than a light electron. It seems therefore natural to look for an explanation of the unique α/β ratio through the effect of ionization density on impurities.

(3) A host atom ionized by a moving particle may appear near an impurity atom. Usually, the ionization potential of the latter is lower than that of the former. In other words, the energy level of a valence impurity electron is above that of a host-atom electron; hence, the capture of a bound impurity electron by a host ion is energetically favorable. Such a capture may occur at any relaxation process in the excited state. A bound impurity electron may also be trapped by a host ion if an impurity atom was excited during scintillation. The ionization of an impurity atom changes the occupancies of excited electron states and shifts their energy levels. Both factors decrease the light output at the fundamental frequency.

(4) Consider now how the ionization density influences the fraction of ionized impurities. An increase in the ionization density raises the average number of ions per unit volume and, thus, shortens the average interionic distance and the distance between host ions and impurity atoms. Eventually, the probability that a bound impurity electron will be trapped by a host ion increases. Consequently, the fraction of ionized impurity grows with the ionization density and the light output drops.

(5) The α/β ratio is the same for different scintillators, because the energetically favorable capture of a bound impurity electron by a host atom may attend any relaxation process. Therefore, for a given ionization density, this capture has only a weak dependence on the energy levels of excited impurity atoms and host-material properties.

(6) It follows from the above that the qualitative features of the light output vs. particle-induced ionization dependence (the existence of the unique α/β ratio and the emission at other frequencies when the ionization density rises) can be accounted for within a single mechanism. According to this mechanism, the capture of a bound impurity electron by a host ion affects the state of scintillation impurities.

(7) It should be noticed that, when an insulator is doped by impurities in which electrons are bound more weakly than in host atoms (in particular, scintillation impurities [5]), the number of displaced atoms in a heavy particle track decreases [6]. Thus, two effects (loss in light output for heavy particles and atomic displacement in heavy particle tracks) result from the

1063-7842/00/4507-0948$20.00

same process: the capture of a loosely bound impurity electron by a host ion.

ACKNOWLEDGMENTS

This work was supported by the Russian Foundation for Basic Research.

REFERENCES

1. I. M. Rozman and S. F. Kilin, Usp. Fiz. Nauk **69**, 469 (1959).
2. M. D. Galanin and Z. A. Chizhikova, Opt. Spektrosk. **48**, 196 (1958).
3. V. V. Averkiev, Ya. A. Valbis, F. Kh. Grigoryan, V. K. Lyapidevskiĭ, *et al.*, *Luminescent Detectors and Transducers of Ionizing Radiation* (Nauka, Novosibirsk, 1985).
4. V. S. Vyazemskiĭ, I. I. Lomonosov, A. N. Pisarevskiĭ, *et al.*, *Scintillation Method in Radiometry* (Atomizdat, Moscow, 1961).
5. V. V. Averkiev, V. K. Lyapidevskiĭ, and N. B. Khokhlov, Izv. Akad. Nauk SSSR, Ser. Fiz. **50**, 568 (1986).
6. V. K. Lyapidevskiĭ and M. I. Ryazanov, Pis'ma Zh. Tekh. Fiz. **23** (16), 51 (1997) [Tech. Phys. Lett. **23**, 638 (1997)].

Translated by V. Isaakyan

Technical Physics, Vol. 45, No. 7, 2000, pp. 950–952. Translated from Zhurnal Tekhnicheskoĭ Fiziki, Vol. 70, No. 7, 2000, pp. 138–140.

BRIEF COMMUNICATIONS

Simulation of an Early Stage of a Conductor's Electrical Explosion

S. I. Tkachenko

Institute of Pulse Research and Engineering, National Academy of Sciences of Ukraine, Nikolaev, 327018 Ukraine

Received August 4, 1999

Abstract—Phase-transformation waves that may arise in a conductor in the course of an electrical explosion are considered. An estimate allowing one to predict the possibility of occurrence of several phase transformations at the front of the single wave is proposed. Mathematical simulation results are presented. © *2000 MAIK "Nauka/Interperiodica".*

The problem of calculating the electrical explosion of the skin layer in a gap for the one-dimensional case in Cartesian coordinates was considered in [1]. This paper is devoted to the simulation of the early stage of the electrical explosion of cylindrical copper conductors. We use a model similar to that employed in [2]; i.e., we solve the one-dimensional set of magnetohydrodynamics equations supplemented with the circuit equation; the electrical conduction in the solid and liquid states is described by a semiempirical equation [3] and in the plasma state, by an equation proposed in [4] for dense plasma. Following [5], we assume that at $\rho/\rho_0 = 0.2$ conduction vanishes completely.

Variation of the distribution of both the local parameters of the conductor (density, temperature, pressure, and electrical conductivity) and the integral ones (current, voltage, resistance, and wire radius) is caused by the propagation of the phase-transformation waves through the conductor [6–8]. Figure 1 displays curves describing the current-density and temperature distributions over the radial coordinate of a copper wire (l = 15 mm and r_0 = 0.1 mm) at various instants at the following circuit parameters: L = 5 nH, C = 25 nF, and U_0 = 40 kV. The curves are shown in two panels of Fig. 1 in order to separate an explosion stage specified by the propagation of only one current wave (Fig. 1a) caused by the redistribution of the current in the conductor due to melting wave propagation through it from another stage in which entire loss of the conduction in the outer layers occurs (Fig. 1b).

In Fig. 1a, numerical-calculation results for instants of 13, 16, and 17 ns are shown. The arrows near the abscissa indicate solid–melt phase transition. It can be seen that their locations correspond to the trailing edge of the current wave. At the instant of 17 ns, another phase transition occurs (it is indicated by the upper arrow) at which the conduction entirely vanishes; at the same time, one more peak in the current-density curve is formed. The descending slope of the peak corresponds to a new phase transition.

Figure 1b displays numerical calculation results corresponding to instants of 17.1, 17.4, 17.7, and 17.8 ns. The bottom arrow indicates the solid–liquid-metal transition. It can be seen that the region of this phase transition is virtually not displaced (during the time interval pointed out in the plots); therefore, the first current wave is stationary.

The upper arrows indicate the transition of the metal into the nonconducting state; in accordance with them, the front of the second current wave is located at the same instants.

It is clear seen that the second current wave, which "takes in" the rest of the current that has remained in the molten conductor layers, moves with a velocity much higher than the first wave (v_2 varies roughly from 7×10^4 to 2×10^5 m/s while $v_1 \sim 5 \times 10^3$ m/s), catches up the latter, joins it, and after that, the joint current wave propagates. Its further propagation gains specific features of skin layer explosion [1] with the only distinction that, in an axially symmetric system, any processes proceed more intensely (in accordance with [1] $v_2 = 10^4$ m/s). This phenomenon features the explosions whose energy characteristics may cause fast heating of the molten layers of a conductor up to the temperature of the next phase transition.

Such a process will be observed if a matter in some phase state (f) is heated up to a temperature at which the next phase transition proceeds so fast that the both phase transitions may occur at a single wave front. In this case, the lifetime of the intermediate phase state is much less than the time necessary for the phase transition wave to travel a distance equal to the phase thickness. The lifetime of any phase state can be evaluated as the time necessary for heating the medium from the

1063-7842/00/4507-0950$20.00

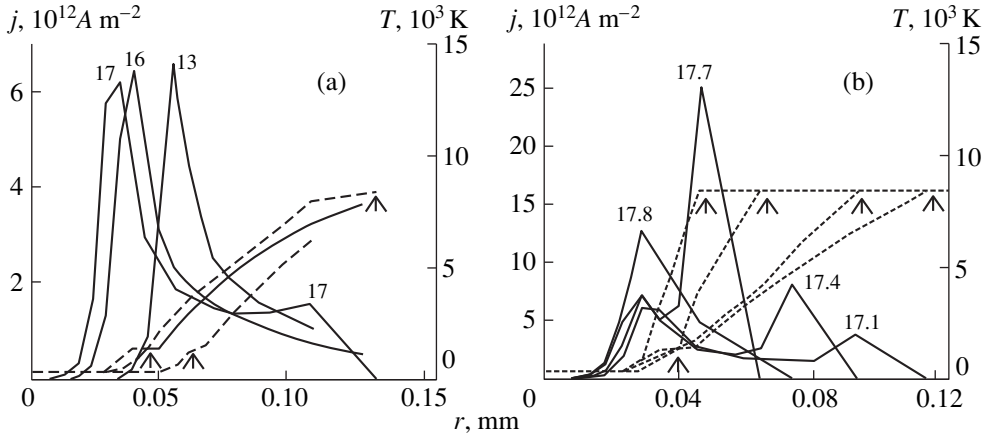

Fig. 1. Distributions of the current density (solid lines) and the temperature (dashed lines) over the radial coordinate at various instants of time (the instants expressed in nanoseconds are denoted by numbers near the curves).

temperature of the preceding phase transition to that of the next phase transition:

$$c_f \Delta T \rho_f \sim j^2 \tau_\lambda / \sigma_f. \quad (1)$$

Here, c_f is the specific heat of the medium at the phase state considered; ρ_f is the density; σ_f is the electrical conductivity; j is the current density; $\Delta T = T_{1f} - T_{2f}$ is the difference between the temperatures of the successive phase transitions; and τ_λ is the phase lifetime which must be less than the time required for the phase-transition wave front to travel through the conductor $\tau_w = r_0/u$ (here u is the velocity of the phase-transition wave front).

If one uses the estimate for the phase-transition front velocity proposed in [8], then, for superfast regimes at $\tau_\lambda \ll \tau_w$, it is possible to write

$$\frac{c_f \Delta T}{\lambda_f} \ll \frac{r_0}{\delta_j}. \quad (2)$$

Here $\delta_j = (0.5\mu\sigma_f\omega)^{-1/2}$ is the skin depth; μ is the magnetic permeability; and $\omega = I^{-1}dI/dt$. According to [9], the existence of the second current wave (in the case of explosion of a copper wire with $r_0 = 0.1$ mm) is possible for $\omega > 10^7$ s^{-1}; it follows from (2) that a regime at which several phase transitions may proceed at the front of a single wave becomes possible at higher rates of the current variation $\omega \gg 10^{10}$ s^{-1}. The regime presented is the limiting one for the second condition since, for the given parameters, $\omega \approx 10^{10}$ s^{-1}. For this particular reason, the liquid metal at first occupies a rather extended region $\sim r_0$ (it can be seen from the temperature curves, for example, at the moment of the second current wave formation) and then it practically disappears when the waves merge into a single one at $t \approx$ 17.8 ns.

Further on, the melting wave first moves toward the center and, only after it reaches the symmetry axis at the instant of 21 ns, does the next phase transition wave start to move towards the center, causing the conduction to vanish (in accordance with [9], the phase transition wave may move only under a certain condition). When this takes place, the current wave moves together with the melting wave crest.

If the stored energy is not sufficient for the regime described to be achieved (for example, for the same parameters and $C = 20$ nF), then only a single current wave is formed and travels similarly to the process shown in Fig. 1a. In this regime, some conduction remains in the expanded outer layers, which results in nonzero current density there. It is only after the melting wave reaches the central layers that a new phase wave is formed in the outer layers which causes the metal conduction to vanish; when this takes place, only a single current-wave crest, which accompanies the wave of the first solid–melt phase transition, is clearly seen.

CONCLUSIONS

The simulation results demonstrate that regimes of the ultrafast (nanosecond) electrical explosion of a conductor differ from ones of the fast (microsecond) [2] explosion (from the standpoint of the phase transition dynamics) in the relation between the running time of the wave of the material phase transition moving from the outer boundary to the center and the lifetime of the phase state considered. In ultrafast regimes, the lifetime of intermediate phases may be much less than the time of the phase boundary displacement from the conductor periphery to its center; therefore, it becomes possible to realize such regimes in which a phase wave catches up to the front of the preceding phase transition and, further on, several phase transitions occur at a single wave front. Exactly in this case ($\omega \gg 10^{10}$ s^{-1}), one can conventionally assume that the conductor material transforms from the condensed state immediately into the

dense plasma. Probably, the products of such an explosion have a more uniform size.

REFERENCES

1. G. A. Shneerson, Zh. Tekh. Fiz. **43**, 419 (1973) [Sov. Phys. Tech. Phys. **18**, 268 (1973)].
2. N. T. Kuskova, S. I. Tkachenko, and S. V. Koval, J. Phys. **9**, 6175 (1997).
3. H. Knoepfel, *Pulsed High Magnetic Fields* (North-Holland, Amsterdam, 1970; Mir, Moscow, 1972).
4. A. Ya. Polishchuk, Doctoral Dissertation (Institute of High Temperatures Scientific Association, Russian Academy of Sciences, Moscow, 1991).
5. S. N. Kolgatin, A. Ya. Polishchuk, and G. A. Shneerson, Teplofiz. Vys. Temp. **31**, 890 (1993).
6. F. D. Bennet, Phys. Fluids **8**, 1425 (1965).
7. V. A. Burtsev, N. V. Kalinin, and A. V. Luchinskiĭ, *Electrical Explosion of Conductors and Its Application in Electrophysical Equipment* (Énergoatomizdat, Moscow, 1990).
8. N. I. Kuskova, Pis'ma Zh. Tekh. Fiz. **24** (14), 41 (1998) [Tech. Phys. Lett. **24**, 559 (1998)].
9. S. I. Tkachenko and N. I. Kuskova, J. Phys. **11**, 2223 (1999).

Translated by N.P. Mende

Technical Physics, Vol. 45, No. 7, 2000, pp. 953–954. Translated from Zhurnal Tekhnicheskoĭ Fiziki, Vol. 70, No. 7, 2000, pp. 141–142.

BRIEF COMMUNICATIONS

High-Frequency Boundary for the Rayleigh–Jeans Approximation in Microwave Radiometry Problems

I. A. Semin

Ryazan State Pedagogical University, Ryazan, 390000 Russia

Received March 17, 1999; in final form, December 24, 1999

Abstract—The Kirchhoff waveguide theorem provides an adequate description of an electrodynamic system of a high-sensitivity microwave radiometer with wideband detector. A transition from the general analytical representation of this theorem to a particular case is analyzed. This transition is equivalent to a transition from the Planck distribution to the Rayleigh–Jeans approximation. A simple relationship is derived that determines, for a preset accuracy, the high-frequency boundary for the above transition as a function of the temperature. © *2000 MAIK "Nauka/Interperiodica".*

The development of nonlinear superconducting elements led, on the one hand, to the creation of novel devices with unique parameters [1] and, on the other hand, to the formulation of new radiophysical problems. This is true, in particular, for the so-called Josephson's edge junctions representing one type of the nonlinear superconducting elements [2].

A theoretical basis for experimental investigations [2–4] of the detector properties of the edge junctions was provided by [5, 6]. In particular, Zavaleev and Likharev [6] calculated the detector characteristics of a junction included into a wideband electrodynamic system modeled by a long line. However, unsatisfactory agreement of the calculated characteristics with experimental results allows us to decline the above model in favor of the Kirchhoff waveguide theorem [7].

One term in the analytical expression of the Kirchhoff theorem represents the average energy of a quantum oscillator described, to within the zero-oscillation energy, by the formula

$$\langle \varepsilon \rangle_P = h\nu(\exp(h\nu/kT) - 1)^{-1}, \quad (1)$$

where h is the Planck constant, k is the Boltzmann constant, and T is absolute temperature.

Equation (1) allows significant simplification in the extremal cases when $h\nu \ll kT$ and $h\nu \gg kT$. From the standpoint of the Kirchhoff waveguide theorem application, only the first case is of interest. Thus, the Kirchhoff theorem can be expressed in two forms: the general, corresponding to rigorous equation (1), and an asymptotic, following from equation (1) in the limit of $h\nu \ll kT$.

It should be noted that a transition from the general formulation of the Kirchhoff theorem to the asymptotic case is equivalent to the transition from the Planck distribution to that described by the Rayleigh–Jeans law (referred to below as the Rayleigh–Jeans approximation). The Rayleigh–Jeans approximation usually provides considerable simplification of the computation, which makes this approach preferred to that based on the Planck distribution. However, this simplicity can sometimes be reached at the expense of lower precision. In particular, Karlov and Chikhachev [8] were among the first researchers pointing out that the Rayleigh–Jeans approximation is inapplicable to the description of the radiation sources operating at ~4.2 K even in the millimeter wavelength range.

The purpose of our work was to elaborate a criterion for determining, for a preset accuracy, a high-frequency boundary for the correct transition from the Planck distribution to the Rayleigh–Jeans approximation.

In this context, let us consider equation (1) for the average energy of a quantum oscillator. In the limit $h\nu \ll kT$, this expression coincides, to within a factor describing the number of oscillators insignificant for the following analysis, with that provided by the Rayleigh–Jeans approximation:

$$\langle \varepsilon \rangle_{RJ} = kT. \quad (2)$$

In order to obtain the desired criterion, let us compare expressions (1) and (2). Note that all $\nu > 0$ and $T > 0$ obey the inequality

$$kT > h\nu(\exp(h\nu/kT) - 1)^{-1}, \quad (3)$$

which can be readily checked by expanding the exponent into a Maclaurin series. On introducing the notation

$$x = h\nu/kT, \quad (4)$$

we may rewrite inequality (3) in the following form:

$$x^{-1} > (\exp x - 1)^{-1}. \quad (5)$$

1063-7842/00/4507-0953$20.00

Table

β	ν_β, GHz		
	T = 10 K	T = 80 K	T = 300 K
0.001	0.4212	3.370	12.64
0.005	2.087	16.70	62.66
0.010	4.181	33.45	125.4
0.050	21.20	169.6	635.9
0.100	43.16	345.3	1294

Introducing a coefficient β such that $0 \le \beta < 1$, this expression can be transformed to an equation relative to x:

$$(1-\beta)(\exp x - 1) = x. \quad (6)$$

The coefficient β possesses the following properties. First, this quantity represents a methodological uncertainty caused by using the Rayleigh–Jeans approximation instead of the Planck distribution. Indeed, using equations (1), (2), (4), and (6), we may express β as

$$\beta = (\langle\varepsilon\rangle_{RJ} - \langle\varepsilon\rangle_P)/\langle\varepsilon\rangle_{RJ} = \Delta\langle\varepsilon\rangle_{RJ}/\langle\varepsilon\rangle_{RJ}. \quad (7)$$

Second, any permissible β value at a given fixed temperature divides the frequency interval into two parts, one of which is conveniently interpreted as the region of applicability of the Rayleigh–Jeans approximation. Indeed, relationship (6) can be used to define β as function of x:

$$\beta = 1 - x/(\exp x - 1). \quad (8)$$

A physical domain for the expression (8) is the interval $(0, \infty)$, in which the function $\beta(x)$ is a monotonically increasing function of x with the range (0, 1). Therefore, an arbitrary ordinate in the plot of $\beta(x)$ determines a level uniquely corresponding to certain x. Since the x and ν values obey a linear relationship (4) at a fixed temperature T, any β level uniquely defines a certain frequency ν_β.

Thus, on the one hand, the β value defined above represents a level determining the certain boundary frequency ν_β. On the other hand, by virtue of the properties of the $\beta(x)$ function, this quantity is a measure of the maximum uncertainty appearing in the frequency interval $(0, \nu_\beta)$ when the Rayleigh–Jeans approximation is used instead of the Planck distribution. In this context, the β value is expediently termed the error level of the transition from the Planck distribution to the Rayleigh–Jeans approximation and the ν_β frequency, the high-frequency boundary for the Rayleigh–Jeans approximation for the β uncertainty level.

Solving equation (6) and taking into account formula (4), we obtain the following expression:

$$\nu_\beta = x(\beta)kT/h, \quad (9)$$

which completes the analytical description.

A quantitative pattern corresponding to equations (6) and (9) is illustrated by data in the table.

ACKNOWLEDGMENTS

The author is grateful to V.A. Il'in for creative support.

REFERENCES

1. V. P. Koshelets and G. A. Ovsyannikov, Zarubezh. Radioélektron., No. 6, 31 (1983).
2. A. L. Gudkov, V. A. Kulikov, V. N. Laptev, *et al.*, Pis'ma Zh. Tekh. Fiz. **12**, 527 (1986).
3. A. L. Gudkov, V. A. Il'in, V. N. Laptev, *et al.*, Pis'ma Zh. Tekh. Fiz. **14**, 826 (1988).
4. V. A. Il'in, V. G. Mirovskiĭ, I. A. Semin, and V. S. Étkin, Radiotekhnika, No. 12, 17 (1988).
5. H. Kanter and F. L. Vernon, J. Appl. Phys. **43**, 3174 (1972).
6. V. P. Zavaleev and K. K. Likharev, Radiotekhn. Élektron. **23**, 1268 (1978).
7. S. M. Rytov, Yu. A. Kravtsov, and V. I. Tatarskiĭ, *Introduction to Statistical Radiophysics. Random Fields* (Nauka, Moscow, 1978), Part. 2.
8. N. V. Karlov and B. M. Chikhachev, Radiotekhn. Élektron. **4**, 1047 (1959).

Translated by P. Pozdeev